

2021

## **Application of the Vortex Fluid Device (VFD) in Polysulfone Synthesis and Ultra-filtration Membrane Fabrication for water treatment purposes**

Aghil Igder  
*Edith Cowan University*

Follow this and additional works at: <https://ro.ecu.edu.au/theses>



Part of the [Engineering Commons](#)

---

### **Recommended Citation**

Igder, A. (2021). *Application of the Vortex Fluid Device (VFD) in Polysulfone Synthesis and Ultra-filtration Membrane Fabrication for water treatment purposes*. Edith Cowan University. Retrieved from <https://ro.ecu.edu.au/theses/2433>

This Thesis is posted at Research Online.  
<https://ro.ecu.edu.au/theses/2433>

# Edith Cowan University

## Copyright Warning

You may print or download ONE copy of this document for the purpose of your own research or study.

The University does not authorize you to copy, communicate or otherwise make available electronically to any other person any copyright material contained on this site.

You are reminded of the following:

- Copyright owners are entitled to take legal action against persons who infringe their copyright.
- A reproduction of material that is protected by copyright may be a copyright infringement. Where the reproduction of such material is done without attribution of authorship, with false attribution of authorship or the authorship is treated in a derogatory manner, this may be a breach of the author's moral rights contained in Part IX of the Copyright Act 1968 (Cth).
- Courts have the power to impose a wide range of civil and criminal sanctions for infringement of copyright, infringement of moral rights and other offences under the Copyright Act 1968 (Cth). Higher penalties may apply, and higher damages may be awarded, for offences and infringements involving the conversion of material into digital or electronic form.

# **Application of the Vortex Fluid Device (VFD) in Polysulfone Synthesis and Ultra-filtration Membrane Fabrication for Water Treatment Purposes**

A thesis with publications presented in fulfilment of the requirement for the degree of

**Doctor of Philosophy**

**Aghil IGDER**



© Aghil Igder, 2021

School of Engineering

Edith Cowan University

2021

## Dedication

*This PhD thesis is proudly dedicated to my beloved supervisor and my best friend **Dr Ataollah Nosrati** who sadly passed away in May 2019. “Ata” was indeed more than a supervisor he became my best friend since I started my PhD journey. As a chemical engineer and metallurgist with years of industry and academic research experiences, he was passionate about doing high quality research and teaching in chemical engineering, materials science and mineral processing, as he did at Edith Cowan University and the University of South Australia.*

*I deeply believe the world loses its value by missing such an honourable, respectful, kind and real human being. From the day we lost Ata, I always have been thinking how a man can be that precious that you feel his absence in every moment of your life. Apart from all of his kindness and beloved personality as a friend, he played the role of my elder brother who showed me how to crawl in the so-called maze of PhD. When I lost him in May 2019 I had just started walking and stepping forward to the goals we both had planned long time before! It was a real shock that may nobody could feel it. Today that I am very close to the outcomes that we planned, I wish he was around to celebrate this day with us and “Roshanak” as we planned it when having hot chocolate in Hillarys.*

*As my friend says, those we love won't go away for ever, they watch us and walk beside us every day, unseen, unheard, but always near. Still loved, still missed, and very dear.*

***I firmly believe that I was so lucky to have a part of my memories shared with “Ata” for the rest of my life, I really needed those moments and experiences with “Ata” and I am so proud that I had this privilege of working with him.***



## Abstract

Extensive studies have been performed to improve key properties of filtration membranes via controlling the fabrication process conditions as well as physical and/or chemical modification of the polymers used in membrane fabrication. The Vortex Fluid Device (VFD) is a newly invented platform which has found many applications in materials science and clean technology. The unique features of the VFD originate from a combination of different effects (e.g., micro-mixing, viscous drag, microfluidic flow, enhanced mass transfer) all resulting in faster, greener, and more efficient and better controlled chemical reactions. The main aims of this project are: (i) to investigate the utility of VFD processing in an environmentally-friendly process for PSF synthesis, (ii) fine-tuning the process conditions and consequently improving the properties of the polymer, and (iii) the application of the VFD in facilitating a time effective process for PSF ultrafiltration membrane fabrication while investigating the effect of changing the rotational speed of the VFD and Graphene Oxide (GO) incorporation into PSF based membranes along with their filtration performances.

Initially, Polysulfone (PSF) was prepared under high shear in the VFD operating in the confined mode, and its properties compared with that prepared using batch processing. Scanning electron microscopy (SEM) established that the VFD synthesised PSFs are sheet-like, for short reaction times, and fibrous for long reaction times, in contrast to spherical like products from the conventional batch synthesis. The operating parameters of the VFD were systematically varied for establishing their effect on the molecular weight ( $M_w$ ), glass transition temperature ( $T_g$ ) and decomposition temperature, featuring gel permeation chromatography (GPC), differential scanning calorimetry (DSC) and thermal gravimetric analysis (TGA) respectively. The optimal VFD prepared PSF was obtained at 6000 rpm rotational speed, 45° tilt angle and 160 °C, for 1 h with the material having a  $M_w \sim 10000 \text{ g mol}^{-1}$ ,  $T_g \sim 158 \text{ °C}$  and decomposition temperature  $\sim 530 \text{ °C}$ , which is comparable to the conventionally prepared PSF. In the next step, the synthesise process has been systematically varied to improve the main properties of the PSF, including the  $M_w$  which is now  $\sim 15500 \text{ g mol}^{-1}$ . Morphological study accompanied by BET measurement were conducted to support the results and investigate the effect of the VFD operational parameters on the properties of the new VFD synthesised PSF.

In another aspect of the research, PSF ultrafiltration (UF) membranes were fabricated using a continuous micro-mixing process under high shear in the vortex fluidic device (VFD) followed by phase inversion process of the cast solution. This involved investigating the effect of PSF concentrations (10, 15, and 20%) in 1-methyl-2-pyrrolidone (NMP) as well as the rotational speed of the VFD for a 0.5 mL/min continuously mixing process at 30 °C, on the properties of the membranes. The properties of the VFD mediated membranes were compared with those fabricated using conventional batch mixed polymer solutions (24 h magnet stirring at 60 °C, 3h sonication), with the membranes fully characterized through structural and morphological studies, hydrophilicity, and filtration performance, as well as thermal and mechanical stabilities. Use of the VFD showed a significant impact on essential mixing time by facilitating a very shorter mixing process. SEM established that in the microfluidic mixing, the PSF membranes have more finger-like cross-section, for 10% PSF concentration, and more sponge-like structure for higher concentrations. Moreover, the higher rotational speed in the VFD mediated membranes, the higher their porosity ( $84.3 \pm 2.4$ ) % and permeability ( $106 \pm 4$ ) LMH/bar which were optimal at 7k rpm.

Furthermore, to improve the properties of the membrane, GO was incorporated into the polymer solutions both using VFD and conventional mixing, resulting in GO/PSF composite membranes with enhanced properties. It was also found that compared to pristine PSF membranes, the incorporation of 1 wt.% of GO increased its permeability from ( $97 \pm 3$ ) to ( $123 \pm 4$ ) LMH/bar, salt rejection from ( $18.5 \pm 1.3$ ) to ( $34.3 \pm 1.7$ ) % and bovine serum albumin (BSA) rejection from ( $53.8 \pm 2$ ) to ( $74.2 \pm 2$ ) %, respectively.

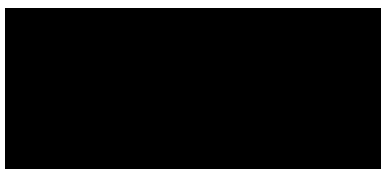
## Declaration

I certify that this thesis does not, to the best of my knowledge and belief:

- i. Incorporate without acknowledgement any material previously submitted for a degree or diploma in any institution of higher education.
- ii. Contain any material previously published or written by another person except where due reference is made in the text; or Contain any defamatory material.
- iii. I also grant permission for the Library at Edith Cowan University to make duplicate copies of my thesis as required.

Signed: Aghil Igder

Data: 10/02/2021



## Acknowledgements

Firstly, I would like to express my sincere gratitude to my family specially my mother and my father, for their continuous support during my educational life. I am forever grateful for their love, prayers, caring and sacrifices for educating and preparing me for my future. I also wish to express a very special gratitude to the love of my life, my wife, Mrs Faezeh Alizadeh, without whom nothing would have been possible. I will be owed her all that I am getting. The support she has provided, sacrifices she has done for me to be focused and successful in my plans over the last few years of my PhD program, along with the pure love she always has had to encourage and motivate me are absolutely the greatest gifts anyone has ever given me, I hope I can do something for her at least close to what she has done.

A very special appreciation goes to my supervisor Prof. Colin Raston without whom it would have not been possible to accomplish this journey. His immense scientific knowledge extensively helped me to overcome the difficulties of this research project and his dynamism, vision, sincerity, patience, motivation deeply inspired me. As an external student at Flinders University, Colin adopted me after Ata, convincingly guided and encouraged me to be professional and do the right thing even when the road got tough. Also, a special appreciation to Mrs Roshanak Armat for the very first-time introducing Colin to Ata and consequently me, which resulted in providing this fruitful journey for me.

I also would like to sincerely thank my principle supervisor Dr. Alireza Keshavarz, who supported me and facilitated the execution of this project. Not only did he scientifically support me through my research, he also, with patience and giving motivation helped me a lot to overcome the difficulties of this research project. I also would like to thank ECU for the funding of this research and specifically Heather Williams, Research Student Support Coordinator at GRS of ECU for her support with providing helpful advices whenever I needed.

In addition, I would like to thank Dr. Abdellah Shafieian, Mr. Peyman Azari, Dr. Xuan Lou, Dr. Ahmed H. Al-Antaki, Dr. Scott Pye, Dr. Masoumeh Zargar, and my other friends and colleagues who were directly and indirectly involved in this project and helped me with their insightful comments and encouragement to widen my research from various perspectives. I wish also to express my gratitude to Flinders University and specifically the Raston lab for providing this period for me to conduct and continue my research for the most part of my PhD journey.

Technical support for this research project from the mechanical workshop teams at ECU and especially physical science building at Flinders University, is gratefully acknowledged.

## List of Journal Publications Arising from this Candidature

### Journal Papers

- Aghil Igder, Scott Pye, Ahmed Hussein Mohammed Al-Antaki, Alireza Keshavarz, Colin L. Raston, Ata Nosrati, "Vortex fluidic mediated synthesis of Polysulfone", RSC Advances, 2020, 10, 14761-14767. <https://doi.org/10.1039/D0RA00602E>.
- Aghil Igder, Ahmed Hussein Mohammed Al-Antaki, Scott Pye, Alireza Keshavarz, Ata Nosrati, Colin L. Raston, "High shear vortex fluidic morphologically controlled polysulfone formed under anhydrous conditions", New J. Chem., 2021, 45, 10268. <https://doi.org/10.1039/D1NJ00834J>.
- Aghil Igder, Wanling Cai, Xuan Luo, Ahmed Hussein Mohammed Al-Antaki, Alireza Keshavarz, Ata Nosrati, Colin L. Raston, "Vortex fluidic mediated fabrication of polysulfone ultrafiltration membrane incorporated with graphene oxide", Submitted to the Journal of Membrane Science, Elsevier.
- Thaar M. D. Alharbi, Matt Jellicoe, Xuan Luo, Kasturi Vimalanathan, Ibrahim K. Alsulami, Bediea S. AL Harbi, **Aghil Igder**, Xianjue Chen, Keith A. Stubbs, Justin M. Chalker, Wei Zhang, Ramiz A. Boulos, Darryl B. Jones, Jamie S. Quinton, and Colin L. Raston, "Sub-micron moulding topological mass transport regimes in angled vortex fluidic flow", *ChemRxiv*, <https://doi.org/10.26434/chemrxiv.13141352.v1>.

# Table of Contents

<b>Dedication.....</b>	<b>ii</b>
<b>Abstract .....</b>	<b>iii</b>
<b>Declaration .....</b>	<b>v</b>
<b>Acknowledgements .....</b>	<b>vi</b>
<b>List of Journal Publications Arising from this Candidature .....</b>	<b>vii</b>
<b>Table of Contents .....</b>	<b>viii</b>
<b>List of Figures .....</b>	<b>xv</b>
<b>List of Tables .....</b>	<b>xxvi</b>
<b>List of Symbols .....</b>	<b>xxvii</b>
<b>1. Topical introduction.....</b>	<b>1</b>
1.1. Rational for research.....	1
1.2. Aims and objectives .....	3
1.3. Project overview .....	3
1.4. Literature review.....	7
1.4.1. General introduction.....	7
1.4.2. Water and wastewater treatment.....	8
1.4.3. Physical approaches.....	8
1.4.4. Chemical approaches .....	9
1.4.5. Biological approaches .....	9
1.4.6. Limitations of the wastewater treatment techniques.....	11
1.4.7. Membrane separation .....	12
1.4.8. Membrane materials types.....	18
1.4.9. Membrane fabrication.....	19

1.4.10 Improving the properties of membranes .....	24
1.4.11. Interfacial polymerisation .....	26
1.4.12. Polymerisation .....	29
1.4.13. Microfluidics.....	36
1.4.14. Microfluidic devices .....	36
1.4.15. Vortex fluid device (VFD) .....	38
1.5. Research questions .....	44
1.6. Research materials and methods .....	45
1.6.1 Materials .....	45
1.6.2. Methodologies .....	45
1.7. Thesis structure.....	49
1.8. Chapter references .....	51
<b>2. Vortex fluidic mediated synthesis of polysulfone† .....</b>	<b>59</b>
Abstract .....	59
2.1. Introduction .....	59
2.2. Experimental .....	62
2.2.1. Materials .....	62
2.2.2. PSF polymerisation .....	63
2.2.3. Characterization .....	63
2.3. Results and discussion .....	64
2.3.1. Synthesis of DiNa salt of BPA .....	64
2.3.2. Synthesis of PSF.....	65
2.3.3. Varying VFD operational parameters.....	66
2.4. Conclusions .....	70

2.5. Conflicts of interest.....	71
2.6. Acknowledgements.....	71
2.7. Chapter references .....	72
<b>3. High shear vortex fluidic morphologically controlled polysulfone formed under anhydrous conditions† .....</b>	<b>75</b>
Abstract.....	75
3.1. Introduction .....	76
3.2.1. Materials and methods.....	79
3.2.2. Preparation of PSF .....	79
3.2.3. Characterisation.....	80
3.3.1. PSF synthesis.....	81
3.3.2. Effect of VFD rotational speed.....	83
3.3.3. Effect of temperature .....	84
3.3.4. Effect of tilt angle.....	87
3.3.5. Effect of time.....	88
3.4. Conclusions .....	90
3.5. Conflicts of interest.....	90
3.6. Acknowledgements.....	90
3.7. Chapter references .....	91
<b>4. Vortex fluidic mediated fabrication of polysulfone ultrafiltration membranes incorporating graphene oxide† .....</b>	<b>94</b>
Abstract.....	95
4.1. Introduction .....	95
4.2. Experimental.....	98
4.2.1. Materials .....	98



4.2.2. Membrane fabrication .....	99
4.2.3. Characterisation .....	101
4.3. Results and discussion .....	104
4.3.1. Structure of pristine PSF and GO/PSF composite membranes.....	104
4.3.2. Contact angle measurement: .....	105
4.3.3. Morphological studies .....	106
4.3.4. Porosity and pore size.....	109
4.3.5. Membrane filtration performance .....	111
4.3.6. Mechanical and thermal stability of the membranes .....	114
4.4. Conclusion.....	116
4.5. Conflicts of interest.....	117
4.6. Acknowledgements.....	117
4.7. Chapter references .....	118
<b>5. General discussion .....</b>	<b>123</b>
5.1. Chapter references .....	130
<b>6. Conclusions and future work recommendations.....</b>	<b>132</b>
6.1. Conclusions.....	132
6.2. Future research directions .....	136
<b>Appendix A. Electronic Supplementary Information (ESI) of “Vortex fluidic mediated synthesis of polysulfone” .....</b>	<b>138</b>
A.1. Schematic structure of polysulfone (PSF).....	139
A.1.1. PSF repeating unit.....	139
A.1.2. Polysulfone (PSF) with a number of repeating units.....	139
A.1.3. PSF polymerization via conventional technique .....	139

A.2. Experimental setup for PSF polymerization via the VFD.....	140
A.3. FTIR spectra .....	142
A.3.1. BPA & DiNa salt of BPA.....	142
A.3.2. Polysulfone (PSF) .....	143
A.4. NMR spectra .....	143
A.4.1. Bisphenol A (BPA) .....	144
A.4.2. Disodium salt of BPA .....	145
A.4.3. 4,4-dichlorodiphenyl sulphone (DCDPS) .....	146
A.4.4. Polysulfone (PSF) .....	146
A.5. GPC curves .....	147
A.5.1. GPC traces of VFD ( $T_4$ , 6000 rpm), commercial and conventional PSF .....	148
A.5.2. Effect of rotational speed .....	149
A.5.3. Effect of temperature .....	150
A.5.4. GPC traces of VFD ( $T_{11}$ , 160 °C), commercial and conventional PSF .....	151
A.5.5. Effect of tilt angle .....	152
A.5.6. Effect of time .....	153
A.5.7. GPC traces on the VFD synthesized PSFs ( $T_1 - T_{22}$ ), conventional and commercial PSFs. ....	154
A.6. Glass transition temperature ( $T_g$ ).....	155
A.6.1. Comparison between $T_g$ obtained for commercial PSF and VFD prepared PSF in different $\omega$ .....	155
A.7. TGA analysis.....	155
A.8. SEM images.....	157
A.9. Chapter references .....	157

**Appendix B. Electronic Supplementary Information (ESI) of “High shear vortex fluidic morphologically controlled polysulfone formed under anhydrous conditions” ..... 158**

B.1. Experimental settings .....	159
B.2. Heating unit calibration curve .....	160
B.3. NMR spectra .....	161
B.3.1. Bisphenol A (BPA) .....	161
B.3.2. 4,4-dichlorodiphenyl sulphone (DCDPS).....	162
B.3.3. Polysulfone (PSF) .....	163
B.4. Chapter references .....	165

**Appendix C. Electronic Supplementary Information (ESI) of “Vortex fluidic mediated fabrication of polysulfone ultrafiltration membranes incorporating graphene oxide” .... 166**

C.1. Experimental setup.....	167
C.2. Thermal stability .....	167
C.3. Contact angle measurements.....	168
C.3. SEM images.....	168
C.3.1. SEM of the top of the membranes .....	168
C.3.2. SEM of the bottom of the membranes.....	169
C.4. BSA rejection using UV light absorbance.....	169
C.5. Mechanical properties .....	170
C.5.1. Effect of PSF concentration in the VFD on tensile strength and elongation to break. .....	170
C.5.2. Effect of VFD rotational speed on tensile strength and elongation to break. ....	170
C.5.3. Effect of GO content on tensile strength and elongation to break of the VFD mediated membranes.....	171

<b>Appendix D. Sub-micron moulding topological mass transport regimes in angled vortex fluidic flow .....</b>	<b>172</b>
Contents of the full paper .....	173
Abstract .....	173
D.1. Introduction .....	174
D.2. General materials and characterisation methods for polymer moulding .....	175
D.3. Moulding of PSF in the VFD .....	176
D.4. Discussion .....	180
D.5. Molecular drilling control experiments .....	182
D.6. Real time VFD processing small angle neutron scattering (SANS) .....	193
D.7. Representation of the different fluid flows in the VFD .....	195
D.8. Conclusion .....	196
D.8. Chapter references .....	198

## List of Figures

Figure 1. 1. Components of a typical interfacially polymerized NF membrane [5].....	5
Figure 1. 2. Two types of MBR technology: (a) Side-stream and (b) submersed configuration [59].....	11
Figure 1. 3. Transport mechanism of suspended particles to the surface of membranes [59]. .....	13
Figure 1. 4. Schematic diagram of the basic membrane separation process [7]. ....	14
Figure 1. 5. Membranes separation capabilities based on their average pore diameter [7]..	15
Figure 1. 6. Structure of a TFC-NF membrane [76].....	19
Figure 1. 7. Schematic diagram of the immersion phase inversion process [78].....	21
Figure 1. 8. Schematic of electrospinning setup [14]. ....	22
Figure 1. 9. Conceptual illustration of hydrophilic “gate” and hydrophobic nanochannel [1]. .....	23
Figure 1. 10. Schematic illustration of fabrication process of TFC membrane using the IP process involving N-aminoethyl piperazine propane sulfonate (AEPPS) to improve hydrophilicity [88].....	27
Figure 1. 11. Schematic model of separation in TFC membrane fabricated via BDSA and TMC [89].....	28
Figure 1. 12. Schematic illustration of hypothesized mechanism of GO TFN membrane [91]. .....	28
Figure 1. 13. Structure of the (a) Diphenylsulfone group as a repeating unit in (b) Dichlorodiphenyl sulfone.....	32
Figure 1. 14. Schematic illustration of the principles of microfluidics and fluid flows[99]. ....	36
Figure 1. 15. Schematic diagram of the spinning disc processor in Chitosan Nanoparticles manufacturing [101]. ....	37

Figure 1. 16. Illustration of feeding two stable stream into a RTP [103].....	37
Figure 1. 17. An overall schematic view of the microfluidic devices placement, feeding and working [42]. .....	38
Figure 1. 18. Cross section showing the components of the VFD [31].....	39
Figure 1. 19. Double-helical fluid flow created in the VFD with a reduction in helical pitch for higher rotational speeds [40].....	43
Figure 1. 20. Experimental setup for conventional method of PSF synthesise .....	46
Figure 1. 21. Experimental setup for the membrane fabrication steps including (a) continuous VFD setup, (b) adjusted casting knife on a glass surface, (c) fabricated membranes (pure PSF and GO/PSF composite membranes), and (d) the dead-end filtration system adjusted on a magnet stirrer for stirring the solution inside. ....	47
Figure 2. 1. $^1\text{H}$ -NMR spectra of (a) BPA and (b) DiNa salt of BPA obtained in the VFD in THF. $^1\text{H}$ -NMR measurements were recorded in DMSO- $d^6$ . ....	65
Figure 2. 2. Effect of VFD operating parameters on ( a) rotational speed (rpm), (b) temperature ( $^{\circ}\text{C}$ ), (c) tilt angle ( $^{\circ}$ ), and (d) time (min) (horizontal axis) on the resulting $M_w$ obtained from UV and RI detectors (blue and red histograms, respectively, in the left vertical axis), and on $T_g$ and yield (%) (green and violet lines, respectively, in the right vertical axis). ....	67
Figure 2. 3. Comparison between (a) GPC traces (UV detector) and (b) DSC thermograms of commercial, conventional and VFD synthesized PSF ( $T_{22}$ at 6000 rpm, $160^{\circ}\text{C}$ , $45^{\circ}$ , and 60 min). (b) Temperature scan in $T_g$ measurements were conducted between $30^{\circ}\text{C}$ and $230^{\circ}\text{C}$ at $10^{\circ}\text{C min}^{-1}$ . ....	69
Figure 2. 4. SEM images of PSF for (a) commercial material, (b) material formed using conventional batch processing, (c) material formed in the VFD at the optimised s ( $T_{22}$ at 6000 rpm, $160^{\circ}\text{C}$ , $45^{\circ}$ , and 60 min). PSF synthesised in the VFD at 6000 rpm, $160^{\circ}\text{C}$ , $\theta 45^{\circ}$ for (d) 15 min, (e) 30 min, and (f) 90 min reaction time. All the sample were drop cast and coated with ca 5 nm layer of Pt. ....	70

Figure 3. 1. (a) Salient features of the VFD housing a quartz tube with a hemispherical shaped base, and associated topological fluid flow, and (b) the one step PSF polymerisation under anhydrous condition. ....	78
Figure 3. 2. FTIR spectra of (a) commercial, conventional, and VFD synthesized PSF, and (b) <sup>1</sup> H-NMR spectra (CDCl <sub>3</sub> ) of the VFD synthesised PSF (S10). VFD processing was at 6k rpm, 160 °C, 45 tilt angle, and 60 min reaction time. ....	82
Figure 3. 3. Comparison between (a) molecular weight distribution, (b) DSC thermograms, (c) SEM images, and (d) nitrogen adsorption analysis of the VFD synthesised PSF at different rotational speeds, (S1-S6, at ω 3k - 8k rpm, θ 45°, T 150 °C, and 60 min). ....	84
Figure 3. 4. Comparison between (a) molecular weight distribution, (b) DSC thermograms, (c) SEM images, and (d) nitrogen adsorption analysis of the VFD synthesised PSF at different temperatures, (S7-S11, at T 120 - 170 °C, ω 6k rpm, θ 45°, and t 60 min). ....	85
Figure 3. 5. Comparison between (a) molecular weight distribution, (b) DSC thermograms, (c) SEM images, and (d) nitrogen adsorption data of the VFD synthesised PSF formed at different tilt angles, S12-S18, θ 0, 15°, 30°, 45°, 60°, 75° and 90°, ω 6k rpm, T 160 °C, and t 60 min. ..	87
Figure 3. 6. Comparison between (a) molecular weight distribution, (b) DSC thermograms, (c) SEM images, and (d) nitrogen adsorption data for VFD synthesised PSF at different reaction times, (S19-S22, at ω 6k rpm, θ 45°, T 160 °C, and t 15, 30, 60 and 180 min), compared to commercial PSF and conventional synthesised PSF. ....	89
Figure 4. 1. Schematic of the membrane fabrication steps: (a) VFD processing step, (b) casting on a glass surface using an adjustable knife, (c) phase inversion of the cast layer into the Milli-Q water as the coagulation bath, and (d) washing and storing the fabricated membranes in Milli-Q water at 5 °C. ....	101
Figure 4. 2. (a) ATR-FTIR spectra and (b) Raman spectra of GO powder, pristine PSF (UFM7) and 2% GO/PSF composite membranes (UFM12), (c) XRD patterns of GO, PSF membrane, and GO/PSF composite membranes with different GO contents (0.25-2%), and (d) water contact angle of PSF membrane and GO/PSF composite membranes for the different GO content in (c). ....	106

Figure 4. 3. SEM cross-sections of the membranes fabricated using the phase inversion process, (a) from 15% PSF solution prepared through conventional mixing (24 h magnet stirring, 3h degassing at 60°C), (b) 10%, (c) 15%, (d) 20% PSF solutions mediated in the VFD (at 6k rpm, 30°C, 45°, and 0.5 mL/min). SEM cross-section of the membranes obtained from a 15% PSF solution processed in the VFD at 30°C,  $\theta$  45°, and 0.5 mL/min flow rate with different rotational speeds (e) 4k, (f) 5k, (g) 6k, (h) 7k, (i) 8k rpm. Cross-sections of the GO/PSF composite membranes obtained from VFD processing of 15% PSF solutions with different GO content (j) 0.25 wt. %, (k) 0.5% wt. %, (l) 1wt. %, (m) 2wt. %, (n) and conventional mixing process of 15% PSF and 1 wt. % GO content. SEM micrographs of the (o) top surface and (p) bottom surface of UFM7 obtained from a 15% PSF solution for the VFD operating at 7k rpm. All the sample were drop casted and sputtered coated with ca 5 nm layer of Pt. ....108

Figure 4. 4. The effect of VFD rotational speed on preparing PSF membranes impacting on their properties: (a) Porosity, pore size, and (c) permeability and salt and BSA rejection performance. The effect of GO concentration (0.25 to 2 wt. %) for GO/PSF composite membranes on their (b) porosity, pore size and (d) permeability, and salt and BSA rejection performance. ....113

Figure 4. 5. (a) Young's modulus measured from mechanical testing for tensile strength under a force ramped at  $1 \text{ N min}^{-1}$  up to 18 N at room temperature for all of the bare PSF (UFM0-8) and GO/PSF membranes (UFM9-13) fabricated using VFD or conventionally prepared solutions, (b) TGA traces of pure PSF and GO/PSF composite membranes with different GO content (0.25-2 wt. %) fabricated using VFD processing (UFM0 and UFM9-13), using heating rate of  $10 \text{ }^{\circ}\text{C min}^{-1}$  up to 850  $^{\circ}\text{C}$  under nitrogen and then air to 1050  $^{\circ}\text{C}$ . Delta Y represents the mass loss percentage. DTG P=DTG Peak represents the decomposition temperature for mass loss obtained from derivative weight % curves, DTG  $P_1$  represents the decomposition temperature of main mass loss under  $\text{N}_2$ . ....115

Figure A. 1. Experimental setup for investigating the experimental parameters in a systematic approach. ....141



Figure A. 2. FTIR spectrums of BPA and DiNa salt of BPA, b) FTIR spectrums of DiNa salt of BPA obtained from first step of polymerization in both VFD and batch processing for different retention times from 30 min to 4h in comparing the effect of time in water dissipation in producing the DiNa salt of BPA, using VFD or batch processing. ....	142
Figure A. 3. FTIR spectra of the VFD and conventional synthesized PSF. VFD product was synthesised at 6000 rpm, 160 °C, 45 tilt angle, and 60 min reaction time. ....	143
Figure A. 4. <sup>1</sup> H-NMR of BPA as a starting material in first step of PSF polymerization, using DMSO-d <sub>6</sub> as the NMR solvent. ....	144
Figure A. 5. <sup>13</sup> C-NMR of BPA as a starting material in first step of PSF polymerization.....	144
Figure A. 6. <sup>1</sup> H-NMR of DiNa salt of BPA, as the intermediate product in PSF polymerization. ....	145
Figure A. 7. <sup>13</sup> C-NMR of DiNa salt of BPA as the intermediate product in PSF polymerization. ....	145
Figure A. 8. <sup>1</sup> H-NMR of DCDPS as a starting material in second step of PSF polymerization. ....	146
Figure A. 9. <sup>13</sup> C-NMR of DCDPS as a starting material in second step of PSF polymerization. ....	146
Figure A. 10. <sup>1</sup> H-NMR spectra of VFD prepared PSF at 6000 rpm, 160 °C, 45 tilt angle, and 60 min reaction time.....	147
Figure A. 11. <sup>13</sup> C-NMR spectra of VFD prepared PSF at 6000 rpm, 160 °C, 45 tilt angle, and 60 min reaction time.....	147
Figure A. 12. Comparison between GPC traces of commercial, conventional and VFD synthesized (T <sub>4</sub> at 6000 rpm, 150 °C, 45°, and 30 min) PSF detected using the UV detector. ....	148
Figure A. 13. Comparison between GPC traces of commercial, conventional and VFD synthesized (T <sub>4</sub> at 6000 rpm, 150 °C, 45°, and 30 min) PSF detected using the UV detector. ....	148

Figure A. 14. GPC curves of the VFD synthesized PSF's in different rotational speed, obtained from T <sub>1</sub> to T <sub>6</sub> using the UV detector.....	149
Figure A. 15. GPC curves of the VFD synthesized PSF's in different rotational speed, obtained from T <sub>1</sub> to T <sub>6</sub> using the RI detector. ....	149
Figure A. 16. GPC curves of the VFD synthesized PSF's in different temperatures, obtained from T <sub>9</sub> to T <sub>12</sub> using the UV detector. ....	150
Figure A. 17. GPC curves of the VFD synthesized PSF's in different temperatures, obtained from T <sub>9</sub> to T <sub>12</sub> using the RI detector.....	150
Figure A. 18. Comparison between GPC traces of commercial, conventional and VFD synthesized (T <sub>11</sub> at 160 °C) PSF detected using the UV detector. ....	151
Figure A. 19. Comparison between GPC traces of commercial, conventional and VFD synthesized (T <sub>11</sub> at 160 °C) PSF detected using the RI detector. ....	151
Figure A. 20. GPC curves of the VFD synthesized PSF's in different tilt angles, obtained from T <sub>13</sub> to T <sub>19</sub> using the UV detector.....	152
Figure A. 21. GPC curves of the VFD synthesized PSF's in different tilt angles, obtained from T <sub>13</sub> to T <sub>19</sub> using the RI detector. ....	152
Figure A. 22. GPC curves of the VFD synthesized PSF's in different retention times, obtained from T <sub>20</sub> to T <sub>22</sub> using the UV detector.....	153
Figure A. 23. GPC curves of the VFD synthesized PSF's in different retention times, obtained from T <sub>20</sub> to T <sub>22</sub> using the RI detector. ....	153
Figure A. 24. GPC curves of the VFD synthesized PSF's in different operational condition, obtained from T <sub>1</sub> to T <sub>22</sub> , vs commercial and conventional PSFs, detected using the UV detector.....	154
Figure A. 25. GPC curves of the VFD synthesized PSF's in different operational condition, obtained from T <sub>1</sub> to T <sub>22</sub> , vs commercial and conventional PSFs, detected using the RI detector. ....	154

Figure A. 26. DSC thermograms of commercial and VFD synthesised PSF of T <sub>2</sub> , T <sub>4</sub> , and T <sub>6</sub> . Samples were cycled from 30 °C to 230 °C at a rate of 10 °C min <sup>-1</sup> .	155
Figure A. 27. TGA traces of commercial, conventional and VFD synthesized PSF (T <sub>9</sub> -T <sub>12</sub> ), heating at a rate of 20 °C min <sup>-1</sup> up to 850 °C under Nitrogen and then air to 1050 °C. ΔY =Delta Y which represents the mass loose percentage in every stage. DTG P=DTG Peak represents the decomposition temperature of every mass losing step obtained from derivative weight % curve, DTG P <sub>1&amp;2</sub> represent the decomposition temperature of main mass losing while using N <sub>2</sub> and air, respectively.	156
Figure A. 28. SEM images of PSF for (a) commercial material, (b) material formed using conventional batch processing, (c) material formed in the VFD at the optimised s (T22 at 6000 rpm, 160 °C, 45°, and 60 min). PSF synthesised in the VFD at 6000 rpm, 160 °C, q 45° for (d) 15 min, (e) 30 min, and (f) 90 min reaction time. All the sample were drop cast and coated with ca 5 nm layer of Pt.	157
Figure B. 1. Calibration curve of the heating unit.	160
Figure B. 2. (a) Experimental setup for distilling, and (b) keeping distilled DMSO under nitrogen.	161
Figure B. 3. <sup>1</sup> H-NMR of BPA as a monomer in PSF polymerization, using DMSO-d <sub>6</sub> as the NMR solvent.[1]	161
Figure B. 4. <sup>13</sup> C NMR of BPA as a monomer PSF polymerization, using DMSO-d <sub>6</sub> as the NMR solvent [1].	162
Figure B. 5. <sup>1</sup> H-NMR of DCDPS as the second monomer in PSF polymerization, using DMSO-d <sub>6</sub> as the NMR solvent [1].	162
Figure B. 6. <sup>13</sup> C-NMR of DCDPS as the second monomer in PSF polymerization, using DMSO-d <sub>6</sub> as the NMR solvent [1].	163
Figure B. 7. <sup>1</sup> H-NMR spectra of commercial PSF, using CDCl <sub>3</sub> as the NMR solvent.	163
Figure B. 8. <sup>13</sup> C-NMR spectra of conventional synthesised PSF, using CDCl <sub>3</sub> as the NMR solvent.	164

Figure B. 9. $^{13}\text{C}$ -NMR spectra of conventional prepared PSF, using $\text{CDCl}_3$ as the NMR solvent.	164
Figure B. 10. $^{13}\text{C}$ -NMR spectra of VFD synthesised PSF at $\omega$ 6k rpm, T 160 °C, $\theta$ 45 tilt angle, and 60 min reaction time, using $\text{CDCl}_3$ as the NMR solvent.	165
Figure C. 1. Experimental setup for the membrane fabrication steps including (a) continuous VFD setup, (b) adjusted casting knife on a glass surface, (c) fabricated membranes (pure PSF and GO/PSF composite membranes), (d) Dead-end filtration system adjusted on a magnet stirrer for stirring the solution inside the system and pressurising the solution using nitrogen gas up to 4 bar to generate the final permeate.	167
Figure C. 2. Images of captive needle drop on (a) pristine PSF and GO/PSF composite membranes with (b) 0.25, (c) 0.5, (d) 1, and (e) 2 wt.% GO content, while 5 $\mu\text{L}$ milli-Q water was dispensed on their surface for a period of 10 seconds, whereupon the droplet surface contact angle was recorded.	168
Figure C. 3. SEM images from the top surface of the bare PSF membranes obtained from a 15% PSF solution (a) conventional mixed, mediated in the VFD at 30 °C, 45°, and 0.5 mL/min with different rotational speeds (b) 4k, (c) 5k, (d) 6k, (e) 7k, and (f) 8k rpm.	168
Figure C. 4. SEM images from the bottom surface of the bare PSF membranes obtained from a 15% PSF solution (a) conventional mixed, mediated in the VFD at 30°C, 45°, and 0.5 mL/min with different rotational speeds (b) 4k, (c) 5k, (d) 6k, (e) 7k, and (f) 8k rpm.	169
Figure C. 5. UV-vis spectra of BSA from the permeate of the BSA filtration process for a 1000 mg/L solution, using pure PSF or GO/PSF membranes in a dead-end filtration system under 3 bars and 1 bar pressures.	169
Figure C. 6. Typical stress–strain curves of PSF membranes fabricated in different PSF concentrations (10, 15, 20%) using VFD mixing.	170
Figure C. 7. Typical stress–strain curves of PSF membranes fabricated from 15% PSF solutions from VFD mixing process in different rotational speeds using conventional mixing process.	170

Figure C. 8. Typical stress–strain curves of bare PSF membrane and GO/PSF composite membranes fabricated from 15% PSF solutions with different GO content (0.25-2%) using VFD and conventional mixing processes. ....171

Figure D. 1. SEM image of the thin-film of PSF created in the VFD tube (20 mm OD, 17.5 mm ID) at 6k rpm rotational speed,  $\theta = 5^\circ$  and room temperature during 15 min, after adding 1 mL of 50 mg/ml of PSF dissolved in DCM. ....176

Figure D. 2. Locations of samples S1, S2 and S3 taken from the PSF thin-film formed in the VFD; sample S1A and S1B refer to the interface of film with the tube and air from the bottom of the tube respectively, and similarly S2A and S2B, and S3A and S3B, from the middle and top of the tube. ....177

Figure D. 3. SEM images of S1, S2, and S3 from both sides (left: bottom of the thin film, right; upper side of the thin-film) of a thin-film created in the VFD (20 mm OD tube) at 6k rpm,  $\theta = 5^\circ$ , at room temperature during 15 min of processing. ....177

Figure D. 4. SEM images of the central inner surface of the film (S2A) after VFD processing (20 mm OD, 17.5 mm ID tube) in toluene, at room temperature  $\omega$  7k rpm,  $\theta$  45° for ~1h, after washing with hexane. ....178

Figure D. 5. SEM images of the central inner surface of the film (S2A) after VFD processing (20 mm OD tube) in water, at room temperature,  $\omega$  7k rpm,  $\theta$  45°, for ~1h, after washing with hexane. ....179

Figure D. 6. SEM images of the central upper surface (S2B) after VFD processing, at room temperature  $\omega$  7k rpm,  $\theta$  45° for ~1h, in (A) toluene and (B) water, after washing with hexane and drying with nitrogen gas for 2h. ....179

Figure D. 7. SEM images of the central inner surface of the film (S2A) after VFD processing (20 mm OD tube) in toluene, at room temperature  $\omega$  7k rpm,  $\theta$  45° for ~1h, and drying with nitrogen gas for 2h, without washing with hexane prior to SEM imaging. ....179

Figure D. 8. Signature of the pattern of the double-helical flows formed at the interface of the glass tube and a thin film of polysulfone (ca 5  $\mu$ m) formed in toluene at 20 °C,  $\theta = 45^\circ$ , 7k rpm

rotational speed, along the length of the tube, with the arrow representing the rotational direction of the axis of the tube [1].	180
Figure D. 9. Schematic steps of shear stress ‘molecular drilling’ of holes on polysulfone with their signature retained at the glass-polymer interface post positional shift of the double-helical fluid flow [1].	181
Figure D. 10. SEM images of PSF thin-film created in the VFD tube (20 mm OD) at 6k rpm, $\theta = 5^\circ$ at room temperature during 15 min of evaporation of DCM: (a) S1A, (b) S2A, (c) S3A and (d) S2B, revealing smooth surfaces present, prior to processing in toluene.	183
Figure D. 11. SEM images of S1, S2, and S3 from both sides (left: bottom of the thin film (A), right; upper side of the thin-film (B) of the thin-film processed in toluene at 7k rpm, $\theta = 45^\circ$ , room temperature, and 30 min processing, then washed with hexane, and dried under nitrogen gas.	184
Figure D. 12. SEM images of S1, S2, and S3 from both sides (left: bottom of the thin-film (A), right; upper side of the thin-film (B) of the thin-film processed in toluene at 5k rpm, $\theta = 45^\circ$ , room temperature, for 30 min processing.	185
Figure D. 13. SEM images of S1, S2, and S3 from both sides (left: bottom of the thin film (A), right; upper side of the thin-film (B) of the thin-film processed in toluene at 3.5k rpm, $\theta = 45^\circ$ , room temperature, for 30 min.	186
Figure D. 14. SEM images of S1, S2, and S3 from both sides (left: bottom of the thin film (A), right; upper side of the thin-film (B) of the thin-film processed in toluene at 7k rpm, $\theta = 30^\circ$ , room temperature, for 30 min.	187
Figure D. 15. SEM images of S1, S2, and S3 from both sides (left: bottom of the thin film (A), right; upper side of the thin-film (B) of the thin-film processed in toluene at 5k rpm, $\theta = 30^\circ$ , room temperature, for 30 min.	188
Figure D. 16. SEM images of S1, S2, and S3 from both sides (left: bottom of the thin film (A), right; upper side of the thin-film (B) of the thin-film processed in toluene at 3.5k rpm, $\theta = 30^\circ$ , room temperature, for 30 min.	189

Figure D. 17. SEM images of S1, S2, and S3 from both sides (left: bottom of the thin film (A), right; upper side of the thin-film (B) of the thin-film processed in toluene at 7k rpm, $\theta = 60^\circ$ , room temperature, for 30 min. ....	190
Figure D. 18. SEM images of S1, S2, and S3 from both sides (left: bottom of the thin film (A), right; upper side of the thin-film (B) of the thin-film processed in toluene at 5k rpm, $\theta = 60^\circ$ , room temperature, for 30 min. ....	191
Figure D. 19. SEM images of S1, S2, and S3 from both sides (left: bottom of the thin film (A), right; upper side of the thin-film (B) of the thin-film processed in toluene at 3.5k rpm, $\theta = 60^\circ$ , room temperature, for 30 min. ....	192
Figure D. 20. Real time SANS scattering in the VFD for 2 mL of toluene-d8 in a 20 mm OD quartz tube (no PSF coating) rotated at 5k rpm for 2 hours, at room temperature, $\theta = 45^\circ$ [1]. ....	194
Figure D. 21. Real time SANS scattering in the VFD for toluene-d8 in a PSF coated 20 mm OD quartz rotated at 3.5k, 5k and 7k rpm (using 5, 2 and 1 mL of toluene-d8, respectively), for 2 hoursroom temperature, $\theta = 45^\circ$ [1]. ....	195
Figure D. 22. Representation of the different fluid flows, and the collapse of circular Coriolis force flow and double-helical flow from Faraday waves into spicular flow [1]. ....	195

## List of Tables

Table 1. 1. Overview of pressure-driven membrane processes and their characteristics [6, 62]. .....	15
Table 1. 2. Pros and cons of polymeric membranes [59]. .....	19
Table 1. 3. Chemical structure and Glass-Transition Temperature, $T_g$ , of PS, PES, PPSF [97].	32
Table 1. 4. $T_g$ of polysulfones prepared from polycondensation of DCDPS with various Bisphenols [97].....	33
Table 2. 1. Chemical structure and glass-transition temperature, $T_g$ , of PSF, PES, PPSF [1]...	61
Table 2. 2. $T_g$ of PSFs formed from poly-condensation of DCDPS with various BP types [1].	61
Table 4. 1. Experimental conditions and material compositions for mixing using conventional batch processing and continuous flow VFD processing. ....	100
Table A. 1. List of experiments conditions for optimizing the PSF polymerisation using the VFD in confined mod. ....	140
Table A. 2. TGA measurements settings .....	156
Table B. 1. Experimental conditions for PSF synthesise using a nitrogen sealed VFD tube in the confined mode. ....	159
Table B. 2. Reported and measured melting point of different materials using melting point measurement and heating unit controller. ....	160
Table B. 3. Calculated experiments temperatures. ....	160
Table C. 1. STA measurements settings.....	167
Table D. 1. Control experiments for determining the ‘molecular drilling’ on a PSF thin film in the VFD tube, in high shear fluid flow at room temperature. * .....	182



## List of Symbols

### Nomenclature

$M_n$	number average molecular weight (kg/mol)
$M_w$	weight average molecular weight (kg/mol)
PDI	polydispersity
$T_g$	glass transition temperature (°C)
$T$	Thickness of the membrane (m, cm)
$T$	Temperature (°C)
$t$	time
$\Delta t$	time of filtration
$A$	Effective surface area of membrane (cm <sup>2</sup> , m <sup>2</sup> )
$J$	permeate flux (L/m <sup>2</sup> h)
$L$	water permeability (L/(m <sup>2</sup> h bar)) or (LMH/bar)
$Q$	volume of the permeate water per unit time (m <sup>3</sup> /s)
$M_w$	wet membrane weight (g)
$M_d$	dry membrane weight (g)
$L$	length (m)
$m$	flow rate (mL/min)
$P$	pressure (bar)
$\Delta P$	operational pressure (bar)
$r_m$	mean pore radius (nm, $\mu$ m)
$C_0$	components (salt and/or BSA) concentration of the feed (g/l)
$C_1$	components (salt and/or BSA) concentration of the permeate (g/l)
$r$	pore size (m, mm, $\mu$ m)
OD	outside diameter of the tube (mm)
ID	inside diameter of the tube (mm)
$S$	salinity
$d$	diameter (m)/ pore dimension (m)
FT-IR	Fourier transform infrared spectroscopy
NMR	Nuclear Magnetic Resonance spectroscopy

GPC	Gel Permeation Chromatography
TGA	Thermal Gravimetric Analysis
DSC	Differential scanning calorimetry
SANS	Small-angle neutron scattering
SAXS	Small-angle x-ray scattering
DLS	Dynamic Light Scattering
STA	Simultaneous Thermal Analysis
SEM	Scanning Electron Microscopy
BET	Brunauer–Emmett–Teller measurement
DMA	Dynamic Mechanical Analysis
UV	Ultraviolet
RI	Refractive Index
NMP	N-methyl pyrrolidone
DCM	Dichloromethane, Methylene chloride
PSF	polysulfone
PES	polyethersulfone
PE	polyethylene
PTFE	polytetrafluoroethylene
PVDF	poly(vinylidene fluoride)
PP	polypropylene
PAN	polyacrylonitrile

### **Greek Letters**

$\omega$	rotational speed (rpm)
$\epsilon$	porosity
$\rho$	density (g/cm <sup>3</sup> )
$\theta$	angle (°)
$\eta$	water viscosity
$\mu$	dynamic viscosity (Pa.s)

# Chapter 1

## Topical introduction

### 1.1. Rational for research

Population growth, globalisation, industrialisation, and urbanisation are major contributors to water scarcity around the world. During last few decades, these factors have led to significant increases in global water consumption (e.g., domestic, agricultural, industrial, and municipal uses), wastewater generation as well as environmental pollution [1]. Under these circumstances, the development of novel industrial water purification processes requiring less energy is of vital importance. To date, different approaches including chemical, physical, and biological techniques have been used to produce purified water from the secondary resources including seawater and industrial wastewater. However, those conventional methods have been facing some limitations such as large footprint, generating large amounts of sludge, high capital and operation costs (CAPEX), and there is an urgent need for precise controlling systems and skilful operators, etc. [2, 3]. Therefore, there is an ongoing research on membrane separation processes to replace conventional separation methods due to their inherently less energy usage requirement, high efficiency, and environmentally friendliness [1].

Currently, pressure-driven membrane processes such as Micro-Filtration (MF), Ultra-Filtration (UF), Nano-Filtration (NF), and Reverse Osmosis (RO) are considered as well established and reliable membrane separation processes [4]. NF membranes with characteristics between RO and UF membranes and the capability of separating the small pollutants with molecular weight in the range of 100-1000 Da are being widely used in water softening, industrial wastewater pre-treatment/treatment, salt recovery and desalination [1, 5-8]. This is mainly due to their low operating pressures, and subsequently, low investment and maintenance costs, suitable permeability and reasonable efficiency [9]. In order to fabricate the UF membrane as well as the support layer in NF membranes suitable for different applications with specific conditions, a variety of fabrication methods such as phase inversion [10-12], interfacial polymerisation [5, 13] and electrospinning [1, 14, 15] have been introduced.

However, the water industry still faces significant challenges including high fabrication cost and limited durability and stability (chemical, mechanical and thermal) of filtration membranes [5, 6]. Hence, there is a pressing need for new knowledge and better understanding of the filtration membranes and improving their properties to develop robust, cost-effective, and environmentally friendly processes for water and wastewater treatment.

Advanced polymers and ceramics are the most common materials used for NF/UF/MF membrane fabrication [10]. Taking into account that the key properties of polymeric membranes strongly depend upon polymer characteristics (e.g., thermal/chemical/mechanical stability, Molecular Weight ( $M_w$ ) and glass transition temperature ( $T_g$ )), synthesizing advanced polymers with desirable properties is gaining significant attention in recent years [10, 12, 16, 17]. However, most of the new processes developed for synthesising polymers [18] or improving their properties are costly and hence, economically unviable [19-28]. The Vortex Fluid Device (VFD) is a newly invented microfluidic platform which has potential to address this major challenge. This is mainly due to the fact that during the last few years, the VFD has found applications in different fields such as exfoliating 2D materials [29, 30], controlling chemical reactivity and selectivity [31], amide synthesis reactions [32], pharmaceutical applications [33, 34], fabricating composite nanomaterials [35, 36], the growth of the nanoparticles on carbon nanotubes [35], controlling Diels–Alder reactions [37], breaking down polyethylenamines [38], and controlling the pore sizes of the mesoporous silica [39], along with an understanding of the topological fluid flow in the VFD and associated processing principles and applications [40].

To date, extensive studies have been done in the application of polymeric materials for fabrication of UF/NF membranes and also in improving their mechanical, chemical, and thermal properties. However, using a novel approach to produce high quality filtration membranes with engineered polymers via a cost-effective process is of great importance. Considering the recent studies performed using the VFD [29-42], its application for synthesizing PSF and also fabricating UF membranes would be new and novel materials processing approaches.

## **1.2. Aims and objectives**

This project aims basically to investigate the ability of better controlling the polymerisation process and/or manipulate the process conditions to enhance the polymers' characteristics and improve the fabricated UF membranes' efficiency and properties. To be more specific, the specific key outcomes of this proposed research project are:

1. Exploring the utility of the VFD as a novel platform in synthesising PSF as a common polymer in UF membrane fabrication, for the first time.
2. Optimising the polymerisation process conditions inside the VFD to manipulate and control the polymer synthesis process in a simple, fast, and scalable approach to improve the properties of the VFD synthesised PSF.
3. Modifying the UF membranes with desired/engineered properties in a more cost-effective and environmentally friendly process while surface modification via incorporating Graphene Oxide (GO) as an additive into the polymer matrix using novel VFD processing.
4. Comparing the UF membranes fabricated using VFD mediated PSF processing and/or GO/PSF membranes, with those fabricated from conventional mixed polymers to develop a new mixing procedure using the high shear generated in the VFD and associated intense micro-mixing and viscous drag.

## **1.3. Project overview**

This research project mainly involves (i) synthesising a common polymer used for fabricating UF membranes using the VFD, and comprehensive characterisation of the material while fine-tuning its properties, (ii) improving the properties of the VFD synthesises PSF under high shear and anhydrous condition with respect to the morphological differences and (iii) fabricating pristine PSF and GO/PSF composite UF membranes, characterising, and testing their properties and rejection performances. The main focus is on using the VFD in polymer synthesis and/or modifying its properties and also fabricating UF membranes. The expected advantages of this novel approach are in being able to scale up the process under continuous

flow, and the overall faster, easier to use, and cost-effective processing. The whole project can be divided into the following three steps:

- Polymer synthesise using VFD and conventional methods supported by comprehensive characterisations

The first step involves synthesising a key polymer, PSF, which is commonly used in fabricating UF/NF membranes. PSF will be prepared using a conventional polymerisation process and by employing VFD as a novel approach for polymerisation. The VFD is a recently invented thin film processing platform which works under semi-microfluidic conditions. The main aim of this step is to investigate the capability of the VFD in polymerisation of PSF and optimising the conditions to make it more efficient and reliable compared with polymers obtained using conventional methods.

In order to compare the key properties of the synthesised polymers obtained from VFD and conventional methods, a comprehensive characterisation will be used. For instance,  $M_w$  and  $T_g$  significantly impact on the mechanical and thermal properties of the polymers, and their measurement is a very important step to evaluate properties of the as synthesized material [43]. Hence,  $M_w$  of the polymers will be measured by Gel Permeation Chromatography (GPC) which is a fast and reliable technique [43]. The glass transition temperature ( $T_g$ ) and thermal stability will be evaluated using Differential Scanning Calorimetry (DSC) and Thermal Gravimetric Analysis (TGA), respectively. Fourier Transform Infrared (FTIR) and Nuclear Magnetic Resonance (NMR) spectroscopy will also be used for structural characterisation of the synthesised polymers [44].

- Manipulating the VFD synthesise process of the PSF for enhancing the products' properties

In the further steps, VFD processing will be further investigated to improve the properties of the PSF in a simpler and faster procedure. The optimal VFD operating conditions for the enhancement process such as temperature, rotational speed, tilt angle, and processing time will be identified with respect to the main characteristics of the polymers such as  $M_w$  and  $T_g$ . A comprehensive investigation on the new VFD mediated material was undertaken using

scanning electron microscopy (SEM) and Brunauer–Emmett–Teller (BET) techniques, to establish the morphological differences and surface area of the polymers.

- UF membrane fabrication from continuous micromixing VFD mediated PSF and GO/PSF solutions

As detailed in Figure 1. 1, thin-film composite nano-filtration (TFC-NF) membrane consists of different layers [5] in which the support layer which is normally a MF or UF membrane can be fabricated by employing phase inversion or electrospinning techniques. Herein, the main focus is on fabricating this support layer using a phase inversion process on the PSF and GO/PSF solutions, mediated using VFD processing and compared with conventional mixing, for testing the UF membranes in salt (NaCl) and bovine serum albumin (BSA) filtration from aqueous solutions.

In this final step, the application of the VFD will be systematically investigated with respect to the effects of polymer concentrations and rotational speed impacting on the properties of the membranes, notably morphology, porosity, permeability, salt/BSA rejection performance, as well as thermal and mechanical properties. Graphene Oxide (GO) was an additive of choice given its unique properties, for enhancing the performance of the membranes, using both VFD mixing and conventional mixing for direct comparison in identifying the optimal processing.

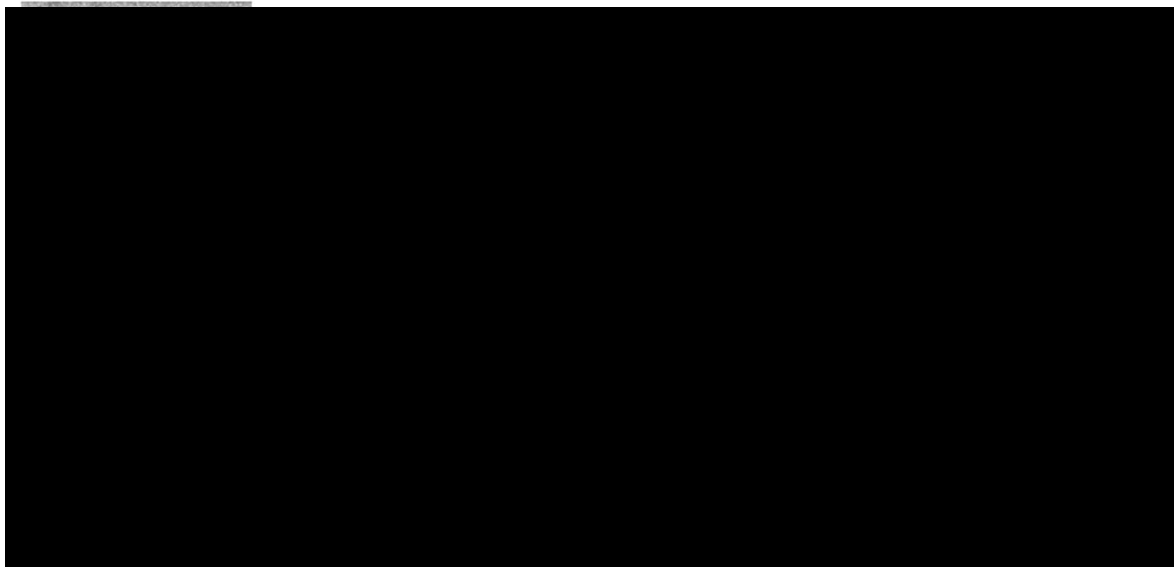


Figure 1. 1. Components of a typical interfacially polymerized NF membrane [5].

The same phase inversion procedure will be followed for polymeric/composite membranes fabricated using VFD or conventional mixing processes. This facilitates a comparison of the obtained membranes in terms of separation performance and properties.

To have an effective separation using UF membrane, reliable data about the chemical structure and properties are required for evaluating its characteristics and performance, and this is taken up as the main aim of the final step of this project. Scanning Electron Microscopy (SEM) is performed to study the morphology and cross-sectional structure of the fabricated UF membranes. Investigating the surface characteristics which influence the contact angle should be identified using acceptable technique such as the “sessile drop” method. Additional information about the chemical structure of the surface layers of the UF membranes of PSF and GO incorporation into GO/PSF composite membranes can be obtained using FTIR and Raman spectroscopy. Investigating the appropriate mechanical and thermal stability is also possible using “TGA” and Dynamic Mechanical Analyzer (DMA) [45, 46]. Finally, the separation efficiency of the UF membranes and their performance will be investigated in a dead-end filtration system involving measuring the permeability and pollutant (protein and salt) rejection efficiency [47].



## 1.4. Literature review

### 1.4.1. General introduction

Water as the vitally important component of the human life, has been recently d to face scarcity due to human activities and is expected to be more influenced by climate change in the future. Rapid industrial development has exacerbated the problem of water pollution by the discharge of wastewaters to the environment without suitable treatments [48, 49]. This together with the increasing demand for water in different aspects of human life highlight an urgent need for the development of wastewater treatment processes and the production of more usable water from secondary resources. Apart from the conventional methods such as chemical precipitation, coagulation - flocculation, ion-exchange, adsorption, evaporation, etc., employing novel green technologies in wastewater treatment has recently attracted considerable interests [49].

To date, there has been extensive research focused primarily on wastewater treatment using eco-friendly nanoparticles [50, 51] and also membrane-based processes and technologies [52, 53]. The application of NF membranes has recently become widely spread due to their advantages such as low operating pressures and subsequently, low investment and maintenance costs, suitable permeate flux and reasonable efficiency [9]. In order to obtain NF membranes suitable for different applications with specific conditions, a variety of methods including phase inversion, interfacial polymerisation, and electrospinning have been introduced [5, 10-15]. However, there is a lack of knowledge and expertise to develop alternative techniques which are more cost effective, environmentally friendly, efficient, and easier to use. It is worth mentioning that polymers, as the common precursors of the UF/NF membranes, are important. Hence, to achieve a cost- and time-efficient processing, the selection of the polymerisation method is crucial. The VFD with different advantages of scalability, being easy to use, fast, and cost effective, is gaining attention in a number of different research fields. Although no studies have been reported on using the VFD as an approach in polymerisation, and in UF membrane fabrication, the novel microfluidic platform has been successfully used for a number of applications [29-35, 37-42, 54]. These results are

indicative of possible application of the VFD in polymerisation, as the main objective of this research, and also in UF membrane fabrication.

#### **1.4.2. Water and wastewater treatment**

Water supply systems have long followed the main aim of providing drinking water free of disease, organisms, and contaminants. Moreover, wastewater treatment has accomplished the purpose of protecting the health of the present community. This has been achieved by preventing contaminants from entering to the water supply, providing suitable water for different purposes, and preparing the water with appropriate quality for different usages by recycling the wastewaters [55]. Generally water and wastewater treatment can be classified into different groups involving physical, chemical, and biological techniques [56, 57].

#### **1.4.3. Physical approaches**

Physical separation techniques in wastewater treatment are mostly referred to as solid-liquid separation, which are mainly related to differences between the physical properties of different components such as specific gravity, surface charge, and particle size, as well as physical barriers [56]. Generally, physical separation techniques do not change the chemical structure and properties of the principle substances. Some examples of this class of separation methods are sedimentation, flotation, and adsorption, while screens, filters, and membranes are examples of barriers [58]. Among different methods in this type of treatment, filtration plays a prominent role [56]. Filtration systems are classified in different types of depth filtration and screen filtration. The main concept of depth filtration is adsorption while the principle mechanism in screen filtration is sieving. In depth filters, the average pore sizes are mainly 10 times bigger than those of the smallest particles that are going to be separated from the liquid depending on their adsorption properties. In this mechanism, there is a saturation point whereby further adsorption will not occur unless regeneration causes desorption of the adsorbed particles, or the filters are substituted. Some examples of depth filtration are granular activated carbon column filters, sand filters, and dual media filters. Membrane filtration systems are a prominent type of screen filters which is defined as a non-conventional method in physical techniques [59]. The principles and also the applicable range of employing this technique are further discussed in the later sections.

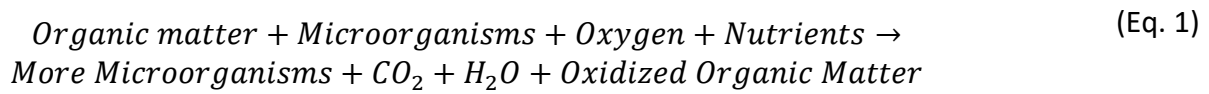
#### **1.4.4. Chemical approaches**

Chemical techniques include a group of treatments involving chemical reactions with the target pollutants as part of the separation process. This can be achieved sometimes by removing the contaminants from the water or by helping the destruction and neutralisation of harmful effects of the contaminants. Based on the application, different chemicals can be used in this method, such as chlorine, iodine, silver, and potassium permanganate. In addition, other processes rely on coagulation or flocculation as part of the separation. These techniques can be employed in a complementary process combined with physical methods or as an standalone process [56]. In other words, this group of technologies take advantage of some properties such as: (1) the chemical characteristics of the pollutants and their tendency to react with treatment chemicals; and (2) the chemical properties of the products of reaction between pollutants and treatment chemicals, such as their solubilities, volatilities, or some other characteristics. In general, six processes are reported where the dominant role in removing contaminants from wastewater, notably 1) an insoluble solid, 2) an insoluble gas, 3) coagulation of a colloidal suspension by reduction of surface charge, 4) biologically degradable substance from a non-biodegradable substance, 5) reactions which destroy or otherwise deactivate a chelating agent, and 6) oxidation or reduction to produce a non-objectionable substance or substances which can be easily removed using other simple methods [58].

#### **1.4.5. Biological approaches**

Wastewater treatment using biological techniques involves the application of microorganisms such as bacteria, fungi, algae, some worms and protozoa [57]. Organic substances present in the wastewaters are the nutrients used by microorganisms in biological treatment systems. These organic complexes are gently broken down and reassembled again in a new protoplasm. Generally, there are aerobic and anaerobic systems in these biological processes, in which the electron acceptor with main part of the reaction is oxygen and substances other than oxygen, respectively. For instance in an aerobic biological treatment system, the reaction shown in (Eq. 1) decreases the quantity of organic contaminants and

increases the quantity of microorganisms, carbon dioxide, water, and other by-products of microbial metabolism [58]:



Due to the urgent need of developing new methods in wastewater treatment, many approaches have been tested. Ardern and Locktee from United Kingdom, as pioneers in biological treatment, introduced “Activated Sludge” in 1914. Conventional Activated Sludge (CAS) processes are mostly based on the application of biological organisms for effective water purification [59]. The main concept of CAS processes is biomass separation from the influent using gravity with microbial sedimentation [60].

Despite all benefits of CAS systems, the increasing demand for a safer environment to protect aquatic life and stricter water quality standards has limited its application [59]. On the other hand, membrane-based separation process, as a newer approach in wastewater treatment, have covered some of the defects of the CAS process such as poor water quality, large footprints, and high biological waste. For example, membrane bioreactors (MBR) which are a combination of membrane filtration and a bioreactor have been used in CAS processing. This was first introduced in 1969. The main differences between MBR and CAS layout is replacement of the sedimentation tanks in the CAS systems the membrane filtration [61]. This type of MBR system, also called a side stream system (Figure 1. 2-a), has higher effluent quality and lower waste sludge production. Because of the high energy costs associated with MBR processes, another approach has been developed, now placing the membrane from outside the bioreactors to inside them. In comparison with the side-stream MBRs, the new MBR systems, having submersed or immersed configurations, show better effluent quality with lower operation costs associated with operating at lower pressures and flow rates, and longer processing times, Figure 1. 2-b [59].

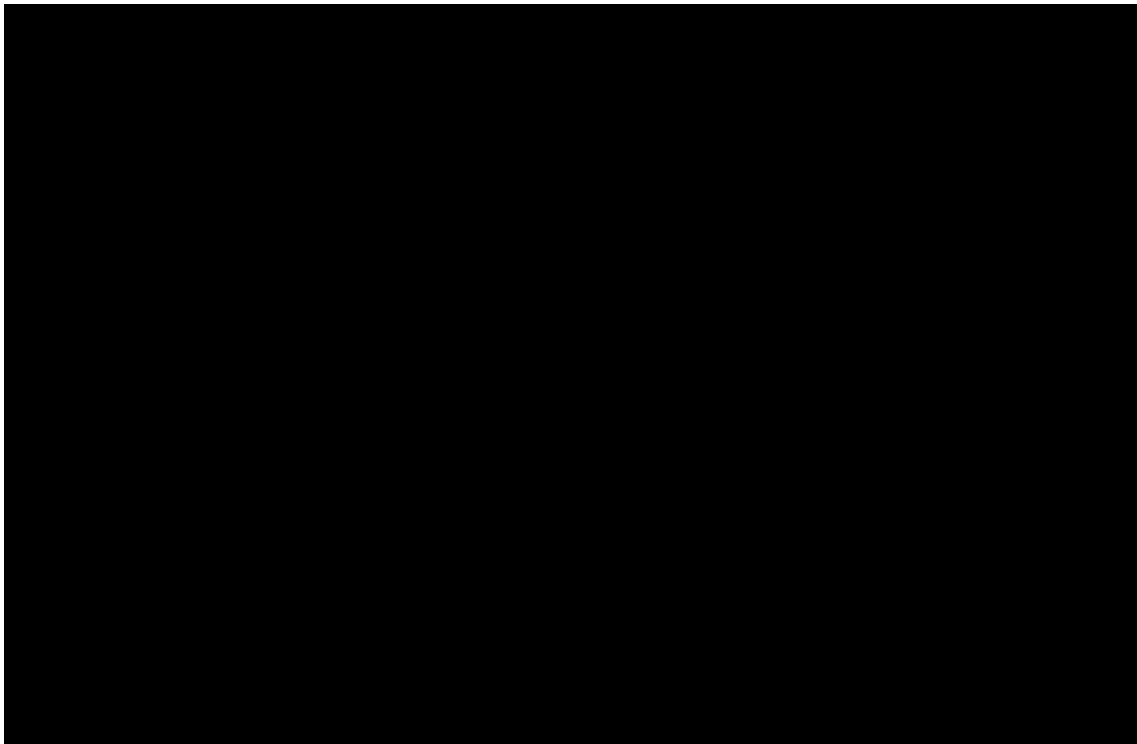


Figure 1. 2. Two types of MBR technology: (a) Side-stream and (b) submersed configuration [59].

With the development of MBR processes and immersed membranes, the production of compact, robust, and cost-effective systems have been investigated to optimize the efficiency, applicability and footprint of this type of membrane-based process [59, 60].

#### **1.4.6. Limitations of the wastewater treatment techniques**

Despite a long history of use of conventional wastewater treatment methods, they have some drawbacks which highlights the need for implementing new techniques. For instance, of the limitations of the chemical approaches include; (i) the process depends upon any changes in influent quality, (ii) the process should be customized for every case in terms of the type and the amount of the chemicals needed, (iii) precise controlling and skilful operators are essential, (iv) a large amount of the waste is produced, (v) the footprint is generally large, and (vi) significant corrosion problems leading to high maintenance costs [2].

Biological methods have also some disadvantageous such as (i) high electrical energy consumption to provide the aeration for aerobic microorganism, (ii) large footprint, (iii) production of large amounts of bio-solids or sludge which need appropriate disposal, (iv) inefficiencies in removal of some chemical, such as pharmaceuticals, detergents, cosmetic

and industrial compounds, and (v) long processing time when using anaerobic microorganisms [3].

Conventional physical approaches also cannot be individually used in a large number of the wastewater treatment systems, because of the limitations in removal of a wide range of contaminants which are small in size. New membrane-based filtration methods have been introduced in recent decades to address some of the disadvantages of the conventional techniques. For instance, membrane separation is widely used in a range of industries. The quality of permeate obtained in membrane processing is generally more uniform compared with that of the other conventional physical methods. Moreover, in comparison with some other approaches such as thermal techniques, energy costs are considerably lower. Also noteworthy, is that membrane processing does not need highly skilled operators, with the systems more practical in an automated mode [2] which is explained in the next sections.

#### **1.4.7. Membrane separation**

Membrane separation has a group of techniques in which particles and molecules are able to be separated from the liquid using some permeable or semi-permeable barriers [59]. In general, the core of the membrane allows certain components to pass while retaining some others. The membrane features a thin separating layer supported by one or more thicker layers with larger pores. The supporting layers do not contribute to the resistance against the mass transfer and it's only the thin separating layer that is active for the permeability [5, 6]. When the feed stream encounters the membrane, it will be separated into two streams with different components concentration, including a permeate with a low concentration of the contaminants and a retentate (or concentrate) with a high amount of contaminants (or solutes) [6, 7]. This approach can be widely used in the food and dairy industries, chemical, biological, and pharmaceutical applications [6]. Particle separation by membranes can be divided into two groups, involving (a) transporting the suspended particles to the surface of membranes (Figure 1. 3), and (b) transporting water molecules through the membrane pores [59].

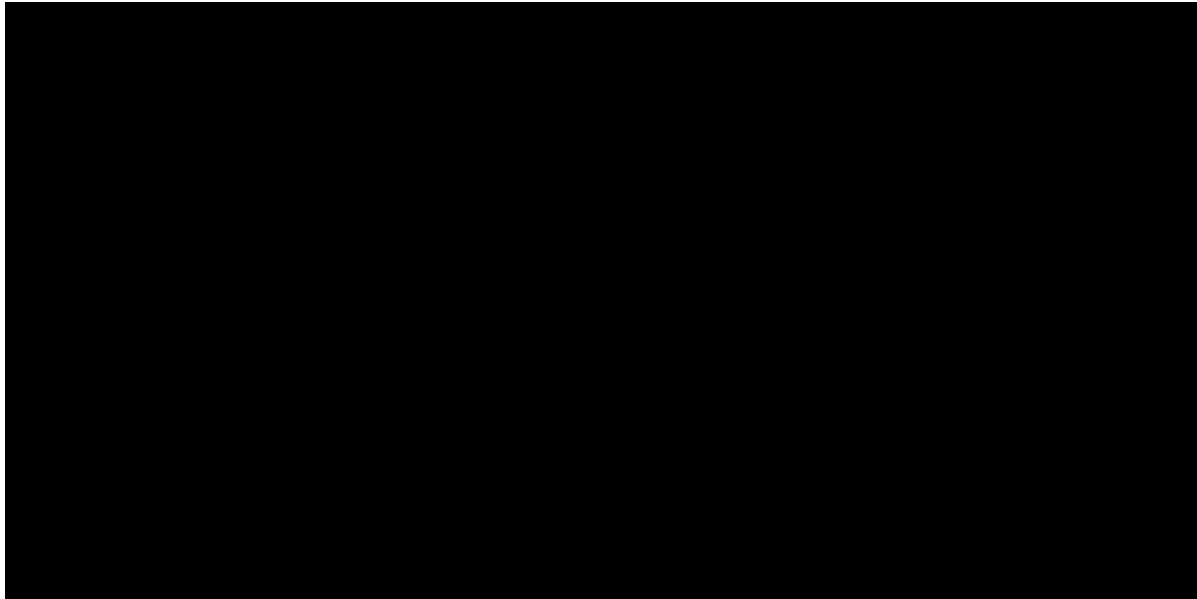


Figure 1. 3. Transport mechanism of suspended particles to the surface of membranes [\[59\]](#).

As shown in Figure 1. 3, there are different types of particle transport and particle-membrane interaction mechanisms such as:

**Hydrodynamic convection:** hydrodynamic pressure difference between the inflow and permeate flow (or concentrate flow).

**Sedimentation and floatation:** relative density of the particles mostly is the dominant mechanisms.

**Particle–Wall Interaction:** when the distance between particles and membrane is so close that other electrokinetic double-layer interactions or van der Waals forces become dominant.

**Sieving:** size-based separation.

**Particle diffusion:** Brownian diffusion for the submicron particles ( $<1\ \mu\text{m}$ ) in liquid filtration [\[59\]](#).

Membrane separation involves different driving forces. When a driving force is applied across the membrane, a portion of the feed will pass through the membrane while transporting one component more readily than the others. Differences in physical or chemical properties of the membrane, such as pore size and surface charge, can be key factors in transporting

components selectively through the membrane. The main type of driving forces include; pressure gradients, concentration gradients, electrical voltage gradients, and temperature gradients [7].

#### **1.4.7.1. Pressure driven membrane processes in water purification**

Pressure driven membrane processes, as the type of membrane featured in this project, typically apply a pressure on the feed side of the membrane as a driving force for the separation (Figure 1. 4).

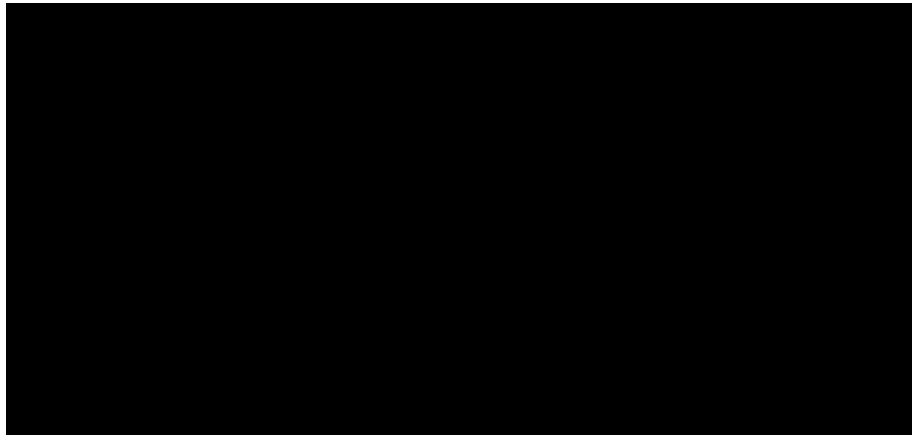


Figure 1. 4. Schematic diagram of the basic membrane separation process [7].

Pressure driven membrane processes can be classified according to different factors such as membrane pore size, size and charge of the retained particles and molecules, and exerted pressure. Based on the different applications and needs, pressure driven membrane processes involves microfiltration (MF), ultrafiltration (UF), nanofiltration (NF), and reverse osmosis (RO) membranes which can be classified as reported in Table 1. 1 [6, 7].

Figure 1. 5 compares the separation capability of the abovementioned pressure driven membranes with using conventional filters based on their pore sizes.



Table 1. 1. Overview of pressure-driven membrane processes and their characteristics [6, 62].

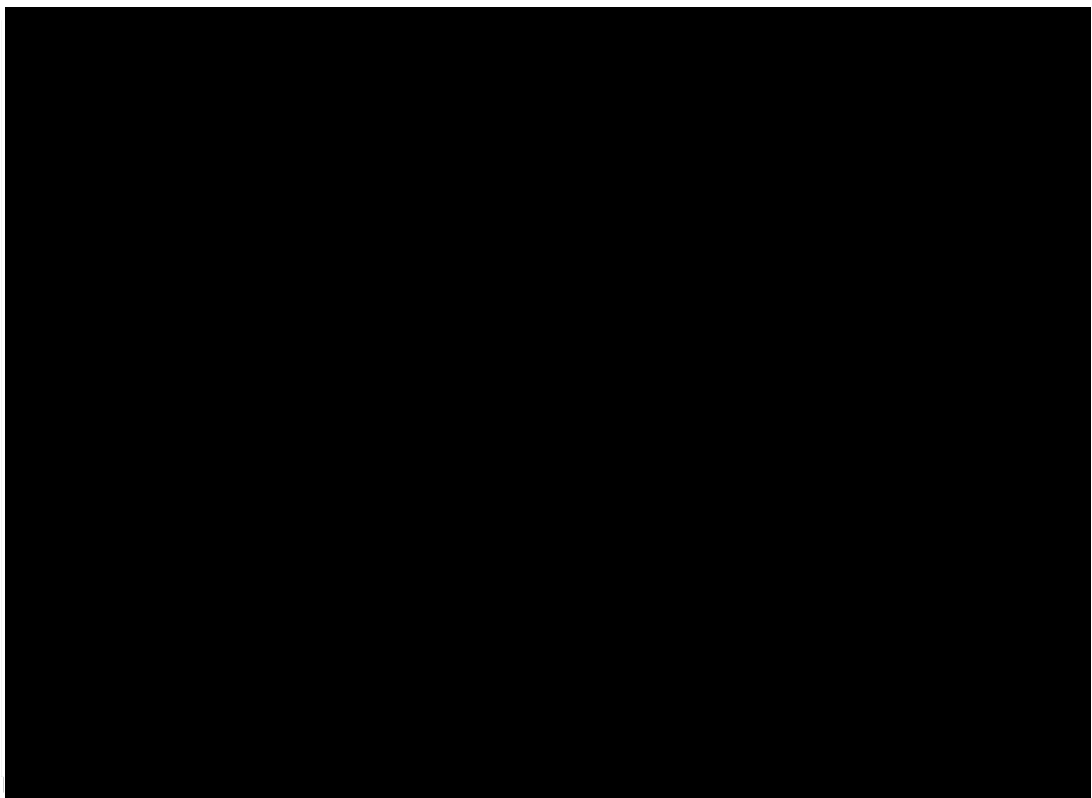
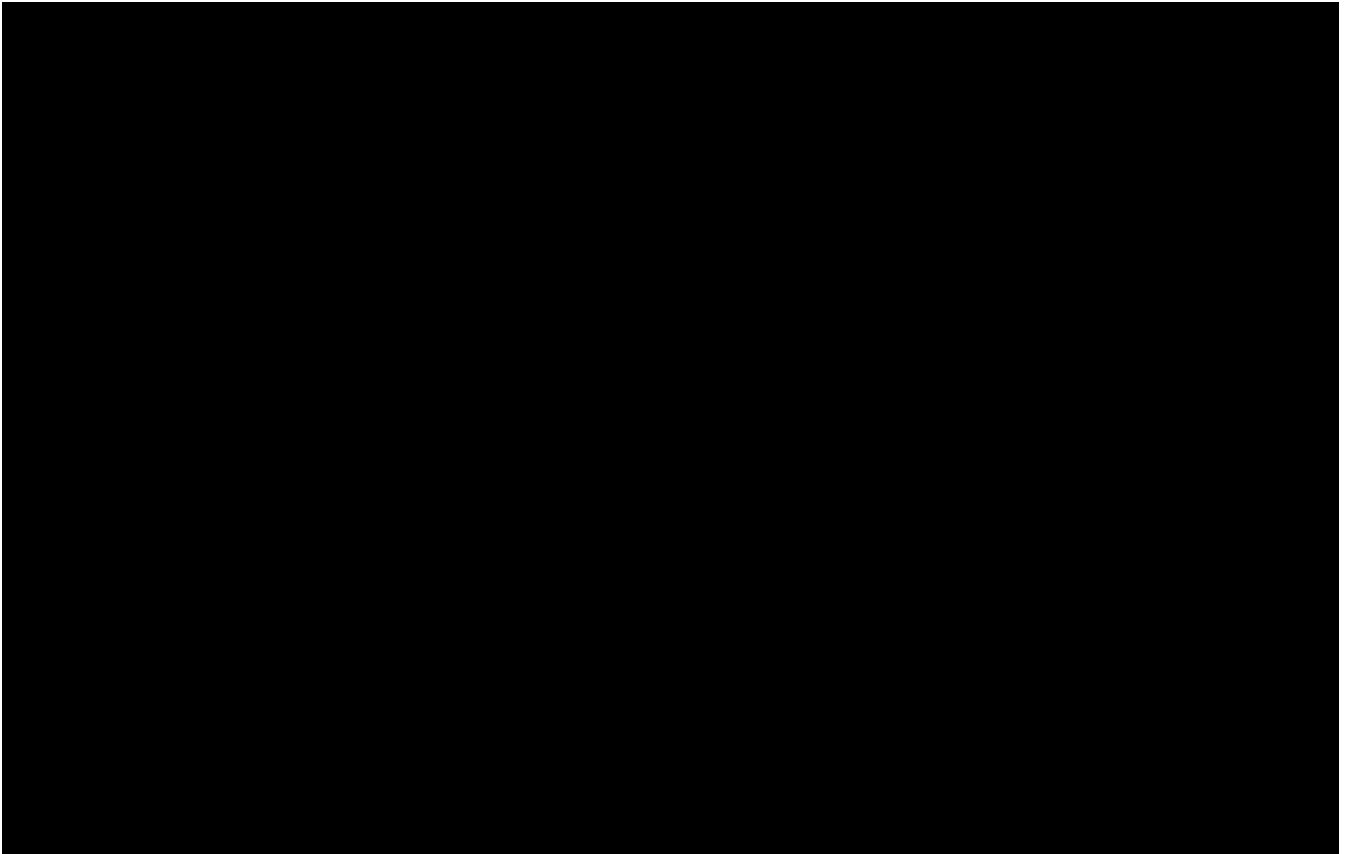


Figure 1. 5. Membranes separation capabilities based on their average pore diameter [7].

#### 1.4.7.2. Microfiltration (MF) membrane

MF membranes have a pore size of approximately 0.1 to 10  $\mu\text{m}$ , for separating particles with a molecular weight ( $M_w$ )  $>1000,000$  Daltons using a relatively low feed operating pressure of approximately 0.1 to 2 bar. A sieving mechanism will be used to remove the components larger than the membrane pore size. MF can mainly be considered as a pre-treatment step before further treatment approaches to remove the contaminants such as suspended solids, colloids, and large bacteria [6].

Ceramic membranes, which are a special class of micro-porous membranes, are widely used in microfiltration applications mainly due to their solvent resistance and thermal stability, having a superior chemical, thermal, and mechanical stability, and better control over pore size [7]. However, polymeric membranes are more common in MF membranes because of their good selectivity, permeability, and mechanical stability, and also in being more cost-effective [6]. The most common polymers used are polysulfone/poly(ether sulfone) (PSF/PES) [6], poly-acrylonitrile (PAN) [63, 64], polytetrafluoroethylene (PTFE) [65], poly(vinylidene fluoride) (PVDF) [66-68], polypropylene (PP) [69, 70], and polyethylene (PE). It is noteworthy that the membranes pore size is an important factor in MF membranes, which is expressed by the manufacturer with reference to the size of the retained particles [6].

#### 1.4.7.3. Ultrafiltration (UF) membrane

UF membranes are similar to MF membranes but they have a smaller pore size (2-100 nm). Molecular weight cut-off (MWCO) as an informative parameter is always used to express the capabilities of UF membranes. Removing the large dissolved molecules including natural organic material (NOM) is a common application of processing using UF membranes. In addition, they can be used in mining operations for the separation and recovery of floatation agents, surfactants and organometallic complexes or as a pre-treatment for other membrane processes such as using RO or NF [6, 7].

Materials which are typically used in UF membranes are often similar to those used in MF membranes, although a different fabrication method is used [20]. To improve the performance of UF membranes, several methods such as polymer blending [22, 23] and surface modifications (e.g. incorporating highly hydrophilic nanoparticles) [19-21] can be

used. Surface modification has long been a prominent step to improve the properties of membranes depending on the specific applications [5, 71].

#### **1.4.7.4. Reverse osmosis (RO) membranes**

RO is used to separate ionic solutes, metals, and macromolecules from aqueous streams such as industrial wastewater, seawater, brackish water, etc. [7]. In comparison with other types of membrane processes, RO membranes have a slower permeation while the separation mechanism is based on solution-diffusion rather than sieving. Due to lower permeability, a higher pressure is required to be applied in order to achieve the targeted permeability, and this is very energy intensive [6]. The dense structure of RO membranes allows only water to pass through, rejecting all the other dissolved and suspended organic and inorganic materials, as shown in Table 1. 1 [5-7]. Although RO membranes have the ability to purify water, a high amount of energy is required to reverse the osmotic flow which is an extra cost penalty for some applications [6, 7].

#### **1.4.7.5. Nanofiltration (NF) membranes**

NF membranes generally operate at lower pressures, having higher fluxes but lower permeate quality compared with RO membranes. However, selectivity and lower energy consumption are the main advantages of using NF membranes instead of RO systems [72]. NF membranes are mainly effective in removing low molecular weight contaminants (e.g. MWCO of about 300 Daltons), small organic micro-pollutants, colourants, and degradation products from the biological treated wastewater [5-7]. The separation mechanism in NF membranes is not only involving sieving and steric hindrance, but also by the Donnan and dielectric effects. Hence, regardless of the size of the components, ions smaller than the pore size of NF membranes can be removed by the surface charge on the membranes [6]. Among other types of membranes, processing using NF membrane is more applicable for treatment of industrial wastewaters. The most important factors in such wastewaters are hardness, salt concentration, presence of colourants which can be overcome using NF membranes in reaching water standards [6, 73].

Different kinds of NF membranes have been investigated to improve their thermal, chemical, and mechanical stabilities, permeability, and separation performances. One of the most

important factors which can affect the stability of the membranes and separation efficiency is the type of the materials used in fabricating the NF membrane [6].

As the focus of this project, different types of UF membrane materials are introduced in the next section.

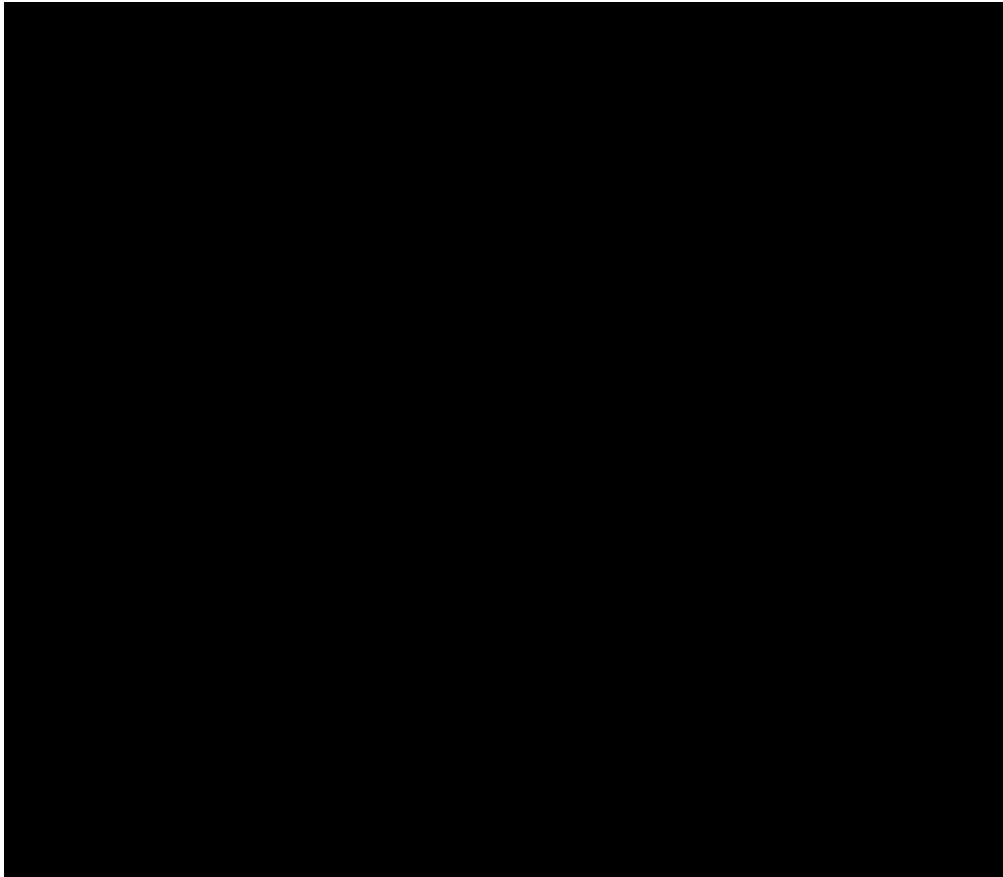
#### **1.4.8. Membrane materials types**

NF membranes are generally classified into two major groups: organic and inorganic membranes. Polymeric membranes constitute the most important group and have been commercially available for many years, due to their advantages of being easy to use, environmentally friendly, good separation performance, suitable controllable pore sizes, and low material costs [6, 25]. The most popular materials used in fabricating polymeric membranes for wastewater treatment are those which have suitable acidic, basic, thermal and mechanical durability for about 5 years operation [59]. Some of the common polymers used in fabrication of NF/UF membranes for commercial and research applications are; PSF/PES, PVDF, PE, aliphatic polyamide (PA), and cellulose acetate (CA) [5, 6]. An overall comparison between some of the membrane characteristics is outlined in Table 1. 2.

Ceramic materials in NF/UF membranes are mostly comprised of alumina ( $\text{Al}_2\text{O}_3$ ) [26], titania ( $\text{TiO}_2$ ) [26], silica ( $\text{SiO}_2$ ) [27, 28], and zirconia ( $\text{ZrO}_2$ ) [25]. Despite high thermal, chemical and mechanical stability, the application of ceramic membranes is limited due to their relatively larger pore size and complex and expensive fabrication processes [25] [6, 25].

In contrast, polymeric membranes are relatively easy to prepare and can be produced cheaper than the ceramic membranes. However, their applications are restricted to operating at moderate temperatures and non-corrosive feed streams. Several studies have been reported for optimizing the water flux, rejection performance, and selectivity and stability of the membranes [10, 12, 16, 17, 19-23, 25-28, 74, 75]. However, there are still a number of limitations to the feeds that can be purified by polymeric membranes [25].

Table 1. 2. Pros and cons of polymeric membranes [\[59\]](#).



#### **1.4.9. Membrane fabrication**

Thin-film composite nanofiltration membranes (TFC-NF) are a type of NF membrane which is schematically shown in Figure 1. 6. TFC-NF membranes are typically made out of a thin PA layer deposited on top of a PSF or PES porous layer on top of a non-woven fabric support sheet.

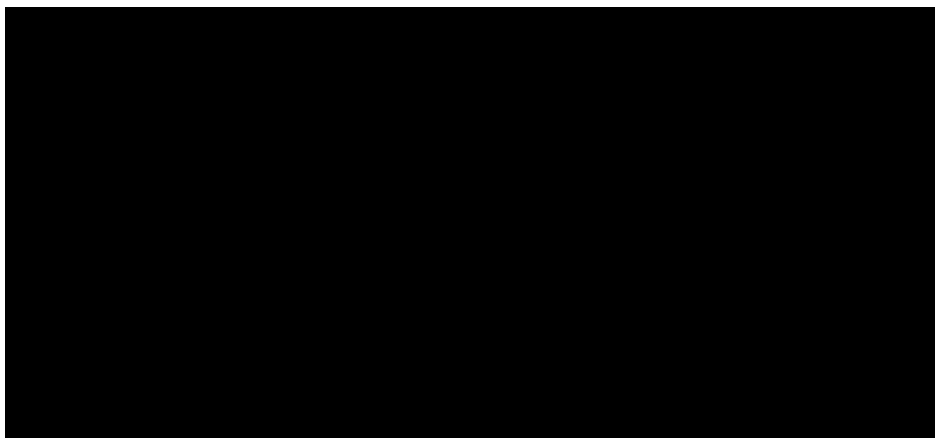


Figure 1. 6. Structure of a TFC-NF membrane [\[76\]](#).

The main advantage of TFC membranes over skinned asymmetric membranes is preparing each layer to independently provide a membrane with engineered properties and performance. The three-layered configuration gives the desired properties of high rejection of undesired components, high filtration rates, and good mechanical stability.

Based on the applications, web layer (the lowest layer in Figure 1. 6) should be included within the structure of the membrane. The main purpose of this layer is to improve the tensile strength of the membranes for protection from deformation under aggressive operating conditions. This layer, which is mostly from non-woven fabrics, is more likely to be used in RO membranes due to the high pressure in RO processes, and it features in the present project. Depending on the application, an upper coating layer may also be fabricated on the ultra-thin layer in order to enhance the rejection (or selectivity of the membrane) and protect the membrane during the operation [5]. The polyamide top layer is responsible for the high rejection and is chosen primarily for its permeability to water and relative impermeability to various dissolved impurities including salt ions and other small, and unfilterable molecules [5]. The ultra-thin top-layer can be obtained using different methods including solution casting (like spin coating, dip coating or spray coating) or polymerisation (interfacial polymerisation (IP), *in situ* polymerisation, plasma polymerisation, and grafting). Support layers can be obtained using other techniques such as phase inversion and electrospinning [10]. The following sections will introduce the procedures for fabricating the support layer of TFC-NF membranes to be used independently as an UF membrane for filtration which is the focus of the ultimate objective of the present research.

#### **1.4.9.1. Phase inversion**

The main purpose of the phase inversion method is to transform the polymer solution from a liquid to a solid state using a liquid-liquid demixing process [10]. The phase inversion method has three key components; polymer, a solvent for dissolving the polymer, and of solvent in which the polymer is only sparingly soluble, with the membranes fabricated by controlling the interaction between the polymer and solvent(s) [59, 77]. Solubility difference of the polymers in solvents is the key factor used in phase inversion. Generally, polymer precipitation occurs because of different solubilities. When a solution of a polymer dissolved in a “good solvent” solution encounters a “poor solvent,” precipitation occurs due to the solvents exchange, and

results in the formation of the membrane structure which comes from a combination of mass transfer and phase separation. Finally the polymer-lean phase forms the membrane pores and the polymer-rich phase will lead to the solid membrane matrices [10, 59, 78]. This method is typically used for fabricating UF membranes and the support layer in thin-film composite nanofiltration (TFC-NF) membranes, which is schematically shown in Figure 1. 7 [10].



Figure 1. 7. Schematic diagram of the immersion phase inversion process [78].

Extensive studies have been carried out to evaluate the influential parameters in preparing membranes using phase inversion. For instance, in a research by Agnieszka et al. [10], some of the parameters which considerably affect the morphology and performance of the membrane fabricated by phase inversion are introduced as; polymer type and concentration, evaporation time and temperature, demixing speed, the use of additives, choice of solvent, humidity, membrane thickness, composition and temperature of the coagulation bath.

#### **1.4.9.2. Electrospinning**

Electrospinning, as a polymeric nanofabrication technique, has recently been an increasingly popular approach to fabricate fibres with a variety of diameters from nanometres to micrometres. This technique is basically a polymer solution spinning process which is driven by electrical force. This process involves the application of a high electric field between the polymer solution and the collector which is a plate [79] or a rotating drum [14]. When the electrostatic potential becomes sufficiently high and overcomes the surface tension of the polymer solution, a charged liquid jet is formed and collected on the rotating collector (Figure 1. 8) [14, 79].

Due to their special interaction between the barrier and support layer, electrospun scaffolds can replace conventional support systems in TFC-NF membranes. Using the electrospinning process, transport properties of TFC membranes can be enhanced by controlling the structure of the support layer without compromising its mechanical integrity and suitability as a substrate for interfacial polymerisation. Hence, improving the flux of the membranes by increasing the interconnected pores allows diffusion of the molecules through a shorter path in electrospun support layers. In TFC-NF membranes, greater openness of the support layer which is produced using electrospinning can also be an advantage [14]. There are different factors which can affect this technique such as polymer type and concentration, applied voltage, distance between spinneret and collector, and temperature.

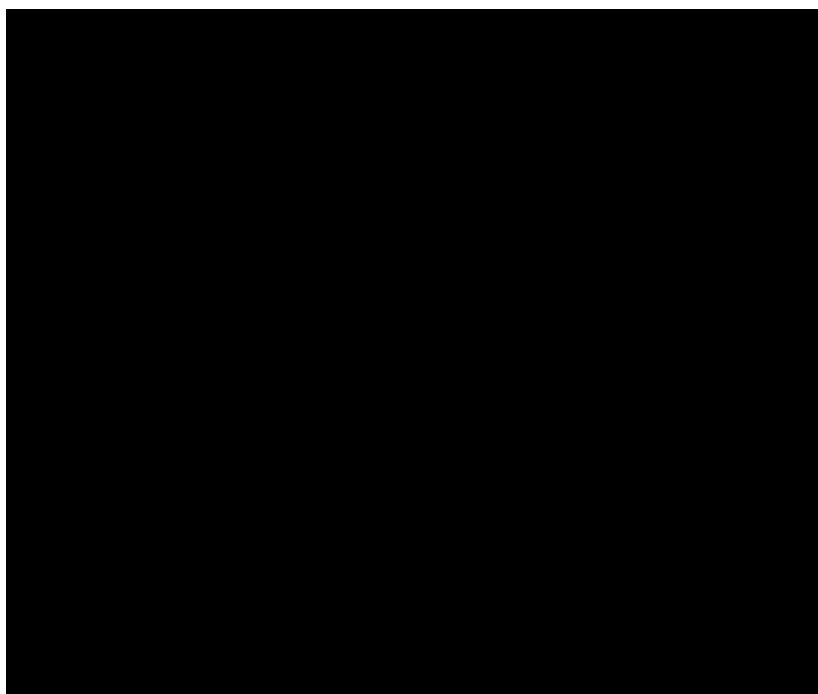


Figure 1. 8. Schematic of electrospinning setup [14].

Among the numerous studies in electrospinning, McCune et al. [80] improved the power conversion efficiency of solar cells using zinc oxide tree-like nanowire structures with enhanced surface area produced by electrospinning. In other research for application in mass transfer, Bai et al. [81] also used the ability of increasing specific surface area of the tree-like structure of the nanomaterial. Despite the high performance of the fabricated tree-like structure, a complicated multi-step method is usually required.



Li et al. [15] used one step electrospinning to fabricate a new polyvinylidene fluoride (PVDF) tree-like nanofiber by adding a salt to the PVDF solution. Thick trunk fibres in the tree-like nanofibers, as the skeleton support, and the thin branch fibres as connection props, lead to mechanical improvement and pore size decrease, respectively. Salt with the longest carbon chain had the most effect on the conductivity and tree-like formation of PVDF nanofibers, while the inorganic salt did prove to have the less effect. The increase in the salt concentration led to increasing the charge density and in consequence splitting the jets, which resulted in thinner branches and a decrease in the pore size [15].

Wang et al. [1] have research on producing polyacrylonitrile (PAN) nanofibers coated with graphene oxide (GO) as a barrier layer. The GO layer was synthesised separately, and then coated on the surface of the PAN electrospun fibres. The final nanofibrous GO@PAN membrane was shown to have high water flux for a low external pressure (1 bar), and also high salt rejection performance. Water flux is assumed to increase due to the high porous electrospun nanofibrous support layer, or because of the relatively long hydrophobic nanochannels between the GO nanosheets. It has been shown that in such a GO@PAN nanofibrous material, there are some hydrophilic gates related to the space between the edges of the nanosheets of the defects of the GO sheets. In addition, the 2D nanochannels between the GO sheets are hydrophobic which can increase the relatively speed of the water molecules and thus the water flux in a GO@PAN nanofibrous (Figure 1. 9) [1].

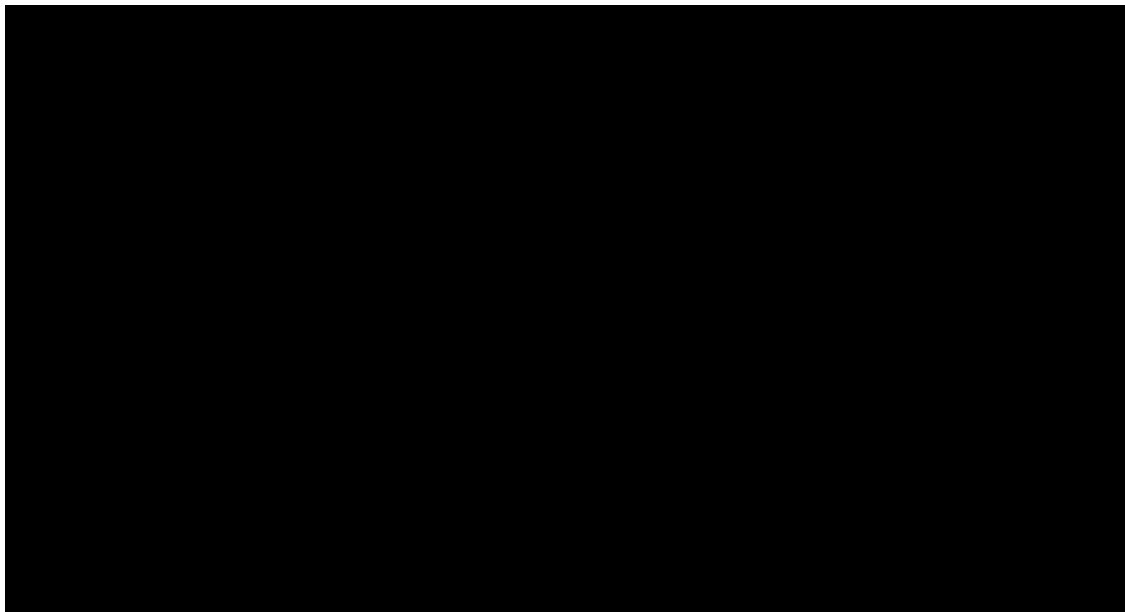


Figure 1. 9. Conceptual illustration of hydrophilic “gate” and hydrophobic nanochannel [1].

Gue et al. [82] have synthesised a polyhydroxybutyrate calcium alginate carbon nanotube (PHB-CaAlg/CMWCNT) as a nanofibrous membrane using the electrospinning method. The as prepared PHB-CaAlg/CMWCNT has improved tensile mechanical strength, good hydrophilic property (19.4° water contact angle) and high dye adsorption capacity [82].

Research reports abound in using electrospinning and phase inversion techniques for different application, especially in fabricating support layer in TFC-NF membranes. A common note in all of these studies is using different approaches or different chemicals for improving the separation prowess of the membranes.

#### **1.4.10 Improving the properties of membranes**

Extensive research has been reported on improving the properties of membranes [10, 12, 16, 17, 82-87]. For example, in improving the membrane properties via phase inversion, Holda et al. [10] established that high polymer concentrations results in higher viscosity and longer time for precipitation resulting in membranes with less macrovoids. Demixing speed is also reported by Holda et al. [10] and Guillen et al. [12] to provide a porous layer with macrovoids (finger-like) and dense layers without macrovoids in instantaneous and delayed demixing, respectively.

Among different approaches to improve the specific properties of membrane, polymer modification by blending different composites and components have been widely studied by different researchers. For instance, metal oxide nanoparticles are introduced as the prominent effective components in improving the properties of the membranes [10]. Safarpour et al. [75] recently reported the fouling resistance and separation performance of PES membranes by incorporating some composites. In this research, the membrane resulting in rGO/TiO<sub>2</sub>/PES membranes with approximately twice the water flux (45.0 kg/m<sup>2</sup>·h) compared with the bare PES membrane (23.1 kg/m<sup>2</sup>·h). Fouling resistance also improved considerably with the incorporation of rGO/TiO<sub>2</sub> composites.

Many studies have also been reported on exploring the effect of the M<sub>w</sub> of the polymer on the performance of the membranes [16, 17, 83]. Holda et al. [16] established that increasing the M<sub>w</sub> using polymer purification increased the membrane permeability and salt rejection. However, in another study, Zhou et al. [17] reported a different result where membrane

permeability increased with increasing the  $M_w$  of the polymer (PES) while salt rejection decreased. Bil'dyukevich et al. [83] also established that a decrease in membrane permeability resulted in an optimised rejection while increasing the  $M_w$  of the polymer.

Polymer blending as a solution for changing the MW of the polymers has always been taken into account. To reach this aim, low  $M_w$  additives have been the priority of research, because the high  $M_w$ s result in an increase in rejection but with a decrease in flux [10]. Nevertheless, some modification processes [16, 17, 83] can improve the  $M_w$  of the polymers and consequently improve the performance of the membranes. Therefore, developing a polymerisation process to remove some of these impurities at the early stages of polymer synthesis is important, and it can make significant contributions in polymer synthesis and the membrane fabrication industry.

Anti-fouling is also one of the prominent issues of membranes. It has been shown that the electrospun fibre with the poor hydrophilicity is more susceptible to irreversible fouling [82]. On the other hand, the hydrogel top layer has been reported to have a positive impact on increasing the hydrophilicity and consequently improving the anti-fouling property of the membrane [82]. In one study, the irreversible fouling ratio ( $R_{ir}$ ) which was a large component of total fouling ratio ( $R_t$ ) in PES, was considerably reduced and reversible fouling ratio ( $R_r$ ) increased in modified PES NF membranes. The improved antifouling performance of rGO/TiO<sub>2</sub>/PES membranes was attributed to more hydrophilicity, more negative zeta potential and lower roughness of the NF membrane surface [75]. Zhu et al. [86] have also modified PES-NF membranes by grafting poly(sulfobetaine methacrylate) (PSBMA) onto the graphene oxide (GO) surface. After the membrane modification, the water flux was enhanced, increasing from 6.44 to 11.98 (L m<sup>-2</sup> h<sup>-1</sup> bar<sup>-1</sup>). The antifouling performance was improved considerably on changing the  $R_{ir}$  from 43.5% to 5.6%.

In another study on hydrophilic hydrogels, Wang et al. [84] prepared ultrafiltration membranes using PAN as the substrate and poly(vinyl alcohol) (PVA) as the top layer. They established that the PAN/PVA nanofibrous material had a very high permeate flux and rejection rate for oil-water separation. The limitations of this research were firstly the potential environmental impact on using glutaraldehyde water/acetone solution for cross-linking purposes, and secondly the low rejection performance for small organic molecules

[85]. Overall, it appears that adding different flexible polymers such as PVA, polyoxyethylene (PEO) and chitosan [22, 23, 74] can improve the performance of the fabricated membranes [82].

Although superhydrophobic surfaces have excellent water repellence, their wetting resistance in the environments containing organic contaminants may result in severe fouling or poor sealing performance by swelling. In this context, Lee et al. [87] have developed a positively charged poly(vinylidene fluoride-co-hexafluoropropylene) (PVDF-HFP) nanofiber grafted with negatively charged Si NPs to obtain an omniphobic membrane for desalinating highly saline feed solutions. Using omniphobic surfaces could be a practical approach, because omniphobic surfaces result in repelling both water and organic liquids while minimising fouling of the membranes [87].

Despite positive outcome on surface modification on membrane performance and special properties, the preparation of these modified membranes is usually [19-23, 25-28, 74] a time, cost, and energy consuming process. For instance, in research by Safarpour et al. [75], the whole process of rGO/TiO<sub>2</sub>/PES NF membrane preparation is reported to take more than 24 h. In order to make a homogenous modified solution and remove any bubbles in the polymer solution, experiments longer processing times at specific temperatures are featured. Hence, to eliminate a large amount of the related time, cost, and energy usage, a process which has the ability of reducing the time for preparing the base polymer solutions for membrane fabrication with or without specific modification can be of the most importance in membrane separation.

#### **1.4.11. Interfacial polymerisation**

Although this is not the focus of the present work, it is worth noting that interfacial polymerisation (IP) is the most common commercial technique to prepare the main barrier layer for TFC membrane in NF and RO systems [5, 6]. In this technique the TFC-NF membrane is prepared by a polycondensation reaction between two monomers on the surface of the support layer. The IP process is carried out by firstly contacting the aqueous phase (containing piperazine (PIP) or m-phenylenediamine (MPD)) with the porous support, followed by removing the extra aqueous solution from the porous support and pouring the organic phase

(containing trimesoyl chloride (TMC)) onto a surface, as schematically shown in Figure 1. 10 . Due to the immiscible nature of the aqueous and organic phases, the polycondensation reaction between these monomers only happens at the interface, making an ultrathin selective PA layer in the boundary layer. *m*-Phenylenediamine (MPD) is mostly used as the aqueous phase for fabricating RO, forward osmosis (FO) and NF membranes, while piperazine (PIP) is usually used for NF membrane fabrication [5, 13, 88, 89]. The IP process has the advantage of synthesising a very thin barrier layer on the substrate. This process is also reliable due to the self-limiting reaction. It means that the process will be continued till there is no unreacted monomer at the interface of the two immiscible solutions [5].

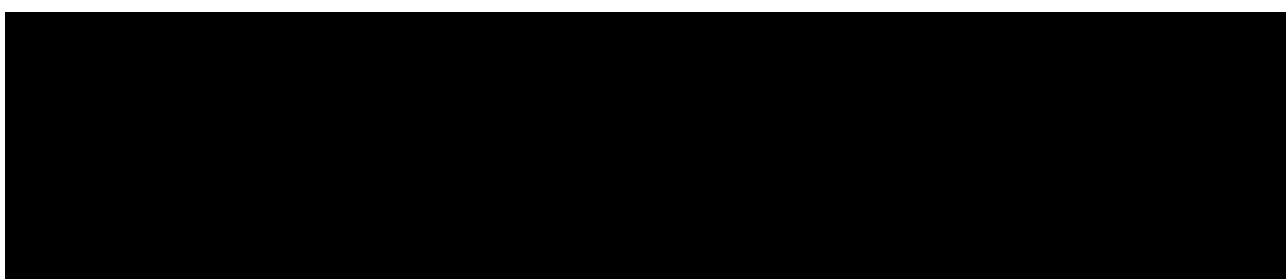


Figure 1. 10. Schematic illustration of fabrication process of TFC membrane using the IP process involving N-aminoethyl piperazine propane sulfonate (AEPPS) to improve hydrophilicity [88].

Tang et al. [90] have done a comprehensive study on 17 widely used commercial RO and NF composite polyamide membranes and found that semi-aromatic TFC-NF membranes formed by the interaction between PIP and TMC are more hydrophilic than the fully aromatic TFC-RO membranes obtained using aromatic MPD and TMC monomers [90]. Monomers used in TFC also affect the surface morphology. Using PIP results in generating membranes with root mean square roughness of less than 10 nm which are smoother than MPD-based membranes with that of greater than 50 nm [13].

Many studies have been conducted to modify the surface properties of the active layer of the TFC membranes. For instance, using N-aminoethyl piperazine propane sulfonate (AEPPS) to improve hydrophilicity [88], and using 2,2'-benzidinedisulfonic acid (BDSA) in aqueous phase [89]. Tang et al. [90] established that negative charge on membranes results from the presence of carboxyl groups obtained by the hydrolysis of non-reacted acyl chloride groups. This finding is also consistent with the results of using BDSA [89], where the optimized TFC membrane showed rejection capability of different inorganic electrolyte in the order of:

$\text{Na}_2\text{SO}_4 > \text{NaCl} > \text{MgCl}_2 > \text{CuSO}_4 > \text{MgSO}_4$ . It means that adsorbed cations coat the surface of the membranes resulting in a decrease in the surface potential and a much weakened Donnan effect (separation mechanism in NF membrane is not only by sieving and steric hindrance, but also the Donnan and dielectric effects play a key role). The schematic model of separation process via the TFC-NF membrane using BDSA is proposed in Figure 1. 11 [89].

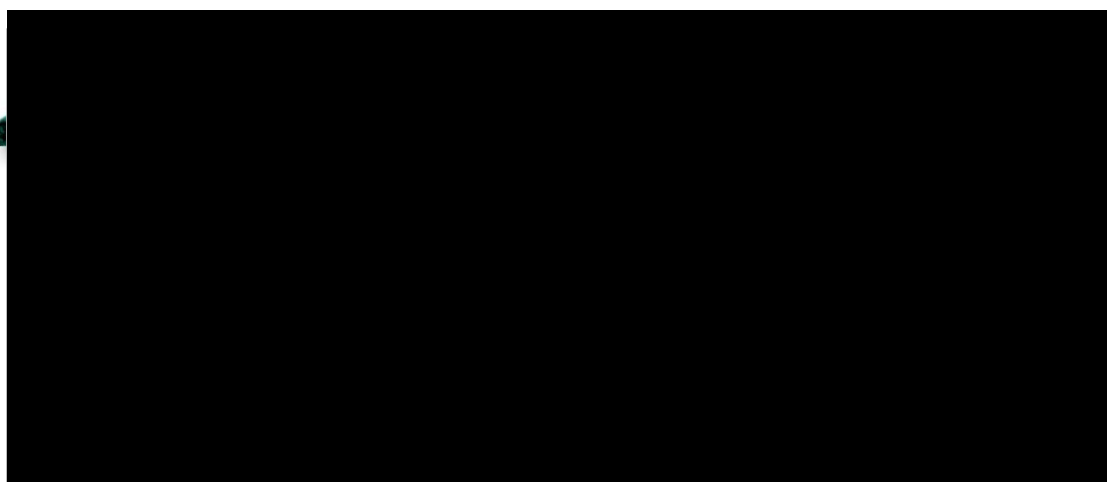


Figure 1. 11. Schematic model of separation in TFC membrane fabricated via BDSA and TMC [89].

Yin et al. [91] also developed a thin-film nanocomposite (TFN) membrane by incorporating graphene oxide (GO) with the GO nano-sheet prepared by the exfoliation of graphite flakes. MPD and TMC-GO mixture were used to do the *in-situ* IP process. The improvement in water permeability in TFN membrane comes from the interlayer spacing from the exfoliated GO nano-sheets which can result in a water channel in filtration process (Figure 1. 12) [91].

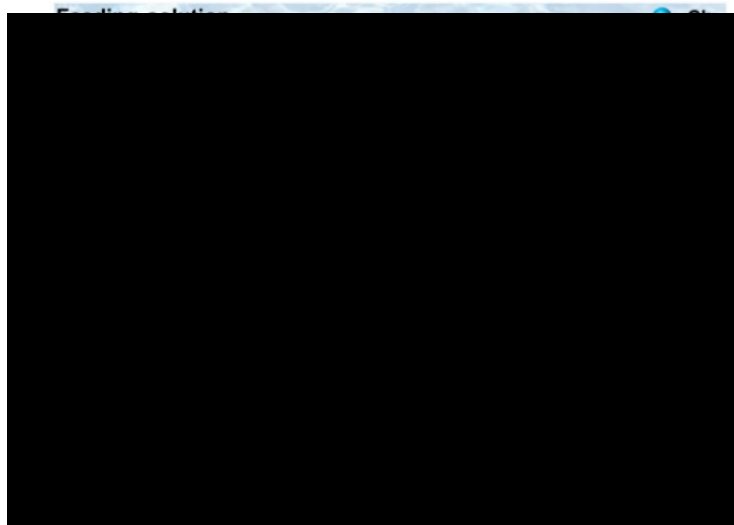


Figure 1. 12. Schematic illustration of hypothesized mechanism of GO TFN membrane [91].

Of note in this research is exfoliating of the graphite flake which uses a specific chemical process involving different steps, as explained in the literature [91]. In other studies, the exfoliation of graphite has been established in microfluidics devices. For example, Chen et al. [29] used shear stress in a Vortex Fluid Device (VFD) to generate a graphene with minimal damage.

The abovementioned studies and other research have been undertaken on the phase inversion, electrospinning, and interfacial polymerisation processes to improve the performance and stabilities of the polymeric membranes. Regardless of the fabrication method of the membrane, starting material polymers can be an essential component of UF membranes. Synthesising the common polymers used in UF membrane fabrication as well as modifying their properties can play a key role in improving the cost-effectiveness, properties, and performance of UF membranes.

#### **1.4.12. Polymerisation**

Polymers, both natural and synthetic, are comprised of many small molecules, known as monomers. Their consequently large molecular mass relative to small molecule compounds produces different physical properties including, polymer architecture, viscoelasticity,  $M_w$ , and  $T_g$ . Depending on how the molecular chains are linked or joined, polymers are divided into thermoplastics, elastomers, and thermosets. Thermoplastics are those in which macromolecules are linked by intermolecular interactions or van der Waals forces, forming linear or branched structures such as polystyrene, polyamide, polyvinyl chloride. Elastomers and thermosets are the groups of polymers in which their macromolecules are joined by chemical bonds. Elastomers such as natural rubber and polyurethanes have slightly or partially cross-linked structure. Thermosets such as epoxy resins, phenolic resins and unsaturated polyester resins, on the other hand, have highly cross-linked structures [92].

Based on their key properties such as  $M_w$ ,  $T_g$ , and viscosity, different polymers reflect different behaviour under the operation conditions which result in defining their chemical, thermal and mechanical stabilities.  $T_g$  generally refers to a range of temperature in which the material is transformed from a solid form into a rubbery state.  $T_g$  is always lower than the

melting temperature ( $T_m$ ) of the specific material with the glass transition occurring over a range of temperatures rather than at a specific temperature [43].

Molecular weight is a measure of the sum of the atomic weight values of the atoms in a macromolecule, which is commonly abbreviated by M.W. or  $M_w$ . Molecular weight is either unitless or expressed in terms of atomic mass units (amu), Daltons (Da), g/mol, or kg/mol. The structure and shape of the polymer is attributed to the way branch points lead to a deviation from a simple linear chain. The structure of polymer affects most of its properties including viscosity, solubility in various solvents and  $T_g$  [92]. Weight average molecular weight ( $M_w$ ), investigated in this thesis, includes the mass of individual chains, which contributes to the overall molecular weight of the polymer.  $M_w$  is the sum of all molecular weights multiplied by their weight fractions.

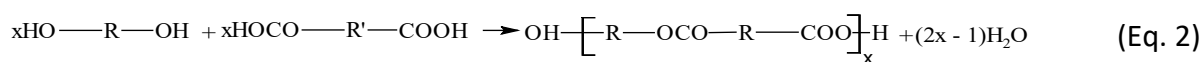
Improvement in the chemical, thermal and mechanical properties is of great importance in polymeric membrane fabrication. Membrane fouling is also an important phenomenon in NF membranes. Increasing the hydrophilicity of membrane has been the focus of some studies to decrease the likelihood of fouling [93, 94]. In order to improve the hydrophilicity and stability of membranes, several physical and chemical modifications can be used including; (i) grafting the hydrophilic monomers, (ii) implementing functional groups by plasma treatment, (iii) physical adsorption of the hydrophilic components such as nanoparticles and surfactants to the membrane surface, or (iv) modifying the polymers during their synthesis before fabrication of the membrane [93]. Modifying the membrane during different membrane fabrications has been discussed before. Hence, in this section the main research is on synthesising a polymer before the membrane fabrication process is reviewed.

#### **1.4.12.1. Principles of polymerisation**

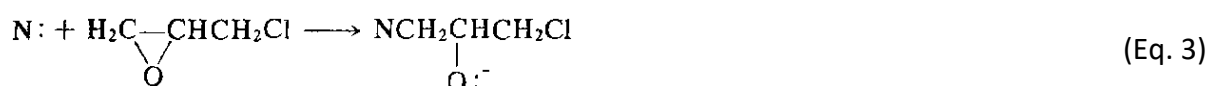
The progressive trend of interests in polymer science in the current century is crystal clear, with the annual production of polymeric based materials has an average growth of 9% per year from about 1.5 million tons in the middle of the twentieth century to more than 200 million tons in this current century. Basically, polymers involve two or more bonds between individual molecules [92]. Based on the reaction mechanism, polymerisation can be classified into step-reaction and chain-reactions which are commonly used for two different groups of polymers, and are referred to as condensation and addition polymers, respectively. The



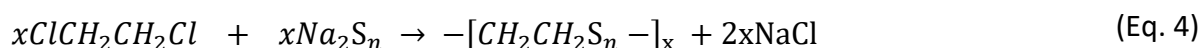
molecular structure of the condensation polymers lacks certain atoms present in their starting monomers. In other words, the polymers can be produced by the reaction between two monomers to make the larger molecule with or without the elimination of a small molecule such as water (Eq. 2 shows the Step-reaction (Condensation polymers)) [95, 96].



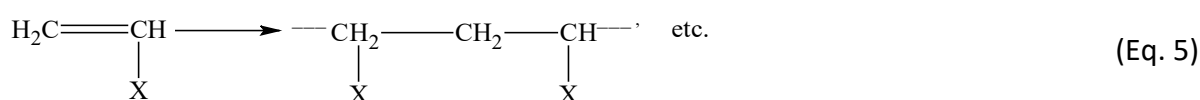
Among different types of condensation reactions, “Nucleophilic Substitution Reaction” is used to synthesise PSF [18] which is commonly used in UF membrane fabrication. This reactions is used mainly in synthesising commercial organic polymers such as epoxide polymerisation where a reaction between a nucleophile N: (typically a bifunctional hydroxy compound such as bisphenol A) and an epoxide monomer (such as epichlorohydrin) occurs (Eq. 3) [95].



Nucleophilic substitution reactions were also used in producing the early polysulfide rubbers from aliphatic dichlorides and sodium sulfide (Eq. 4) [18, 95]:

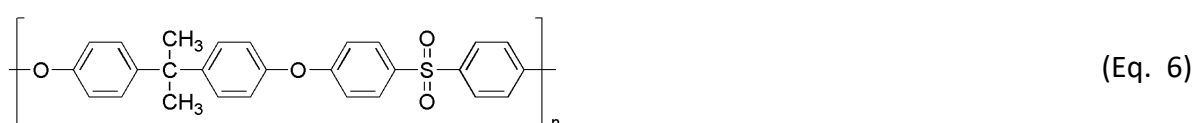


Generally, chain reactions usually consist of many repeating elementary steps, each of which has a chain carrier. Once started, chain reactions continue until the reactants are exhausted. Most chemical chain reactions involve very reactive intermediates called free radicals. The intermediate that maintains the chain reaction is called a chain carrier, and they are usually free radicals. However, addition polymerisation involves a chain reaction in which a free radical, an ion is covalently attached to the catalysts and can be the chain carrier. In this type of polymerisation, the loss of small molecules does not occur. Unsaturated vinyl monomers can produce important polymers (e.g. polyvinyl chloride) via this process, as shown in (Eq. 5) [95].



#### 1.4.12.2. Polysulfone (PSF) and polyethersulfone (PES)

PSF, as a very common polymer from the thermoplastic groups, is classified as aliphatic and aromatic polysulfones. The term aliphatic is used for the compounds which does not contain benzene ring or phenyl group, whereas aromatic compounds get aromaticity by benzene ring. Due to unattractive physical properties of the aliphatic polysulfones, the aromatic group has always gained more attention from both in academia and industry. The aromatic polysulfones which are often called PS, PSU or PSF are characterized by their sulphone groups as their repeating unit (Eq. 6) [97].



This group of polymers has long been of importance for different applications due to their desirable thermal, chemical, and mechanical stabilities. According to the basic repeating units as the main parts of backbone structures of these polymers, they are also known as polyethersulfone (PES) or polyphenylsulfone (PPSF) which are shown in Table 1. 3 [93, 97].

Table 1. 3. Chemical structure and Glass-Transition Temperature,  $T_g$ , of PS, PES, PPSF [97].

From Table 1. 3, a diphenylsulfone group (Figure 1. 13-a) is a similar repeating unit in all of the polysulfones which is reported to be derived from dihalodiphenylsulfone (Figure 1. 13-b).

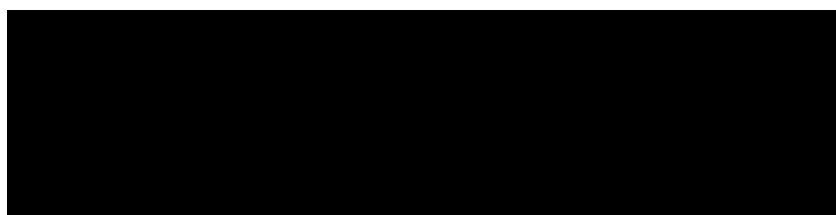
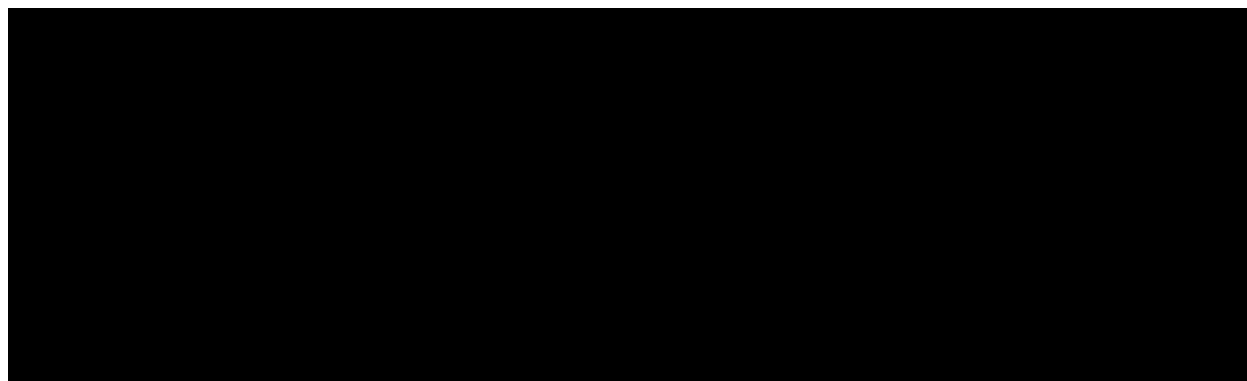


Figure 1. 13. Structure of the (a) Diphenylsulfone group as a repeating unit in (b) Dichlorodiphenyl sulfone.

The main difference between the various types of polysulfones comes from the type of bisphenol (Table 1. 4) used during polymerisation process. The  $T_g$  of a polymer can be affected by different monomer used during the polymerisation process. For instance, different types of Bisphenols, as indicated in Table 1. 4, result in different  $T_g$  values in polysulfone synthesising [97].

Table 1. 4.  $T_g$  of polysulfones prepared from polycondensation of DCDPS with various Bisphenols [97].

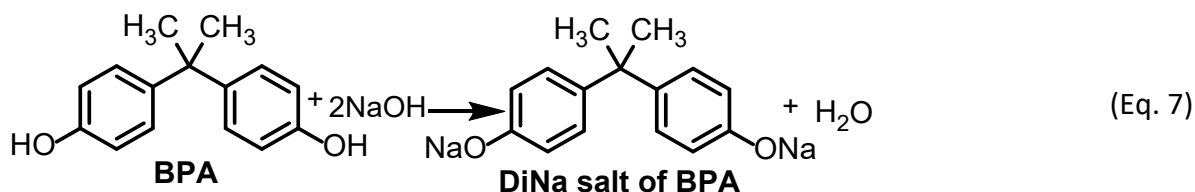


PES and PSF are widely used in UF membranes. Their hydrophobic properties result in increase in membrane fouling [93]. Although PES has better thermal stability ( $T_g = 225^\circ\text{C}$ ) compared with PSF ( $T_g = 190^\circ\text{C}$ ), both are amongst the most common polymers used in membrane fabrication [98]. The “Nucleophilic substitution route” is a common approach in preparing commercial polysulfone polymers (PS, PES, or PPSF) [18, 97].

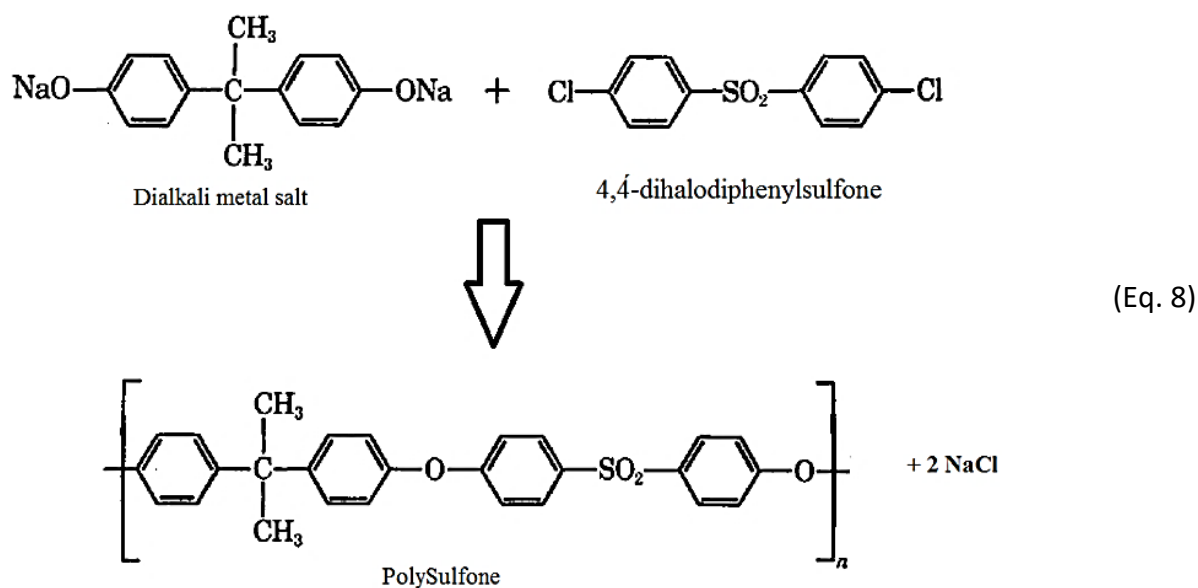
#### 1.4.12.3. Nucleophilic substitution route for polysulfone synthesis

This approach is the most common and efficient method of synthesising commercial polysulfone. As the main precursors, several essential components are introduced in this approach, including a bisphenol of choice and a dihalodiphenylsulfone in a dipolar aprotic solvent in the presence of an alkali base. In this polycondensation reaction, the aromatic ether bond is formed in a reaction between equimolar quantities of 4,4-dihalodiphenylsulfone and a bisphenol in the presence of base which results in generating an alkali salt as a by-product that needs to be filtered at the end of polymerisation [18, 97]. Synthesising polysulfones by this nucleophilic substitution is reported to be completed in two separate steps;

Step one: bisphenol A is converted to the dialkali metal salt by reacting with a base (Eq. 7) [18, 97].



Step two: substitution reaction of the dialkali metal salt (obtained in previous step) with a 4,4'-dihalodiphenylsulfone (Eq. 8). It is worth mentioning that the dichloride is more economical than the difluoride, although the difluoride-based monomer is more reactive. The difficulty in dissolving the alkali bisphenate (di sodium salt of BPA, DiNa salt of BPA) under anhydrous condition is overcome by a careful choice of solvent to both solubilise the organic halide and the growing polymer chain. DMSO and sulfolane have been shown to be good solvents, although DMSO is the preferred option in conventional PS polymerisation method. Furthermore, a co-solvent such as chlorobenzene or toluene can be used in low concentration to enhance the solubility of precursors and the polymer [18, 97].



The water generated in the first step should be removed to create anhydrous conditions. Water removal is an essential step to prevent hydrolysis of the dihalodiphenylsulfone and to complete the polymerisation to generate suitable polymers with high molecular weight [97]. In this approach, the solubility of the alkali bisphenate in a specific solvent under anhydrous condition is an important factor for selecting the solvent. Increasing the temperature to ~120 °C for removing the water and to above 150 °C to allow the polymerisation to be driven to

completion, necessitate that this method is exclusively carried out at high temperatures. For temperatures below 150 °C, terminal bound sodium- polymers of low molecular weight might precipitated on the internal surface of the reaction vessel [18].

Different alternatives for the aprotic solvents that have been investigated for synthesising different polysulfones, including N-methyl-2-pyrrolidinone (NMP), dimethyl acetamide (DMAc), sulfolane, and dimethyl sulfoxide (DMSO), with the latter reported as the best solvent for the polymerisation process. Such a high polar solvent is believed to be essential for providing the solubility and also rapid polymerisation rates. Polymerisation rates also depends on the basicity and electron-withdrawing capacity of the activating groups (sulfone groups, in this case) [18].

Sodium hydroxide, potassium hydroxide, and potassium carbonate are also different alternatives for the base to be used in the polysulfone synthesising process. NaOH and K<sub>2</sub>CO<sub>3</sub>, have been reported as the suitable bases for PS and PES synthesising, respectively [18].

#### **1.4.12.4. Limitations of conventional polysulfone synthesising**

Although synthesising polymers by nucleophilic substitution can be carried out using conventional methods [18, 97], these techniques have some disadvantages such as being time consuming, the high cost providing enough energy for completing the reactions, as well as additional steps of removing the by products such as NaCl. To achieve the benefits of a lower time- and cost-effective process with the minimal need energy input, novel technologies need to be investigated. One of the alternative technologies which can be a potential approach for polymerisation process is microfluidics, although this has not been widely used. The Vortex Fluid Device (VFD) as a thin film microfluidic system, and it can be used in polymer synthesis. The VFD has some unique advantages such as the processing being fast, simplicity and scalability of the processing, and cost-effective operation conditions. Also noteworthy is that this platform not only can be used in synthesising the basic polymers, but it has potential in modifying the properties of the polymers. This has been discussed in earlier studies [1, 19-23, 25-28, 74, 75, 91] to improve the properties of polymers in a time and cost-effective manner while being a simple and more effective process. The principles and applications of this technology are explained in the following section.

#### 1.4.13. Microfluidics

Micro-technology in general, and microfluidics in particular, can facilitate the accurate study of cellular behaviour *in vitro*. Microfluidics involve the handling and manipulation of very small fluid volumes ( $10^{-9}$  to  $10^{-18}$  litres), enabling creation and control of microliter-volume channels (with ten to several hundred micro-meters as it is shown in Figure 1. 14) [99].

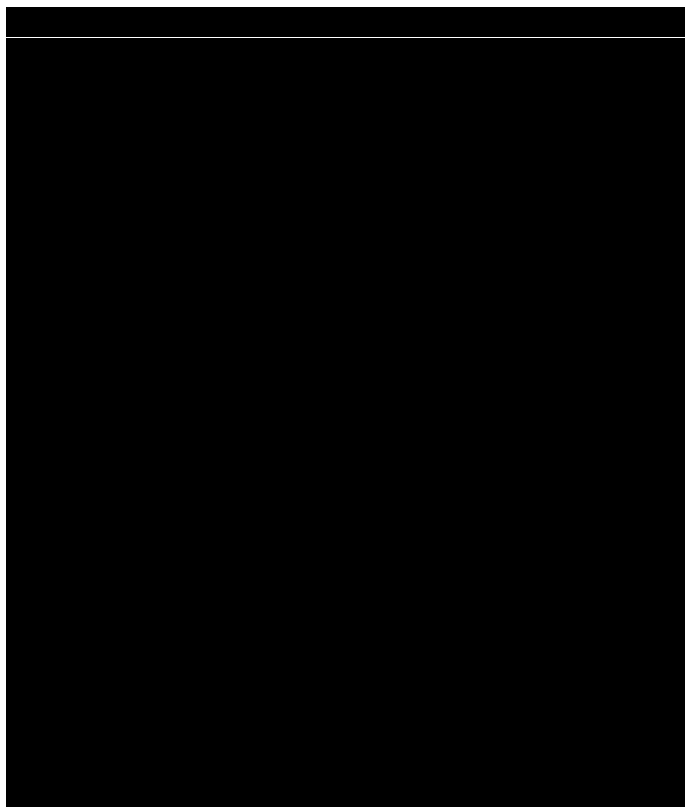


Figure 1. 14. Schematic illustration of the principles of microfluidics and fluid flows [99].

The fluid flow in micro-channels has different behaviour and consequently some special principles are employed compared with large channels [100]. This new field of research has been extensively applied for medical diagnostics and bio-analysis applications [100]. The microfluidic devices which can be used in different applications have some advantages such as low reagent and power consumption, portability, high resolution and sensitivity in separations and detections at low cost and faster processes [99, 100].

#### 1.4.14. Microfluidic devices

Microfluidic systems have been employed in a wide range of applications including microanalysis, microelectronics, molecular biology, chemistry and biochemistry using their

specific devices [\[101-103\]](#). Spinning disc processors (SDPs) and rotating tube processors (RTPs) are the devices firstly invented to be applied in microfluidics systems. An SDP consists of feed jets which are directed to almost the central part of a spinning disk in where micro-mixing occurs. The residence time in this device is less than a second which is a weakness of this instrument for some of the reactions which require longer processing times (Figure 1. 15) [\[31\]](#).

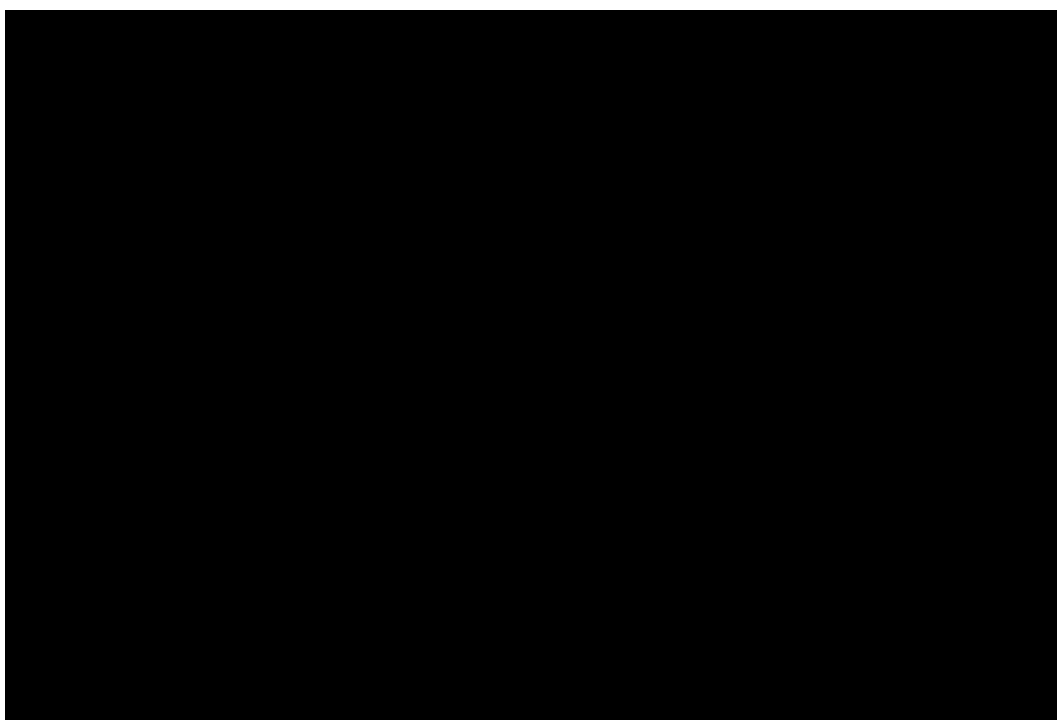


Figure 1. 15. Schematic diagram of the spinning disc processor in Chitosan Nanoparticles manufacturing [\[101\]](#).

RTP (Figure 1. 16) has a longer residence time that can be about minute, depending on some operational parameters such as flow rate and the tube length. Feed solutions that are delivered by jet feeds are mixed at one end of the tube by its rapid rotation, and the mixed product is collected on the other end of the tube [\[31\]](#).

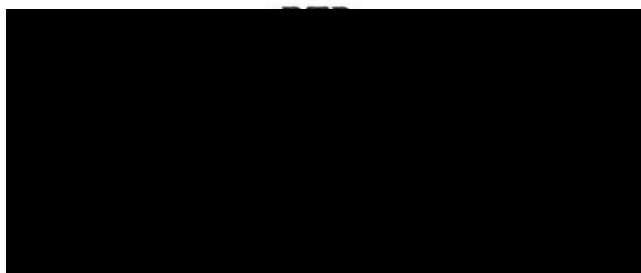


Figure 1. 16. Illustration of feeding two stable stream into a RTP [\[103\]](#).

The abovementioned devices as well as another device patented by Cowen. et al [104] for chemical processing on the surface of a rotating body can be used for some applications such as controlling chemical reactions, probing the structure of self-organised systems, and graphene production by graphite exfoliating. However, they suffer from some limitations including specific liquid volumes required to reach a constant fluids shear intensity, limited residence time and the expensive infrastructure constructions. Moreover, conventional batch processing methods have always had some limitations regarding the scalability, and reproducibility [31, 33]. Hence, such limitations make developing the novel approaches sensible and essential.

#### **1.4.15. Vortex fluid device (VFD)**

While conventional microfluidic devices are applicable only in laminar flow with low Reynolds numbers, VFD has been developed and used in some studies interested in microfluidics systems working in turbulent flow with high Reynolds numbers [29-35, 37-42, 54]. The VFD is a novel platform developed for continuous flow applications operating by a combination of effects, such as micro-mixing, viscous drag, microfluidic flow, Faraday waves, and enhanced mass transfer all resulting in specific improvement in the efficiency of different processing applications [29-35, 37-42, 54].

Microfluidic platforms have been developed based on the need to produce thin films in different methods. This started with SDPs with a short residence time followed by RTPs where the residence time is increased to minute and finally led to invention of the VFD with a longer controllable residence time (Figure 1. 17) [42].

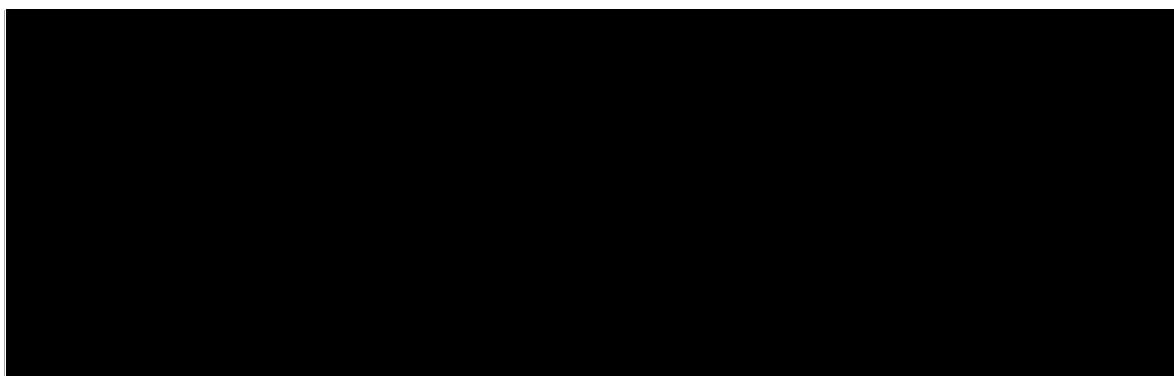


Figure 1. 17. An overall schematic view of the microfluidic devices placement, feeding and working [42].



Although the thinness of the films using SDP and RTP has improved the heat and mass transfer observed using conventional batch methods, they suffer from some limitations including residence time and their inapplicability in different angles relative to the horizontal positions, while the VFD has solved these problems. In addition to the viscous drag in SDPs and RTPs, the shear in the thin film in VFDs has been resulted from the combination of the centrifugal and gravitational forces at tilt angle  $\neq 0^\circ$  [31].

The VFD consists of a rotating open-end tube which can be positioned in different tilt angles, and the feed jets (Figure 1. 18). The open-end tube can be adjusted with a controller to be rotated in different rotational speed which results in different shear intensity. Efficiency of the processes carried out by VFD is mainly based on the flow rate of the feedstock, tube's inclination angle, rotational speed and some other operational parameters (e.g., temperature and residence time) [41].

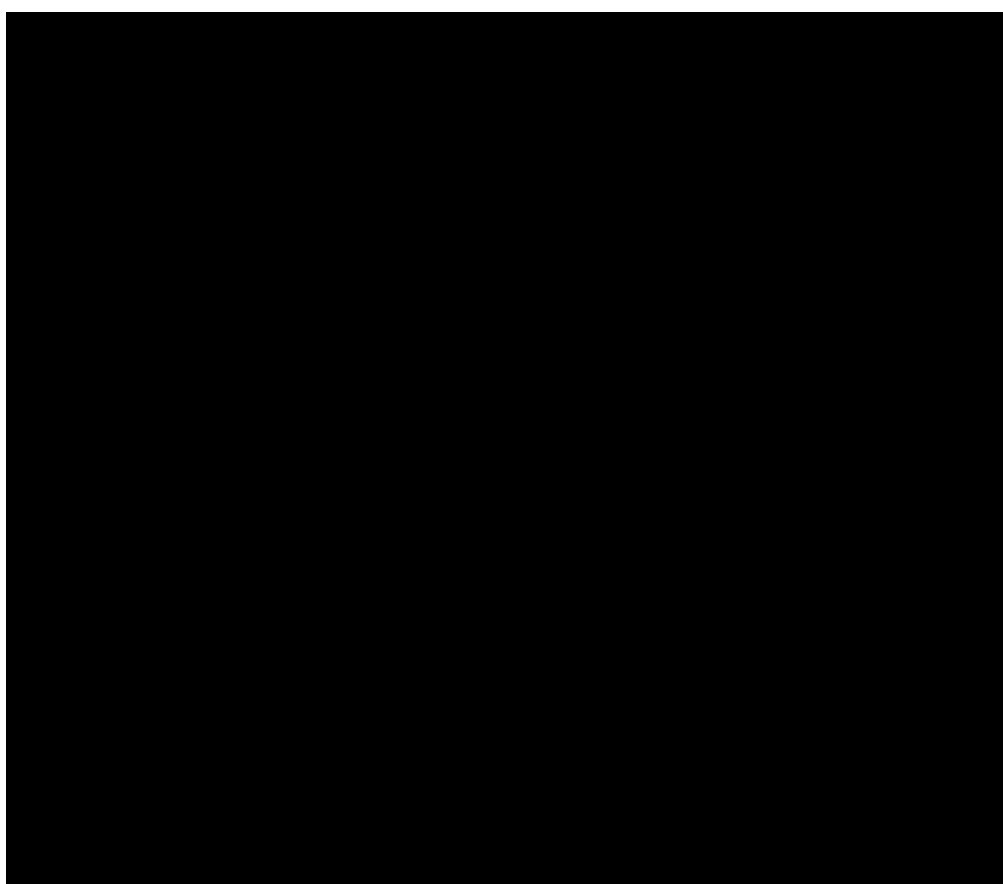


Figure 1. 18. Cross section showing the components of the VFD [31].

The borosilicate or quartz tube in VFD is able to be rotated up to 9k rpm and tilted at any angle between  $0^\circ$  and  $\pm 90^\circ$ . The dynamic thin film is formed on the internal surface of the

tube due to the centrifugal force and associated intense shearing and consequently, intense solution micro-mixing. The residence time and mixing efficiency can be adjusted based on the length of the tube and feed flow rates. In comparison with the products of the SDPs and RTPs, a finite volume of liquid in the thin film layer in the VFD has a longer residence time with enhanced mixing of the reactants both, mediated the completion of certain organic reactions within significantly shorter times [31].

The VFD mediates reactions when performed using the confined mode (batch) or continuous flow operation mode, depending on the applications under investigation. Using continuous flow processing can facilitate transfer of research to be industry in being able to scale-up and being advantageous in minimising the generation of waste and energy usage while reducing the hazardous risk of the processing. However, the continuous mode has shorter residence time which can limit the utility of this mode for some organic reactions [37]. In the confined mode, the reactions involve adding a finite volume of reagents under specific conditions for a specified time. Continuous flow mode can be carried out by delivering starting solutions materials directly to the base of the rotating tube using feed jets, where the rotation results in formation of a dynamic thin film, with the liquid moving up and out of the tube for collection. Changing the rotational speed and flow rate can control the residence time of the reactants even in large scale processing [31, 41].

During the last few years, VFD processing has been widely used in different studies focused on graphite exfoliating [29], chemical reactivity and selectivity [31], amide synthesis reactions [32], pharmaceutical applications [33, 34], growth of the nanoparticles on carbon nanotubes [35], fabricating composite nanomaterials [35, 36], breaking down polyethylenamines [38], topological fluid flow in the VFD [40], and controlling the pore sizes of the mesoporous silica [39]. For example, Tong et al. [39] used the VFD in the continuous flow mode to establish a new approach for synthesising a well-ordered 2D hexagonal mesoporous silica (SBA-15). The conventional hydrothermal process used for SBA-15 synthesis requires high temperature (35 to 100°C) and pressure (in an autoclave) and long residence time (24 -48 h). In addition, producing small particles with controlled pore size and thickness with significantly shorter processing times, are limitations of the conventional process [39].

The results established that the turbulent flow conditions prevail in the VFD with dramatic reduction in processing times and the number of different steps required [39]. This is attributed to the high shear during the processing, being beyond the limits of diffusion-controlled processing with an increase in collisions of the different species, resulting in reduced processing times and importantly the ability to avoid the conventional thermal step. Moreover, due to the high shear generated in the tube, micro-mixing process and viscous drag, the liquid inside the VFD is more homogenous [39]. Tong et al. concluded that not only is the overall time of the processing reduced from 48 h in conventional hydrothermal process to less than 5 h using VFD, but also the pore size can be varied by varying the shear in thin films inside the VFD (by varying the rotational speed), which plays a key role in controlling the thickness of the pore walls [39].

Britton et al. [32] studied the application of the VFD as a novel approach in the synthesis of polymeric products. Forming amine bonds is important in preparing pharmaceuticals, biologically active compounds, synthetic polymers, and proteins, and they can be readily controlled in the VFD, in contrast to conventional batch processing. Different parameters such as rotational speed and tilt angle of the glass tube, feed flow rate, and temperature were optimised. Results show a dramatic increase in the yields of the amides obtained by VFD compared with the traditional batch techniques. High heat transfer in the VFD was effective in controlling exothermic reactions, which were complete in less than 80 s at room temperature via the VFD. In contrast, batch-type reactions typically suffer from violent exotherms that result in reagent degradation, lower yields, and safety concerns [32].

Gandy et al. [33] have studied the formation of C-N bonds, as a common bond in natural and synthetic compounds in organic chemistry, using the VFD in a confined mode, with the results were compared with the batch method. The rotational speed in the VFD can be varied along with the tilt angle of the tube, with optimal conditions resulting in 64% yield in short processing times relative to traditional batch processing [33].

The VFD was also used by Tong et al. [34] to carry out so-gel processing of silica hydrogel with reduced processing time, without the need for using alcohol or additional acid or base and with in situ incorporations of curcumin. The advantages of this microfluidic platform in this

study include faster kinetics, with controllable pore volume, and avoiding the main difficulties of the traditional batch processing, especially the long processing times.

The VFD can be used in controlling the reactivity and selectivity of the reactions including Diels–Alder reaction [31], condensation of phenols with aldehydes in forming calixarenes [41], and sequential aldol condensation and Michael addition reactions [31]. Research by Yasmin et al. [31] focused on using different shear regimes in promoting the Diels–Alder dimerisation of cyclopentadienes, and adol condensation and Michael reactions which is not possible using conventional approaches

Chen et al. [29] used the VFD to exfoliate graphite and generate a graphene with minimal damage. Other solution-based methods or high energy ball milling, and high power conventional sonication impart defects in the generated graphene. Results confirmed the application of the VFD in top down fabrication methods in synthesising different nano-materials relatively free of the defects [29].

From what has been discussed, the most efficient UF membranes are those with the suitable chemical/thermal/mechanical durability which can be obtained economically from the ceramic and polymeric materials [59]. In spite of the high chemical/thermal/mechanical stability of ceramic materials their application in UF membrane is limited because of their weakness in controlling the pore size and also costly fabrication processes [6, 25]. While polymeric membranes are relatively more popular due to their easier and cheaper preparation procedure, to improve their stability, different costly and time consuming modifications need to be carried out [25]. Based on the literature, the most important and effective parameters to fabricate an engineered UF membrane are polymer types and their specific properties such as  $T_g$  and  $M_w$ . Hence, synthesising the common polymers which are used in UF membrane or modifying them via a more time and cost-effective procedure is very important. The VFD has potential for polymer synthesis and modification thereof, which relates to the high shear stress driving the processing, ease of use of the device, scalability, time and cost-effective procedure.

The benefits of VFD processing in chemical synthesis includes reaction scalability and efficiency. The dynamic thin film created in continuous flow in the VFD has advantages regarding the (a) rapid heat dissipations, (b) enhanced mass transfer, (c) reaction

homogeneity, and (d) reduced clogging in the reaction vessels [105]. In research by Britton et al. [105] the high yields of synthesising the di-carboxylate esters was likely to be a result of water removal by using VFD in continuous flow. Water evaporation increased because of the large surface area of the thin film created inside the VFD tube. Using VFD results in changing the surface tension of the fluids due to high shear stress rates at the micro-scale. Hence, changing the surface tension could facilitate water removal at a lower temperature compared with the conventional methods. Therefore, to investigate the application of VFD as an efficient device in polymer and membrane science in this research project, it will be attempted to answer the research questions outlined in the following section.

In a comprehensive study by Raston group, topological fluid flow in the VFD has been investigated [40] with respect to the circular flow in the surface of the tube, double-helical flow across the thin film, and spicular flow, a transitional region where both effects contribute. This includes new phenomenological shear stressed crystallization and molecular drilling on a polymeric thin-film in the VFD. As one of the main findings of this research was introducing the double helical fluid flow inside the VFD which is affected by the VFD rotational speed. As shown in Figure 1. 19, the higher the rotational speed,  $\omega$ , the smaller double helices pitches obtained along the tube. This phenomenon which occurs under shear stress resulted in some topological effects in material processing which can be of highly importance in the present research in membrane fabrication of the VFD mediated polymer solutions.

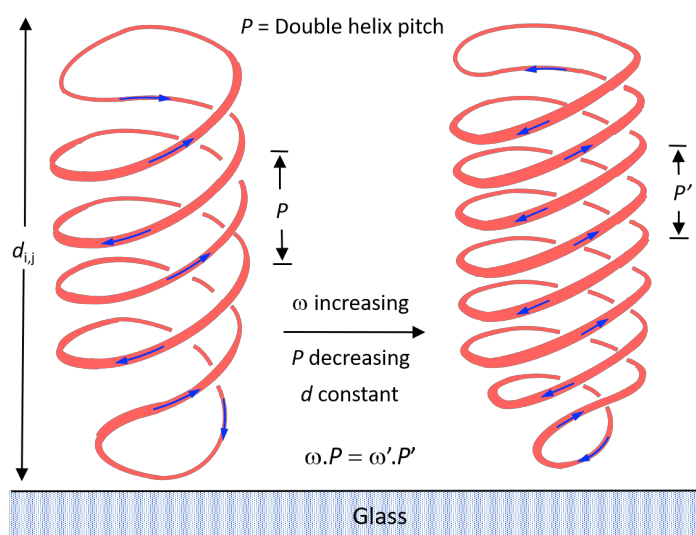


Figure 1. 19. Double-helical fluid flow created in the VFD with a reduction in helical pitch for higher rotational speeds [40].

## **1.5. Research questions**

### **RQ1. Is it possible to use the VFD platform in PSF polymerisation process?**

This research question will be addressed in chapter 2, which resulted in a publication in RSC Advances journal.

### **RQ2. How the key properties of the polymers can be manipulated and fine-tuned during VFD-based polymerisation process?**

This research question has been vastly addressed in chapter 2 and 3, with details of experimental outcomes in VFD synthesised PSF under high shear conditions.

### **RQ3. How the polymerisation process inside the VFD can be optimised (e.g., lower temperature, shorter process time, higher product purity and lesser waste or by-product generation) to become more time and cost effective and eco-friendly?**

This question has been answered by details in chapter 3, which has recently been submitted to Polymer Chemistry in Royal Society of Chemistry publication.

### **RQ4. How the VFD operating conditions can affect the UF membrane fabrication process?**

This research question has been nicely addressed in chapter 4, and the results are under review in the Journal of Membrane Science.

### **RQ5. How the VFD features would be helpful in facilitating a continuous mixing process in fabricating enhanced UF composite membranes while GO incorporation in the PSF compared to the conventional mixing procedure?**

This question has been addressed with interesting results on VFD mediated fabrication of the UF composite membranes in chapter 4.

## 1.6. Research materials and methods

To answer the main research questions in this project, comprehensive and well-designed experimental studies will be conducted using the following materials and methodologies.

### 1.6.1 Materials

The materials needed for PSF polymerisation (by conventional approach or by using VFD) and membrane fabrication are listed below:

- 1) Bisphenol A [2, 2- bis (4-hydroxyphenyl) propane] (Sigma-Aldrich Pty. Ltd).
- 2) Dimethyl sulfoxide (DMSO) (Sigma-Aldrich Pty. Ltd).
- 3) Chlorobenzene (Sigma-Aldrich Pty. Ltd).
- 4) 4, 4'-dichlorodiphenyl sulfone (DCDPS) (Sigma-Aldrich Pty. Ltd).
- 5) Sodium hydroxide (NaOH) (Sigma-Aldrich Pty. Ltd).
- 6) Methyl chloride (BOC Limited (Australia)).
- 7) Ethanol (Merck Pty. Limited).
- 8) Tetrahydrofuran (THF) (Merck Pty. Limited).
- 9) Dimethylformamide (DMF) (Sigma-Aldrich Pty. Ltd).
- 10) Nitrogen gas (N<sub>2</sub>).
- 11) Acetone (Chem-Supply Pty. Ltd).
- 12) N-hexane (Sigma-Aldrich Pty. Ltd).
- 13) Graphene oxide (GO) (Graphenea Inc).
- 14) 1-methyl-2-pyrrolidone (NMP) (purity > 99.5%) (Sigma-Aldrich Pty. Ltd).
- 15) Milli-Q water.

### 1.6.2. Methodologies

#### 1.6.2.1. PSF synthesise via VFD and conventional methods supported by comprehensive characterisations

The above research questions are addressed in this thesis by firstly conducting PSF synthesise process both using conventional methods as shown in Figure 1. 20 ([18], Appendix A) and via the VFD processing in confined mode, using the nucleophilic substitution route. In addition, improving the properties of PSF generated in a VFD will require the processing to be under

anhydrous conditions with the mechanical energy in the rotating tube generating high shear within the thin film to drive the processing. The experimental steps are elaborated in detail in the following chapters. Determining the optimised VFD operating conditions, such as  $\omega$  rotational speed,  $T$  temperature,  $\theta$  tilt angle, and process time, were systematically investigated with respect to their  $M_w$ ,  $T_g$ , thermal stability, morphological properties, surface area and reaction yield, to be established using GPC, DSC, TGA, SEM, and BET, respectively. FTIR and NMR were used for chemically characterising the intermediate DiNa salt of BPA and the final PSF product.



Figure 1. 20. Experimental setup for conventional method of PSF synthesis

#### **1.6.2.2. Pristine PSF and GO/PSF UF membrane fabrication from conventional or continuous VFD mixed solutions, along with analytical studies on their properties and performances**

Research was undertaken in the VFD in taking advantage of its high micromixing performance in preparing bubble-free homogenous polymer solution in different PSF concentrations and VFD rotational speeds. This was fabricating pristine PSF UF membranes using a phase inversion process. The fabricated membranes from both conventional mixing procedures and VFD mixing processing were tested for their main characteristics including morphological differences, mechanical stabilities, permeabilities and salt/BSA filtration performances. Furthermore, in this research, incorporating GO into PSF using a VFD was evaluated for determining its micromixing effectiveness under high shear and intense micro-mixing on the



filtration performances of the properties of the GO/PSF UF composite membranes. Chemical structures, hydrophilicity, thermal and mechanical stabilities, morphological differences, water flux and salt/BSA rejection performances of the pristine PSF and GO/PSF UF composite membranes were fully investigated using Raman FTIR spectroscopy, water contact angle measurements, TGA, DMA, SEM and dead-end filtrations system, respectively. Processing time in both conventional and VFD mediated mixing are important in preparing the PSF and GO/PSF solutions prior to the phase inversion process. A casting knife at a fixed height of 250  $\mu\text{m}$  (Figure 1. 21-b) was used for casting the polymer/composite solutions on a flat glass surface, with a dead-end filtration system (Figure 1. 21-d) was used to check the performance of the fabricated membranes (Figure 1. 21-c). The dead-end filtration system was designed and constructed in workshops at Flinders University.

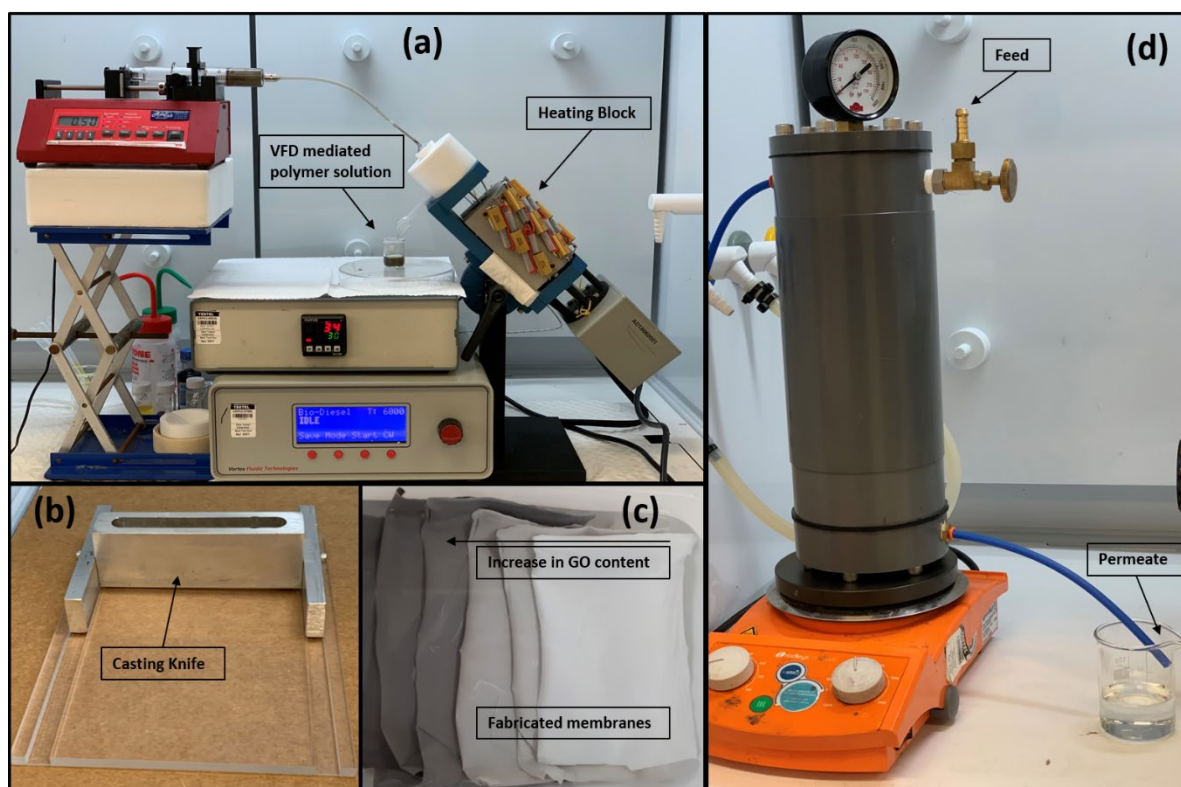


Figure 1. 21. Experimental setup for the membrane fabrication steps including (a) continuous VFD setup, (b) adjusted casting knife on a glass surface, (c) fabricated membranes (pure PSF and GO/PSF composite membranes), and (d) the dead-end filtration system adjusted on a magnet stirrer for stirring the solution inside.

### **1.6.2.3. Topological fluid flow in the VFD supported by molecular drilled PSF thin-film fabricated under high shear**

To understand the fluid flow behaviours in the VFD a series of experiments were undertaken on the PSF thin-film previously attached to the inside of the tube. Specific topological mass transport in the VFD was established through material processing in the VFD which resulted in establishing a double-helical flow across the thin film [\[40\]](#), Figure D. 8. The phenomenological shear stressed molecular drilling was hypothesised to be due to the presence of double helices in the PSF thin-film effectively 'drilling holes' in thin films of the polymer Figure D. 9. To show this phenomenon further, different concentrations of a PSF solutions were investigated to generate a uniform thin-film adhering to the surface of the tube. This was followed by drilling holes in them using the high shear fluidic flow in the VFD at different rotational speeds, then peeling them from the inner surface of the tube at different locations. The films were then studying using SEM imaging. The overall steps are presented in detail in Appendix D.

## 1.7. Thesis structure

The current thesis is written based on “Thesis with publication” format<sup>1</sup>; and is organised in six chapters as follows:

**Chapter 1** presents the general overview of the project topic, aims and objectives and motivations for this research. This is followed by a comprehensive literature review on water treatment techniques including filtration membranes, membrane fabrications, polymers synthesise, and the application of the VFD in different areas including material processing. Thereafter, research questions were suggested followed by a research methodology applied herein to address them.

**Chapter 2** discusses the use of the VFD for the synthesis of PSF, with process optimisation with respect to the main properties of PSF such as  $M_w$ ,  $T_g$ , and reaction yield.

**Chapter 3** studies the manipulating of the PSF synthesise process inside the VFD in a high shear and anhydrous conditions to enhance the properties of the VFD derived PS, while paying specific attention to the morphological differences and surface area of the polymer formed under different operating conditions.

**Chapter 4** provides information about the application of the VFD in fabricating higher quality UF membranes. It presents a comprehensive study on the effect of rotational speed on preparing the polymer solution for fabricating the UF membranes prior to the phase inversion process with mainly respect to reducing the processing time from >24 h at conventional mixing to <4 h in VFD mixing. It reveals a significant impact of the VFD in providing bubble-free polymers solutions, obtained in a shorter process time from the intense micromixing

---

<sup>1</sup> “Thesis with Publication” is an acceptable format of thesis for postgraduate research at ECU policy. The current thesis has been written based on the guideline provided at [http://www.ecu.edu.au/GPPS/policies\\_db/policies\\_view.php?rec\\_id=0000000434](http://www.ecu.edu.au/GPPS/policies_db/policies_view.php?rec_id=0000000434). In this format, the submitted thesis can consist of publications that have already been published, are in the process of being published, or a combination of these.

properties in the VFD relative to batch processing. Surface modification of the pristine PSF using GO incorporation also is presented in this chapter. It establishes how significant micromixing and viscose drag under high shear conditions is on obtaining uniformity of the GO particles incorporated into the PSF matrix compared to conventionally mixed composite membranes.

**Chapter 5** provides a general discussion of the results presented in each chapter and addresses the research questions of the project.

**Chapter 6** integrates the findings of all chapters and also outlines directions for future research.

## 1.8. Chapter references

1. Wang, J., Zhang, P., Liang, B., Liu, Y., Xu, T., Wang, L., Cao, B. and K. Pan, *Graphene Oxide as an effective barrier on a porous nanofibrous membrane for water treatment*. ACS Appl Mater Interfaces, 2016. **8**(9): p. 6211-8.
2. Cheryan, M. and N. Rajagopalan, *Membrane processing of oily streams. Wastewater treatment and waste reduction*. Journal of Membrane Science, 1998. **151**(1): p. 13-28.
3. M, L.B. *Pros & Cons of Biological Wastewater Treatments*. 2017.
4. Obaid, M., Ghouri, Z. K., Fadali, O. A., Khalil, K. A., Almajid, A. A., Barakat, N. A., *Amorphous SiO<sub>2</sub> NP-Incorporated Poly(vinylidene fluoride) Electrospun Nanofiber Membrane for High Flux Forward Osmosis Desalination*. ACS Appl Mater Interfaces, 2016. **8**(7): p. 4561-74.
5. Paul, M. and S.D. Jons, *Chemistry and fabrication of polymeric nanofiltration membranes: A review*. Polymer, 2016. **103**: p. 417-456.
6. Van der, B.B., Vandecasteele, C., Van Gestel, T., Doyenb, W., Leysenb, R., *A Review of Pressure-Driven Membrane Processes in Wastewater Treatment and Drinking Water Production*. Environmental Progress 2003. **22**(1).
7. Baker, R.W., *Membrane Technology and Applications*. Second ed. 2004, Membrane Technology and Research, Inc., Menlo Park, California: John Wiley & Sons Ltd.
8. Cheng, S., et al., *Characterisation and application of a novel positively charged nanofiltration membrane for the treatment of textile industry wastewaters*. Water Res, 2012. **46**(1): p. 33-42.
9. Rahimpour, A., Rajaeian, B., Hosienzadeh, A. Madaeni, S. S. and F. Ghoreishi, *Treatment of oily wastewater produced by washing of gasoline reserving tanks using self-made and commercial nanofiltration membranes*. Desalination, 2011. **265**(1-3): p. 190-198.
10. Hołda, A.K., Vankelecom, I F. J., *Understanding and guiding the phase inversion process for synthesis of solvent resistant nanofiltration membranes*. Journal of Applied Polymer Science, 2015. **132**(27).
11. Loeb, S., Sourirajan, S., , *Sea Water Demineralization by Means of an Osmotic Membrane*. 1963. **38**: p. 117-132.
12. Guillen, G.R., Pan, Y., Li, M., Hoek, E. M. V., *Preparation and Characterization of Membranes Formed by Nonsolvent Induced Phase Separation: A Review*. Industrial & Engineering Chemistry Research, 2011. **50**(7): p. 3798-3817.
13. Werber, J.R., C.O. Osuji, and M. Elimelech, *Materials for next-generation desalination and water purification membranes*. Nature Reviews Materials, 2016. **1**(5): p. 16018.
14. Farah Ejaz, A., Boor Singh, L. and H. Raed, *A review on electrospinning for membrane fabrication: Challenges and applications*. Desalination, 2015. **356**: p. 15-30.
15. Li, Z., Xu, Y., Fan, L., Kang, W. and B. Cheng, *Fabrication of polyvinylidene fluoride tree-like nanofiber via one-step electrospinning*. Materials & Design, 2016. **92**: p. 95-101.

16. Hořda, A.K., et al., *The influence of polymer purity and molecular weight on the synthesis of integrally skinned polysulfone membranes*. Journal of Membrane Science, 2013. **446**: p. 113-120.
17. Chen, Z., et al., *Effect of Polyethersulfone Molecular Weight on Structure and Performance of Ultrafiltration Membranes*. Ind. Eng. Chem. Res., 2010. **49**: p. 9988-9997.
18. Johnson, R.N., et al., *Poly(ary1 Ethers) by Nucleophilic Aromatic Substitution. I. Synthesis and Properties*. Journal of Polymer Science: Part A-1, 1967. **5**: p. 2375-2398.
19. Jamshidi Gohari, R., Halakoo, E., Nazri, N. A. M., Lau, W. J., Matsuura, T. and A.F. Ismail, *Improving performance and antifouling capability of PES UF membranes via blending with highly hydrophilic hydrous manganese dioxide nanoparticles*. Desalination, 2014. **335**(1): p. 87-95.
20. Rabiee, H., Farahani, M. H. D. A. and V. Vatanpour, *Preparation and characterization of emulsion poly(vinyl chloride) (EPVC)/TiO<sub>2</sub> nanocomposite ultrafiltration membrane*. Journal of Membrane Science, 2014. **472**: p. 185-193.
21. Zhao, S., Yan, W., Shi, M., Wang, Z., Wang, J. and S. Wang, *Improving permeability and antifouling performance of polyethersulfone ultrafiltration membrane by incorporation of ZnO-DMF dispersion containing nano-ZnO and polyvinylpyrrolidone*. Journal of Membrane Science, 2015. **478**: p. 105-116.
22. Shahidul, I.M. and K.M. Rezaul, *Fabrication and characterization of poly(vinyl alcohol)/alginate blend nanofibers by electrospinning method*. Colloid Surface A, 2010. **366**(1-3): p. 135-140.
23. Park, S.A., K.E. Park, and W.D. Kim, *Preparation of sodium alginate/poly(ethylene oxide) blend nanofibers with lecithin*. Macromolecular Research, 2010. **18** (9): p. 891-896.
24. Jeong, S.I., et al., *Electrospun chitosan-alginate nanofibers with in situ polyelectrolyte complexation for use as tissue engineering scaffolds*. Tissue Engineering Part A, 2011. **17**(1-2): p. 59-70.
25. Van G., T., Kruidhof, H., Blank, D. H. A., Bouwmeester, H. J. M., *ZrO<sub>2</sub> and TiO<sub>2</sub> membranes for nanofiltration and pervaporationPart 1. Preparation and characterization of a corrosion-resistant ZrO<sub>2</sub> nanofiltration membrane with a MWCO<300*. Journal of Membrane Science, 2006. **284**(1-2): p. 128-136.
26. Van G, T., Vandecasteele C., Buekenhoudt A., Dotremont C., Luyten J., Leysen R., Van der, B. B. and G. Maes, *Alumina and titania multilayer membranes for nanofiltration: preparation, characterization and chemical stability*. Journal of Membrane Science 2002. **207**: p. 73-89.
27. Jin, L.M., Yu, S. L., Shi, W. X., Yi, X. S., Sun, N., Ge, Y. L., Ma, C., *Synthesis of a novel composite nanofiltration membrane incorporated SiO<sub>2</sub> nanoparticles for oily wastewater desalination*. Polymer, 2012. **53**(23): p. 5295-5303.

28. Jin, L., Shi, W., Yu, S., Yi, X., Sun, N., Ma, C. and Y. Liu, *Preparation and characterization of a novel PA-SiO<sub>2</sub> nanofiltration membrane for raw water treatment*. Desalination, 2012. **298**: p. 34-41.
29. Chen, X., J.F. Dobson, and C.L. Raston, *Vortex fluidic exfoliation of graphite and boron nitride*. Chemical Communications, 2012. **48**: p. 3703-3705.
30. Al-Antaki, A.H.M., et al., *Inverted vortex fluidic exfoliation and scrolling of hexagonal-boron nitride*. RSC Adv., 2019. **9**(38): p. 22074-22079.
31. Yasmin, L., et al., *Optimising a vortex fluidic device for controlling chemical reactivity and selectivity*. Sci Rep, 2013. **3**: p. 2282.
32. Britton, J., J.M. Chalker, and C.L. Raston, *Rapid Vortex Fluidics: Continuous Flow Synthesis of Amides and Local Anesthetic Lidocaine*. Chemistry, 2015. **21**(30): p. 10660-5.
33. Gandy, M.N., C.L. Raston, and K.A. Stubbs, *Towards aryl C-N bond formation in dynamic thin films*. Org Biomol Chem, 2014. **12**(26): p. 4594-7.
34. Tong, C.L., Stroehler, U. H., Brown, M. H., and C.L. Raston, *Continuous flow vortex fluidic synthesis of silica xerogel as a delivery vehicle for curcumin*. Rsc Advances, 2015. **5**(11): p. 7953-7958.
35. Yasin, F.M., et al., *Microfluidic size selective growth of palladium nano-particles on carbon nano-onions*. Chem Commun (Camb), 2012. **48**(81): p. 10102-4.
36. Al-antaki, A.H.M., et al., *Vortex Fluidic Mediated Synthesis of TiO<sub>2</sub> Nanoparticle/MXene Composites*. ChemNanoMat, 2020. **6**(4): p. 657-662.
37. Yasmin, L., K.A. Stubbs, and C.L. Raston, *Vortex fluidic promoted Diels–Alder reactions in an aqueous medium*. Tetrahedron Letters, 2014. **55**(14): p. 2246-2248.
38. Luo, X., et al., *High-Shear-Imparted Tunable Fluorescence in Polyethylenimines*. ChemPhotoChem, 2018. **2**(4): p. 343-348.
39. Tong, C.L., et al., *Continuous flow tuning of ordered mesoporous silica under ambient conditions*. RSC Advances, 2013. **3**(41): p. 18767.
40. Alharbi, T.M.D., et al., *Sub-micron moulding angled vortex fluid flow*. Chem.Rxiv, 2020: p. <https://doi.org/10.26434/chemrxiv.13141352.v1>.
41. Yasmin, L., Coyle, T., Stubbs, K. A., Raston, C. L., *Stereospecific synthesis of resorcin[4]arenes and pyrogallol[4]arenes in dynamic thin films*. Chem Commun (Camb), 2013. **49**(93): p. 10932-4.
42. Luo, X., et al., *Vortex Fluidic-Mediated Fabrication of Fast Gelated Silica Hydrogels with Embedded Laccase Nanoflowers for Real-Time Biosensing under Flow*. ACS Appl Mater Interfaces, 2020. **12**(46): p. 51999-52007.
43. Saldivar G, E. and E. Vivaldo L, *Handbook of polymer Synthesis, characterization, and processing*. 2013, Hoboken, New Jersey: John Wiley & Sons, Inc. 653.
44. Guiver M. D., S.C., Hazlett. J. D., O. Kutow, *Synthesis and Characterization of Carboxylated Polysulfones*. British Polymer Journal, 1990. **23**: p. 29-39.

45. Agboola, O., J. Maree, and R. Mbaya, *Characterization and performance of nanofiltration membranes*. Environmental Chemistry Letters, 2014. **12**(2): p. 241-255.
46. Ionita, M., et al., *Improving the thermal and mechanical properties of polysulfone by incorporation of graphene oxide*. Composites, Part B,, 2014. **59**: p. 133-139.
47. Meihong, L., Sanchuan, Y., Yong, Z., Congjie, Gao, *Study on the thin-film composite nanofiltration membrane for the removal of sulfate from concentrated salt aqueous: Preparation and performance*. Journal of Membrane Science, 2008. **310**(1-2): p. 289-295.
48. Vorosmarty, C.J., McIntyre, P. B., Gessner, M. O., Dudgeon, D., Prusevich, A., Green, P., Glidden, S., Bunn, S. E., Sullivan, C. A., Liermann, C. R. and P.M. Davies, *Global threats to human water security and river biodiversity*. Nature, 2010. **467**(7315).
49. Zhu, W.-P., et al., *Dual-layer polybenzimidazole/polyethersulfone (PBI/PES) nanofiltration (NF) hollow fiber membranes for heavy metals removal from wastewater*. Journal of Membrane Science, 2014. **456**: p. 117-127.
50. A. Igder, A.A.R., A. Fazlavi, M. H. Ahmadi Azghandi, M. H. Omid, *Box-Behnken Design of Experiments Investigation for Adsorption of Cd<sup>2+</sup> onto carboxymethyl Chitosan Magnetic Nanoparticles*. Journal of Mining & Environment, 2012. **3**: p. 51-59.
51. Lakshmanan, R., *Application of magnetic nanoparticles and reactive filter materials for wastewater treatment*. 2013, Royal Institute of Technology, Stockholm.
52. Ong, Y.K., et al., *Nanofiltration hollow fiber membranes for textile wastewater treatment: Lab-scale and pilot-scale studies*. Chemical Engineering Science, 2014. **114**: p. 51-57.
53. Zulaikha, S., Lau, W. J., A.F. Ismail, and J. Jaafar, *Treatment of restaurant wastewater using ultrafiltration and nanofiltration membranes*. Journal of Water Process Engineering, 2014. **2**: p. 58-62.
54. Pye, S.J., et al., *Organic oxidations promoted in vortex driven thin films under continuous flow*. Green Chem, 2018. **20**(1): p. 118-124.
55. Spellman, F.R., *Handbook of Water and Wastewater Treatment Plant Operations*. 2003, LEWIS PUBLISHERS: A CRC Press Company, Boca Raton London New York Washington, D.C. p. 669.
56. Cheremisinoff, N.P., *Handbook of Water and Wastewater Treatment Technologies*. 2002: Butterworth-Heinemann.
57. Sperling, M.v., *Basic Principles of Wastewater Treatment*. Vol. 2. 2007: IWA Publishing.
58. Woodard & Curran, I., *Industrial Waste Treatment Handbook*. Second Edition ed. 2006: Butterworth-Heinemann. 533.
59. Park, H.-D., I.-S. Chang, and K.-J. Lee, *Principles of Membrane Bioreactors for Wastewater Treatment*. 2015: Taylor & Francis Group. 436.
60. D. Mallon, F.S.a.K.B. *Performance on a Real Industrial Effluent using a ZenoGem® MBR*. 2000. University of Lanchaster, UK: Royal Society of Chemistry.



61. Thomas, H., S. Judd, and J. Murrer, *Fouling characteristics of membrane filtration in membrane bioreactors*. Membrane Technology, 2000. **2000**(122): p. 10-13.
62. Salbarde, G.R. and K.D. Bhuyar, *Design, Fabrication Application and Advantages of Nanofiltration Unit*. International Journal of Innovations in Engineering and Technology (IJET), 2015. **5**(1).
63. Aslan, T., et al., *A novel nanofiber microfiltration membrane: Fabrication and characterization of tubular electrospun nanofiber (TuEN) membrane*. Journal of Membrane Science, 2016. **520**: p. 616-629.
64. Nico, S., Heinz B., *Polyacrylonitrile (PAN) membranes for ultra- and microfiltration*. Desalination, 2001. **139**: p. 191-198.
65. Zhang, B., et al., *Optimization of cleaning conditions on a polytetrafluoroethylene (PTFE) microfiltration membrane used in treatment of oil-field wastewater*. RSC Adv., 2015. **5**(127): p. 104960-104971.
66. He, Z., et al., *Fouling propensity of a poly(vinylidene fluoride) microfiltration membrane to several model oil/water emulsions*. Journal of Membrane Science, 2016. **514**: p. 659-670.
67. Ji, J., Liu, Fu., Hashim, N. A., Abed, M. R. M., Li, Kang,, *Poly(vinylidene fluoride) (PVDF) membranes for fluid separation*. Reactive and Functional Polymers, 2015. **86**: p. 134-153.
68. Kang, G.-d. and Y.-m. Cao, *Application and modification of poly(vinylidene fluoride) (PVDF) membranes – A review*. Journal of Membrane Science, 2014. **463**: p. 145-165.
69. Farjadian, F., S. Schwark, and M. Ulbricht, *Novel functionalization of porous polypropylene microfiltration membranes: via grafted poly(aminoethyl methacrylate) anchored Schiff bases toward membrane adsorbers for metal ions*. Polym. Chem., 2015. **6**(9): p. 1584-1593.
70. Ren, P., Fang. Y., Wan, L. S., Ye. X. Y., Xu, Z. g., *Surface modification of polypropylene microfiltration membrane by grafting poly(sulfobetaine methacrylate) and poly(ethylene glycol): Oxidative stability and antifouling capability*. Journal of Membrane Science, 2015. **492**: p. 249-256.
71. Yamagishi, H., J.V. Crivello, and G. Belfort, *Development of a novel photochemical technique for modifying poly(arylsulfone) ultrafiltration membranes*. Journal of Membrane Science 105, 1995. **105**: p. 237-247.
72. Wang, D.X., Su, M., Yu, Z. Y, Wang, X. L., Ando, M., Shintani, T., , *Separation performance of a nanofiltration membrane influenced by species and concentration of ions*. Desalination, 2005. **175**(2): p. 219-225.
73. Akbari, A., et al., *New UV-photografted nanofiltration membranes for the treatment of colored textile dye effluents*. Journal of Membrane Science, 2006. **286**(1-2): p. 342-350.

74. Jeong, S.I., Krebs, M. D., Bonino, C. A., Samorezov, J. E., Khan, S. A., and E. Alsberg, *Electrospun Chitosan-Alginate Nanofibers with In Situ Polyelectrolyte Complexation for Use as Tissue Engineering Scaffolds*. Tissue Engineering Part A, 2011. **17**(1-2): p. 59-70.
75. Safarpour, M., Vatanpour, V. and A. Khataee, *Preparation and characterization of graphene oxide/TiO<sub>2</sub> blended PES nanofiltration membrane with improved antifouling and separation performance*. Desalination, 2016. **393**: p. 65-78.
76. Manish Kumar, T.C., and Yuexiao Shen, *Water Desalination: History, Advances, and Challenges*. 2016, National Academy of Engineering. 2017. Frontiers of Engineering: Reports on Leading-Edge Engineering from the 2016 Symposium.: Washington, DC, The National Academies Press.
77. Jung, J.T., Kim, J. F., Wang, H. H., Di Nicolo, E., Drioli, E. and Y.m. Lee, *Understanding the non-solvent induced phase separation (NIPS) effect during the fabrication of microporous PVDF membranes via thermally induced phase separation (TIPS)*. Journal of Membrane Science, 2016. **514**: p. 250-263.
78. Marcel, M., *Basic Principles of Membrane Technology*. 1991, Springer-Science+Business Media, B.v.
79. Wang, X. and B.S. Hsiao, *Electrospun nanofiber membranes*. Current Opinion in Chemical Engineering, 2016. **12**: p. 62-81.
80. McCune, M., W. Zhang, and Y. Deng, *High efficiency dye-sensitized solar cells based on three-dimensional multilayered ZnO nanowire arrays with "caterpillar-like" structure*. Nano Lett, 2012. **12**(7): p. 3656-62.
81. Bai, H., Z. Liu, and D.D. Sun, *Hierarchical ZnO/Cu "corn-like" materials with high photodegradation and antibacterial capability under visible light*. Phys Chem Chem Phys, 2011. **13**(13): p. 6205-10.
82. Guo, J., Zhang, Q., Cai, Z., Zhao, K., *Preparation and dye filtration property of electrospun polyhydroxybutyrate–calcium alginate/carbon nanotubes composite nanofibrous filtration membrane*. Separation and Purification Technology, 2016. **161**: p. 69-79.
83. Bil'dyukevich, A.V., N.G. Semenkevich, and S.A. Pratsenko, *Effect of polyethersulfone molecular weight up on membrane transport characteristics*. Ser.Chem. Sci. , 2007. **2**: p. 74.
84. Wang, X., et al., *Development of hydrophilic barrier layer on nanofibrous substrate as composite membrane via a facile route*. Journal of Membrane Science, 2010. **356**(1-2): p. 110-116.
85. Fang, D., et al., *Effect of intermolecular interaction on electrospinning of sodium alginate*. Carbohydrate Polymers, 2011. **85**(1): p. 276-279.
86. Zhu, J., Tian, M., Hou, Jingwei., Wang, J, Lin, J., Zhang, Y., Liu, J., Van der B, B., *Surface zwitterionic functionalized graphene oxide for a novel loose nanofiltration membrane*. J. Mater. Chem. A, 2016. **4**(5): p. 1980-1990.

87. Lee, J., Boo, C., Ryu, W. H., Taylor, A. D. and M. Elimelech, *Development of Omniphobic Desalination Membranes Using a Charged Electrospun Nanofiber Scaffold*. ACS Appl Mater Interfaces, 2016. **8**(17): p. 11154-61.
88. Ma, R., et al., *High-flux and fouling-resistant reverse osmosis membrane prepared with incorporating zwitterionic amine monomers via interfacial polymerization*. Desalination, 2016. **381**: p. 100-110.
89. Hu, J., et al., *Fabrication of a high-flux sulfonated polyamide nanofiltration membrane: Experimental and dissipative particle dynamics studies*. Journal of Membrane Science, 2016. **505**: p. 119-129.
90. Tang, C.Y., Y.N. Kwon, and J.O. Leckie, *Effect of membrane chemistry and coating layer on physiochemical properties of thin film composite polyamide RO and NF membranes*. Desalination, 2009. **242**: p. 168–182.
91. Yin, J., Zhu, G. and B. Deng, *Graphene oxide (GO) enhanced polyamide (PA) thin-film nanocomposite (TFN) membrane for water purification*. Desalination, 2016. **379**: p. 93-101.
92. A. Dieter S., C.J.H. and J. S., *Synthesis of polymers, new structures and methods*. Vol. 1. 2011, Wiley-VCH Verlag GmbH & Co. KGaA. 1203.
93. Van der Bruggen, B., *Chemical modification of polyethersulfone nanofiltration membranes: A review*. J. Appl. Polym. Sci., 2009. **114**(1): p. 630-642.
94. Agenson, K.O. and T. Urase, *Change in membrane performance due to organic fouling in nanofiltration (NF)/reverse osmosis (RO) applications*. Separation and Purification Technology, 2007. **55**(2): p. 147-156.
95. Billmeyer, F.W., *Textbook of Polymer Science*. Third ed. 1984: John Wiley & Sons Inc.
96. Saraf, M.K., *Polymerization of Vinylidene Fluoride in Supercritical Carbon Dioxide: Molecular Weight Distribution*, in *DEpartment of Chemical Engineering, Nort Carolina State University*. 2001, Nort Carolina State University. p. 135.
97. Othmer, K., *Encyclopedia of in Chemical Technology*. 1996, John Wiley & Sons: New York.
98. Wayne W.Y. L., M.D.G. and T. Matsuura, *Phase separation in polysulfone/solvent/water and polyethersulfone/solvent/water systems*. Journal of Membrane Science, 1991. **59**: p. 219-227.
99. Radenovic, A., *Microfluidics Lab on Chip*. Ecole Polytechnique Federal De Lausanne.
100. Slapar, V. and I. poberaaj, *Microfluidics*. 2008, University of Ljubljana. p. 20.
101. Loh, J.W., M. Saunders, and L.Y. Lim, *Potential for Scaled-up Manufacture of Chitosan Nanoparticles Using the Spinning Disc Processor*, 2008, NSTI-Nanotech.
102. Loh, J.W., Schneider, J., Carter, M., Saunders, M., and L.Y. Lim, *Spinning disc processing technology: potential for large-scale manufacture of chitosan nanoparticles*. J Pharm Sci, 2010. **99**(10): p. 4326-36.

103. Vigderman, L., B.P. Khanal, and E.R. Zubarev, *Functional gold nanorods: synthesis, self-assembly, and sensing applications*. Adv Mater, 2012. **24**(36): p. 4811-41, 5014.
104. G Cowen, P Norton-Berry, ML Steel, "Chemical Process on the Surface of a Rotating Body", US 4,311,570, 19th January 1982. Filed 21<sup>st</sup> February 1979.
105. Britton, J., Dalziel, Stuart B. and C.L. Raston, *The synthesis of di-carboxylate esters using continuous flow vortex fluidics*. Green Chem., 2016. **18**(7): p. 2193-2200.

## Chapter 2

### Vortex fluidic mediated synthesis of polysulfone†

Published in Royal Society of Chemistry Advances, 2020, 10, 14761-14767

<https://doi.org/10.1039/D0RA00602E>

#### Abstract

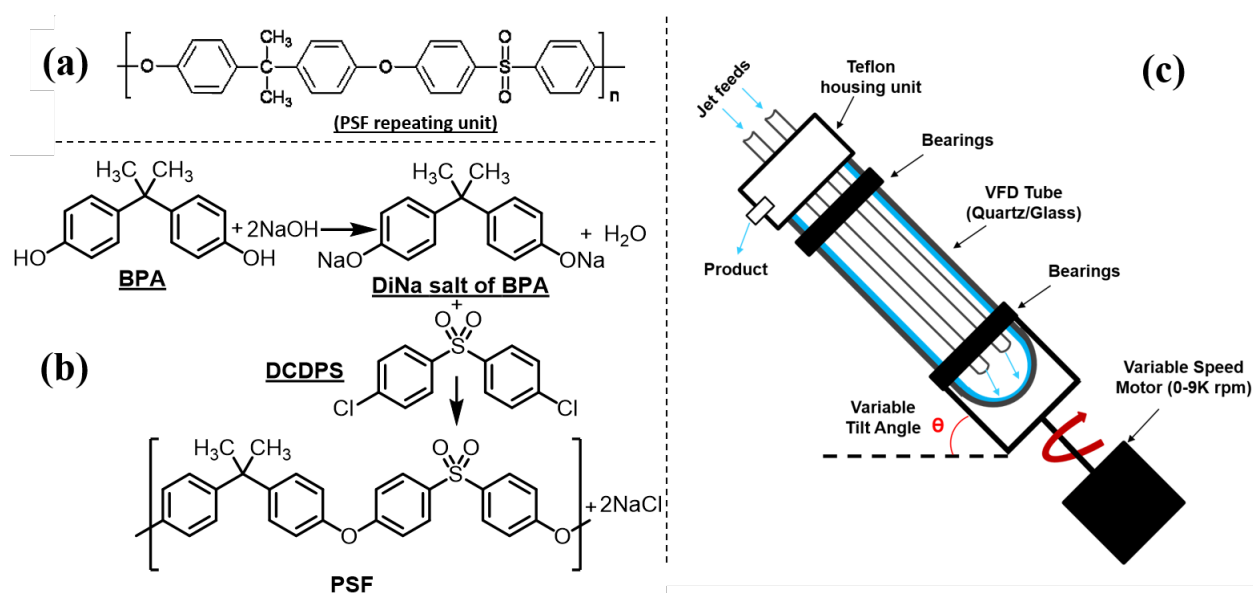
Polysulfone (PSF) was prepared under high shear in the vortex fluidic device (VFD) operating in confined mode, and its properties compared with that prepared using batch processing. This involved reacting the pre-prepared disodium salt of bisphenol A (BPA) with a 4, 4'-dihalodiphenylsulfone under anhydrous condition. Scanning electron microscopy (SEM) established that in the thin film microfluidic platform, the PSF particles are sheet-like, for short reaction times, and fibrous for long reaction times, in contrast to spherical like particles for the polymer prepared using the conventional batch synthesis. The operating parameters of the VFD (rotational speed of the glass tube, its tilt angle and temperature) were systematically varied for establishing their effect on the molecular weight (MW), glass transition temperature (T<sub>g</sub>) and decomposition temperature, featuring gel permeation chromatography (GPC), differential scanning calorimetry (DSC) and thermal gravimetric analysis (TGA) respectively. The optimal VFD prepared PSF was obtained at 6000 rpm rotational speed, 45° tilt angle and 160°C, for 1 h of processing with MW ~ 10000 g/mol, T<sub>g</sub> ~ 158°C and decomposition temperature ~ 530 °C, which is comparable to the conventionally prepared PSF.

#### 2.1. Introduction

Polymerisation reactions can be classified as arising from step-growth and chain-growth mechanisms, corresponding to condensation and addition reactions respectively [1, 2]. Condensation polymers involve the reaction between two monomers in building the macromolecule, with or without the elimination of a small molecule such as water [3, 4]. Among different types of condensation reactions, nucleophilic substitution feature the most

for preparing commercial organic polymers, such as in epoxide polymerisation [3], or in the production of polysulfide rubbers from aliphatic dichlorides and sodium sulphide [3, 5].

Polysulfone (PSF) is a common thermoplastic polymer and a popular polymer incorporated in nano-filtration (NF) membranes. Aliphatic PSFs have unattractive physical properties including melting point and glass transition temperature, in contrast to PSFs incorporating aromatic moieties, which are prepared commercially via nucleophilic substitution reactions, Scheme 2. 1-a [1, 5]. with the structure of a PSF repeating unit shown in the Electronic Supplementary Information file (Appendix A)<sup>†</sup>. Aromatic based PSFs feature in different applications, having desirable thermal [6], chemical and mechanical stabilities [7, 8]. These polymers are also known as polyethersulfone (PESs) or polyphenylsulfone (PPSFs), depending on the nature of the backbone, Table 2. 1 [1, 9]. The main difference between different types of PSF comes from the bisphenol (BP) repeating unit which controls certain properties, including glass transition temperature (T<sub>g</sub>), Table 2. 2 [1]. Aromatic PSF is commercially obtained by condensation of equimolar quantities of 4,4-dihalodiphenylsulfone (DHDPS) and a BP in the presence of a base [1, 5]. This involves two separate steps, Scheme 2. 1-b; firstly, BPA is converted to the disodium salt (DiNa salt) by the addition of base, followed by a substitution reaction with dichlorodiphenyl-sulfone (DCDPS).



Scheme 2. 1. (a) Aromatic PSF repeating unit in PSF, (b) schematic of PSF synthesis involving nucleophilic substitution, and (c) diagram of the vortex fluidic device (VFD).<sup>[10]</sup>

Removal of water by-product generated in the first step is required to prevent hydrolysis of the DCDPS and facilitates the formation of higher molecular weight polymer [1, 5]. Dimethyl sulfoxide (DMSO) and sulfolane have been used to overcome the otherwise limited solubility of the DiNa salt of BPA under anhydrous conditions. Co-solvents such as chlorobenzene or toluene have also been used to increase the solubility of the salt [1, 5]. Reaction temperatures  $>120^{\circ}\text{C}$  are effective in removing water from the reaction with  $>150^{\circ}\text{C}$  effective in driving the polymerisation to completion, and below this, low molecular weight sodium-capped oligomers precipitate on the internal surface of the reaction vessels.<sup>5</sup> Preparing PSF using conventional batch processing [1, 5], has some limitations, including that the processing is time consuming and energy intensive, and downstream processing is required to remove by-products.

We hypothesised that the high shear stress and intense micro-mixing in thin film microfluidics has potential to overcome these issues, imparting fast kinetics and with simplicity of the processing [11, 12].

Table 2. 1. Chemical structure and glass-transition temperature,  $T_g$ , of PSF, PES, PPSF [1].

Polymer	Repeat Unit Structure	$T_g$ , $^{\circ}\text{C}$
Polysulfone (PSF)		185
Polyethersulfone (PES)		220
Polyphenylsulfone (PPSF)		220

Table 2. 2.  $T_g$  of PSFs formed from poly-condensation of DCDPS with various BP types [1].

Bisphenol Type	Structure	X	$T_g$ , $^{\circ}\text{C}$
4,4'-dihydroxydiphenyl oxide		O	170
4,4'-dihydroxydiphenyl sulfide		S	175
4,4'-dihydroxydiphenyl methane		$\text{CH}_2$	180
2,2'-bis(hydroxyphenyl)-propane		$\text{C}(\text{CH}_3)_2$	185

The VFD, is a relatively new thin film microfluidic platform with a diverse range of applications, including graphene exfoliating, enhancing chemical reactivity and selectivity

[13, 14], as in the synthesis of small molecule pharmaceuticals [15, 16], fabricating composite nanomaterials [17], and controlling the pore size of mesoporous silica [18], to mention a few. The rate of water evaporation in the VFD is dramatically increased, due to the large surface area of the thin film created inside the rapidly rotating VFD tube, and there is high heat and mass transfer, with improved reaction homogeneity, and when operating under continuous flow conditions, clogging is not an issue, unlike conventional channel based microfluidics [19]. It has also been used in synthesising polymeric nanoparticles such as polyethylenimine (PEI) nanoparticles [20] and polymer coated superparamagnetic magnetite nanoparticles [21] as well as manipulating the florescent properties of hyper-branched polymers [22]. However, to the best of our knowledge nobody has used the shear stress in dynamic thin film in the VFD for PSF synthesis. We have explored the utility of preparing PSF in the VFD, in taking advantage of such benefits, as well avoiding the use of potentially toxic reagents such as chlorinated co-solvents. This led to a new synthesis of the PSF, which is reported herein, with the optimal conditions established by systematically exploring the operating parameter space of the VFD, including rotational speed, processing time, tilt angle of the tube, and temperature. The processing outcomes were also assessed relative to the glass transition temperature ( $T_g$ ), molecular weight ( $M_w$ ), particle size and shape, production yield and thermal stability of the PSF, in comparison with the polymer prepared using conventional batch processing.

## **2.2. Experimental**

### **2.2.1. Materials**

All chemicals were used as received unless otherwise stated. High purity bisphenol A, [2,2-bis(4-hydroxyphenyl) propane], (BPA) (99%) and 4,4'-dichlorodiphenyl sulfone (DCDPS) (98%) and sodium hydroxide pellets (> 97%) were purchased from Sigma Aldrich. Dimethyl sulfoxide (DMSO) (99.9%) and chlorobenzene (99.9%) were purchased from RCI Labscan Limited, with tetrahydrofuran (THF) (99.95%) purchased from Chem-Supply. Ultrapure Milli-Q water was used for preparing aqueous solutions. DMSO was triple distilled before use and kept under nitrogen to limit adsorption of water. The vortex fluidic device (VFD) had a mounted heating block, effective in heating liquids in the tube, up to 175°C.



### 2.2.2. PSF polymerisation

PSF was initially prepared according to the batch procedure [5] detailed in the SI<sup>†</sup> (Appendix A)<sup>†</sup>. For VFD processing, BPA (228 mg, 1.0 mmol) and DMSO (1.0 ml) were placed in the VFD tube (20 mm O.D., 17.5 I.D., 18.5 cm long) and rotated at 4000 rpm at 60°C for 5 min, affording a clear colourless solution.

This reaction was also effective at room temperature, but the processing took 20 minutes. In contrast to the conventional method, no co-solvent was required. An aqueous solution of NaOH (103  $\mu$ L, 50.2 % w/w, 2 mmol) was then added to the tube, which was rotated at 4000 rpm, 45° tilt angle and 60°C for 15 min. A solution of DCDPS (287 mg, 1 mmol) in DMSO (1.0 mL) was then added to the tube rotating at specific speeds (rpm), tilt angle (°), temperatures (°C), for specified times (min), for every designated experiment in Table A. 1<sup>†</sup> & Figure A. 1<sup>†</sup>. At the end of each reaction, the sample was purified by filtration and any solid (NaCl by-product) discarded, whereupon, ethanol (10 mL) was added. The resulting coagulated white solid was washed twice and centrifuged (4 min, 805 RFC).

The product was then filtered and dried for 2h at 70°C, affording PSF as a white solid, with the yield of product determined. In addition, for specific operational conditions,  $M_w$ ,  $T_g$  and temperature variation profiles were determined at the optimal conditions, using gel permeation chromatography (GPC), differential scanning calorimetry (DSC) and thermal gravimetric analysis (TGA) respectively.

### 2.2.3. Characterization

The intermediate DiNa salt of BPA and the final VFD mediated PSF were characterised using NMR spectroscopy, recorded in DMSO- $d_6$  and  $CDCl_3$  respectively (600 MHz Bruker instrument), and FT-IR spectroscopy (PerkinElmer ATR Fourier Transform spectrometer).  $^1H$ -NMR spectra were acquired using a relaxation delay-time of 4 seconds. All chemical shifts are presented in ppm, using residual solvent as the internal standard. Scanning electron microscope (SEM) images were recorded on an Inspect FEI F50 SEM. Average molecular weights ( $M_w$ ) and molecular weight distributions [23] were determined using a double detection Shimadzu GPC instrument equipped with an Ultraviolet (UV) and Refractive Index (RI) detectors.  $T_g$  and thermal stability measurements used a Perkin Elmer DSC 8000 and TGA

8000 instrument, respectively, with instrument settings included in the SI (Appendix A)<sup>†</sup>. These properties were established for all polymers prepared in this study, in establishing the optimal operating parameters of the VFD, namely rotational speed ( $\omega$ ), tilt angle ( $\theta$ ), reaction time ( $t$ ) and temperature ( $T$ ). The optimal operational conditions are defined as those for forming the polymer with the highest  $T_g$ ,  $M_w$ , thermal stability, and formed in the highest yield.

## 2.3. Results and discussion

The synthesis of PSF was conducted in the VFD and using batch processing for direct comparison on the effect of the unique fluid flow in the microfluidic platform. The production of the intermediate and final products was firstly confirmed using NMR and FTIR spectroscopy. Then the operating parameters of the VFD were systematically explored in mapping out how these affect the nature of the PSF with respect to  $T_g$ ,  $M_w$  and thermal stability (DSC, GPC and TGA). Products were also studied for their morphological properties using SEM images.

### 2.3.1. Synthesis of DiNa salt of BPA

FT-IR and NMR spectroscopy [24] confirmed the formation of the DiNa salt of BPA and PSF, for both VFD and batch processing. The choice of solvent is critical for any process [25]. The DiNa salt of BPA, as the product of first step, is highly soluble in high boiling point DMSO (189°C) [25] but this is difficult to remove for the isolation of the polymer and isolating the product to be characterized. In contrast, the DiNa salt is only sparingly soluble in THF, and to be able to isolate it for characterisation purposes, this was the solvent of choice, with the precipitated salt washed with EtOAc. FTIR spectra of DiNa salt of BPA (Figure A. 2-a<sup>†</sup>) obtained in the first step in the VFD, at  $\omega$  4000 rpm,  $\theta$  45° and  $T$  60°C for 5 min, clearly showed the removal of –OH stretching in forming the corresponding conjugate base, with peaks assignable to aromatic C=C (1508 - 1611 cm<sup>-1</sup>), C-O (1050 – 1300 cm<sup>-1</sup>) and C-H (1365 - 1465 cm<sup>-1</sup>) [26, 27]. Peaks at 3000 cm<sup>-1</sup> and above 3500 cm<sup>-1</sup>, are attributed to THF [28, 29] which can bind to metal centres, including sodium. <sup>1</sup>H-NMR of BPA in DMSO-d<sub>6</sub> (Figure 2. 1-a) has peaks at ~ 1.53 and 9.13 ppm, assigned to the aliphatic protons and hydroxyl groups,

respectively, with the later removed on reacting with base in forming DiNa. There are also peaks at 6.97 and 6.64 ppm corresponding to the aromatic protons of BPA (Figure 2. 1-b) [30]. Overall, changes in the  $^1\text{H}$ -NMR spectra [29] are consistent with the formation of the DiNa salt (Figure 2. 1-a) and the removal of water from the reaction mixture in the VFD. Such removal of water has been reported for the continuous flow synthesis of di-carboxylate esters synthesis [19]. For batch synthesis of DiNa, FTIR established that the longer the reaction time, the broader the  $-\text{OH}$  stretching peak, whereas for VFD processing the  $-\text{OH}$  stretching is smaller [26, 27], which is attributed to water dissipation in the VFD (Figure A. 2-b $^+$ ).

### 2.3.2. Synthesis of PSF

Figure A. 3 $^+$  and Figure A. 4 - 11 $^+$  show the FTIR and NMR spectra for PSF prepared using both conventional [31] and VFD processing, as well as starting material for comparison. Figure A. 10 & 11 $^+$  show the  $^1\text{H}$  and  $^{13}\text{C}$  NMR of VFD synthesized PSF at the optimised VFD condition, respectively, matching the corresponding spectra for highly porous PSF membranes [32]. The smaller peaks for the aromatic region in Figure A. 10 $^+$ , can be assigned to terminal groups of the polymer. In targeting the formation of high molecular weight polymer in the VFD, this region should be minimal [32].

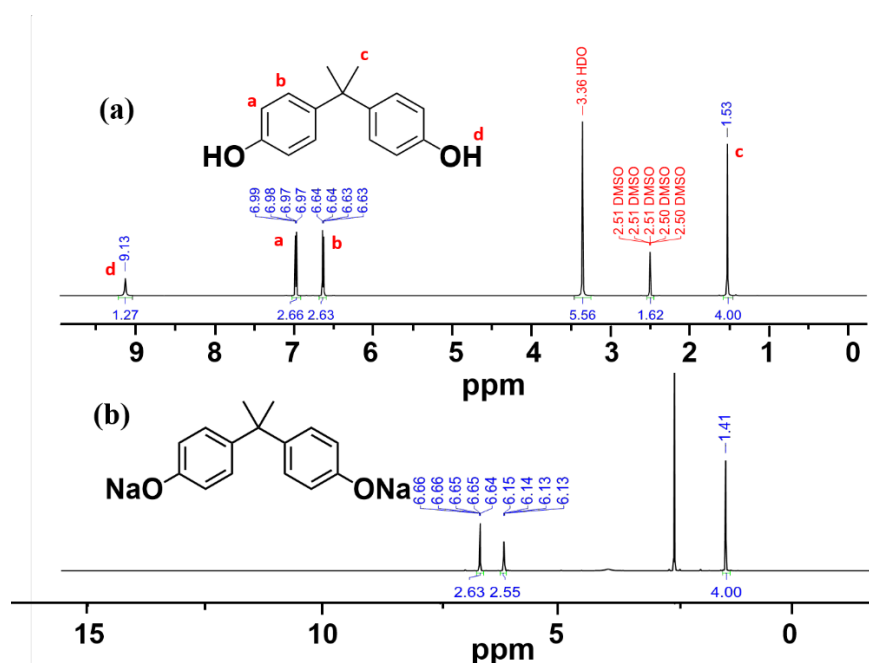


Figure 2. 1.  $^1\text{H}$ -NMR spectra of (a) BPA and (b) DiNa salt of BPA obtained in the VFD in THF.  $^1\text{H}$ -NMR measurements were recorded in  $\text{DMSO-d}^6$ .

### 2.3.3. Varying VFD operational parameters

Experiments T<sub>1</sub> to T<sub>6</sub> in Table A. 1<sup>†</sup> were carried out to establish the effect of varying  $\omega$ , from 3000 to 8000 rpm. Average molecular weight ( $M_w$ ),  $T_g$ , and decomposition temperature, as well as yield were determined for all experiments.  $M_w$ , measured using GPC, were in the range  $\sim 2000$  to  $\sim 11000$  g/mol, with the highest,  $\sim 4300$  g/mol, formed at  $\omega$  6000 rpm, heating at 150 °C over 30 min., and  $\theta$  45° (T<sub>4</sub>), with little change at higher speeds (Figure 2-a). DSC measurements to determine  $T_g$  were carried out under a nitrogen/air atmosphere, with the highest  $T_g$  reported thus far for PSF at  $\sim 187$  °C [32].  $T_g$  values for T<sub>1</sub>, to T<sub>6</sub> were  $\sim 126$ , 125, 135, 142, 141, and 138 °C respectively, with the highest for PSF formed at 6000 rpm. The highest yield of isolated PSF, 53%, also corresponds to experiment T<sub>4</sub>, with yields lower for increasing and reducing  $\omega$ , at 37% and 39% for 3000 and 8000 rpm, respectively.

Experiments T<sub>7</sub> to T<sub>12</sub>, Table A. 1<sup>†</sup>, were at  $\omega$  6000 rpm,  $\theta$  45°, for 30 min at different temperatures. The effect of temperature has a large variation on molecular weight. There is clearly an effect on the temperature of the processing on the  $M_w$  of the polymer, and consequently  $T_g$ . The highest  $M_w$  and  $T_g$  were for the PSF prepared at 170°C, 12000 g/mol and 168°C, respectively, Figure 2. 2-b. However, the yield of the isolated product dropped from 61% at 160°C to 19.4% at 170°C, and thus 160°C reaction temperature was regarded as optimal, which is in accordance with temperature in conventional batch polymerisation (155°C) [5]. For experiments T<sub>7</sub> and T<sub>8</sub>, at 80 and 120°C respectively, there was no evidence for the formation of PSF. The  $T_g$  of batch prepared PSF in this research with  $M_w \sim 6300$  g/mol was  $\sim 106$ °C, significantly smaller than the PSF prepared in the VFD with the same  $M_w$ , summarised for entry T<sub>11</sub>, Table A. 1<sup>†</sup>,  $M_w \sim 6300$  g/mol,  $T_g \sim 152$ °C. The relatively high  $T_g$  for such a low molecular weight PSF is noteworthy and highlights the novel process in the VFD under high shear.

The tilt angle,  $\theta$ , in the VFD was varied from 0° (horizontal position) to 90° (vertical position) at intervals of 15°, entries T<sub>13</sub>-T<sub>19</sub>, Table A. 1<sup>†</sup>. There is a significant increase in yield from 21.7% at  $\theta$  30° to 59.2% at 45°, Figure 2-c. For  $\theta$  at 30° and 90° the yields were also relatively high, at 58.3% and 58.1% respectively, but given the higher  $M_w$  ( $\sim 7100$  g/mol) and  $T_g$  ( $\sim 153$ °C) at  $\theta$  45°, this angle was regarded as optimal for the synthesis of PSF in the VFD, and

this is in agreement with the outcome of optimisation studies for a number of application of the device [10-17].

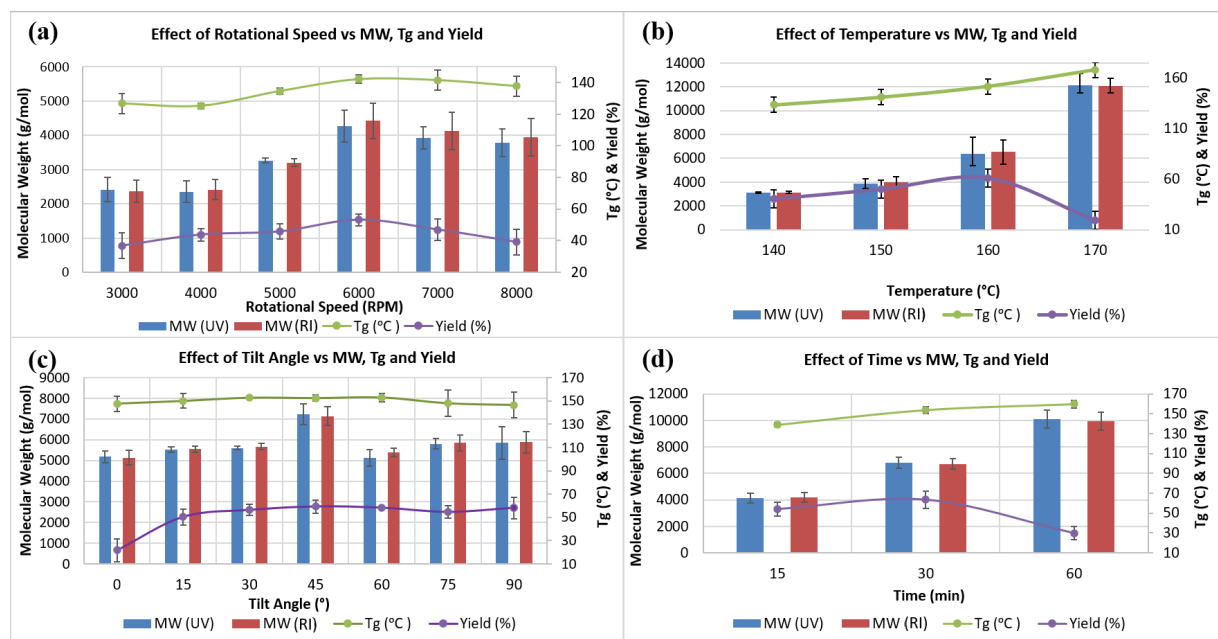


Figure 2. 2. Effect of VFD operating parameters on (a) rotational speed (rpm), (b) temperature (°C), (c) tilt angle (°), and (d) time (min) (horizontal axis) on the resulting M<sub>w</sub> obtained from UV and RI detectors (blue and red histograms, respectively, in the left vertical axis), and on T<sub>g</sub> and yield (%) (green and violet lines, respectively, in the right vertical axis).

The synthesis of PSF in the VFD was then carried out at 160°C, with  $\omega$  6000 rpm and  $\theta$  45° for different processing times, entries T<sub>20</sub>-T<sub>22</sub>, Table A. 1†. M<sub>w</sub> and T<sub>g</sub> increased to ~ 10000 g/mol and ~ 160 °C, respectively, by increasing the processing time up to 60 min. However, this resulted in a reduction in the yield, down to ~ 30% yield, in contrast to 63.7% for 30 min processing time, which has a lower M<sub>w</sub> at ~ 6700 M<sub>w</sub>, Figure 2. 2-d. GPC curves for commercial, conventional and VFD synthesized PSF at 6000 rpm, 160 °C, 45 tilt, and 60 min, now regarded as optimal conditions for processing in the VFD, are shown in Figure 2. 3-a. The shorter retention time for commercial PSF is in agreement with its much higher M<sub>w</sub>, ~ 60000 g/mol, with M<sub>w</sub> for conventional batch prepared PSF, M<sub>w</sub> ~ 6000 g/mol, and that for PSF prepared in the VFD at optimal processing parameters, T<sub>22</sub>, ~10000 g/mol. The GPC results showed the obvious decrease in the retention time of the VFD PSF, resulting a higher M<sub>w</sub> compared to the conventional batch synthesised PSF. The polydispersity index (PDI) for all these samples were 1.76, 1.78 and 1.76, respectively, and while they are similar, that

prepared in the VFD has a narrower  $M_w$  distribution, and for the optimal processing parameters in general. In addition, PDIs for specific VFD optimised processing parameters are consistently lower, for example, in the optimal rotational speed,  $\omega$  6000 rpm, the PDI is 1.52,  $T_4$ , Figure A. 12 & 13<sup>†</sup>. Lower PDIs for material generated in the VFD are associated with more uniform particle size distributions and highlight the benefit of using the VFD microfluidic platform, SI (Figure A. 14-24<sup>†</sup>). DSC thermograms in Figure 2. 3-b are for commercial and conventional PSF, and optimised VFD fabricated PSF ( $\omega$  6000 rpm, 160 °C,  $\theta$  45°, and 60 min). All  $T_g$  values were collected from the second heating scan to minimise the effect of any evaporation of low volatiles or moisture. The heating curve of the VFD synthesised PSF (black curve) has a glass transition at 157.9 °C (mid-point) with a change in the specific heat capacity,  $c_p$  0.213 J/(g\*°C). Conventional batch synthesised PSF (red curve) has a lower  $T_g$  at 105.13 °C with  $c_p$  0.159 J/(g\*°C). For all samples, the glass transition is superimposed by a small endotherm at 190.1, 108.5, and 160.4 °C, during heating scan, for commercial, conventional and VFD polymers, respectively. The DSC results (Figure 2. 3-b) presented a significantly higher  $T_g$  for the VFD PSF compared to the conventional batch synthesised PSF, although it has a lower  $T_g$  than the commercial PSF (blue curve). This could arise from the intense micro-mixing and high shear rates, and the high rate of loss of water from the reaction mixture in the VFD, as established elsewhere [19]. Comparative DSC thermograms plots were also recorded in ascertaining the effect of  $\omega$  on  $T_g$ , Figure A. 26<sup>†</sup>, showing the best  $T_g$  measured is in accordance with the highest  $M_w$  polymer obtained at  $\omega$  6000 rpm ( $\sim$  142 °C) while it is  $\sim$  125 and 137 °C at  $\omega$  4000 and 8000 rpm, respectively.

TGA measurements, carried out based on the setting suggested in Table A. 2<sup>†</sup>, and Figure A. 27<sup>†</sup>, establish a mass loss between 100 and 200 °C (DTG peak) of 7.4 and 0.5% for conventional VFD generated samples respectively, which is attributed to the loss of moisture and lower volatiles. The main decompositions of PSF for VFD processes  $T_9$  (140 °C),  $T_{10}$  (150 °C),  $T_{11}$  (160 °C) and  $T_{12}$  (170 °C), conventional processes and commercial material, are at 530.0, 531.9, 533.0, 534.4, 534.6, and 536.4 °C (DTG Peak<sub>1</sub>), with a mass loss of 68.7, 68.9, 68.9, 66.2, 65.0, and 66.2%, respectively (Figure A. 27<sup>†</sup>).

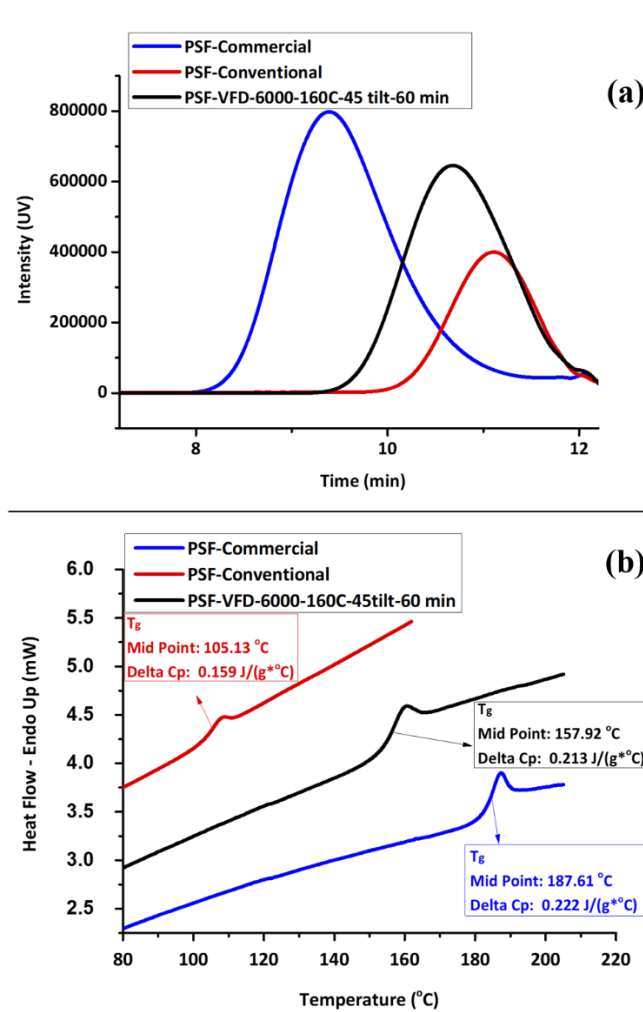


Figure 2. 3. Comparison between (a) GPC traces (UV detector) and (b) DSC thermograms of commercial, conventional and VFD synthesized PSF ( $T_{22}$  at 6000 rpm, 160 °C, 45°, and 60 min). (b) Temperature scan in  $T_g$  measurements were conducted between 30 °C and 230 °C at 10 °C min<sup>-1</sup>.

The results show that increasing the temperature up to 10 °C during the polymerization reaction has little effect on the main decomposition temperature, and accordingly  $M_w$ ,  $T_g$ , and percent yield were more informative for optimising the processing in the VFD.

The morphology of PSF is important in its applications, for example, in membranes [33, 34]. Figure 2. 4 shows SEM images for drop cast samples of commercial, conventional, and optimised VFD prepared PSF, and coated with ~ 5 nm layer of platinum. Commercial PSF has large globular shaped particles, ca 30  $\mu$ m in diameter, whereas that formed under batch processing herein are much smaller at submicron dimensions, Figure 2. 4 (a & b), respectively. Interestingly, the size of the particles formed under the optimised VFD processing conditions in the VFD, Figure 2. 4-c, are similar to those of the commercial sample, yet the  $M_w$  of the



material is significantly less, and the surface morphology is distinctly different. Also, of note is that PSF prepared away from optimised conditions in the VFD, Figure 2. 4 (d-f) have different morphology and apparent particle size. For the shortest reaction time, 15 min, the product is sheet-like, Figure 2. 4-d, changing to semi-spherical particles for 30 min, Figure 2. 4-e, and fibrous material after 90 min, Figure 2. 4-f. More images of the samples are shown in Figure A. 28<sup>†</sup> in establishing that the images in Figure 2. 4 are representative of the bulk materials. The origin of this difference possibly relates to the complex fluid dynamics in the VFD becoming increasingly important over time, in moulding the polymer particles. This morphological variation is important in any downstream applications.

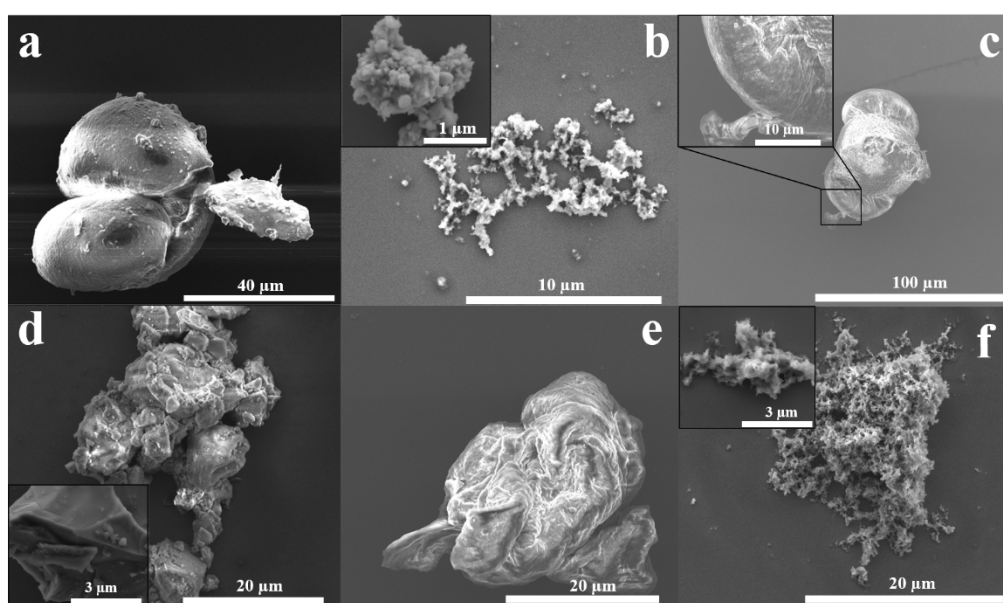


Figure 2. 4. SEM images of PSF for (a) commercial material, (b) material formed using conventional batch processing, (c) material formed in the VFD at the optimised  $s$  ( $T_{22}$  at 6000 rpm, 160°C, 45°, and 60 min). PSF synthesised in the VFD at 6000 rpm, 160°C,  $\theta$  45° for (d) 15 min, (e) 30 min, and (f) 90 min reaction time. All the sample were drop cast and coated with ca 5 nm layer of Pt.

## 2.4. Conclusions

The preparation of PSF under high shear in the VFD using the confined mode of operation of the device has been established as an optimised process relative to  $M_w$ ,  $T_g$  and percent yield, and compared with commercially available material, and that prepared using conventional batch processing. The optimised VFD processing parameters were  $T$  170°C,  $\omega$  6000 rpm,  $\theta$  45° and  $t$  30 min, which corresponds  $M_w \sim 12000$  g/mol,  $T_g$  168°C and decomposition



temperature  $\sim 530^{\circ}\text{C}$ . However, the lower yield (18%) at this temperature,  $160^{\circ}\text{C}$  was deemed more optimal, affording  $M_w \sim 7000 \text{ g/mol}$ ,  $T_g \sim 154^{\circ}\text{C}$ , and  $\sim 64\%$  yield, and for a longer reaction time, 60 min, now affording  $M_w \sim 10000 \text{ g/mol}$  and  $T_g \sim 158^{\circ}\text{C}$ . While the latter results in a lower yield ( $\sim 30\%$ ), the reaction time can be defined based on the importance of either the  $M_w$  or yield of the process.

The VFD prepared PSF has comparable properties relative to that prepared using conventional batch processing, with  $M_w \sim 6000 \text{ g/mol}$ , but this is much smaller than that of commercially prepared PSF,  $\sim 60000 \text{ g/mol}$ . Removal of water is an important part of using the VFD relative to batch processing, in avoiding termination reactions. Also important is the processing time, in changing the morphology of the particles, which may be important in down-stream applications. Indeed, the lower  $M_w$  VFD material may open new particle size/chain length specific applications of PSF, further tuned by morphology considerations, sheet like versus globular like particles. We note that the fluid dynamics in the VFD is inherently complex and that this determines the rate of the reactions (high shear and intense micro-mixing) as well as the shape, determined by how the fluid actually flows in the device. This is a major research effort underway involving a number of laboratories. The reduction in percent yield for increasing processing time may arise also from the shear stress resulting in bond cleavage and reduction in the length of the polymer chain. In this context, it is noteworthy that the VFD is effective in breaking down polyethylenamines [20].

## 2.5. Conflicts of interest

There are no conflicts to declare.

## 2.6. Acknowledgements

The paper is dedicated to our beloved co-author, Dr. Ataollah Nosrati, who sadly passed away before submitting the manuscript. Support of this research by the Australian Research Council and the School of Engineering, Edith Cowan University, is gratefully acknowledged, as is the Raston research group, especially Jessica Philips at the start of the project, and Flinders Analytical for access to their GPC instrument. Microscopy Australia (MA).

## 2.7. Chapter references

1. Othmer, K., *Encyclopedia of Chemical Technology*. 1996, John Wiley & Sons: New York.
2. Schlüter, D.A., C. Hawker, and J. Sakamoto, *Synthesis of polymers, new structures and methods*. Vol. 1. 2012, Weinheim, Germany: Wiley-VCH Verlag GmbH & Co. KGaA. 1184.
3. Billmeyer, F.W., *Textbook of polymer science*. Third ed. 1984, New York: John Wiley & Sons Inc.
4. Saraf, M.K., *Polymerization of Vinylidene Fluoride in Supercritical Carbon Dioxide: Molecular Weight Distribution*, in *Department of Chemical Engineering, North Carolina State University*. 2001, North Carolina State University. p. 135.
5. Johnson, R.N., et al., *Poly(aryl Ethers) by nucleophilic aromatic substitution. I. synthesis and properties*. J. Polym. Sci.: Part A-1, 1967. **5**: p. 2375-2398.
6. Zhu, S., G. Xiao, and D. Yan, *Synthesis of aromatic polyethersulfone-based graft copolyacrylates via ATRP catalyzed by FeCl<sub>2</sub>/isophthalic acid*. J. Polym. Sci. Part A: Polym Chem, 2001. **39**(17): p. 2943-2950.
7. Jung, M.J., et al., *Polysulfone-based anion exchange membranes demonstrate excellent chemical stability and performance for the all-vanadium redox flow battery*. J. Mater. Chem. A, 2013. **1**(35): p. 10458-10464.
8. Ciobanu, M., et al., *Aromatic polysulfones used in sensor applications*. Rev. Adv. Mater. Sci, 2009. **22**: p. 89-96.
9. Van der Bruggen, B., *Chemical modification of polyethersulfone nanofiltration membranes: A review*. J. Appl. Polym. Sci., 2009. **114**(1): p. 630-642.
10. Pye, S.J., et al., *Organic oxidations promoted in vortex driven thin films under continuous flow*. Green Chem, 2018. **20**(1): p. 118-124.
11. Chen, X., J.F. Dobson, and C.L. Raston, *Vortex fluidic exfoliation of graphite and boron nitride*. ChemComm., 2012. **48**(31): p. 3703-3705.
12. Yasmin, L., et al., *Optimising a vortex fluidic device for controlling chemical reactivity and selectivity*. Sci Rep, 2013. **3**(2282): p. 6pp.
13. Britton, J., J.M. Chalker, and C.L. Raston, *Rapid Vortex Fluidics: Continuous Flow Synthesis of Amides and Local Anesthetic Lidocaine*. Chem.Eur.J., 2015. **21**(30): p. 10660-5.
14. Yasmin, L., K.A. Stubbs, and C.L. Raston, *Vortex fluidic promoted Diels–Alder reactions in an aqueous medium*. Tetrahedron Lett., 2014. **55**(14): p. 2246-2248.
15. Gandy, M.N., C.L. Raston, and K.A. Stubbs, *Towards aryl C–N bond formation in dynamic thin films*. Org. Biomol. Chem., 2014. **12**(26): p. 4594-4597.
16. Tong, C.L., et al., *Continuous flow vortex fluidic synthesis of silica xerogel as a delivery vehicle for curcumin*. RSC Adv., 2015. **5**(11): p. 7953-7958.
17. Yasin, F.M., et al., *Microfluidic size selective growth of palladium nano-particles on carbon nano-onions*. ChemComm., 2012. **48**(81): p. 10102-10104.

18. Tong, C.L., et al., *Continuous flow tuning of ordered mesoporous silica under ambient conditions*. RSC Adv., 2013. **3**(41): p. 18767-18770.
19. Britton, J., Dalziel, Stuart B. and C.L. Raston, *The synthesis of di-carboxylate esters using continuous flow vortex fluidics*. Green Chem., 2016. **18**(7): p. 2193-2200.
20. Luo, X., et al., *High-Shear-Imparted Tunable Fluorescence in Polyethylenimines*. ChemPhotoChem, 2018. **2**(4): p. 343-348.
21. D'Alonzo, N.J., P.K. Eggers, and C.L. Raston, *Vortex fluidics synthesis of polymer coated superparamagnetic magnetite nanoparticles*. New Journal of Chemistry, 2017. **41**(2): p. 552-558.
22. Tavakoli, J., et al., *A hyper-branched polymer tunes the size and enhances the fluorescent properties of aggregation-induced emission nanoparticles*. Nanoscale Advances, 2020. **2**(2): p. 633-641.
23. Saldivar-Guerra, E. and E. Vivaldo-Lima, *Handbook of Polymer Synthesis, Characterization, and Processing*. 2013, New Jersey: Wiley. 653.
24. Agboola, O., J. Maree, and R. Mbaya, *Characterization and performance of nanofiltration membranes*. Environ. Chem. Lett., 2014. **12**(2): p. 241-255.
25. Shailesh P. Zala , K.P.P., Khyati S. Patel, Jayshri P. Parmar and Dhruvo Jyoti Sen, *Laboratory Techniques of Purification and Isolation*. International Journal of Drug Development & Research 2012. **04**(02).
26. Nikje, M.M.A. and M. Askarzadeh, *Green and inexpensive method to recover Bisphenol-A from polycarbonate wastes*. Polímeros, 2013. **23**(1): p. 29-31.
27. Zou, T., et al., *Comparison of two bisbenzoxazines containing carboxylic groups and their thermal polymerization*. Designed Monomers and Polymers, 2012. **16**(1): p. 25-30.
28. Dwivedi, A., V. Baboo, and A. Bajpai, *Fukui Function Analysis and Optical, Electronic, and Vibrational Properties of Tetrahydrofuran and Its Derivatives: A Complete Quantum Chemical Study*. Journal of Theoretical Chemistry, 2015. **2015**: p. 1-11.
29. Fulmer, G.R., et al., *NMR Chemical Shifts of Trace Impurities: Common Laboratory Solvents, Organics, and Gases in Deuterated Solvents Relevant to the Organometallic Chemist*. Organometallics, 2010. **29**(9): p. 2176-2179.
30. Shah, P.N., et al., *Environmentally benign synthesis of vinyl ester resin from biowaste glycerin*. RSC Advances, 2015. **5**(48): p. 38673-38679.
31. Nechifor, G., et al., *Nanostructured hybrid membrane polysulfone-carbon nanotubes for hemodialysis*. Desalination, 2009. **241**: p. 342-348.
32. Xie, Y., et al., *Synthesis of highly porous poly(tert-butyl acrylate)-b-polysulfone-b-poly(tert-butyl acrylate) asymmetric membranes*. Polymer Chemistry, 2016. **7**(18): p. 3076-3089.
33. Menachem Elimelech, X.Z., Amy E. Childress, Seungkwan Hong, *Role of membrane surface morphology in colloidal fouling of cellulose acetate and composite aromatic*

- polyamide reverse osmosis membranes.pdf*. Journal of Membrane Science, 1997. **127**: p. 101-109.
34. Fu, X., et al., *Effect of surface morphology on membrane fouling by humic acid with the use of cellulose acetate butyrate hollow fiber membranes*. Journal of Membrane Science, 2008. **320**(1-2): p. 483-491.

The published version of chapter 3 can be found at <https://doi.org/10.1039/D1NJ00834J>

## Chapter 3

### High shear vortex fluidic morphologically controlled polysulfone formed under anhydrous conditions†

Under Review in Polymer Chemistry at RSC Group, since December 2020.

Aghil Igder<sup>a,b</sup>, Ahmed Hussein Mohammed Al-Antaki<sup>b,c</sup>, Scott J. Pye<sup>b</sup>, Alireza Keshavarz<sup>a</sup>, Ata Nosrati<sup>a</sup>  
and Colin L. Raston<sup>\*b</sup>

#### Abstract

Polysulfone (PSF) was prepared under scrupulously anhydrous condition, under high shear in a vortex fluidic device (VFD) operating under confined mode, in DMSO, thereby avoiding the use of chlorinated solvents, unlike in conventional batch processing in generating the polymer. The effect of systematically varying the operational parameters of the VFD (rotational speed ( $\omega$ ) and tilt angle ( $\theta$ ) of the 20 mm diameter quartz tube housed in the device, and temperature and processing time) was investigated with respect to  $M_w$  and  $T_g$  of the polymer, with the product further characterised using FTIR, NMR, GPC, DSC, SEM and BET. As a comparison, for the optimal processing parameters ( $\omega$  6k rpm,  $\theta$  45°, 160 °C, 60 min), the  $M_w$  and  $T_g$ , ~ 16 kg/mol and ~ 170 °C respectively, were significantly improved relative to those prepared without scrupulous exclusion of moisture, ~ 6.7 kg/mol and ~ 154 °C respectively. SEM established that increasing  $\omega$  resulted in different morphologies of the PSF, forming sheet-like structures at lower rotational speeds then pseudo-spherical structures followed by a mixture of sheet-like and rod-shape structures for increasing  $\omega$ . Change in temperature of the reaction also impacted on the nature of the product, with sheet-like structures formed at 140 °C and fibrous material at 170 °C. BET findings correlated with SEM images with a higher surface area for fibrous material, ~ 4000 m<sup>2</sup>/g, compared to ~ 1470 m<sup>2</sup>/g for the sheet-like structures. The different morphologies arising from change in  $\omega$  and temperature relate to different topological fluid flows in the VFD.

### 3.1. Introduction

The nucleophilic substitution route is the most common and efficient method for the commercial synthesis of polysulfone (PSF) [1]. This method involves two separate steps; firstly, the bisphenol of choice is dissolved in a dipolar aprotic solvent in the presence of an alkali base, such as 50% NaOH, in creating a dialkali metal salt, with the second step then reacting this with a 4, 4'-dihalodiphenylsulfone (mostly dichlorodiphenylsulfone, DCDPS) [1-3]. However, dissolving the alkali bisphenate under anhydrous condition is required to prevent the hydrolysis of DCDPS and for gaining access to higher molecular weight ( $M_w$ ) polymer [1, 2]. Removing the water generated in the first step can be controlled by increasing the reaction temperature to  $\sim 120^\circ\text{C}$  [2, 3].

Different aprotic solvents have been used for preparing PSFs include N-methyl-2-pyrrolidinone (NMP), dimethyl acetamide (DMAc), sulfolane, and dimethyl sulfoxide (DMSO). The latter is regarded as the best solvent of choice in terms of enhancing the solubility and increasing polymerisation rates [2], with NaOH and  $\text{K}_2\text{CO}_3$  suitable bases for generating PSF and polyethersulfone (PES), respectively [2]. However, this conventional nucleophilic substitution process is time-consuming, high in energy usage, and also requires removing the NaCl by-products. Overcoming these requires innovative processing solutions, and in this context we have introduced the use of the vortex fluidic device (VFD), as a candidate for the synthesis of PSF [3]. This thin film microfluidic platform has potential in chemical synthesis, having simplicity in design along with cost effect scalability of the processing. The induced mechano-energy (shear stress) in the thin film in the VFD can be harnessed for accelerating and simplifying chemical reactions [3-15]. Britton et al. [8] established high yielding syntheses of di-carboxylate esters, with the water by-product removed *in situ* in driving the reactions. Such removal of water relates to the large surface area of the thin film which has surface Faraday waves [6].

In addition to using the VFD to prepare polymers [3], it also has potential in modifying polymers, as in reducing the molecular weight of polyethylenimine [4], improving the performance and antifouling capability of ultrafiltration (UF) membranes [16, 17], preparing composite nanofiltration (NF) membranes [18], and incorporating graphene oxide (GO) as an

effective barrier in a nanofibrous membrane for water treatment [19, 20], as we recently established for fabricating a GO/PSF composite UF membranes [5]. There is now an understanding of different high shear topological fluid flows in the VFD which can be harnessed to control such processes, and more [3-10].

PSF is a polymer of choice in filtration membranes used in industry [21, 22], which relates to its molecular weight ( $M_w$ ), glass transition temperature ( $T_g$ ), and viscosity. Polymers behave differently under different conditions, depending on their chemical, thermal and mechanical stabilities [23]. The structure of polymers affects most of its properties including viscosity, solubility in different solvents,  $T_g$  and  $M_w$  [24], with the latter two being particularly important [25, 26]. SEM is primarily used to determine the morphology of the materials, with the surface area and pore size determined using positron annihilation lifetime spectroscopy, adsorption isotherm models, X-ray or neutron scattering, and Brunauer–Emmett–Teller (BET) measurements [27-30]. Material surface area determinations has also been coupled with theoretical consideration [28-31], for example, Hart et al. [30] have investigated the applicability of BET theory for determining the surface area of microporous materials. The BET method is acceptable for ultra-microporous materials [29], but not so for polymers with intrinsic microporosity, which may prevent monolayer formation before the pores are filled with gas [30]. Scattering techniques have also gained prominence in structure elucidation of materials at the mesoscopic scale (1-1000 nm) [32], as well as growth mechanisms of mesoporous nanostructures [33]. Small angle X-ray or neutron scattering (SAXS or SANS) have been extensively used for studying polymers solutions [34], copolymers [35], polymer blends [36], branched or grafted polymers [37], polymer gels [38], polymeric nanomaterials [39], and polymer membranes [40].

Herein we report on the utility of the VFD, Figure 3. 1-a, for improving the properties ( $M_w$  and  $T_g$ ) of PSF [3]. This involved systematically exploring the effect of changing the operational parameters the VFD including temperature, rotational speed, tilt angle, and processing time, with the salient features of the device and the associated topological fluid flows in the liquid are presented in Figure 3. 1-a. The targeted VFD processing featured carrying the PSF synthesis in a single step Figure 3. 1-b, rather than using two steps as discussed above [1, 2], under anhydrous conditions. The high shear stress in the dynamic thin film of liquid in the



VFD, was effective in being able to avoid the use of a chlorinated solvent, as in chlorobenzene, unlike in conventional PSF synthesis [2]. Furthermore, morphological differences between the different VFD generated material, depending on the processing parameters, have been determined using SEM with the surface area determined using BET measurements. Combining these techniques with the novel processing features of the VFD allows for processing under anhydrous conditions, as a new approach in the synthesis of PSF with high molecular weight and glass transition temperature.

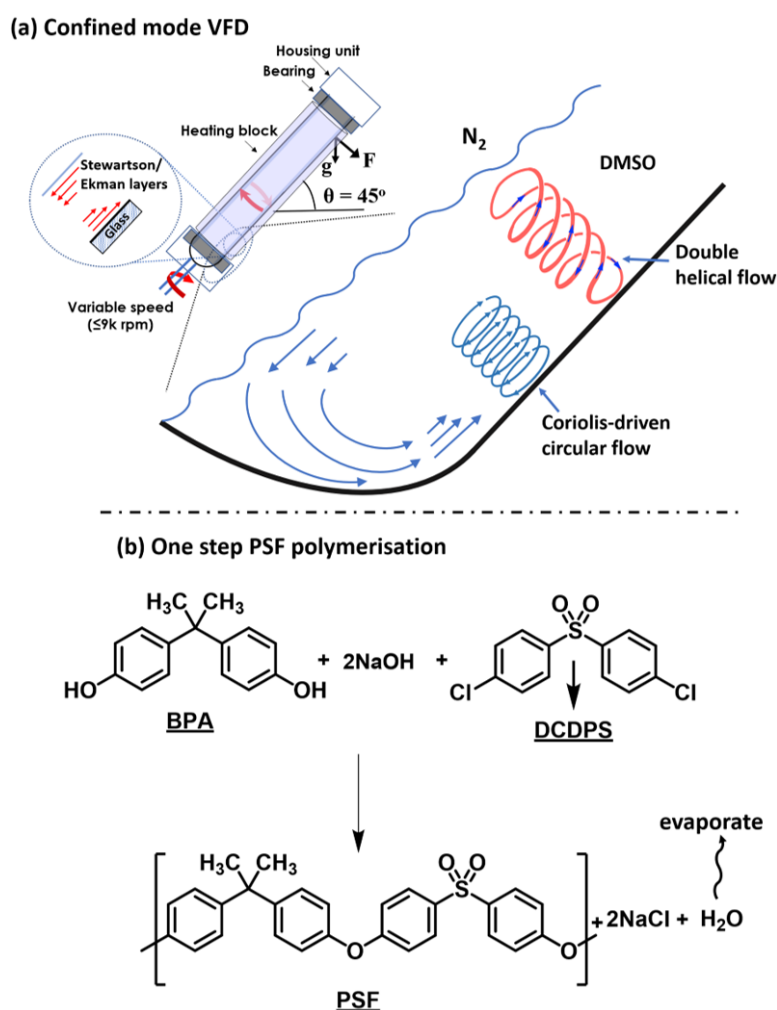


Figure 3. 1. (a) Salient features of the VFD housing a quartz tube with a hemispherical shaped base, and associated topological fluid flow, and (b) the one step PSF polymerisation under anhydrous condition.

## 3.2. Experimental

### 3.2.1. Materials and methods

All chemicals were used as received unless otherwise stated. Bisphenol A, [2,2-bis(4-hydroxyphenyl) propane] (BPA) (99%), 4,4'-dichlorodiphenyl sulfone (DCDPS) (98%), and sodium hydroxide (pellets, > 97%) were purchased from Sigma Aldrich. Dimethyl sulfoxide (DMSO) (99.9%) was purchased from RCI Labscan Limited and ethyl Alcohol (100%) was provided by Chem-Supply. DMSO was distilled three times before use and kept under nitrogen to minimise the water adsorption. Specifications of the VFD have been detailed elsewhere [6]. An in house developed heating block was mounted on the VFD to heat the rotating quartz tube (up to 170°C).

### 3.2.2. Preparation of PSF

The PSF was synthesised using a nucleophilic substitution route as in conventional batch processing [2], using the VFD involving modification of earlier studies [3]. The new process operates under anhydrous conditions with considerable improvement in polymer outcome. For this purpose, the DMSO solvent of choice was triple distilled and stored over molecular sieves under a nitrogen atmosphere. All glassware including the quartz tube (20 mm O.D., 17.5 mm ID, 18.5 cm in length) was oven dried at 160 °C overnight prior to use. Furthermore, dry crushed NaOH pellets were used to minimize adding water to the system which will hydrolyse the DCDPS. The oven dried VFD tube was kept under vacuum using a rubber stopper with a needle connected to a vacuum and nitrogen gas. Air was removed by purging with nitrogen gas while the quartz tube was flame heated. The required amount of BPA (228 mg, 1.0 mmol), DCDPS (287 mg, 1 mmol), and crushed NaOH (80 mg, 2 mmol) were placed in the tube at the same time and then evacuated followed by introducing dry nitrogen, with the process repeated three times also using flame drying. After cooling the tube, 2 mL of DMSO was injected into the VFD tube. Polymerisation occurred on heating the VFD tube up to the specified temperature (refer to Table B. 1<sup>†</sup>), using a heating block, and rotating the reaction tube at certain rotational speed for a specified time, depending on the experimental conditions, Table B. 1<sup>†</sup>. The tilt angle  $\theta$  of the quartz tube was systematically varied along with temperature, rotational speed ( $\omega$ ), and reaction time. Noting that the temperature is critical

in controlling the reaction, [3], the heating block was calibrated against the melting point of several compounds as detailed in the SI (Appendix B)†.

After a specified  $\omega$ ,  $\theta$ ,  $T$ , and time for each experiment, the reaction was terminated with the static tube cooled to room temperature, whereupon the NaCl by-product was removed by vacuum filtration. The resulting solution was then added dropwise to ethanol (10 mL) resulting in a white coagulated product which was washed three times with ethanol followed by centrifugation (5 min, 805 RFC) prior to vacuum filtration. The resulting PSF was then dried *in vacuo* overnight.

### 3.2.3. Characterisation

The as prepared PSF was characterised relative to  $M_w$ , structure, morphologies, and thermal stabilities.  $^1\text{H}$ -NMR data was collected using a 600 MHz Bruker NMR spectroscopy, recorded in  $\text{CDCl}_3$ , with 64 scans and a relaxation delay-time of 4 seconds and 512 scans with relaxation delay-time of 10 seconds in the  $^{13}\text{C}$ -NMR spectra. All chemical shifts are presented in ppm, using residual solvent as the internal standard. Attenuated Total Reflection (ATR) Fourier Transform Infrared Spectroscopy (FT-IR) spectra were recorded on a PerkinElmer ATR-FTIR spectrometer. Molecular weight ( $M_w$ ) and polydispersity (PDI) were determined by gel permeation chromatography (GPC) using a Waters e2690 instrument equipped with a differential Refractive Index (RI) detector and column operated with tetrahydrofuran (THF) used as the eluent (at 25 °C with 1.0 ml/min flow rate). The column was calibrated using polystyrene standards with molecular weight covering the range of 1000–2704000 g/mol. Differential scanning calorimetry (DSC) was used to record the  $T_g$  of the product, using a Perkin Elmer DSC 8000 instrument. In order to eliminate the thermal history of the polymers, the  $T_g$  of each sample was recorded from the heat flow changes on the second heating scan of a cyclic heating-cooling-heating staged, from 30 to 230°C, and then cooled to 30 °C followed by heating again to 230°C with a ramping rate of 10 °C per minute.

The morphology of the as synthesised PSFs was investigated using scanning electron microscope (SEM), using an Inspect FEI F50 SEM instrument with an operating voltage of 5 kV and working distance of 10 mm. Samples for SEM were drop cast on a silicon wafer and coated with 5 nm platinum to prevent charging during SEM imagery. Specific surface areas were

investigated using the standard Barrett–Emmett–Teller (BET) method, using a TriStar II, Micrometric Ltd, Lincoln LN6 3RX, United Kingdom. PSF samples were degassed at 90 °C for ~ 6 h prior to measurement. Nitrogen absorption isotherms were recorded at 77 K with 20 s equilibrium intervals, in the relative pressure range of 0.1–1  $P/P_0$ .

### 3.3. Results and Discussion

#### 3.3.1. PSF synthesis

We have established the synthesis of PSF as a one step process in the VFD Figure 3. 1-a, conditional upon using anhydrous conditions, starting with solid BPA, NaOH, and DCDPS suspended in DMSO. Importantly, the processing avoids the use of chlorinated solvents, unlike in conventional batch processing to generate PSF, for example in using chlorobenzene. FTIR confirmed the completion of the reaction in the VFD, matching that of commercial PSF, Figure 3. 2-a. Peaks at (i) 3100-2850  $\text{cm}^{-1}$  correspond to aromatic and aliphatic ( $\text{CH}_2$ ) stretching vibrations, (ii) 1293 and 1147  $\text{cm}^{-1}$  correspond to asymmetric and symmetric  $-\text{S}=\text{O}$  stretch of the backbone of PSF, (iii) 1102 and 1234  $\text{cm}^{-1}$  correspond to symmetric and asymmetric  $-\text{CO}$  bands, and (iv) 1584 and 1486  $\text{cm}^{-1}$  correspond to the presence of aromatic rings [5, 41, 42].

$^1\text{H}$  and  $^{13}\text{C}$  NMR of the starting materials (BPA and DCDPS) have been reported in our previous work [3], and are also presented in Figures B. 3-6†.  $^1\text{H}$  NMR of the VFD mediated, conventional synthesised and commercial PSF presented in Figure 3. 2-b confirm the formation of the polymer with the doublets corresponding to protons a, b, d and e in phenol moieties,  $\delta = 7.84$ , 7.23, 6.99 and 6.23 ppm. The peak at  $\delta = 1.69$  ppm is assigned to the methyl group (c) in the main polymer chain of the VFD synthesised PSF. The smaller doublets at  $\delta = 6.74$ , 7.08 ppm correspond to terminal groups of the polymer in the aromatic region, a' and b', and the peak at 1.65 ppm corresponds to aliphatic methyl groups c'. The smaller these terminal groups peaks relative to other peaks, the higher the molecular weight of the polymers [26]. Figures B. 7-9† shows the  $^1\text{H}$  NMR of the conventional synthesised and commercial PSF which confirm the smaller peaks for the terminal groups in commercial PSF corresponding to a higher  $M_w$  (~ 63 kg/mol) compared to the conventionally synthesised polymer which has a lower  $M_w$  (~ 6 kg/mol).  $^{13}\text{C}$  NMR spectra for PSF (VFD mediated and conventional synthesised) are presented

in Figures B. 8-10<sup>†</sup>. In contrast to our previous study [3], no intermediate, notably DiNa salt of BPA, was present in the final product, as established using NMR spectroscopy. In the present study, the processing circumvents the need for first preparing the DiNa salt of BPA for then reaction with DCDPS.

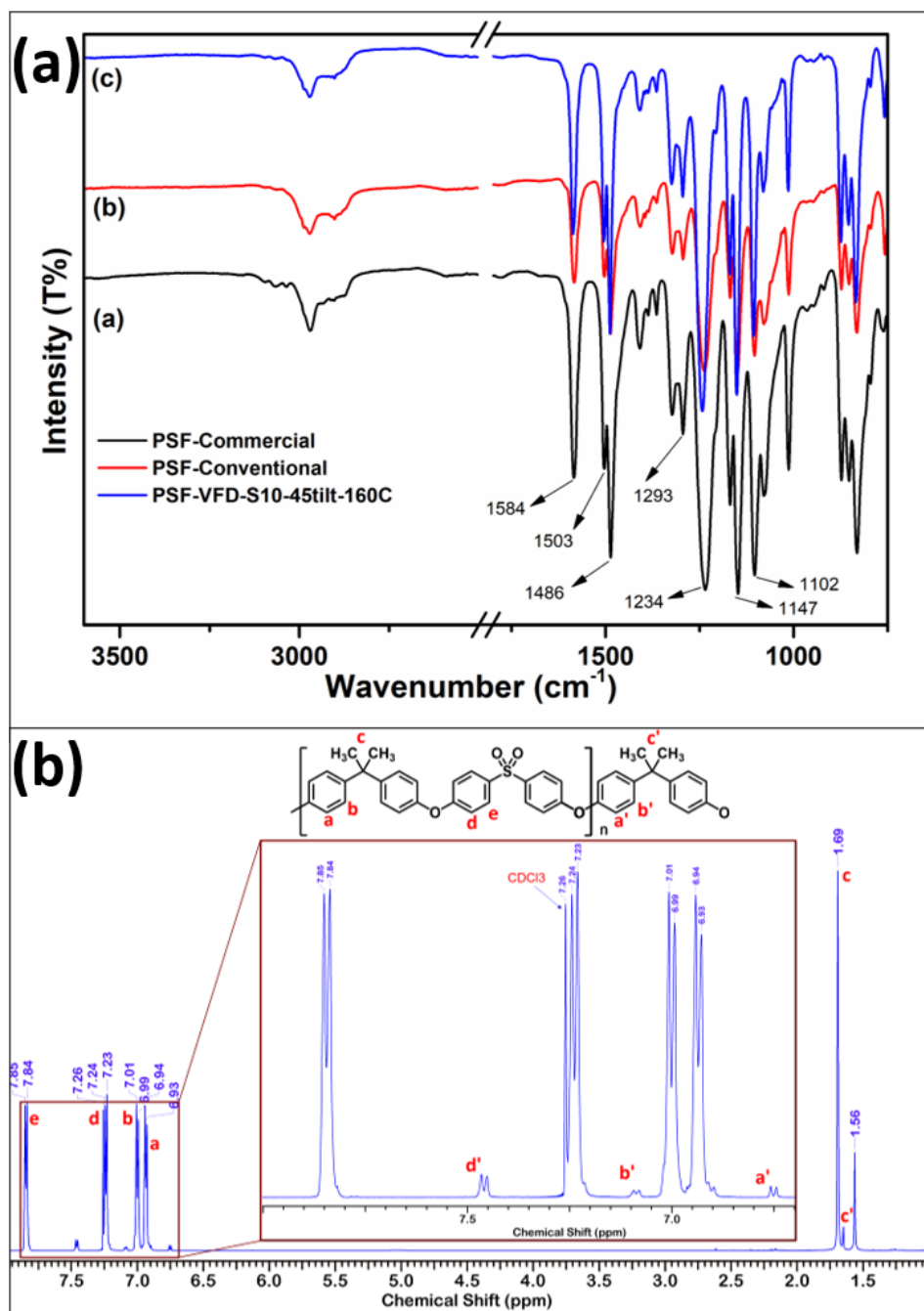


Figure 3. 2. FTIR spectra of (a) commercial, conventional, and VFD synthesized PSF, and (b) <sup>1</sup>H-NMR spectra (CDCl<sub>3</sub>) of the VFD synthesised PSF (S10). VFD processing was at 6k rpm, 160 °C, 45 tilt angle, and 60 min reaction time.

### 3.3.2. Effect of VFD rotational speed

The rotational speed,  $\omega$ , of the VFD was varied (3k to 8k rpm over 1k rpm increments) while fixing the temperature,  $T$ , at 150 °C, tilt angle,  $\theta$ , 45 °, and reaction time 60 min., Table B. 1†.  $M_w$ ,  $T_g$ , surface area and the morphology of the samples are presented in Figure 3. 3. GPC curves, Figure 3. 3-a, show the molecular weight distribution (MWD) of the samples prepared at different rotational speeds.  $M_w$  values were in the range ~ 6.5 to 9.8 kg/mol with the highest at 6k rpm, having PDIs in the range 1.6 to 2. The narrower MWD curves, lower PDIs compared to that of commercial PSF, which has a PDI of 2.9 (Figure 3. 5-a), relates to the high shear in the VFD associated with different topological fluid flow regimes at the  $\mu\text{m}$  dimensions which are beginning to be understood Figure 3. 1-a [6]. In particular, the type of topological fluid flow depends dramatically on the rotational speed, and this is in accordance with the present findings in having one speed, 6k rpm, which is optimal in terms of  $M_w$  of the polymer. Heat flow changes, Figure 3. 3-b, also show the same trend as that for the  $M_w$  curves; the highest  $M_w$  also corresponds to the highest  $T_g$  which is at 152.5 °C and is associated with a change in specific heat capacity,  $c_p$  0.229 J/(g\*°C). Higher rotational speeds, 7 and 8 k rpm, can also lead to polymer breakdown, noting that the VFD has been used for slicing polyethylenimines [4].

As to the morphology of the PSF, sheet-like structures are formed at lower rotational speeds with needle-like structures formed at higher  $\omega$ , 8k rpm, Figure 3. 3-c. BET studies, Figure 3. 3-d), show slightly lower surface area for the PSF prepared at lower  $\omega$ , increasing from ~915 to ~1670 m<sup>2</sup>/g for  $\omega$  increasing from 3k to 8k rpm, in accordance with  $M_w$  and  $T_g$  data, Figure 3. 3-a, b. However, in increasing  $\omega$  from 6k rpm to 8 k rpm, the  $M_w$  and consequently the  $T_g$  decreases with the surface area increasing, confirming more intrinsic porosity at higher rotational speeds. This can be attributed to the double helical topological flow produced at higher  $\omega$  [6], as presented in Figure D. 8 and Figure D. 22 in Appendix D†. The increase in surface area at higher  $\omega$  also corresponds to the morphological differences depending on  $\omega$ , Figure 3. 3-c, i.e. sheet-like structures having lower surface area than needle-like structures.

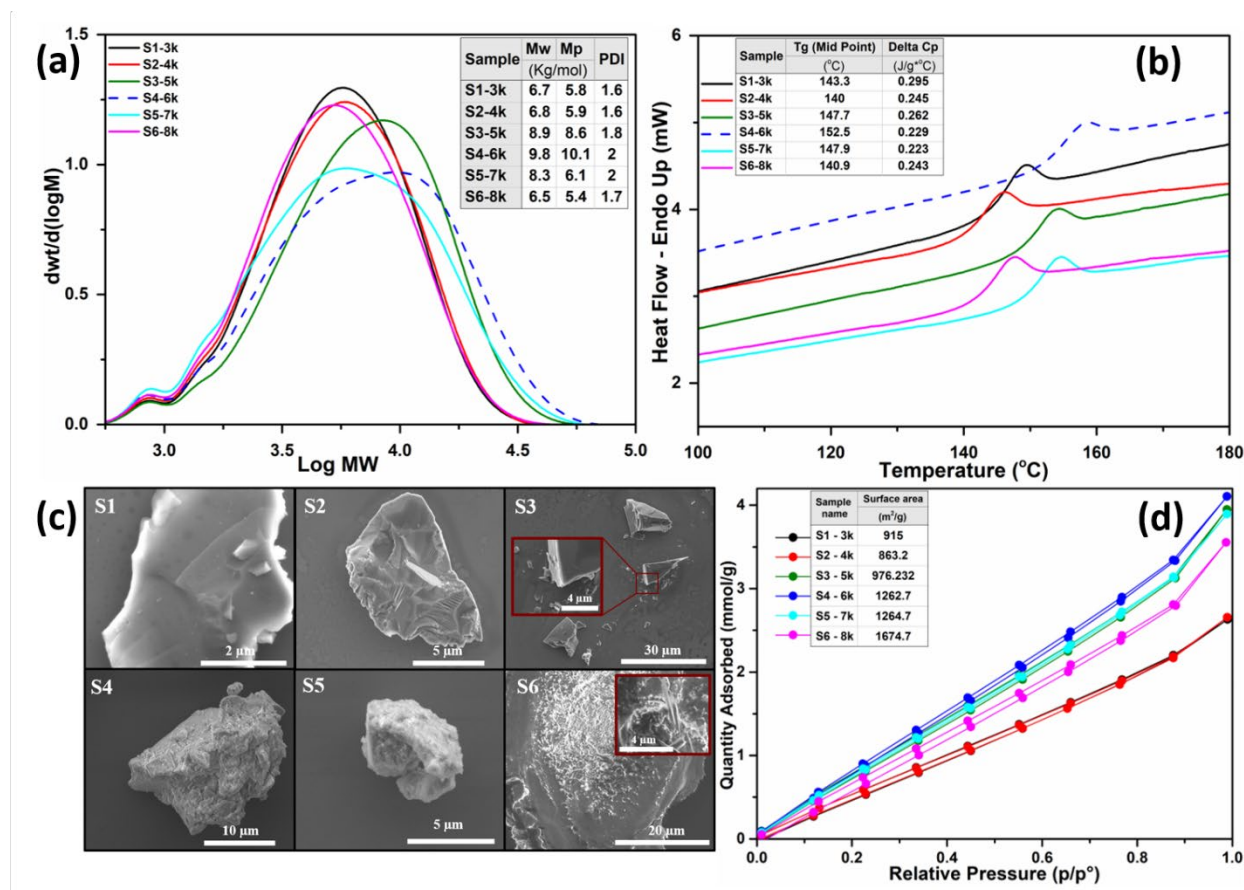


Figure 3.3. Comparison between (a) molecular weight distribution, (b) DSC thermograms, (c) SEM images, and (d) nitrogen adsorption analysis of the VFD synthesised PSF at different rotational speeds, (S1-S6, at  $\omega$  3k - 8k rpm,  $\theta$  45°, T 150 °C, and 60 min).

### 3.3.3. Effect of temperature

The temperature was then systematically varied relative to  $\omega$  with all experiments carried out at 6k rpm, for reasons discussed above, and the tilt angle  $\theta$  set at 45° for 60 min processing. As previously established [3], the processing temperature plays a pivotal role in the PSF synthesis in the VFD, with the reaction taking place  $> 140^{\circ}C$  with  $\geq 160^{\circ}C$  producing higher  $M_w$  polymers, for example,  $170^{\circ}C$  affording material with  $M_w$  12 kg/mol and  $T_g$  168 °C. However, the higher the temperature the lower the yield, dropping to 19.4% at this temperature. This we ascribe the presence of adventitious moisture, and in the present study care was taken to minimise this, by carrying the reaction out under anhydrous conditions, while also minimising evaporation under processing in the VFD which is associated with high heat and mass transfer [8]. Under such conditions, the product was consistently formed in much higher yield. Figure 3.4 shows the effect of temperature on  $M_w$ ,  $T_g$ , morphology, and



surface area of the VFD produced PSF - the higher the temperature the higher the  $M_w$  ( $\sim 16$  and  $15.2$  kg/mol) and  $T_g$  ( $\sim 169$  and  $174$  °C) at  $160$  °C and  $170$  °C, respectively. At  $160$  °C and  $170$  °C the yield of PSF was  $\sim 67\%$  and  $64\%$ , respectively, and surprisingly the polymer was formed at lower temperatures, at  $120$  °C, (S8), albeit in  $\sim 45\%$ , in contrast to no apparent reaction for operating the VFD open to the air [3], although the  $M_w$  ( $\sim 3.3$  kg/mol) and  $T_g$  ( $\sim 126$  °C) were low.

The morphology of the PSF now generated at different temperatures are strikingly different. SEM images, Figure 3. 4-c, revealed sheet-like structure for PSF synthesised at  $120$  and  $140$  °C, semi-spherical (mixture of sheet and spherical) at  $150$  °C, globular at  $160$  °C and fibrous structures at  $170$  °C.

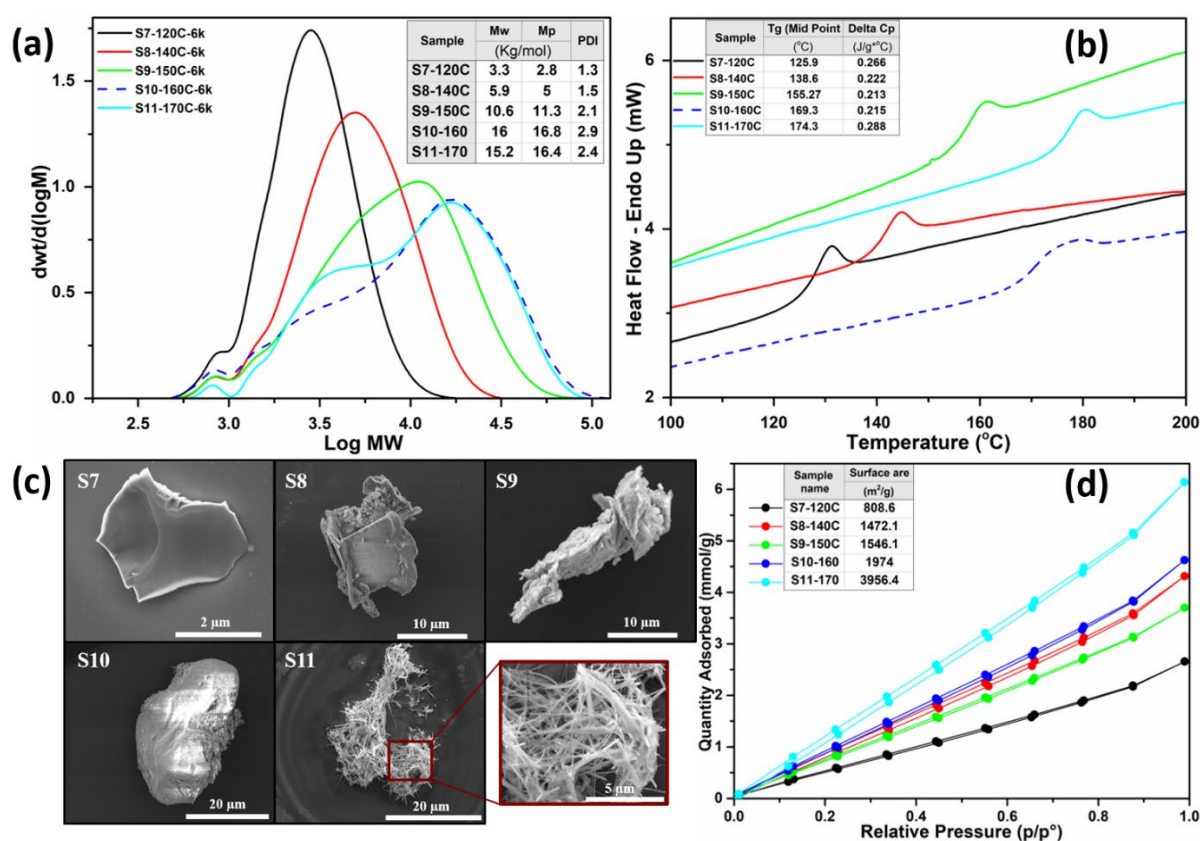


Figure 3. 4. Comparison between (a) molecular weight distribution, (b) DSC thermograms, (c) SEM images, and (d) nitrogen adsorption analysis of the VFD synthesised PSF at different temperatures, (S7-S11, at  $T$  120 - 170 °C,  $\omega$  6k rpm,  $\theta$  45°, and  $t$  60 min).

BET measurements, Figure 3. 4-d, established a large difference between the surface area of the PSFs obtained at  $140$  and  $170$  °C, with  $\sim 1472$  and  $\sim 3956$   $m^2/g$ , respectively. This



correlates with different morphology of sheets and rods at low and high rotational speeds, Figure 3. 4-c.

As discussed above, the formation of sheets is consistent with circular topological fluid flow in the VFD being dominated at low  $\omega$ , where there is high heat and mass transfer at the glass liquid interface associated with a circular Coriolis from the hemispherical base of the rotating tube [6], Figure D. 22<sup>†</sup>, with the rods formed under high shear within the confines of the double helical flow generated by the Coriolis twisted eddies from the Faraday waves generated as the tube rotates at 45° tilt with an expected oscillating thin thick layer of liquid under gravity [6], as presented in in Appendix D<sup>†</sup>. The diameter of the rods are mainly between ca ~70-200 nm which correlates with the diameter of rods of fullerene C<sub>60</sub> formed in such confines, as a shear stress induced crystallisation process [6]. Thus, the dimensionality of the topological fluid flow in the 20 mm O.D. tube, from one fluid to another, at different temperatures, specifically at  $\theta$  45° is consistent.

In accordance with our previous results, 170 °C can result in high M<sub>w</sub> polymer. In the present study, the outcome of processing at 160 °C was also comparable and was considered the optimal temperature hereafter, taking energy usage as an important consideration in the processing. It has the highest M<sub>w</sub> and T<sub>g</sub> of VFD synthesised PSF, although the PDI (2.9) was higher than for other temperatures. M<sub>w</sub> and T<sub>g</sub> increased from ~3.3 kg/mol and ~126 °C to 16 kg/mol and ~169 °C, on increasing the temperature from 120 to 160 °C. There is a narrower MWD for lower temperatures, Figure 3. 4-a, with the lowest PDI of 1.5 at 140 °C, then 2.1, 2.9, and 2.4 for 150, 160 and 170 °C respectively. As shown in Figure 3. 4-a, The MWD of PSF synthesised at 160 and 170 °C was broader, but with higher M<sub>w</sub> relative to PSF formed at lower temperatures. Thus, the growth of higher M<sub>w</sub> polymers takes place at higher temperatures. There is a shoulder for the smaller M<sub>w</sub> region of the MWD curve of PSF formed at 170 °C (S11), which disappears for processing at lower temperatures, and is indicative of some polymer chain degradation [43] occurring at the higher temperature of 170 °C. It is also reflected in the molecular weight value which drops slightly from ~16 kg/mol at 160 °C to ~15 kg/mol at 170 °C. A sharper shoulder is expected in the lower M<sub>w</sub> region for temperatures > 170 °C. This is consistent with the earlier research outcomes [2] which showed that the reaction is mildly exothermic and extremely rapid above 160 °C, possibly resulting in solvent

decomposition and/or discoloration or even gelation of the reaction mixtures. Hence, preventing the excessive overheating of the reaction is essential.

### 3.3.4. Effect of tilt angle

The use of different tilt angles,  $\theta$ , of the quartz tube, between  $0^\circ$  (horizontal) and  $90^\circ$  (vertical) were then investigated, with  $\omega$  fixed at 6k rpm, for  $T$  160  $^\circ\text{C}$  and 60 min processing (S12-S18, Table B. 1<sup>†</sup>) to ascertain the effect of the interplay between gravitational and centrifugal forces on the fluid flow and thus the outcome of the polymerization process. For  $\theta$   $30^\circ$  to  $90^\circ$ , Figure 3. 5, there is minimal effect on the  $M_w$  and the  $T_g$  of the as prepared polymers, but there is a significant reduction in  $M_w$  of the polymer for  $\theta$   $0^\circ$  and  $15^\circ$ . MWD also shows a shoulder in the lower  $M_w$  region for the polymer formed at  $\theta$   $30^\circ$ .

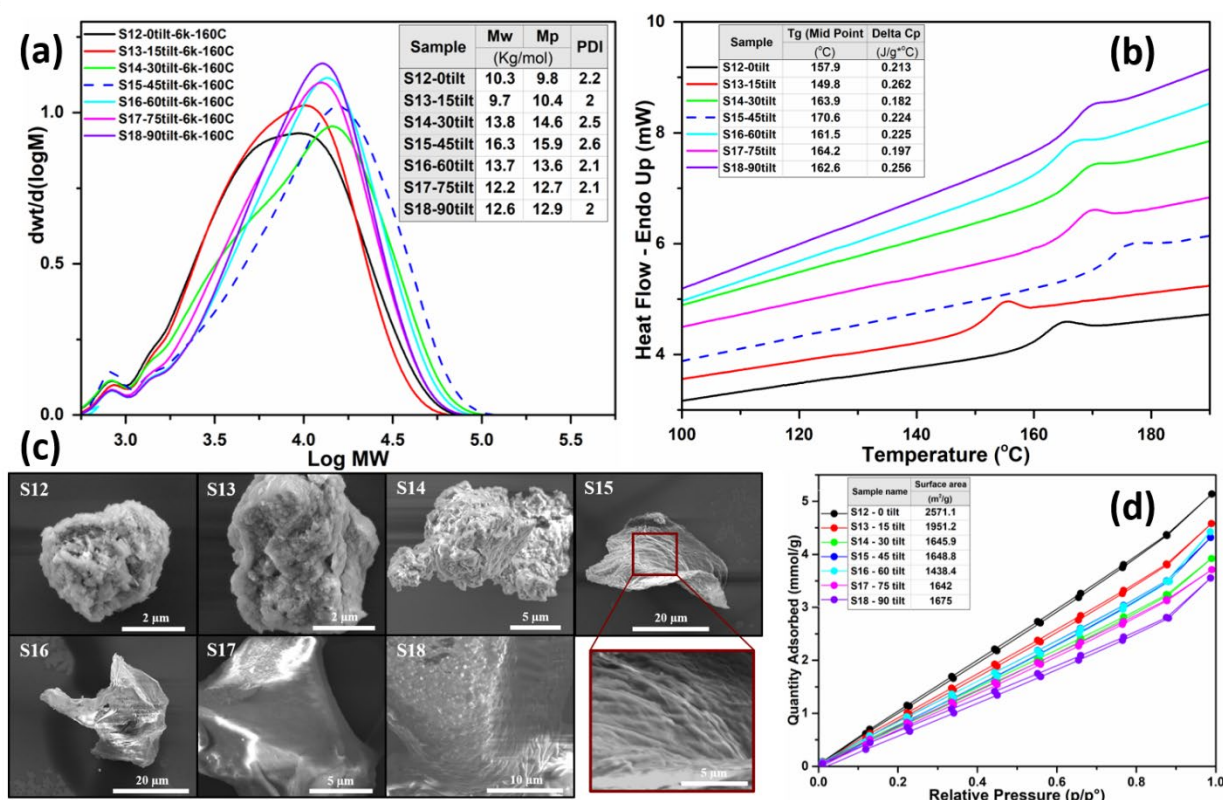


Figure 3. 5. Comparison between (a) molecular weight distribution, (b) DSC thermograms, (c) SEM images, and (d) nitrogen adsorption data of the VFD synthesised PSF formed at different tilt angles, S12-S18,  $\theta$   $0^\circ$ ,  $15^\circ$ ,  $30^\circ$ ,  $45^\circ$ ,  $60^\circ$ ,  $75^\circ$  and  $90^\circ$ ,  $\omega$  6k rpm,  $T$  160  $^\circ\text{C}$ , and  $t$  60 min.

SEM images show dramatic changes in morphology relative to  $\theta$ , with semi-flat surfaces for  $\theta \geq 30^\circ$  and irregular porous-like structures at  $\theta$   $0^\circ$  and  $15^\circ$ . This is reflected in BET

measurements, with higher surface areas for  $\theta$  0° and 15°, ~2571 and ~1951 m<sup>2</sup>/g respectively. These are higher than those formed at  $\theta$  30° 45°, 60°, 75° and 90°, at ~1646, 1649, 1438, 1642, and 1675 m<sup>2</sup>/g, respectively, Figure 3. 4-c. Presumably this difference is related to differences in specific topological fluidic flow in the VFD [6], Figure D. 22†. Although  $\theta$  45° did not show any significant difference in the  $M_w$  and  $T_g$  of the synthesised PSFs, is a much easier to implement at this angle for carrying out the experiments. Given that 45° tilt angle is typically optimal for processing in the VFD [4, 7, 11-15], this angle was selected as the optimum tilt angle for the rest of the experiments.

### 3.3.5. Effect of time

Previously we established that increasing the reaction time up to 60 min in the VFD resulted in higher  $M_w$  PSF, although this resulted in lower yields [3]. Given that in the present study we are operating the VFD under anhydrous conditions, we have explored the effect of processing time, for 15, 30, 60, and 180 min. Under such conditions, the yield does not significantly change with time, being ~ 65±4% for S19-22 (Table B. 1†). However, the  $M_w$  and  $T_g$  significantly increased from ~4.5 kg/mol and ~138 °C to ~15.5 kg/mol and ~172 °C by extending the reaction time from 15 to 60 min, Figure 3. 6-a and b, with only a slight decrease in  $M_w$  and  $T_g$  after 180 min of processing. The shoulder in the lower  $M_w$  region, Figure 3. 6-a, suggests that the polymer is undergoing fragmentation during longer processing time [43], where it is subjected to extensive shear stress. SEM and BET results, Figure 3. 6-c and d, are consistent with changes to the PSF for long processing times. Sheet-like structures are generated for the shorter reaction times, 15 and 30 min, bulk structures for 60 min and a combination of needle-like and sheet-like structures for 180 min. BET measurements revealed higher surface areas for longer processing time, which can be attributed to the higher intrinsic porosity, with 15 min and 180 min processing resulting in ~677 and ~4060 m<sup>2</sup>/g surface areas, respectively. High shear in the VFD accelerates the polymerisation reaction and the longer the processing time, the greater scope for remoulding the size and shape of the polymer particles, as well as the intrinsic porosity, depending on the topological fluid flows, Figure 3. 1-a [6, 7] as well as breaking the longer polymer chains. MWD and heat flow thermograms in Figure 3. 6-a and b show a significant increase in  $M_w$  ~15.4 kg/mol, and  $T_g$  ~172 °C, for PSF synthesised in the VFD at optimal conditions relative to conventional synthesised PSF, with

corresponding values at  $\sim 6.6$  kg/mol and  $\sim 106$  °C. While commercial PSF has a much higher  $M_w \sim 63$  kg/mol, MWD curves shows a smaller PDI for the VFD synthesised PSF at optimal conditions (S21), 2.4 compared with 2.9 for commercial PSF, Figure 3. 6-a.

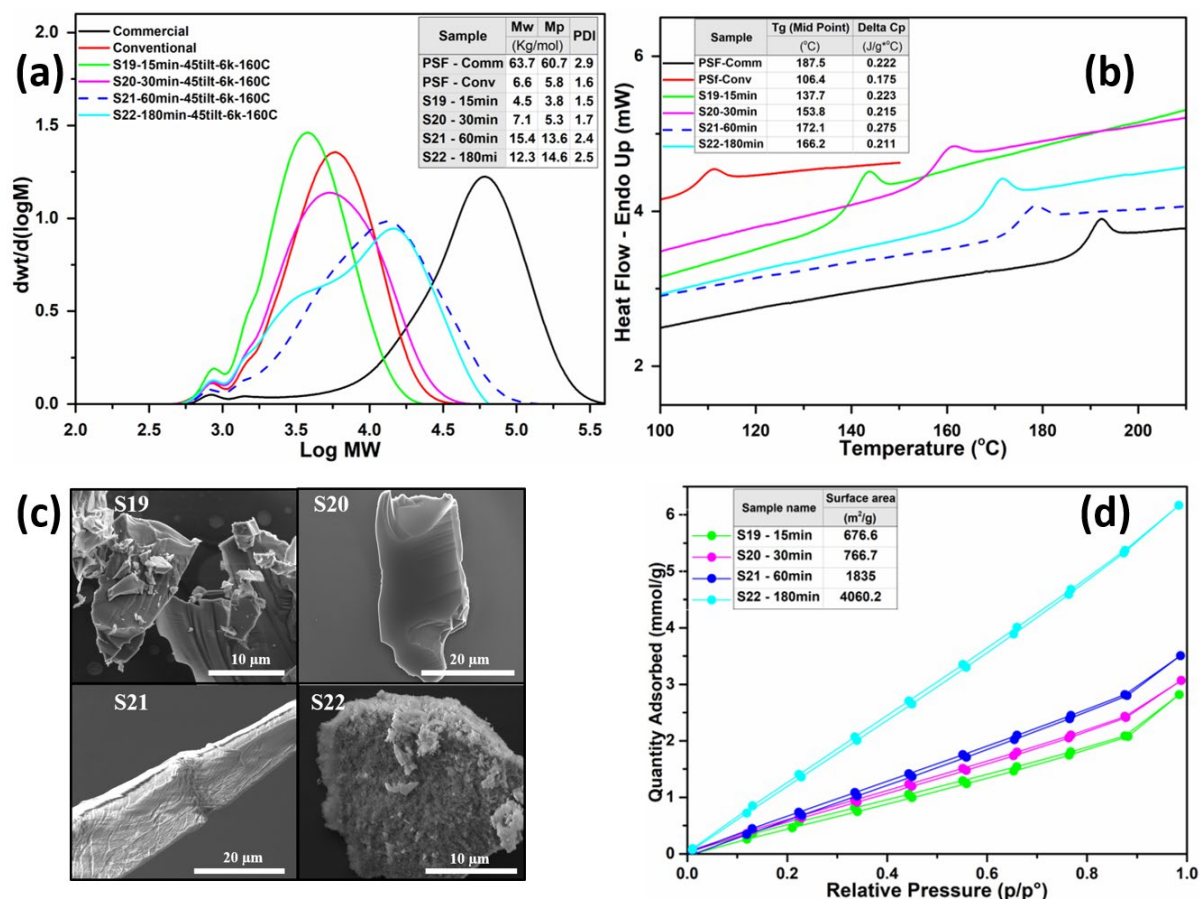


Figure 3. 6. Comparison between (a) molecular weight distribution, (b) DSC thermograms, (c) SEM images, and (d) nitrogen adsorption data for VFD synthesised PSF at different reaction times, (S19-S22, at  $\omega$  6k rpm,  $\theta$  45°, T 160 °C, and t 15, 30, 60 and 180 min), compared to commercial PSF and conventionally synthesised PSF.

A striking result for VFD processed PSF relative to conventionally prepared PSF is a significant increase in  $T_g$ , from 106 °C to 172 °C. Furthermore, the high  $T_g$  for VFD generated PSF is close to that of commercial PSF, although there is a distinct difference in  $M_w$ . This outcome in using VFD high shear and intense micromixing mediated formation of PSF shows that the microfluidic device is effective for enhancing the thermal properties of the products, as we have recently established in a parallel study on using the VFD to modify the thermal and mechanical properties of membranes of PSF [5].

### 3.4. Conclusions

We have established the utility of the VFD in the synthesis of PSF in the confined mode of operation of the microfluidic platform, as a one step process, in being able to control the molecular weight, the glass transition temperature and the morphology of the particles. This is contingent on operating the VFD and the materials and solvent under anhydrous conditions, for which the operation of the VFD is readily adaptable. The findings overcome some of the limitations of conventional bath synthesis of PSF, as well as translating a two-step process into just one step. The systematic approach used in determining the optimal conditions maps out a path forward for translating the findings into the synthesis of other polymers.

The VFD operating parameters ( $\omega$  rotational speed,  $T$  temperature,  $\theta$  tilt angle, and  $t$  time) were systematically varied with respect to their effects on the  $M_w$ ,  $T_g$ , morphology, and nitrogen adsorption capacity. The enhanced VFD synthesised PSF provided a product with  $M_w \sim 16$  kg/mol,  $T_g \sim 170$  °C with a change in the specific heat capacity,  $c_p$  0.224 J/(g\*°C). SEM imagery established a clear morphological difference in the products obtained under different conditions, with sheet-like structures formed at low temperatures, notably 120 and 140 °C, semi-spherical structures at 150 °C, globular like structures at 160 °C and fibrous structures at 170 °C. The porosity of the PSF is also dependent on the temperature of the VFD processing, with a higher surface area formed at 170 °C,  $\sim 4000$  m<sup>2</sup>/g, relative to 140 °C,  $\sim 1470$  m<sup>2</sup>/g. In addition, the morphology of the product can be altered by changing the rotational speed, which correlates with an understanding of the different topological fluid flows in the VFD [6], as does the degradation of the polymer, particularly under double helical flow, noting that the degradation is also evident for long processing times.

### 3.5. Conflicts of interest

There are no conflicts to declare.

### 3.6. Acknowledgements

The paper is dedicated to our beloved co-author, Dr. Ataollah Nosrati, who sadly passed away before submitting the manuscript. Support of this research by the Australian Research Council

and the School of Engineering, Edith Cowan University, is gratefully acknowledged, as is Microscopy Australia (MA).

### 3.7. Chapter references

1. Othmer, K., *Encyclopedia of Chemical Technology*. 1996, John Wiley & Sons: New York.
2. Johnson, R.N., et al., *Poly(aryl Ethers) by nucleophilic aromatic substitution. I. synthesis and properties*. J. Polym. Sci.: Part A-1, 1967. **5**: p. 2375-2398.
3. Igder, A., et al., *Vortex fluidic mediated synthesis of polysulfone*. RSC Adv, 2020. **10**(25): p. 14761-14767.
4. Luo, X., et al., *High-Shear-Imparted Tunable Fluorescence in Polyethylenimines*. ChemPhotoChem, 2018. **2**(4): p. 343-348.
5. Aghil Igder, et al., *Vortex fluidic mediated fabrication of polysulfone ultrafiltration membrane incorporated with graphene oxide*. Chemical Engineering Journal, (Submitted MEMSCI-D-21-00137).
6. Alharbi, T.M.D., et al., *Sub-micron moulding angled vortex fluid flow*. Chem.Rxiv, 2020: p. <https://doi.org/10.26434/chemrxiv.13141352.v1>.
7. Britton, J., Chalker, J. M. and C.L. Raston, *Rapid Vortex Fluidics: continuous flow synthesis of Amides and local anesthetic lidocaine*. Chem. Eur.J., 2015. **21**(30): p. 10660-10665. .
8. Britton, J., Dalziel, Stuart B. and C.L. Raston, *The synthesis of di-carboxylate esters using continuous flow vortex fluidics*. Green Chem., 2016. **18**(7): p. 2193-2200.
9. Al-antaki, A.H.M., et al., *Vortex Fluidic Mediated Synthesis of TiO<sub>2</sub> Nanoparticle/MXene Composites*. ChemNanoMat, 2020. **6**(4): p. 657-662.
10. Al-antaki, A.H.M., W.D. Lawrance, and C.L. Raston, *Dynamic thin film mediated slicing of boron nitride nanotubes*. Nanoscale Adv, 2019. **1**(12): p. 4722-4728.
11. Pye, S.J., et al., *Organic oxidations promoted in vortex driven thin films under continuous flow*. Green Chem, 2018. **20**(1): p. 118-124.
12. Luo, X., et al., *Vortex Fluidic-Mediated Fabrication of Fast Gelated Silica Hydrogels with Embedded Laccase Nanoflowers for Real-Time Biosensing under Flow*. ACS Appl Mater Interfaces, 2020. **12**(46): p. 51999-52007.
13. Chen, X., J.F. Dobson, and C.L. Raston, *Vortex fluidic exfoliation of graphite and boron nitride*. ChemComm., 2012. **48**(31): p. 3703-3705.
14. Yasmin, L., Chen, X., Stubbs, K. A., and C.L. Raston, *Optimising a vortex fluidic device for controlling chemical reactivity and selectivity*. Sci. Rep., 2013. **3**: p. 2282.
15. Gandy, M.N., C.L. Raston, and K.A. Stubbs, *Towards aryl C-N bond formation in dynamic thin films*. Org. Biomol. Chem., 2014. **12**(26): p. 4594-4597.

16. Jamshidi Gohari, R., Halakoo, E., Nazri, N. A. M., Lau, W. J., Matsuura, T. and A.F. Ismail, *Improving performance and antifouling capability of PES UF membranes via blending with highly hydrophilic hydrous manganese dioxide nanoparticles*. Desalination, 2014. **335**(1): p. 87-95.
17. Zhao, S., Yan, W., Shi, M., Wang, Z., Wang, J. and S. Wang, *Improving permeability and antifouling performance of polyethersulfone ultrafiltration membrane by incorporation of ZnO-DMF dispersion containing nano-ZnO and polyvinylpyrrolidone*. Journal of Membrane Science, 2015. **478**: p. 105-116.
18. Safarpour, M., Vatanpour, V. and A. Khataee, *Preparation and characterization of graphene oxide/TiO<sub>2</sub> blended PES nanofiltration membrane with improved antifouling and separation performance*. Desalination, 2016. **393**: p. 65-78.
19. Wang, J., et al., *Graphene Oxide as an Effective Barrier on a Porous Nanofibrous Membrane for Water Treatment*. ACS Appl Mater Interfaces, 2016. **8**(9): p. 6211-6218.
20. Yin, J., Zhu, G. and B. Deng, *Graphene oxide (GO) enhanced polyamide (PA) thin-film nanocomposite (TFN) membrane for water purification*. Desalination, 2016. **379**: p. 93-101.
21. Zargar, M., B. Jin, and S. Dai, *An integrated statistic and systematic approach to study correlation of synthesis condition and desalination performance of thin film composite membranes*. Desalination, 2016. **394**: p. 138-147.
22. Ravishankar, H., J. Christy, and V. Jegatheesan, *Graphene Oxide (GO)-Blended Polysulfone (PSf) Ultrafiltration Membranes for Lead Ion Rejection*. Membranes (Basel), 2018. **8**(3).
23. Saldivar G, E. and E. Vivaldo L, *Handbook of polymer Synthesis, characterization, and processing*. 2013, Hoboken, New Jersey: John Wiley & Sons, Inc. 653.
24. A. Dieter S., C.J.H. and J. S., *Synthesis of polymers, new structures and methods*. Vol. 1. 2011, Wiley-VCH Verlag GmbH & Co. KGaA. 1203.
25. Saldivar-Guerra, E. and E. Vivaldo-Lima, *Handbook of Polymer Synthesis, Characterization, and Processing*. 2013, New Jersey: Wiley. 653.
26. Xie, Y., et al., *Synthesis of highly porous poly(tert-butyl acrylate)-b-polysulfone-b-poly(tert-butyl acrylate) asymmetric membranes*. Polymer Chemistry, 2016. **7**(18): p. 3076-3089.
27. McKeown, N.B. and P.M. Budd, *Polymers of intrinsic microporosity (PIMs): organic materials for membrane separations, heterogeneous catalysis and hydrogen storage*. Chem Soc Rev, 2006. **35**(8): p. 675-83.
28. McDermott, A.G., et al., *Structural Characterization of a Polymer of Intrinsic Microporosity: X-ray Scattering with Interpretation Enhanced by Molecular Dynamics Simulations*. Macromolecules, 2011. **44**(1): p. 14-16.
29. Bae, Y.S., A.O. Yazaydin, and R.Q. Snurr, *Evaluation of the BET method for determining surface areas of MOFs and zeolites that contain ultra-micropores*. Langmuir, 2010. **26**(8): p. 5475-83.



30. Hart, K.E., L.J. Abbott, and C.M. Colina, *Analysis of force fields and BET theory for polymers of intrinsic microporosity*. Molecular Simulation, 2013. **39**(5): p. 397-404.
31. Heuchel, M., et al., *Atomistic packing model and free volume distribution of a polymer with intrinsic microporosity (PIM-1)*. Journal of Membrane Science, 2008. **318**(1-2): p. 84-99.
32. Spalla, O., *General theorems in small-angle scattering*, in *Neutrons, X-rays, and light: scattering methods applied to soft condensed matter*, Lindner, P.; Zemb, T., Eds. Elsevier, 2004. p. 49-71.
33. Yi, Z., et al., *A New Insight into Growth Mechanism and Kinetics of Mesoporous Silica Nanoparticles by in Situ Small Angle X-ray Scattering*. Langmuir, 2015. **31**(30): p. 8478-87.
34. Yun, S.I., *Solution properties of 1, 3-cyclohexadiene polymers by laser light scattering and small-angle neutron scattering*. Macromolecules, 2006. **39**(2): p. 897.
35. Jacquin, M., *Chemical analysis and aqueous solution properties of charged amphiphilic block copolymers PBA-b-PAA synthesized by MADIX®*. Journal of Colloid and Interface Science, 2007. **316**(2): p. 897.
36. Wanakule, N.S., *Characterization of micron-sized periodic structures in multicomponent polymer blends by ultra-small-angle neutron scattering and optical microscopy*. Macromolecules, 2008. **41**(2): p. 471.
37. Yun, S.I., *Conformation of arborescent polymers in solution by small-angle neutron scattering: Segment density and core shell morphology*. Macromolecules, 2008. **41**(1): p. 175.
38. Agrawal, S.K., *Structural Characterization of PLA PEO PLA Solutions and Hydrogels: Crystalline vs Amorphous PLA Domains*. Macromolecules, 2008. **41**(5): p. 1774.
39. Sen, S., et al., *Chain conformations and bound-layer correlations in polymer nanocomposites*. Phys Rev Lett, 2007. **98**(12): p. 128302.
40. Zhao, Y., et al., *Elucidation of the morphology of the hydrocarbon multi-block copolymer electrolyte membranes for proton exchange fuel cells*. Polymer, 2016. **86**: p. 157-167.
41. Kumar, M., et al., *Quaternized polysulfone and graphene oxide nanosheet derived low fouling novel positively charged hybrid ultrafiltration membranes for protein separation*. RSC Adv., 2015. **5**(63): p. 51208-51219.
42. Kibechu, R.W., et al., *Effect of incorporating graphene oxide and surface imprinting on polysulfone membranes on flux, hydrophilicity and rejection of salt and polycyclic aromatic hydrocarbons from water*. Phys. Chem. Earth Part A/B/C,, 2017. **100**: p. 126-134.
43. Yang, L., et al., *Star Shaped Long Chain Branched Poly (lactic acid) Prepared by Melt Transesterification with Trimethylolpropane Triacrylate and Nano-ZnO*. Polymers (Basel), 2018. **10**(7).



## **Chapter 4**

### **Vortex fluidic mediated fabrication of polysulfone ultrafiltration membranes incorporating graphene oxide†**

Chapter 4 is not available in this version of the thesis

## Chapter 5

### General discussion

The main aim of this chapter is to integrate the research outcomes to provide an overall picture in this area. To do that, this chapter will not only establish connections among the chapters but will also address the research questions presented in Chapter 1.

The first research question in this study was mainly about introducing the VFD and its application in different fields and specifically the possibility of using this platform in synthesising PSF as a common polymer in membrane fabrication. This involved a two-step polycondensation reaction as a nucleophilic substitution route which has been elaborated in chapter 2 involving pre-prepared DiNa salt of BPA and DCDPS. The two-step polymerisation was conducted using both the VFD and conventional [1] methods for comparing the properties of the different synthesised PSFs with respect to their  $M_w$ ,  $T_g$ , and reactions yields. In this chapter the intermediate DiNa salt of BPA was prepared and used in the synthesis of the PSF with the product characterised for each step using FTIR and NMR spectroscopy. NMR analysis clearly confirmed the successful production of DiNa salt of BPA as the intermediate product obtained from the first step in the VFD.  $^1\text{H}$ -NMR of BPA in DMSO- $d_6$  (Figure 2. 1-a) confirmed peaks at  $\sim 1.53$  and  $9.13$  ppm, assigned to the aliphatic protons and hydroxyl groups, respectively, with the later removed on reacting with base in forming DiNa salt of BPA. There were also peaks at  $\sim 6.97$  and  $6.64$  ppm corresponding to the aromatic protons of BPA (Figure 1-b) with changes in the  $^1\text{H}$ -NMR spectra [2] consistent with the formation of the DiNa salt (Figure 2. 1-a) as well as the removal of water from the reaction mixture in the VFD as has been reported for the continuous flow synthesis of di-carboxylate esters synthesis [3].  $^1\text{H}$  and  $^{13}\text{C}$  NMR of VFD synthesized PSF at the optimised VFD condition, matched the corresponding spectra for PSF [4]. To answer the second research question on the effect of operational parameters on the VFD products, VFD operational conditions (rotational speed ( $\omega$ ), temperature ( $T$ ), tilt angle ( $\theta$ ) and processing time ( $t$ )) were systematically investigated, Figure 2. 2, in comparing the main properties of the synthesised PSF using GPC, DSC, and TGA. The products synthesised in the optimised VFD conditions have a higher  $M_w$  and  $T_g$  of  $\sim 10$  kg/mol and  $\sim 154$  °C respectively, relative to that of the polymer prepared using conventional

batch processing, of 6 kg/mol and 106 °C, respectively. Recognising a trade-off between increasing the temperature/processing time and the  $M_w$  and yield of the process, the optimised VFD conditions could be identified based on the importance of the  $M_w$  of the final product or the yield of the reaction.

To further ascertain the aforementioned trade-off between the main operational parameters using in the VFD, research was continued to address the third research question in chapter 3, with an enhanced polymerisation approach resulting in improved PSF in terms of  $M_w$ . In this approach, a one-step VFD mediated PSF polymerisation in a more scrupulously anhydrous condition was conducted under high shear in the VFD operating in the confined mode. In this chapter, VFD synthesised PSF was prepared in just a single step synthesis reaction between the solid starting materials in triple distilled DMSO, thereby avoiding the use of aqueous base and chlorinated solvents, unlike in conventional batch processing in synthesising the PSF [1]. To provide the base needed for the reaction, dry crushed NaOH pellets were used to avoid hydrolysis of DCDPS. The water content in the reaction mixture was minimised by purging with nitrogen gas with the oven dried quartz tube flame heated prior to use.  $^1\text{H}$  NMR of the VFD mediated processing confirmed the formation of PSF with the doublets assigned to phenol groups and peak at  $\delta = 1.69$  ppm assigned to the methyl group (Figure 3. 2-b). The smaller peaks close to the main peaks confirmed the terminal groups of the polymer in the aromatic and aliphatic regions. The effects of operational parameters of the VFD ( $\omega$ ,  $\theta$ ,  $T$ , and  $t$ ) were investigated systematically, varying them with respect to  $M_w$  and  $T_g$  of the PSF, followed by further characterising of the product using FTIR, SEM and BET. GPC curves and heat flow thermograms presented in Figure 3. 3-a and b, established the highest  $M_w$  and  $T_g$  to be at 6k rpm rotational speed. As the VFD was effective in slicing polyethylenimines [5] at higher rotational speeds, 7k and 8k rpm, VFD processing in the present study is likely to lead to polymer breakdown, which was confirmed by a reduction in  $M_w$ , and an increase in the surface area in smaller particles at 8k rpm, Figure 3. 3-a and d. Increase in the surface area of the as prepared polymer at higher  $\omega$  corresponds to the effect of double helical topological flow produced at such speeds [6]. The morphology of the product changes from sheet-like structures at lower rotational speeds to needle-like structures formed at higher  $\omega$ , 8k rpm, Figure 3. 3-c, and are associated with breakdown of the polymer at higher rotational speeds.

The formation of needle-like structures at higher  $\omega$ , Figure 3. 3-c, and rods at higher temperature, Figure 3. 4-c, are consistent with the presence of high shear within the confines of the double helical flow generated by Coriolis twisted eddies from Faraday waves at  $\theta$  45°. This similarity showed the presence of heat and transfer at the glass liquid interface in the VFD rotating tubes even at temperatures lower than 170 °C [6], although the effect of higher temperature resulted in a clearer formation of rods in a fibrous structure with their diameter mainly between ca ~70 and 200 nm which correlates with the diameter of rods of fullerene C<sub>60</sub> as a VFD mediated shear stress induced crystallisation process [6]. The BET measurements, Figure 3. 4-d, show a dramatic increase in the surface area of the fibrous samples produced at higher temperature, 170 °C, with that of ~ 3956 m<sup>2</sup>/g, compared to ~ 1472 m<sup>2</sup>/g for those sheet-like prepared at lower temperature, 140 °C. Results in Figure 3. 4-a and b, established the formation of higher M<sub>w</sub> PSF at higher temperatures, 160 and 170 °C, as was concluded from our previous research in the second chapter, but with a similar yield of the reactions, ~ 67% and 64% at 160 and 170 °C respectively, as opposed to those of 61% and 19.4% in chapter 2, Figure 2. 2-b. Although the growth of the higher M<sub>w</sub> polymers took place at higher temperatures, in the MWD curve of PSF formed at 170 °C a shoulder was detected in the smaller M<sub>w</sub> region, Figure 3. 4-a, which disappeared for the polymer formed at lower temperatures, which corresponds to polymer chain degradation [7]. Investigating the effect of tilt angle and time on high shear synthesis of PSF revealed dramatic changes in morphology relative to  $\theta$ , with semi-flat surfaces for  $\theta \geq 30^\circ$  and irregular porous-like structures at  $\theta \leq 30^\circ$ , Figure 3. 5-c, as well as sheet-like structures for shorter reaction times  $\leq 30$  min, bulk structures for 60 min processing, and a combination of needle-like and sheet-like structures for 180 min, Figure 3. 6-c. These results supported by the increased surface area in more porous and needle-like structures could be related to differences in specific topological fluidic flow in the VFD [6]. For instance, a higher surface area was revealed for product formed during longer processing time, can be attributed to the higher intrinsic porosity resulting from longer topological fluid flow effect [6, 8], with ~ 4060 m<sup>2</sup>/g surface area at 180 min compared to ~ 677 m<sup>2</sup>/g for sheet-like products formed during 15 min processing time, Figure 3. 6-d. Overall, the products synthesised in this chapter under more scrupulously anhydrous conditions resulted higher M<sub>w</sub>, T<sub>g</sub> and yields, which could be attributed to minimising DCDPS hydrolysis otherwise associated with water being present.

Taking the advantage of the high shear processing of PSF synthesis under anhydrous conditions presented in this chapter showed a dramatic reduction in deviation of reaction yields, resulting in them all being in the range  $\sim 64\pm 4\%$  which varied between  $\sim 19\%$  to  $\sim 60\%$  in product yield as synthesised in chapter 2.

Furthermore, in chapter 4, to investigate the application of the VFD in fabricating UF membranes from PSF, and addressing the fourth research question, a series of continuous flow micro-mixing processes under high shear in the VFD were conducted followed by phase inversion of the cast solution. Mixing time and type, temperature, polymer concentrations, solvent type, coagulant, additive type and concentrations are amongst various important operational parameters in membrane fabrication [9-16]. The effect of polymer concentrations, mixing time and type, and VFD rotational speed on the structure of the UF membranes and filtration performance were investigated and compared with those for conventional processed membranes in this chapter. Fabricated UF membranes were morphologically evaluated and compared to conventional mixed (24 h magnet stirrer at 50 °C, and 3 h sonication at UFM0) with those fabricated from 10 %, 15 %, and 20 % PSF solution (UFM1-3) using VFD mixing ( $\omega$  6000 rpm, 30 °C,  $\theta$  45°, and 0.5 mL/min flow rate, Figure 4. 3. The required mixing times for VFD processing were significantly shorter compare to conventional mixing, being reduced from  $> 24$  h to  $< 4$  h. Uniform finger-like pores along the thickness of 10 % PSF membrane (Figure 4. 3-b) with an open porous structure at the bottom of the membrane, and sponge-like structure with macro-voids on the bottom of the membranes fabricated from 15 % and 20 % PSF membranes (Figure 4. 3-b, c and d) were observed. A denser structure with smaller pores on the membranes from higher concentrated solutions showed a good agreement with the literature in conventional mixing processes [9, 10]. Higher viscosity of 20% PSF solution resulted in some defects on the surface of the membrane, due to the presence of persistent bubbles before casting [11], thus 15% PSF solution was used as the optimal concentration for the rest of the experiments which was in accordance with the published works [9].

Apart from the shortening the preparation process from over 24 h in conventional mixing to less than 4 h in the VFD mixing, by taking the advantage of high shear in the VFD, the higher rotational speed, with the optimal value of 7k rpm, provided; shorter finger-like sections at

the top of the membrane, denser sponge section at the bottom of the membranes, smaller pore sizes, higher porosity, higher Young's modulus and mechanical stability, and better salt/BSA rejection performance, Figures 4. 3-5. The higher permeability of membranes derived from VFD processing,  $\sim 97$ -106 LMH/bar, compared to that of membranes prepared using conventional mixing,  $\sim 86$  LMH/bar, could be attributed to the topological fluid flow under high shear and intensive micromixing [6] which resulted in decreasing the pore sizes and consequently increasing the porosity and surface areas of the membranes. Moreover, increasing the rotational speeds could result in generating higher shear within dynamic thin films in the inclined rapidly rotating VFD tube [8, 17], and consequently increasing the water-flux permeability up to 106 LMH/bar at 7k rpm. At  $\omega > 7$  k rpm. The intensive micromixing could result in reducing the pore sizes and finally resulting in some blockages in the porous media of the membranes as was clearly established in SEM images and presented in the pore size diagram. This resulted in a decrease in porosity at  $\omega$  higher than 7k rpm which is in agreement with the topological fluid flow identified in earlier research [6], and in chapter 3.

The fifth research question was specifically about the application of the VFD in continuously mixing GO in polymer matrix and fabricating enhanced composite UF membranes which addressed in the second part of chapter 4. GO was successfully incorporated into PSF matrices using both VFD and conventional mixing prior to the phase inversion process to enhance the properties of the fabricated UF membranes. The broad band from  $\sim 2900$  to  $\sim 3700$   $\text{cm}^{-1}$  in FTIR spectra, Figure 4. 2-a, is attributed to the O–H stretch of surface functional groups or water adsorbed on the GO layers. Incorporation of GO into the membrane under continuous VFD mixing was confirmed using FTIR with bands at 1660 to 1700  $\text{cm}^{-1}$  in the GO/PSF composite assigned to  $\text{C=O}$  membrane [18, 19]. This was also confirmed with the 2 peaks in Raman spectra of GO/PSF composites, Figure 4. 2-b, at 1328 and 1584  $\text{m}^{-1}$ , assigned as the relative D and G bands in GO [12, 19-21]. Further confirmation of the successful GO incorporation into the PSF matrix was identified with the distinct GO peak at  $2\theta \sim 12.8^\circ$  in the powder diffraction data for GO/PSF UF composites, as evident in Figure 4. 2-c. Incorporating GO into the composites resulted in increasing the hydrophilicity of the membranes by decreasing the water contact angle from  $\sim 75^\circ$  in pristine PSF membranes to  $\sim 62^\circ$  for a composite membrane with 2 wt. % loading of GO, in accordance with previous studies [16,

[22](#), [23](#)]. Playing a prominent role in solvent/non-solvent exchange during phase inversion [[23](#)], GO incorporation into the PSF membranes significantly changed the morphology of the composite cross-sections, producing larger pores and macro-voids attributed to the higher GO content, Figure 4. 3-j-n. The unique structure of layers of GO provided a pathway for diffusion of water, with a significant water flux increase as the GO loading increases, Figure 4. 4-b and d. There is a uniform dispersion of GO into the polymer matrix up to 1 wt. % with no visible agglomerates of the 2D-material, (Figure 4. 3-j-l), with an increase in porosity, pore size, permeability and salt/BSA rejection performances were detected. However, in further increasing the GO content a dramatic decrease of the abovementioned characteristics occurred due to agglomeration of the GO and possibly blocking the pores with excess GO and forming smaller pores and slowing down the de-mixing by blocking available pathways as evident in the SEM image in Figure 4. 3-m.

Comparing the VFD composite membranes at optimal conditions (UFM11, 1 wt. % GO content at 5k rpm, 0.5 mL/min, overall < 4 h) with conventional processing for GO/PSF composite membranes (UFM13, 1 wt. % GO content, 24 h magnet stirring, 3 h degassing), confirmed a higher porosity ( $86.6 \pm 1.7\%$ ) and water permeability ( $122.9 \pm 3.9$  LMH/bar) in VFD processed composite membranes, Figure 4. 4-d. This increase from the conventional processed membranes to  $80.2 \pm 2.2\%$ ,  $108.5 \pm 3.5$  LMH/bar relates to the high shear and unique topological fluid flows in the microfluidic platform at a tilt angle of  $45^\circ$  [[6](#)]. In accordance with the literature [[15](#), [22](#), [23](#)], the higher permeability of the VFD composite membranes ( $\sim 102$ - $123$  LMH/bar) relative to pristine PSF membranes ( $\sim 97$ - $106$  LMH/bar) confirmed the well dispersed GO in PSF. The higher permeability and rejection performance for VFD composites (UFM9-13) relative to those of conventional processed composite (UFM13), arising from high shear and intense micromixing in the VFD relative to conventional mixing, creating a more uniform solution and an higher dispersity of GO in the polymer matrix. Investigating the effect of GO incorporation into the polymer matrix resulted in a higher rejection performance in the composite membranes compared to the pristine PSF membrane with the NaCl rejection from  $18.5 \pm 1.3$  to  $34.3 \pm 1.7\%$ , and bovine serum albumin (BSA) rejection from  $53.8 \pm 2.0$  to  $74.2 \pm 2.0\%$ , respectively, Figure 4. 4-d.

GO loading in the polymer matrix also resulted in increasing the mechanical and thermal properties of the membranes [23], Figure 4. 5. This was highlighted with a Young's modulus of  $\sim 137.2 \pm 12.1$  MPa at UFM11 for 1 wt. % GO content, compared to the pristine PSF membrane at UFM5  $\sim 106.6 \pm 4.8$  MPa (both in the same operational conditions), as well as a lower mass loss ( $\sim 58$  to  $\sim 68\%$ ) in GO integrated membranes (UFM9-12), compared to the pristine PSF membrane (UFM0) with that of  $\sim 72\%$ . In addition, the Young's modulus of VFD processed composite (UFM11) compared to the conventional processed composite (UFM13), with the same GO content (1 wt. %), revealed higher mechanical stabilities in the VFD products which arises from the high shear and intensive micromixing of the VFD platform.



## 5.1. Chapter references

1. Johnson, R.N., et al., *Poly(ary1 Ethers) by nucleophilic aromatic substitution. I. synthesis and properties*. J. Polym. Sci.: Part A-1, 1967. **5**: p. 2375-2398.
2. Fulmer, G.R., et al., *NMR Chemical Shifts of Trace Impurities: Common Laboratory Solvents, Organics, and Gases in Deuterated Solvents Relevant to the Organometallic Chemist*. Organometallics, 2010. **29**(9): p. 2176-2179.
3. Britton, J., Dalziel, Stuart B. and C.L. Raston, *The synthesis of di-carboxylate esters using continuous flow vortex fluidics*. Green Chem., 2016. **18**(7): p. 2193-2200.
4. Xie, Y., et al., *Synthesis of highly porous poly(tert-butyl acrylate)-b-polysulfone-b-poly(tert-butyl acrylate) asymmetric membranes*. Polymer Chemistry, 2016. **7**(18): p. 3076-3089.
5. Luo, X., et al., *High-Shear-Imparted Tunable Fluorescence in Polyethylenimines*. ChemPhotoChem, 2018. **2**(4): p. 343-348.
6. Alharbi, T.M.D., et al., *Sub-micron moulding angled vortex fluid flow*. Chem.Rxiv, 2020: p. <https://doi.org/10.26434/chemrxiv.13141352.v1>.
7. Yang, L., et al., *Star Shaped Long Chain Branched Poly (lactic acid) Prepared by Melt Transesterification with Trimethylolpropane Triacrylate and Nano-ZnO*. Polymers (Basel), 2018. **10**(7).
8. Britton, J., Chalker, J. M. and C.L. Raston, *Rapid Vortex Fluidics: continuous flow synthesis of Amides and local anesthetic lidocaine*. Chem. Eur.J., 2015. **21**(30): p. 10660-10665.
9. Zargar, M., B. Jin, and S. Dai, *An integrated statistic and systematic approach to study correlation of synthesis condition and desalination performance of thin film composite membranes*. Desalination, 2016. **394**: p. 138-147.
10. Zinadini, S., et al., *Preparation and characterization of antifouling graphene oxide/polyethersulfone ultrafiltration membrane: Application in MBR for dairy wastewater treatment*. J. Water Process Eng. , 2015. **7**: p. 280-294.
11. Bhamidipati, K.L., *Detection and elimination of defects during manufacture of high-temperature polymer electrolyte membranes*, in Georgia Institute of Technology. 2011. p. 260.
12. Li, J., et al., *Improved water permeability and structural stability in a polysulfone-grafted graphene oxide composite membrane used for dye separation*. J. Membr. Sci. , 2020. **595**: p. 117547.
13. Shen, Z., et al., *Fabrication of a Novel Antifouling Polysulfone Membrane with in Situ Embedment of Mxene Nanosheets*. Int. J. Environ. Res. Public Health, 2019. **16**(23): p. 4659.
14. Ravishankar, H., J. Christy, and V. Jegatheesan, *Graphene Oxide (GO)-Blended Polysulfone (PSf) Ultrafiltration Membranes for Lead Ion Rejection*. Membranes (Basel), 2018. **8**(3).

15. Abdel-Karim, A., et al., *High flux and fouling resistant flat sheet polyethersulfone membranes incorporated with graphene oxide for ultrafiltration applications*. Chem. Eng. J., 2018. **334**: p. 789-799.
16. Safarpour, M., Vatanpour, V. and A. Khataee, *Preparation and characterization of graphene oxide/TiO<sub>2</sub> blended PES nanofiltration membrane with improved antifouling and separation performance*. Desalination, 2016. **393**: p. 65-78.
17. Igder, A., et al., *Vortex fluidic mediated synthesis of polysulfone*. RSC Adv., 2020. **10**(25): p. 14761-14767.
18. Kumar, M., et al., *Quaternized polysulfone and graphene oxide nanosheet derived low fouling novel positively charged hybrid ultrafiltration membranes for protein separation*. RSC Adv., 2015. **5**(63): p. 51208-51219.
19. Kibechu, R.W., et al., *Effect of incorporating graphene oxide and surface imprinting on polysulfone membranes on flux, hydrophilicity and rejection of salt and polycyclic aromatic hydrocarbons from water*. Phys. Chem. Earth Part A/B/C,, 2017. **100**: p. 126-134.
20. Lee, J., et al., *Graphene oxide nanoplatelets composite membrane with hydrophilic and antifouling properties for wastewater treatment*. J. Membr. Sci., 2013. **448**: p. 223-230.
21. Kang, Y., et al., *Novel sulfonated graphene oxide incorporated polysulfone nanocomposite membranes for enhanced-performance in ultrafiltration process*. Chemosphere, 2018. **207**: p. 581-589.
22. Jiang, Y., et al., *Graphene oxides as nanofillers in polysulfone ultrafiltration membranes: Shape matters*. J. Membr. Sci. , 2019. **581**: p. 453-461.
23. Ionita, M., et al., *Improving the thermal and mechanical properties of polysulfone by incorporation of graphene oxide*. Composites, Part B,, 2014. **59**: p. 133-139.

## Chapter 6

### Conclusions and future work recommendations

This chapter integrates the findings of all chapters and offers suggestions for possible future research.

#### 6.1. Conclusions

This thesis mainly focused on the application of the VFD in polymer synthesis and UF membrane fabrication. In the second chapter, the possibility of synthesising PSF as a common polymer in UF membranes using the VFD was investigated, followed by enhancing the properties of the VFD synthesised PSF under anhydrous conditions in the third chapter. Finally, in the fourth chapter, the VFD mediated PSF and GO/PSF UF membranes were fabricated and their main properties and rejection performances were compared with the conventional processed membranes. The following conclusions were derived from the analysis of the synthesised polymers and fabricated membranes:

- PSF synthesis was conducted in a two-step polycondensation reaction between BPA, 50% NaOH aqueous solution and DCDPS using the VFD and conventional nucleophilic substitution route, and the main properties of the synthesised PSF were investigated while systematically exploring the operating parameters of the VFD, including rotational speed, processing time, tilt angle of the tube, and temperature.
- $^1\text{H}$ -NMR spectra showed the removal of hydroxyl groups on forming the DiNa salt of BPA obtained in the first step in the VFD. This was confirmed with the loss of  $-\text{OH}$  stretching bands in the FTIR spectra of the DiNa salt, and is associated with water dissipation in the VFD as a high mass transfer process.
- The optimised VFD operational conditions were  $T$  170°C,  $\omega$  6000 rpm,  $\theta$  45° and  $t$  30 min, which afforded  $M_w \sim 12000$  g/mol,  $T_g$  168°C and decomposition temperature  $\sim 530^\circ\text{C}$ . A lower yield of 18% at 170 °C resulted in choosing 160 °C as the optimal temperature which afforded  $M_w \sim 7000$  g/mol,  $T_g \sim 154^\circ\text{C}$ , and  $\sim 64\%$  yield in a 30 min reaction and  $M_w \sim$

10000 g/mol,  $T_g \sim 158^\circ\text{C}$ , and  $\sim 30\%$  yield in a 60 min reaction. Results presented in this chapter defined a trade-off between the yield and  $M_w$  and reaction time.

- The reduction in reaction yield in longer processing time may attribute to the shear stress arises from the fluid flow in the VFD resulting in bond cleavage and the polymer chain length reduction.
- PSF synthesis was modified in using the VFD, by translating a two-step process into just one step process under scrupulously anhydrous condition, for the VFD operating in confined mode, in DMSO, thereby avoiding the use of aqueous base and chlorinated solvents.
- A systematic approach was used to determine the optimal conditions for the synthesis of PSF mapping out a path forward for translating the findings into the synthesis of other polymers.
- The VFD operating parameters were systematically varied with respect to their effects on the  $M_w$ ,  $T_g$ , morphology, and surface area of the polymer.
- The enhanced VFD synthesised PSF provided a product with  $M_w \sim 16 \text{ kg/mol}$ ,  $T_g \sim 170^\circ\text{C}$  with a change in the specific heat capacity,  $c_p 0.224 \text{ J/(g}^\circ\text{C)}$ , at  $\omega 6 \text{ k rpm}$ ,  $T 160^\circ\text{C}$  and  $\theta 45^\circ$  during a 60 min processing time, with an overall  $\sim 65\%$  reaction yield.
- As opposed to the two-step reaction, the yield did not significantly change on extending the processing time, being  $\sim 65 \pm 4\%$  under such scrupulously anhydrous conditions. However, the  $M_w$  and  $T_g$  of the products were significantly affected by changing the reaction time, with an increase in  $M_w$  and  $T_g$  while increasing the process up to 60 min with a gradually decrease thereafter. The degradation is also evident for long processing times and arises from the different topological fluid flows particularly double helical flow in the VFD.
- A clear morphological difference was established in the SEM images of the products synthesised under different conditions. Temperature as a main parameter in PSF synthesis resulted in sheet-like structures formed at  $120^\circ\text{C}$  and  $140^\circ\text{C}$ , semi-spherical structures at  $150^\circ\text{C}$ , globular like structures at  $160^\circ\text{C}$  and fibrous structures at  $170^\circ\text{C}$ .

- The porosity of the PSF is also dependent on the operational conditions, specifically temperature of the process, with a higher surface area of the product synthesised at 170 °C, ~4000 m<sup>2</sup>/g, relative to 140 °C, ~1470 m<sup>2</sup>/g.
- Continuous flow micro-mixing under high shear in the VFD involved investigating the effect of PSF concentrations (10, 15, and 20%), as well as rotational speed of the VFD on the properties of the PSF UF membrane. GO incorporation into the PSF membrane also was investigated with respect to the effect of GO concentration in a VFD mixing process prior to the phase inversion.
- VFD processing showed a significant effect on both types (PSF and GO/PSF) of the UF membranes by (i) shortening the mixing time relative to conventional mixing, ca 4h versus ca 24h, concurrently (ii) enhancing the properties of the membranes for filtration purposes.
- More sponge-like membranes fabricated from the highest PSF concentration (20%) presented a higher mechanical stability (Young's modulus ~ 190 MPa).
- Changing the shear stress fluid flow and dimensions of the topological fluid flow in the higher rotational speed VFD mixing resulted in smaller pore size and higher porosity, permeability, and Young's modulus of the membranes with the optimal values at 7k rpm for pristine PSF and 5k rpm for GO/PSF composite membranes.
- VFD mixing at 7k rpm afforded a 22% increase in porosity and permeability relative to the control experiment using conventional mixing.
- Moreover, it was established using SEM imagery that higher rotational speeds resulted in more sponge-like structures relative to the membranes formed from the lower rotational speeds provided longer finger-like section in the structure of the membranes.
- The different topological fluid flow also resulted in a slight decrease in porosity, permeability, and rejection performance in membranes of solutions prepared at 8k relative to 7k rpm, by some pore blockage at 8k rpm.
- Hydrophilicity of the GO/PSF composite membranes gradually increased with the highest being for the composites with 2 wt.% of GO and a water contact angle of 62° relative to

that of 75° in pristine PSF. However, the optimal Go loading was adjusted at 1 wt.% because of the negative impact of excess GO content resulting in higher viscosity of the cast solution and the inherent difficulty in uniformly dispersing the GO, which could result in reduced permeability, porosity and mechanical stability.

- Increasing GO content from nil to 1 wt. %, resulted in a significant increase in BSA rejection at 3 bar, from  $53.8 \pm 2.0$  % to  $74.2 \pm 2.0$  % associated with increasing the repulsion between composite membranes and BSA.
- Comparing the BSA rejection performance of membranes showed that the VFD mixed composite membrane with 1 wt. % GO content resulted in higher BSA rejection (~ 74%) relative to the conventional mixed composite membrane with the same GO content (~ 65%). This is attributed to the effect of the unique high shear fluid flow in the VFD, impacting the performance of UF membranes.
- Finally, in comparison with the pristine PSF membrane, enhanced GO/PSF composite membranes loaded with 1 wt.% GO through VFD mixing, improved the permeability, salt, and BPA rejection from  $(97.3 \pm 3.3)$  to  $(123 \pm 3.9)$  LMH/bar,  $(18.5 \pm 1.3)$  to  $(34.3 \pm 1.7)$  %, and  $(53.8 \pm 2.0)$  to  $(74.2 \pm 2.0)$  %, respectively.

## 6.2. Future research directions

Recommendations for future research directions include:

- The systematic approach used in determining the optimal conditions maps out a path forward for translating the findings into the synthesis of other polymers via VFD in the confined or continuous mode of operation of the device.
- To fully investigate the effect of different operational parameters on the properties of the synthesised polymers or fabricated membranes, with respect to the effect of interaction between different variables, mathematical and statistical methods for modelling and analysing the processes have significant research potential. For instance, response surface methodology (RSM) has potential for designing of experiments (DOE).
- Although the continuous PSF synthesis was not successful in our attempts, due to clogging of the jet feeds and delivering the solid materials in the VFD tube, there are other polymers that can be synthesised in a more straight forward procedure which can be investigated for developing faster and greener processing for uptake by industry.
- A very hot topic well aligned with the direction of this research could be fabricating the VFD processed membranes from the VFD synthesised polymers with high MW (PSF, PESF, PVDF,...) and comparing them with the VFD membranes fabricated from the conventional synthesised polymers.
- Given that different morphologies of PSF have been obtained using the VFD, under different conditions, specific topological fluid flow in the VFD could result in producing selective morphologies of the polymers, for instance, in producing fibrous polymers which could have potential in different applications .
- Electrospinning is popular for fabricating membranes based on fibrous structures and these can be compared with the membranes fabricated using the VFD, thereby exploring the effectiveness of the topological fluid flow in the VFD in producing fibrous materials.
- Investigating the antifouling properties of the VFD processed membranes compared to the conventional processed membranes is potentially important, given that the high shear stress and micro-mixing in the VFD result in smaller pore size with increased porosity.

- In addition to incorporating GO into the polymer matrix, other additives such as silica, carbon nano tubes, TiO<sub>2</sub> etc. can be also incorporated into the target polymers using VFD processing, in regard to fabricate composite membranes with different applications.
- Green graphene oxide (GGO) has been developed in the Raston research group as a low waste process, having significantly different properties relative to conventional Hummer's method derived GO. Using GGO as an additive to the polymer matrix for making hybrid polymers (GGO/polymer) has potential for different applications.
- Evaluating the performance of VFD fabricated graphene composites (graphene or GO in polymer matrix) in regard to heat dissipation control for application in LED lights.
- In situ membrane fabrication in the VFD without further processing can be an immaculate topic for further research on the application of the VFD in polymer and membrane science.
- Stepping forward to prepare NF membranes, using VFD for processing other solutions for creating a thin active layer on top of the UF membranes has high potential (and novelty) future research direction in this field.
- Apart from the polymeric membranes, other types of nonpolymeric membranes can also be investigated for fabrication using VFD processing.



## Appendix A

### Electronic Supplementary Information (ESI) of “Vortex fluidic mediated synthesis of polysulfone”

Aghil Igder<sup>a,b</sup>, Scott J. Pye<sup>b</sup>, Ahmed Hussein Mohammed Al-Antaki<sup>b</sup>, Alireza Keshavarz<sup>a</sup>, and  
Colin L. Raston<sup>\*b</sup>, Ata Nosrati<sup>a</sup>

---

*a. School of Engineering, Edith Cowan University, Joondalup, Perth, WA 6027, Australia.*

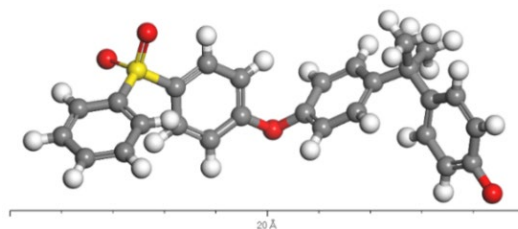
*b. Flinders Institute for Nanoscale Science and Technology, College of Science and Engineering, Flinders University, Adelaide, SA 5042, Australia.*

*E-mail: [colin.raston@flinders.edu.au](mailto:colin.raston@flinders.edu.au).*

*DOI: <https://doi.org/10.1039/D0RA00602E>*

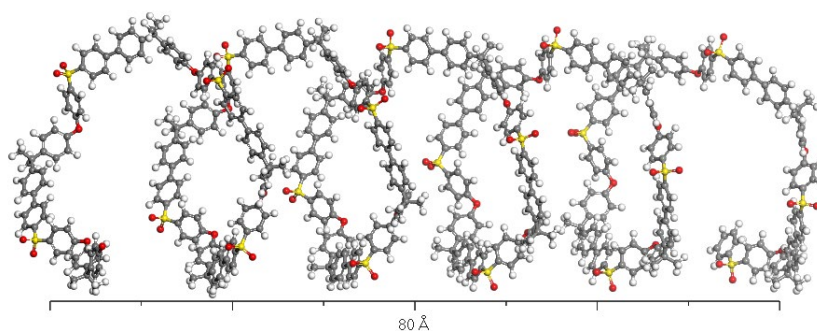
## A.1. Schematic structure of polysulfone (PSF)

### A.1.1. PSF repeating unit



Scheme A. 1. PSF repeating unit.

### A.1.2. Polysulfone (PSF) with a number of repeating units



Scheme A. 2. Polysulfone (PSF) with a number of repeating units.

### A.1.3. PSF polymerization via conventional technique

Bisphenol A (6.42 g, 0.028 mol) accompanied with DMSO (13.07 mL) and chlorobenzene (37.16 mL) were placed in a triple neck rounded bottom flask. This flask was fitted with a nitrogen inlet, mechanical stirrer, and a condenser. Dissolving BPA in the solvents were performed at 60-80 °C using an overhead mechanical stirrer with 500 rpm rotational speed in 30 min resulted in a clear solution. Following this, 50% NaOH solution (4.48 g, 2.92 mL, 0.056 mol) was added to the reaction mixture over a period of 10 minutes, and the reaction was continued for 1 h at 120 °C. This resulted in a two-phase mixture of chlorobenzene, and DiNa salt of BPA in DMSO. For water removal, the temperature was increased to 140 °C, resulting in precipitation of the disodium salt of BPA.

A 50 % w/w solution of DCDPS (8.07 g, 0.028 mol), in chlorobenzene (7.27 mL) was heated to 110 °C, then added to the reaction over a period of about 10 min. The

solution was then stirred at 1000 rpm for 1 h at 160 °C [1]. The obtained solution was cooled and diluted with chlorobenzene (90 mL). The solid NaCl was then filtered from the solution. The final polymer was coagulated in ethanol (300 mL) and washed with ethanol 3 times and filtered from the coagulant followed by drying in an oven at 135 °C for 5 hours, resulting in pure PSF as a goldish solid [2].

## A.2. Experimental setup for PSF polymerization via the VFD

Table A. 1. List of experiments conditions for optimizing the PSF polymerisation using the VFD in confined mod.

Test No	Speed (RPM)	T (°C)	Tilt Angle (°)	Time (min)
T1	3000	150	45	30
T2	4000	150	45	30
T3	5000	150	45	30
T4	6000	150	45	30
T5	7000	150	45	30
T6	8000	150	45	30
T7	Optimal	80	45	30
T8	Optimal	120	45	30
T9	Optimal	140	45	30
T10	Optimal	150	45	30
T11	Optimal	160	45	30
T12	Optimal	170	45	30
T13	Optimal	Optimal	0	30
T14	Optimal	Optimal	15	15
T15	Optimal	Optimal	30	30
T16	Optimal	Optimal	45	60
T17	Optimal	Optimal	60	30
T18	Optimal	Optimal	75	30
T19	Optimal	Optimal	90	30
T20	Optimal	Optimal	Optimal	15
T21	Optimal	Optimal	Optimal	30
T22	Optimal	Optimal	Optimal	60

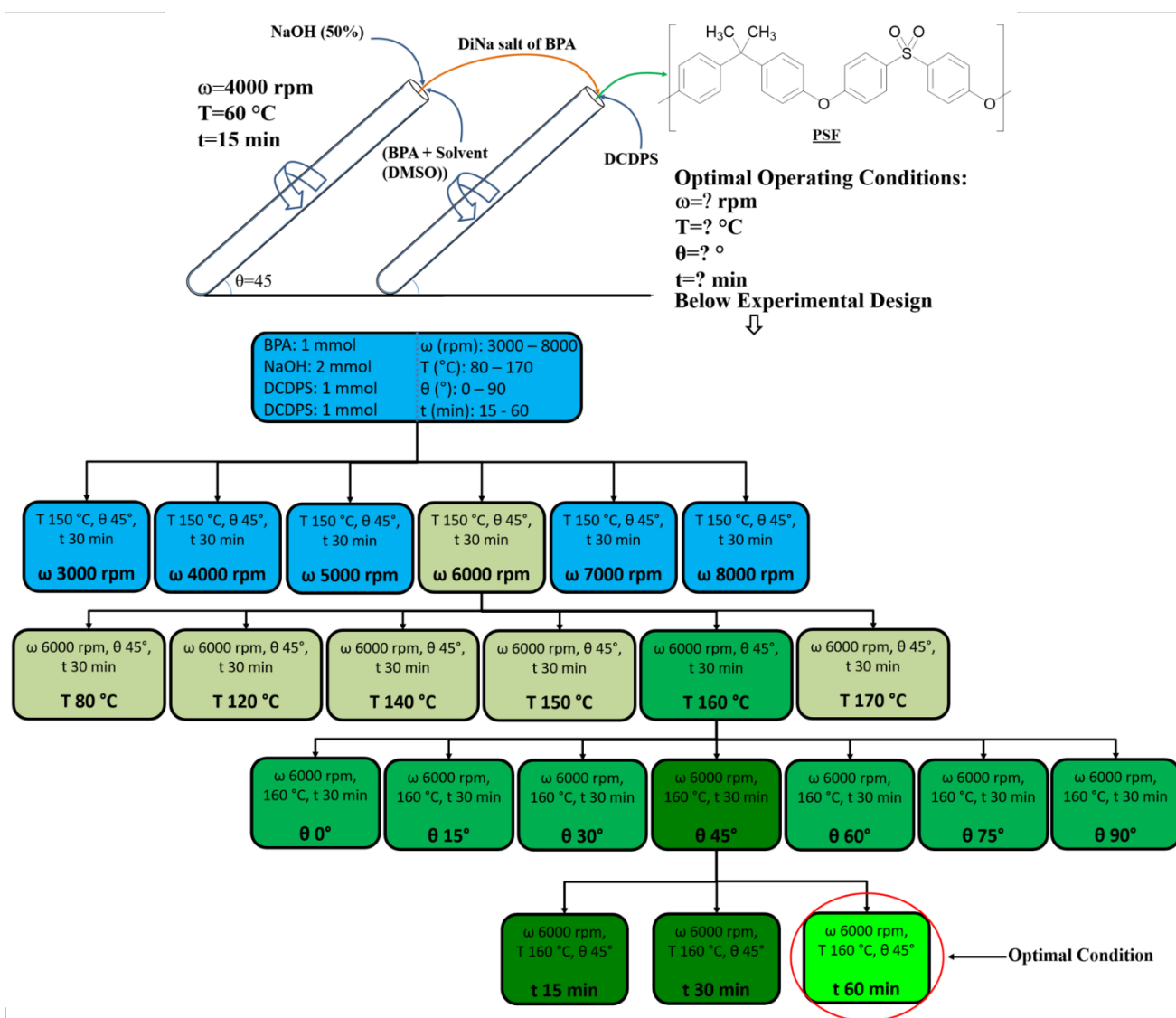


Figure A. 1. Experimental setup for investigating the experimental parameters in a systematic approach.

### A.3. FTIR spectra

#### A.3.1. BPA & DiNa salt of BPA

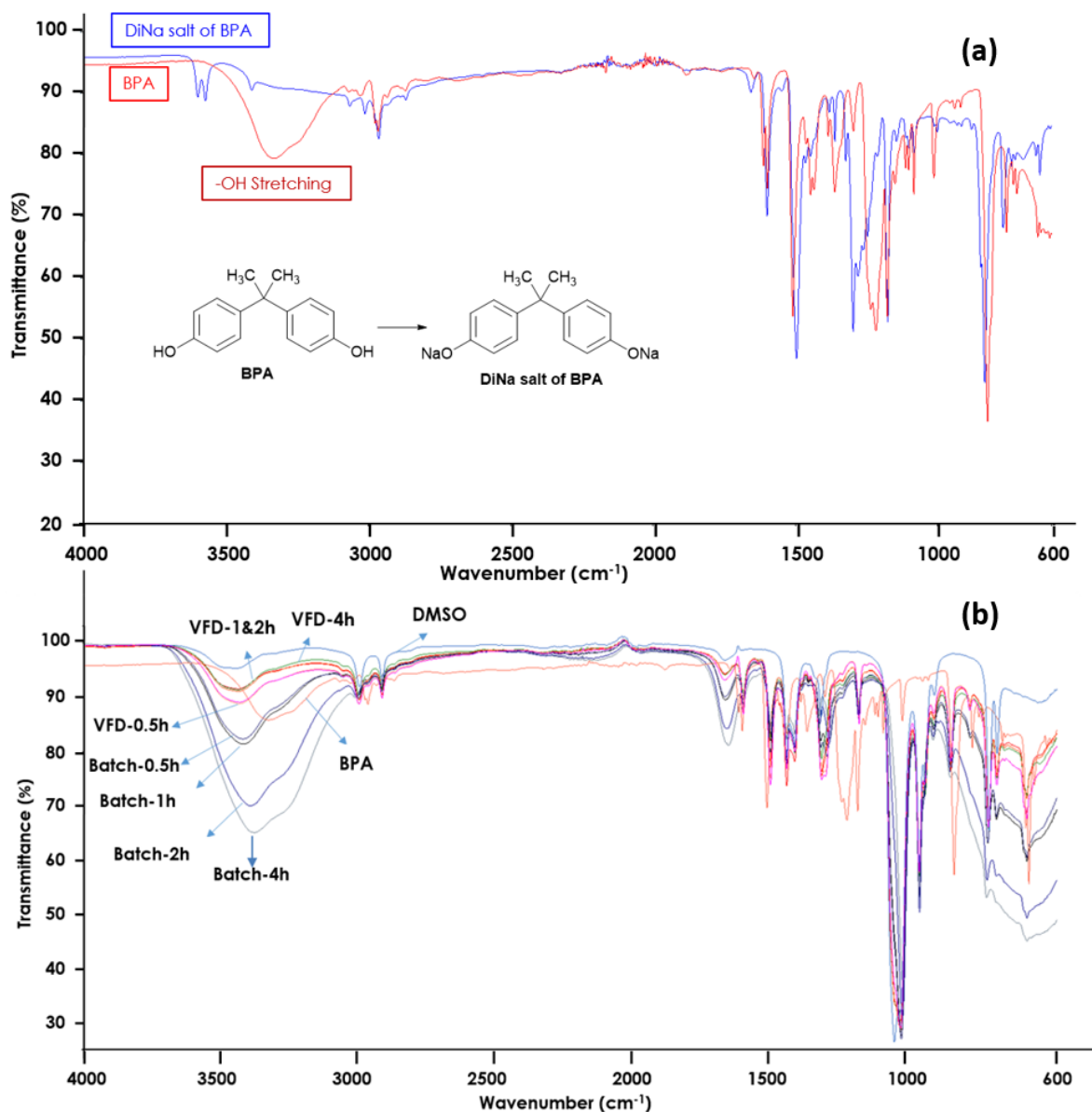


Figure A. 2. FTIR spectrums of BPA and DiNa salt of BPA, b) FTIR spectrums of DiNa salt of BPA obtained from first step of polymerization in both VFD and batch processing for different retention times from 30 min to 4h in comparing the effect of time in water dissipation in producing the DiNa salt of BPA, using VFD or batch processing.

### A.3.2. Polysulfone (PSF)

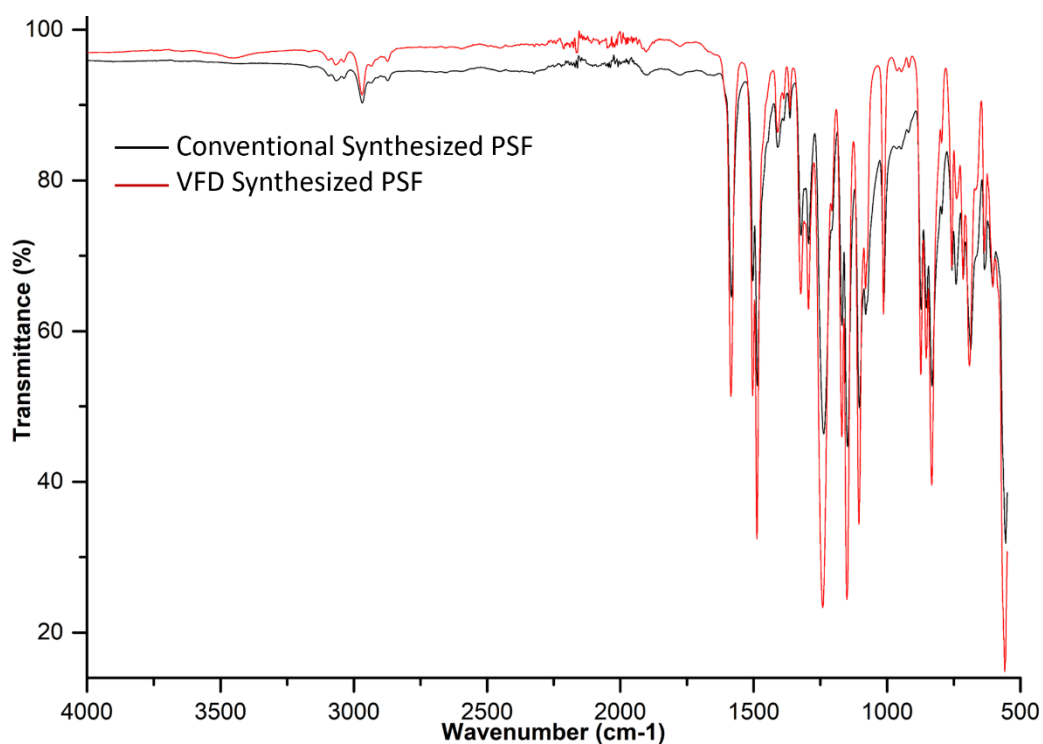


Figure A. 3. FTIR spectra of the VFD and conventional synthesized PSF. VFD product was synthesised at 6000 rpm, 160 °C, 45 tilt angle, and 60 min reaction time.

### A.4. NMR spectra

All NMR was performed on either 600 or 400 MHz Bruker advance spectrometers, using CDCl<sub>3</sub> or D<sub>2</sub>O as the solvent, as specified. Spectra were acquired using a relaxation delay-time of 4 seconds. All chemical shifts are presented in ppm, using residual solvent as the internal standard. 2D COSY and HSQC experiments were used for peak allocation.

#### A.4.1. Bisphenol A (BPA)

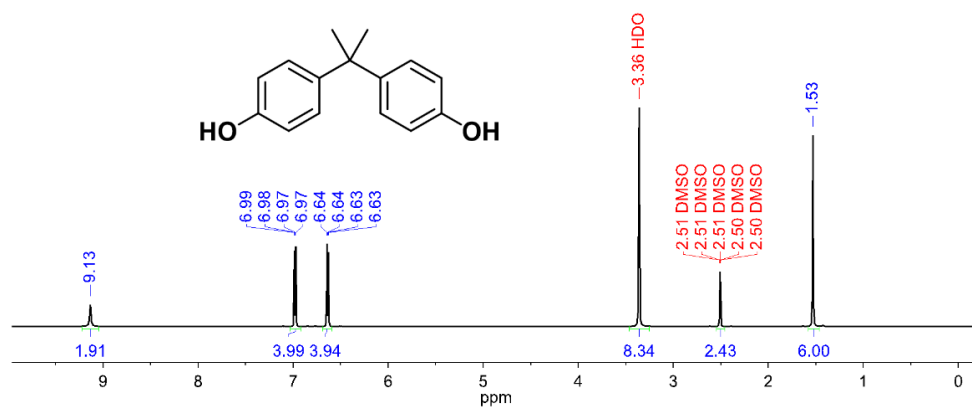


Figure A. 4. <sup>1</sup>H-NMR of BPA as a starting material in first step of PSF polymerization, using DMSO-d<sub>6</sub> as the NMR solvent.

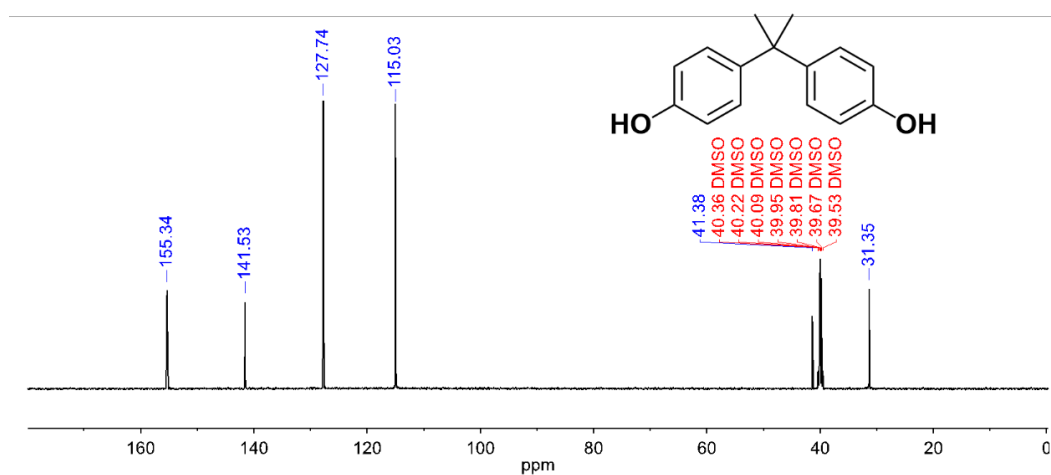


Figure A. 5. <sup>13</sup>C-NMR of BPA as a starting material in first step of PSF polymerization.

#### A.4.2. Disodium salt of BPA

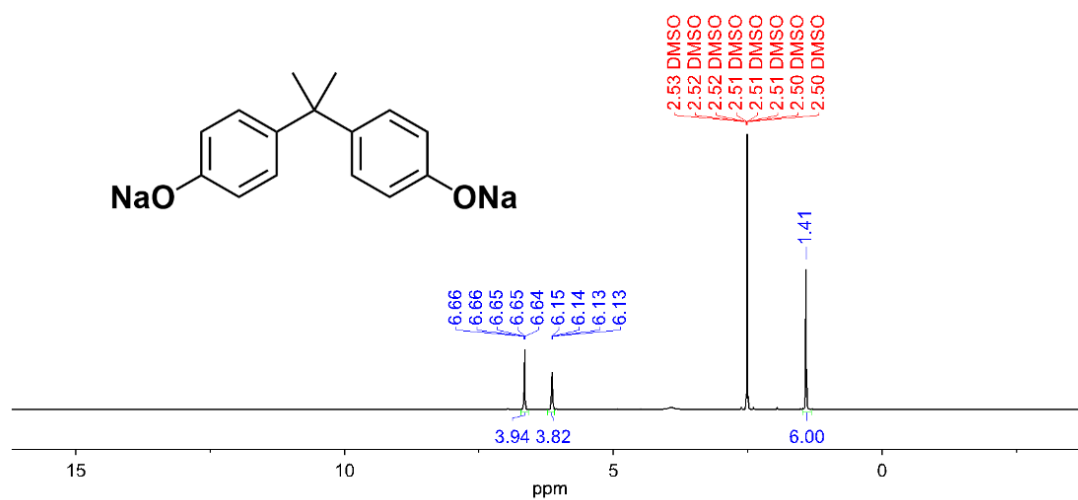


Figure A. 6. <sup>1</sup>H-NMR of DiNa salt of BPA, as the intermediate product in PSF polymerization.

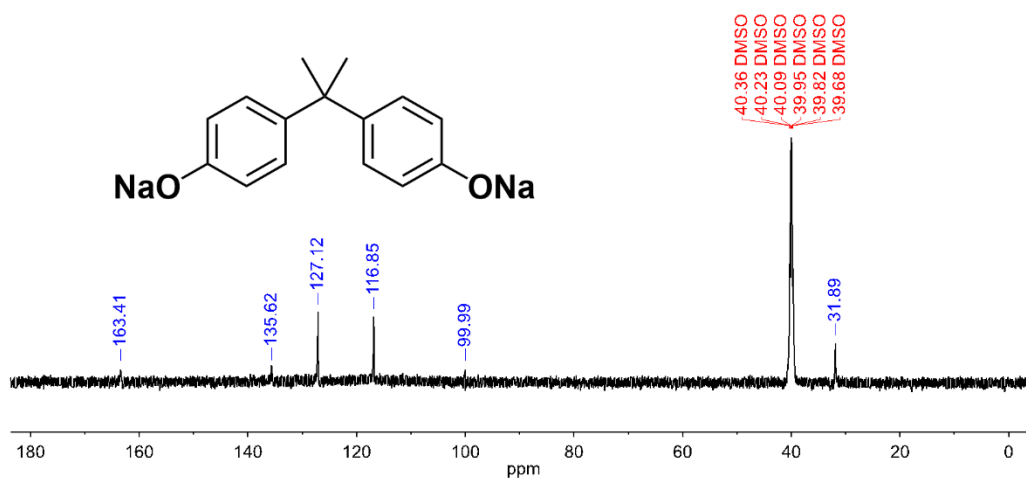


Figure A. 7. <sup>13</sup>C-NMR of DiNa salt of BPA as the intermediate product in PSF polymerization.



#### A.4.3. 4,4-dichlorodiphenyl sulphone (DCDPS)

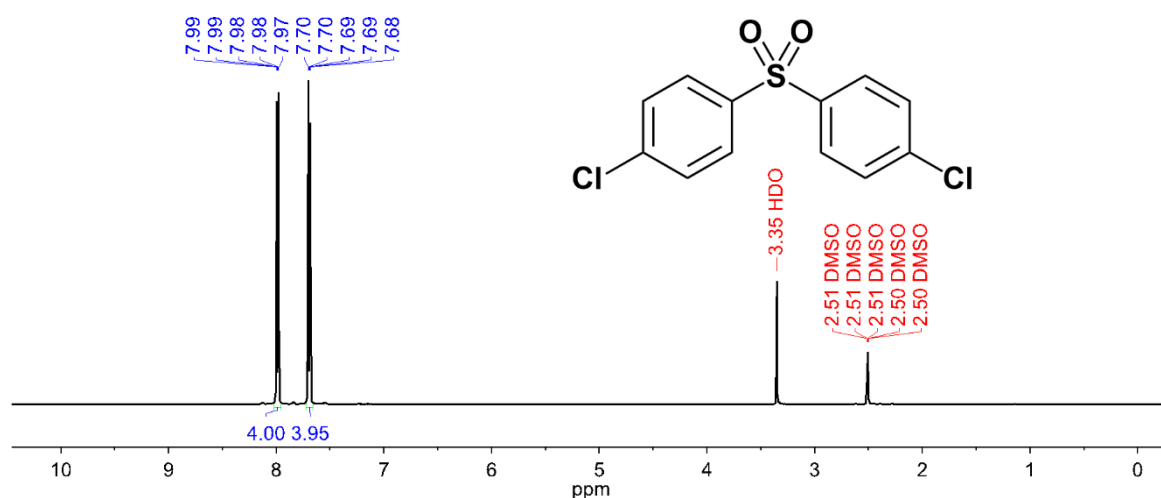


Figure A. 8. <sup>1</sup>H-NMR of DCDPS as a starting material in second step of PSF polymerization.

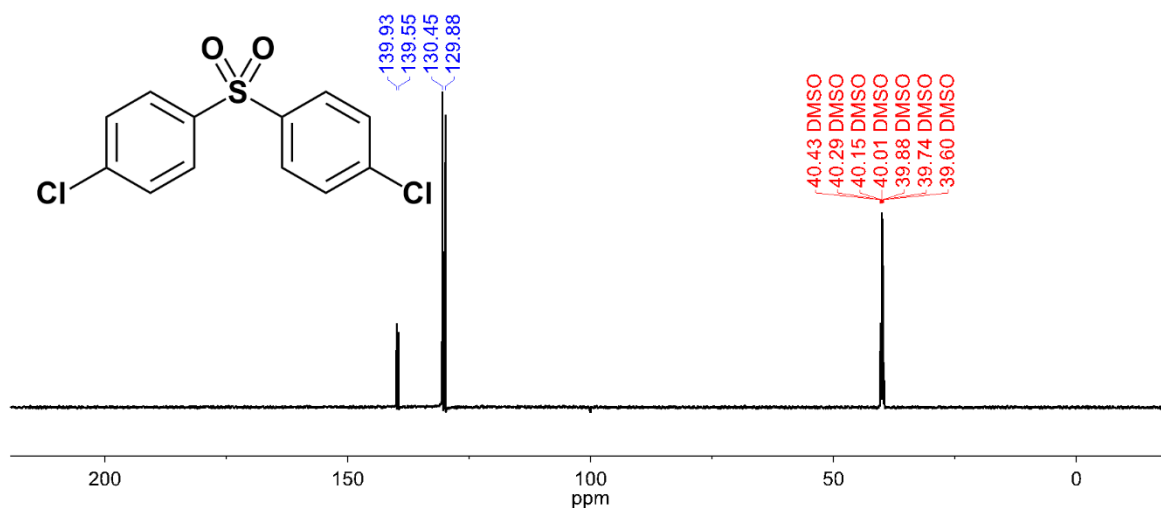


Figure A. 9. <sup>13</sup>C-NMR of DCDPS as a starting material in second step of PSF polymerization.

#### A.4.4. Polysulfone (PSF)

The NMR data suggests that the reaction of BPA and DCDPS resulted in PSF. This is evident from the consumption of peaks corresponding to both starting materials, and the production of new, broadened peaks indicative of PSF. In the aromatic region, there are smaller peaks present that are likely due to terminal groups of the polymer.

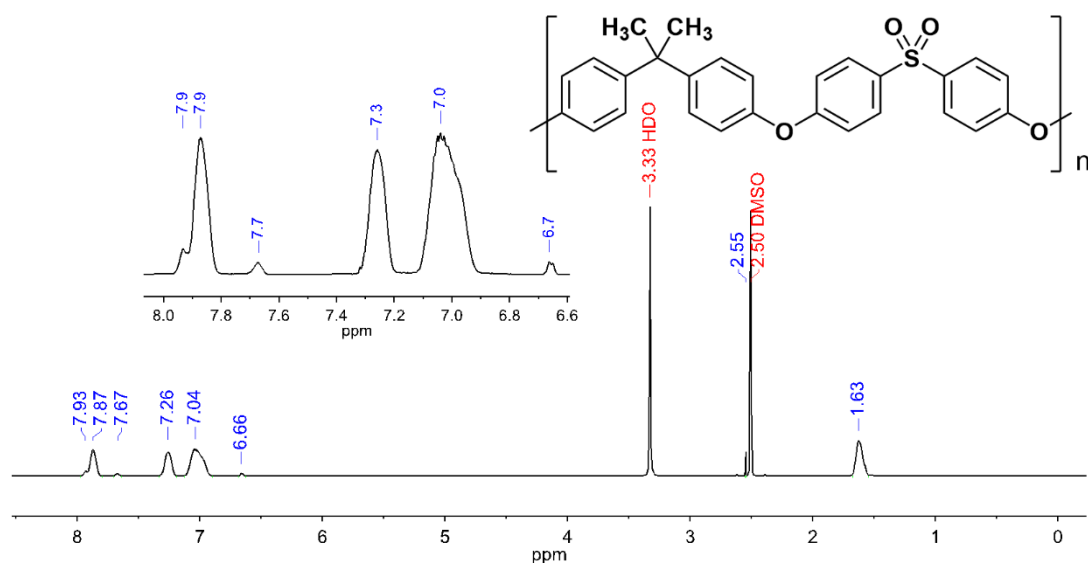


Figure A. 10. <sup>1</sup>H-NMR spectra of VFD prepared PSF at 6000 rpm, 160 °C, 45 tilt angle, and 60 min reaction time.

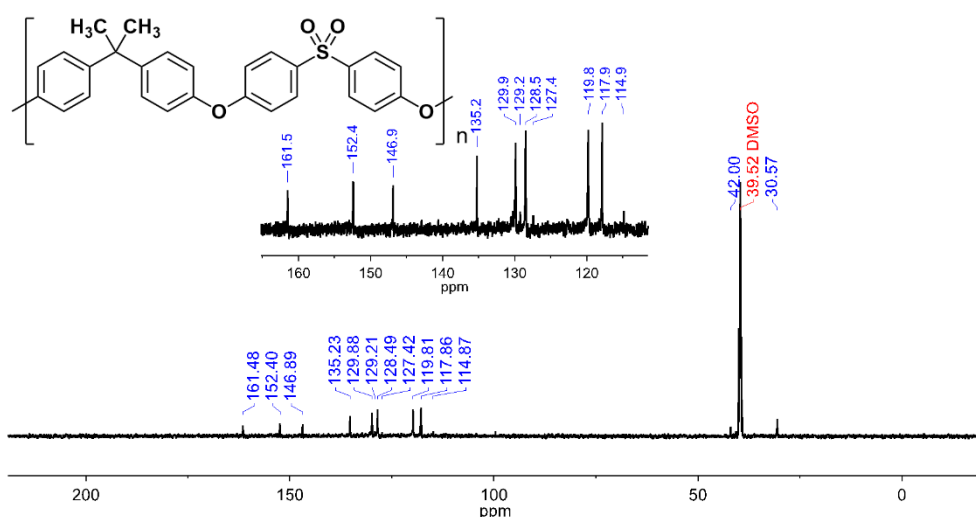


Figure A. 11. <sup>13</sup>C-NMR spectra of VFD prepared PSF at 6000 rpm, 160 °C, 45 tilt angle, and 60 min reaction time.

## A.5. GPC curves

Molecular weight average molar mass ( $M_w$ ) and distribution of the synthesized PSF were determined using a double detection Shimadzu GPC instrument equipped with an Ultra Violet (UV) and Refractive Index (RI) detectors, a guard column and a Phenogel™ 5μm Linear (2), 300 \* 7.8 mm LC column. Tetrahydrofuran (THF) was used

as the eluent (at 25 °C with 1.0 ml/min flow rate). The column was calibrated using polystyrene standards with molecular weight covering the range of 1000–2704000 g/mol.

#### A.5.1. GPC traces of VFD ( $T_4$ , 6000 rpm), commercial and conventional PSF

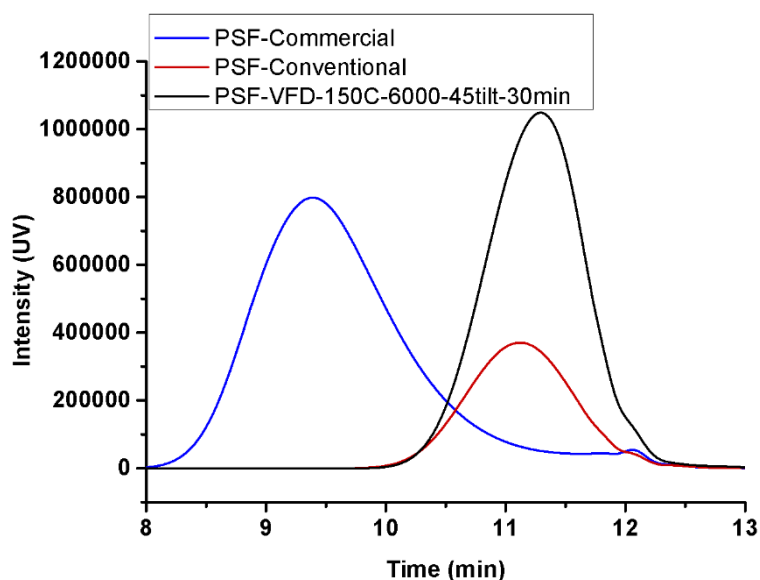


Figure A. 12. Comparison between GPC traces of commercial, conventional and VFD synthesized ( $T_4$  at 6000 rpm, 150 °C, 45°, and 30 min) PSF detected using the UV detector.

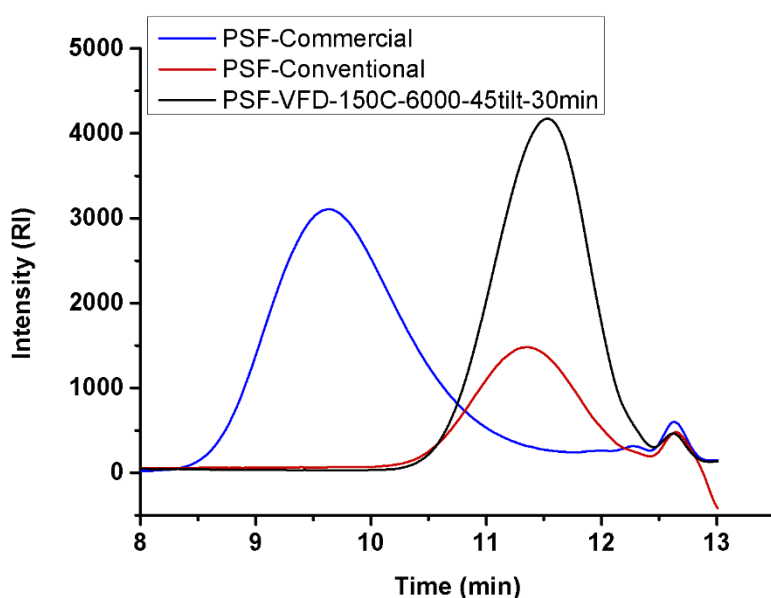


Figure A. 13. Comparison between GPC traces of commercial, conventional and VFD synthesized ( $T_4$  at 6000 rpm, 150 °C, 45°, and 30 min) PSF detected using the RI detector.

### A.5.2. Effect of rotational speed

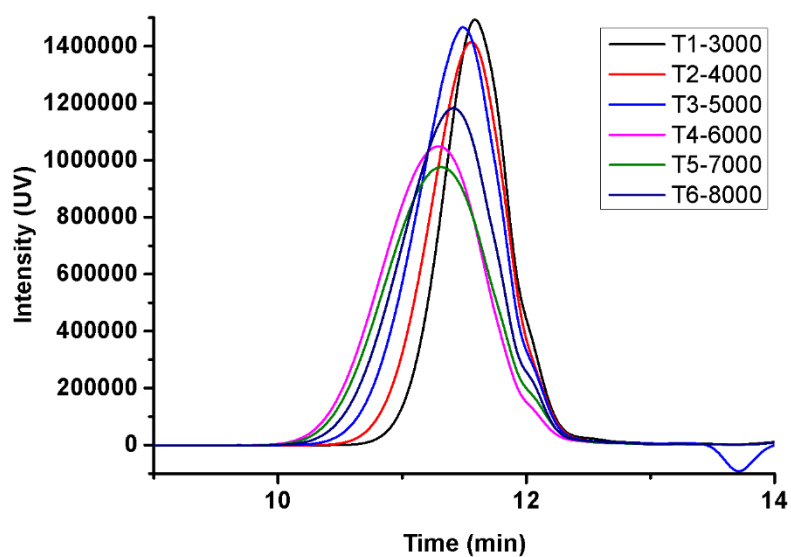


Figure A. 14. GPC curves of the VFD synthesized PSF's in different rotational speed, obtained from T<sub>1</sub> to T<sub>6</sub> using the UV detector.

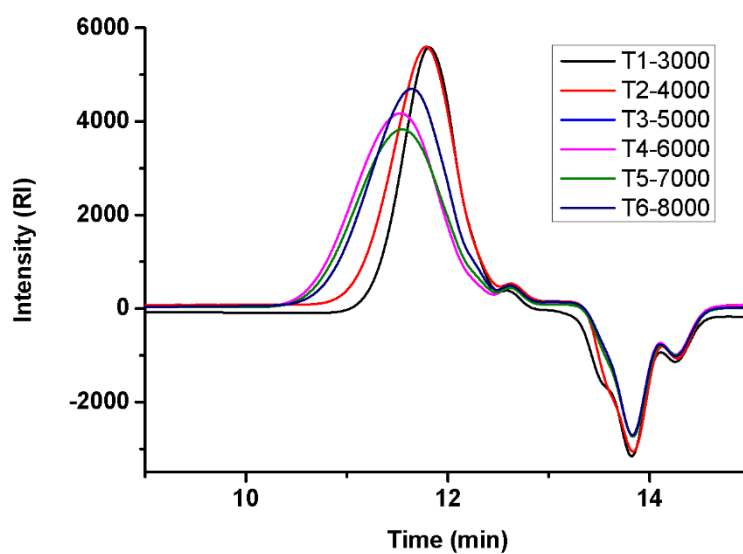


Figure A. 15. GPC curves of the VFD synthesized PSF's in different rotational speed, obtained from T<sub>1</sub> to T<sub>6</sub> using the RI detector.

### A.5.3. Effect of temperature

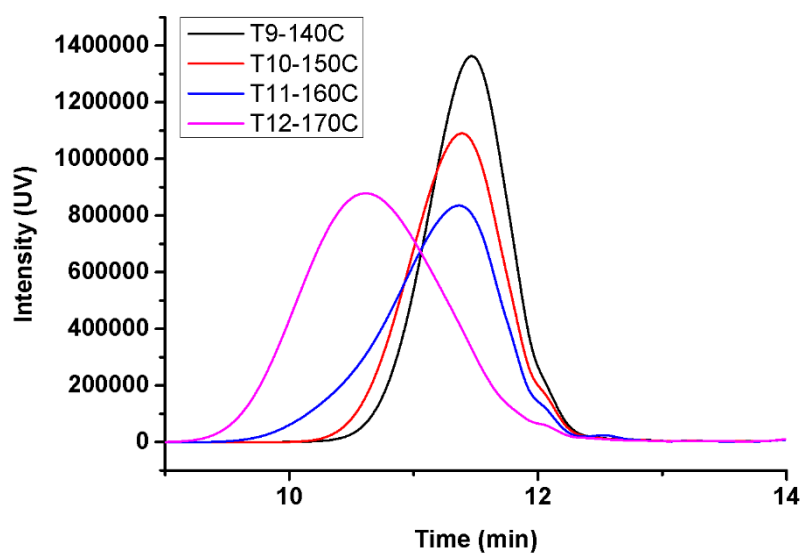


Figure A. 16. GPC curves of the VFD synthesized PSF's in different temperatures, obtained from T<sub>9</sub> to T<sub>12</sub> using the UV detector.

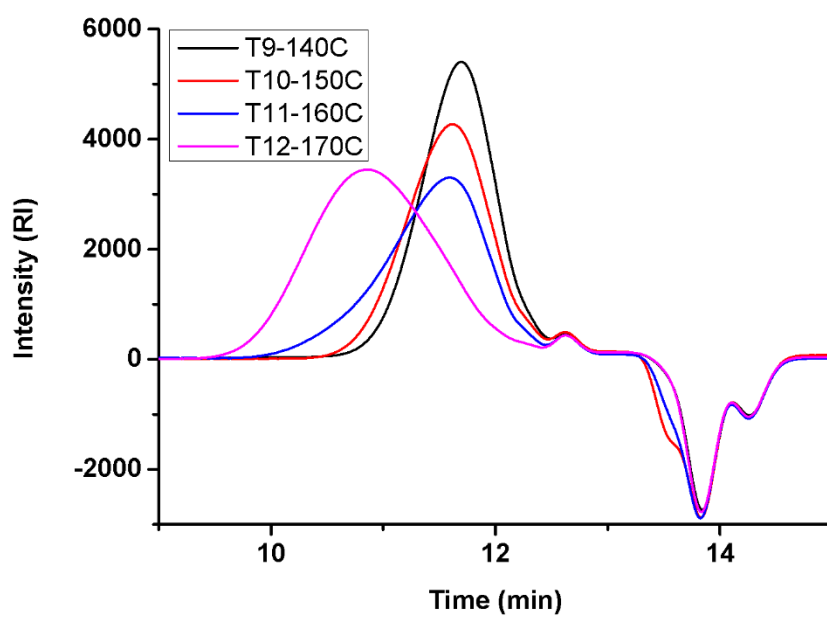


Figure A. 17. GPC curves of the VFD synthesized PSF's in different temperatures, obtained from T<sub>9</sub> to T<sub>12</sub> using the RI detector.

#### A.5.4. GPC traces of VFD ( $T_{11}$ , 160 °C), commercial and conventional PSF

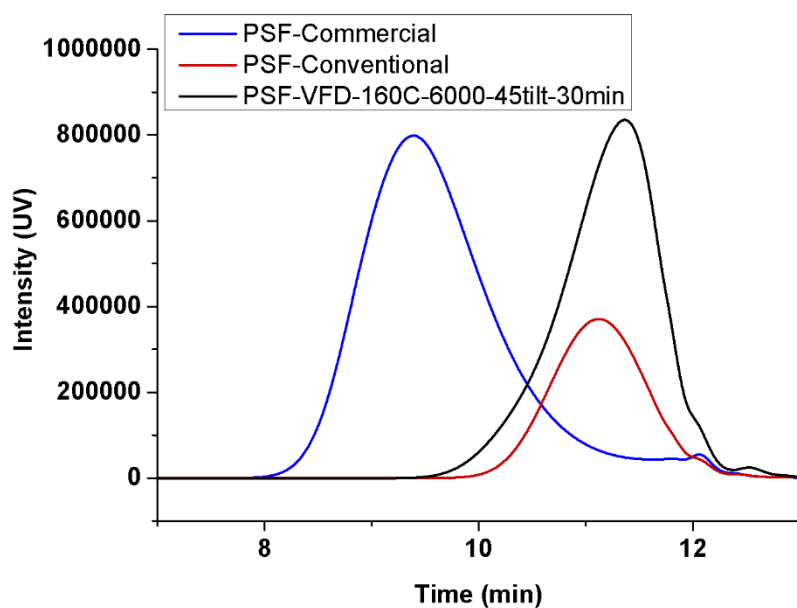


Figure A. 18. Comparison between GPC traces of commercial, conventional and VFD synthesized ( $T_{11}$  at 160 °C) PSF detected using the UV detector.

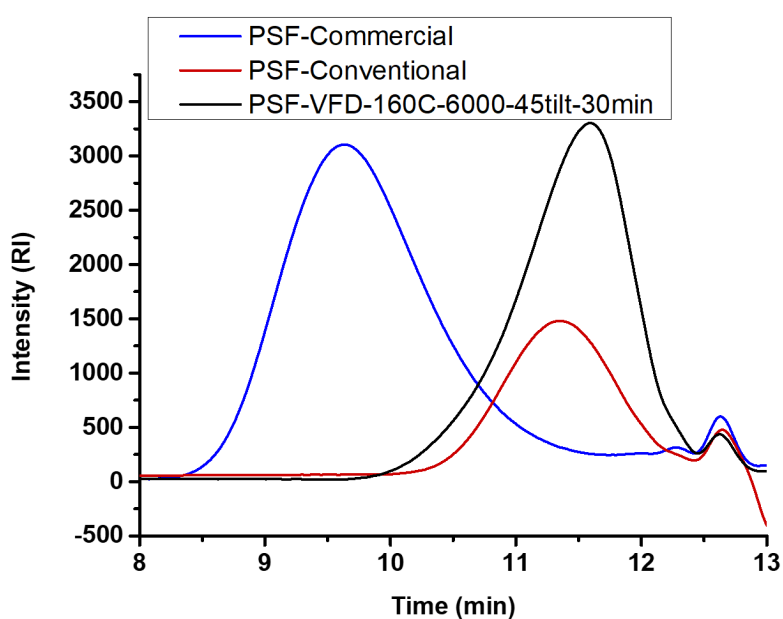


Figure A. 19. Comparison between GPC traces of commercial, conventional and VFD synthesized ( $T_{11}$  at 160 °C) PSF detected using the RI detector.

### A.5.5. Effect of tilt angle

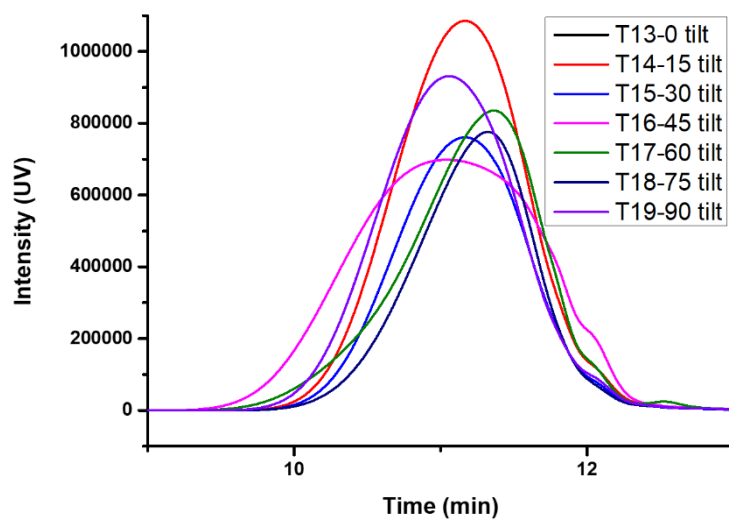


Figure A. 20. GPC curves of the VFD synthesized PSF's in different tilt angles, obtained from T<sub>13</sub> to T<sub>19</sub> using the UV detector.

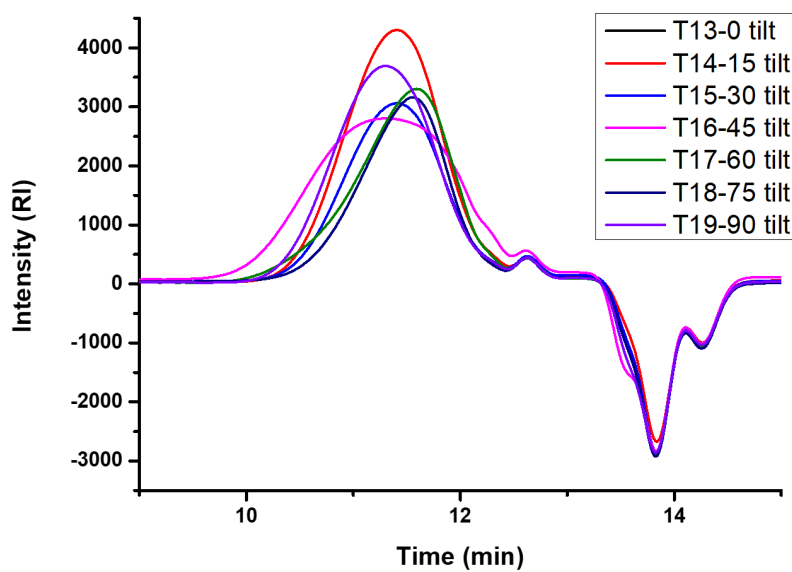


Figure A. 21. GPC curves of the VFD synthesized PSF's in different tilt angles, obtained from T<sub>13</sub> to T<sub>19</sub> using the RI detector.

### A.5.6. Effect of time

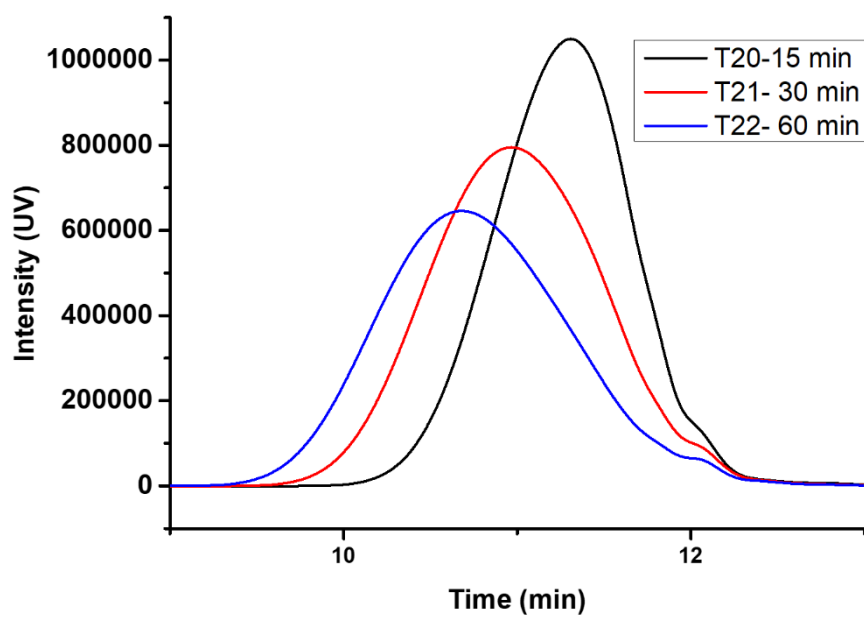


Figure A. 22. GPC curves of the VFD synthesized PSF's in different retention times, obtained from  $T_{20}$  to  $T_{22}$  using the UV detector.

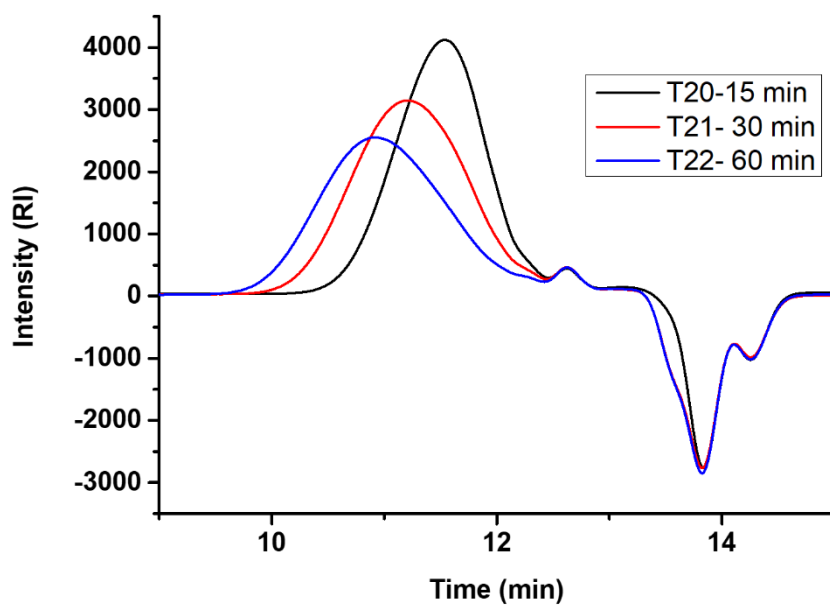


Figure A. 23. GPC curves of the VFD synthesized PSF's in different retention times, obtained from  $T_{20}$  to  $T_{22}$  using the RI detector.



### A.5.7. GPC traces on the VFD synthesized PSFs ( $T_1 - T_{22}$ ), conventional and commercial PSFs.

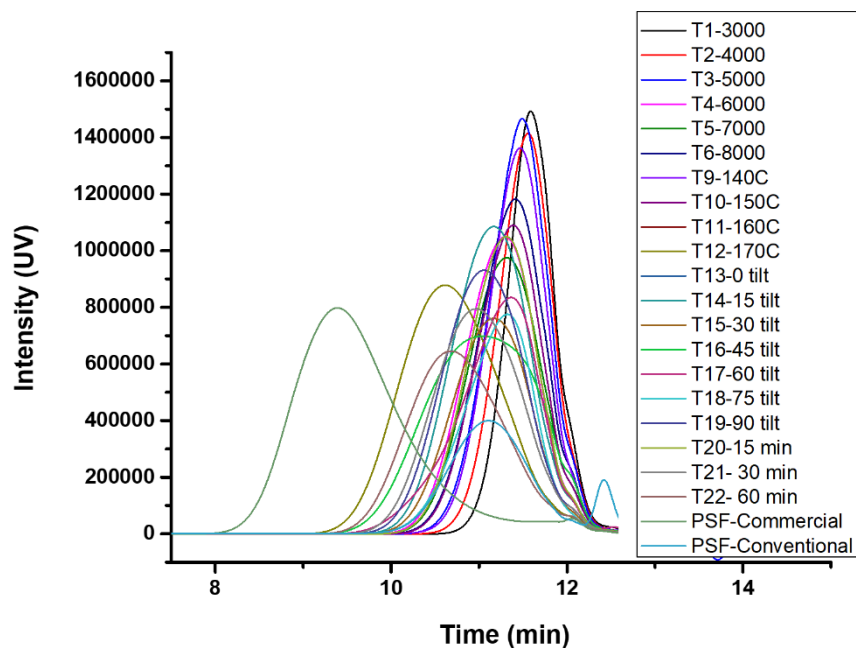


Figure A. 24. GPC curves of the VFD synthesized PSF's in different operational condition, obtained from  $T_1$  to  $T_{22}$ , vs commercial and conventional PSFs, detected using the UV detector.

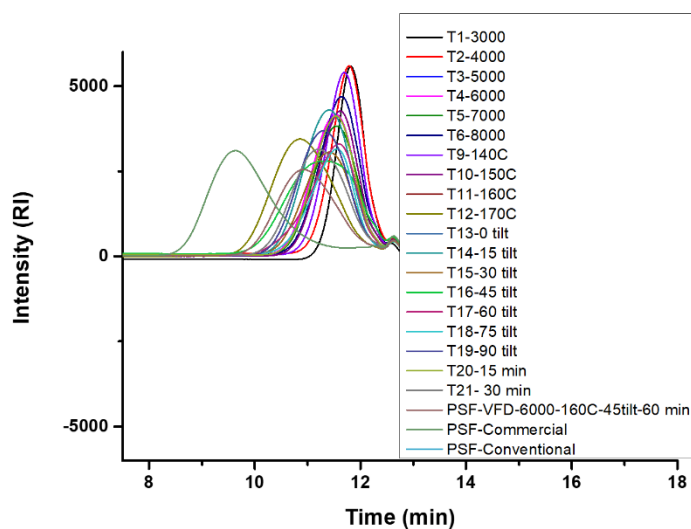


Figure A. 25. GPC curves of the VFD synthesized PSF's in different operational condition, obtained from  $T_1$  to  $T_{22}$ , vs commercial and conventional PSFs, detected using the RI detector.

## A.6. Glass transition temperature ( $T_g$ )

$T_g$  measurements were proceeded using a Perkin Elmer DSC 8000 Instruments. A cyclic heating-cooling-heating was carried out to eliminate thermal history in first heating from 30 to 230°C and then cooling to 30 °C followed by heating up again to 230°C. The ramping rates were 10 °C per minute for heating and cooling stages.  $T_g$  of each sample was obtained from the heat flow changes on the second heating scan.

### A.6.1. Comparison between $T_g$ obtained for commercial PSF and VFD prepared PSF in different $\omega$

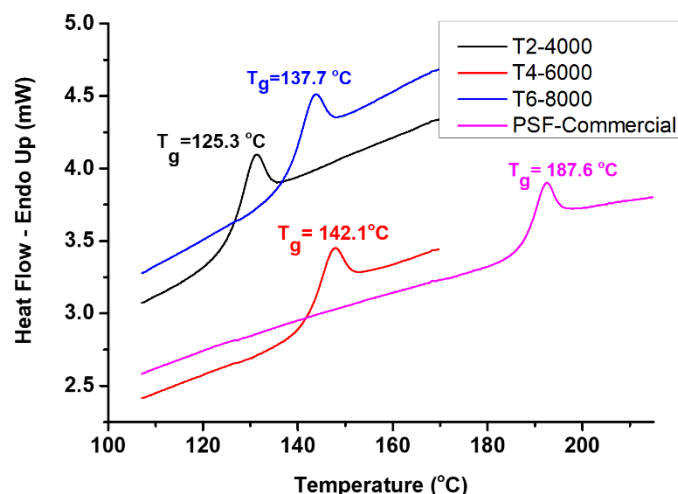


Figure A. 26. DSC thermograms of commercial and VFD synthesised PSF of  $T_2$ ,  $T_4$ , and  $T_6$ . Samples were cycled from 30 °C to 230 °C at a rate of 10 °C min<sup>-1</sup>.

## A.7. TGA analysis

TGA also is used for characterizing the thermal stabilities of materials by identifying the mass loss or gain, due to heating the samples.<sup>[3]</sup> Thermal stability of the polymers was also investigated through a thermogravimetric analysis on a Perkin Elmer TGA 8000 under nitrogen and air atmosphere. To do so, samples were heated up to 850 °C from 50 °C with 20 °C/min under nitrogen atmosphere and then held isothermal at 850 °C for 1 min followed by heating up again to 1050 °C with the same ramping rate under switched atmosphere to air.

Table A. 2. TGA measurements settings

<b>Sample name</b>	Polysulfone (PSF)
<b>Sample mass [mg]</b>	≈ 4
<b>Crucible</b>	Ceramic
<b>Temperature Program</b>	50 ... 850 ... 1050 °C
<b>Heating rate</b>	20 °C / min
<b>Atmosphere</b>	Nitrogen, switch to air at 850 °C

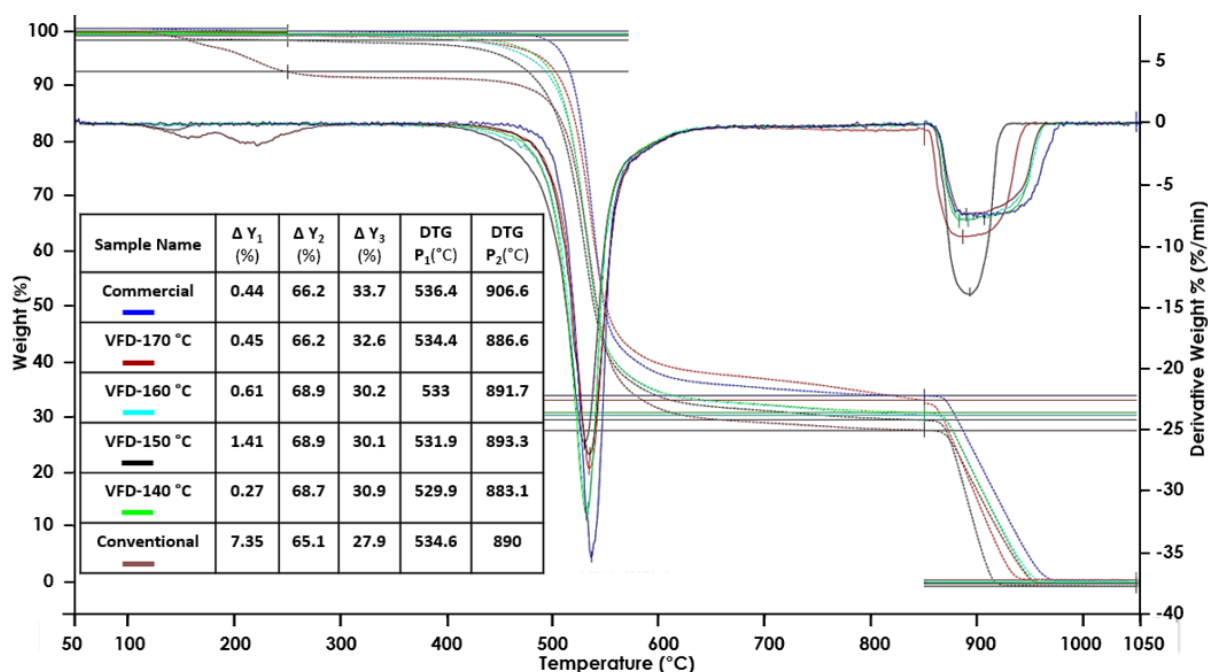


Figure A. 27. TGA traces of commercial, conventional and VFD synthesized PSF ( $T_9$ - $T_{12}$ ), heating at a rate of 20 °C min<sup>-1</sup> up to 850 °C under Nitrogen and then air to 1050 °C.  $\Delta Y$  =Delta Y which represents the mass loose percentage in every stage. DTG P=DTG Peak represents the decomposition temperature of every mass losing step obtained from derivative weight % curve, DTG  $P_{1\&2}$  represent the decomposition temperature of main mass losing while using N<sub>2</sub> and air, respectively.

After switching to air, burning of the pyrolytic soot as a mass loss of ~ 30 % was also observed which resulted in no residual mass at the end of the measurement.

## A.8. SEM images

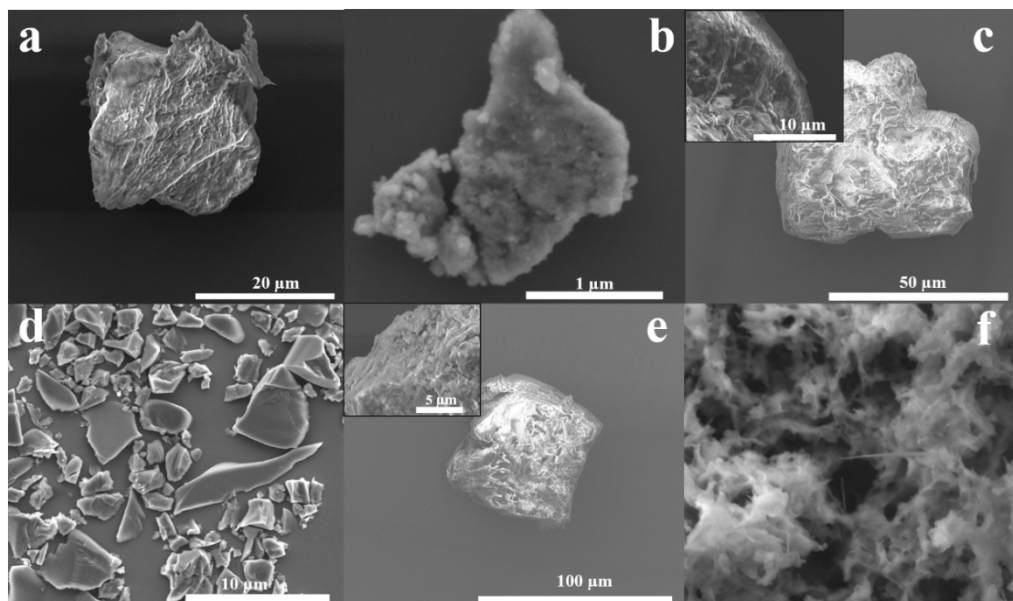


Figure A. 28. SEM images of PSF for (a) commercial material, (b) material formed using conventional batch processing, (c) material formed in the VFD at the optimised s (T22 at 6000 rpm, 160 °C, 45°, and 60 min). PSF synthesised in the VFD at 6000 rpm, 160 °C,  $\phi$  45° for (d) 15 min, (e) 30 min, and (f) 90 min reaction time. All the sample were drop cast and coated with ca 5 nm layer of Pt.

## A.9. Chapter references

1. Othmer, K., *Encyclopedia of Chemical Technology*. 1996, John Wiley & Sons: New York.
2. Johnson, R.N., et al., *Poly(ary1 Ethers) by nucleophilic aromatic substitution. I. synthesis and properties*. J. Polym. Sci.: Part A-1, 1967. **5**: p. 2375-2398.
3. Agboola, O., J. Maree, and R. Mbaya, *Characterization and performance of nanofiltration membranes*. Environ. Chem. Lett., 2014. **12**(2): p. 241-255.

## Appendix B

### **Electronic Supplementary Information (ESI) of “High shear vortex fluidic morphologically controlled polysulfone formed under anhydrous conditions”**

Aghil Igder<sup>a,b</sup>, Ahmed Hussein Mohammed Al-Antaki<sup>b</sup>, Scott J. Pye<sup>b</sup>, Alireza Keshavarz<sup>a</sup>, Colin  
L. Raston<sup>\*b</sup>, and Ata Nosrati<sup>a</sup>

---

*a. School of Engineering, Edith Cowan University, Joondalup, Perth, WA 6027, Australia.*

*b. Flinders Institute for Nanoscale Science and Technology, College of Science and  
Engineering, Flinders University, Adelaide, SA 5042, Australia.*

*E-mail: [colin.raston@flinders.edu.au](mailto:colin.raston@flinders.edu.au).*

## B.1. Experimental settings

Table B. 1. Experimental conditions for PSF synthesise using a nitrogen sealed VFD tube in the confined mode.

Test No	Speed, $\omega$ (rpm)	T (°C)	Tilt Angle, $\theta$ (°)	Time, t (min)
S1	3k	150	45	60
S2	4k	150	45	60
S3	5k	150	45	60
S4	6k (optimal)	150	45	60
S5	7k	150	45	60
S6	8k	150	45	60
S7	6k	120	45	60
S8	6k	140	45	60
S9	6k	150	45	60
S10	6k	160 (optimal)	45	60
S11	6k	170	45	60
S12	6k	160	0	60
S13	6k	160	15	60
S14	6k	160	30	60
S15	6k	160	45 (optimal)	60
S16	6k	160	60	60
S17	6k	160	75	60
S18	6k	160	90	60
S19	6k	160	45	15
S20	6k	160	45	30
S21	6k	160	45	60 (optimal)
S22	6k	160	45	180

## B.2. Heating unit calibration curve

Since there is a difference between the real temperature inside the tube and the temperature which is shown on the controller of the heating unit, the heating unit was calibrated by measuring the melting point of several compounds (Table S2).

Table B. 2. Reported and measured melting point of different materials using melting point measurement and heating unit controller.

Standard Sample	Reported Melting Point (°C)	Melting Point Machine (°C) (T in the tube)	Melting Point on the VFD (°C)
Vanillian	81-88	81	88
Phenacetin	134	133.5	145
DCDPS	143-146	145	159
Citric Acid	153-159	152	163
BPA	158-159	155.5	168

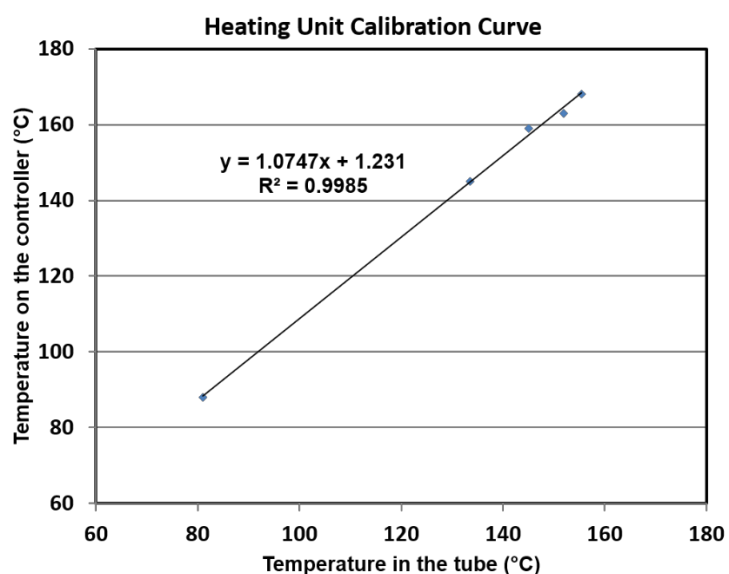


Figure B. 1. Calibration curve of the heating unit.

Table B. 3. Calculated experiments temperatures.

$y = 1.0747x + 1.231$ $R^2 = 0.9985$	T on the Controller (°C)	87	109	136	152	162	173	179	184	189
	T in the Tube (°C)	80	100	125	140	150	160	165	170	175

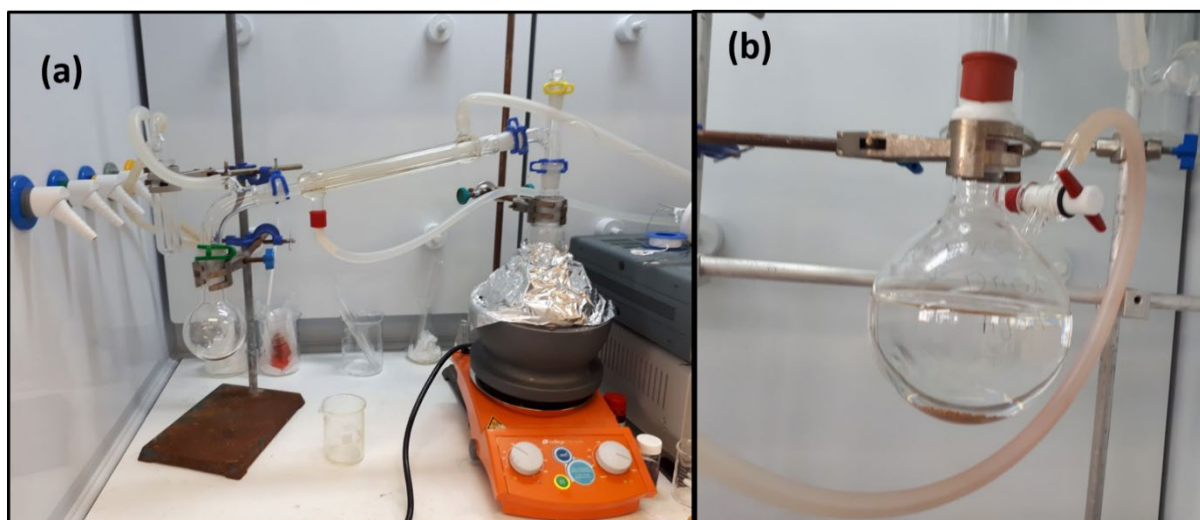


Figure B. 2. (a) Experimental setup for distilling, and (b) keeping distilled DMSO under nitrogen.

## B.3. NMR spectra

### B.3.1. Bisphenol A (BPA)

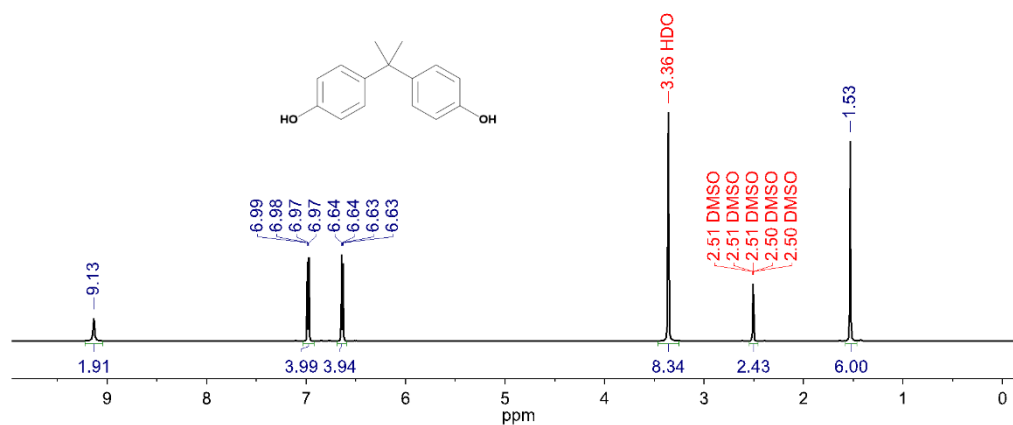


Figure B. 3.  $^1\text{H}$ -NMR of BPA as a monomer in PSF polymerization, using  $\text{DMSO-d}_6$  as the NMR solvent.[\[1\]](#)



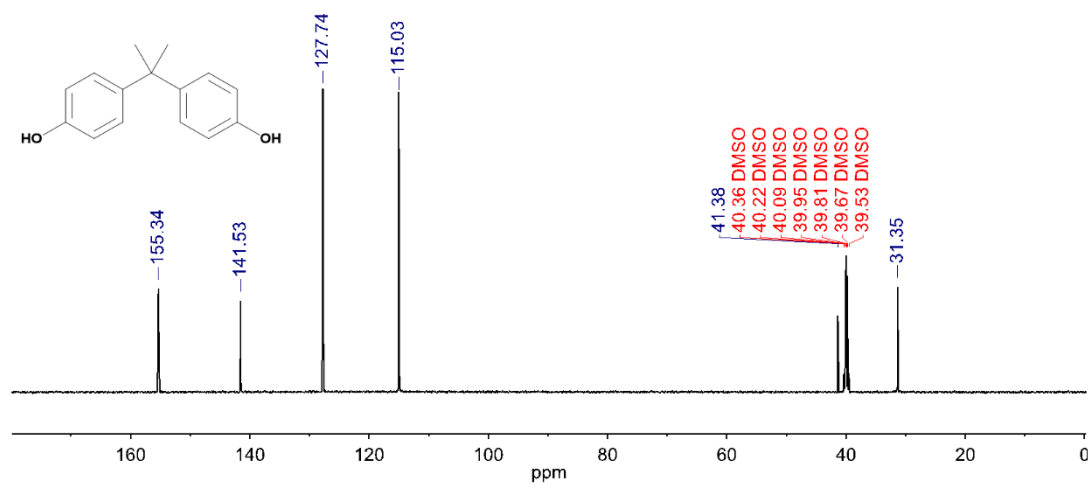


Figure B. 4. <sup>13</sup>C NMR of BPA as a monomer PSF polymerization, using DMSO-d<sub>6</sub> as the NMR solvent [1].

### B.3.2. 4,4-dichlorodiphenyl sulphone (DCDPS)

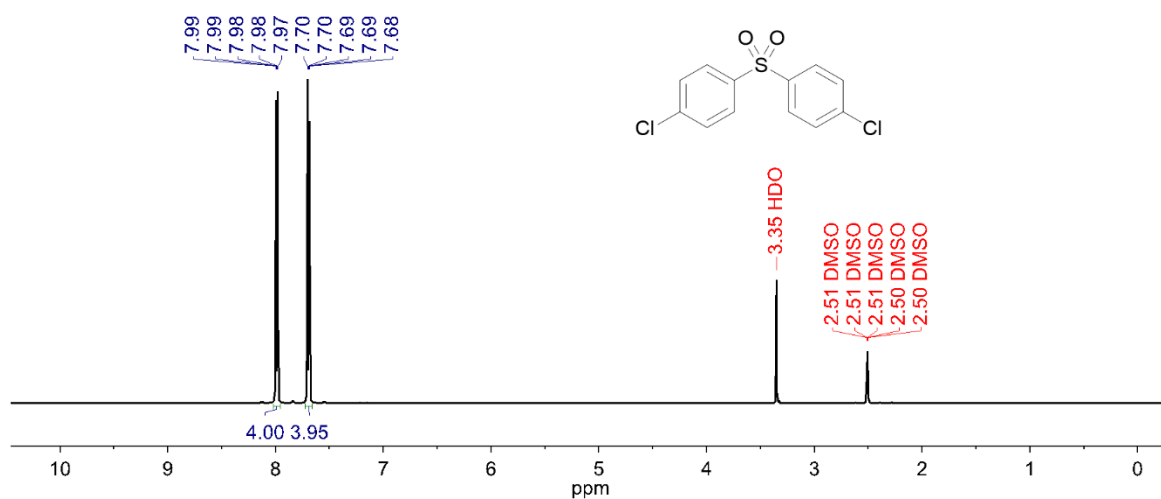


Figure B. 5. <sup>1</sup>H-NMR of DCDPS as the second monomer in PSF polymerization, using DMSO-d<sub>6</sub> as the NMR solvent [1].

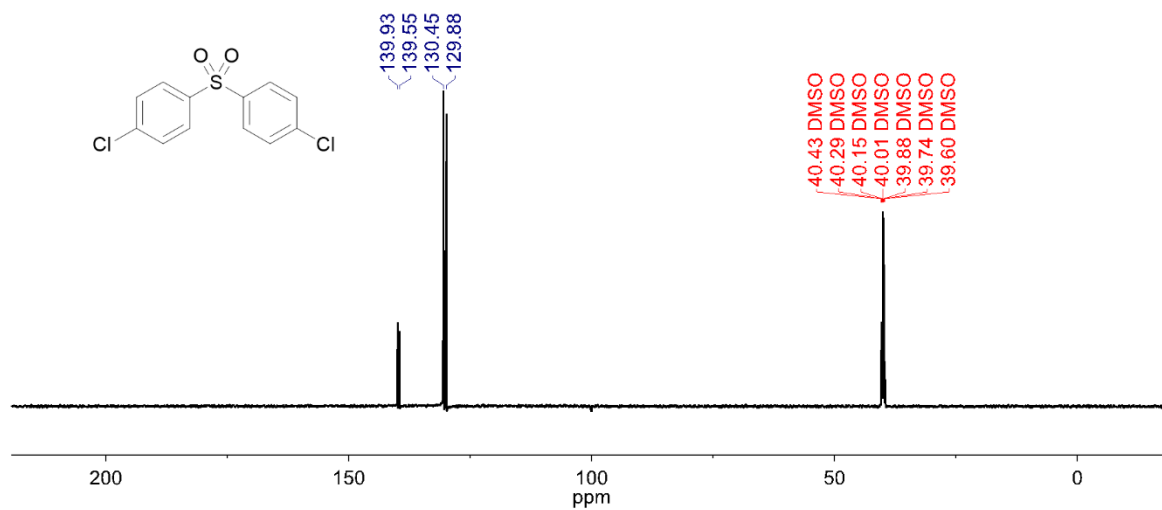


Figure B. 6. <sup>13</sup>C-NMR of DCDPS as the second monomer in PSF polymerization, using DMSO-d<sub>6</sub> as the NMR solvent [1].

### B.3.3. Polysulfone (PSF)

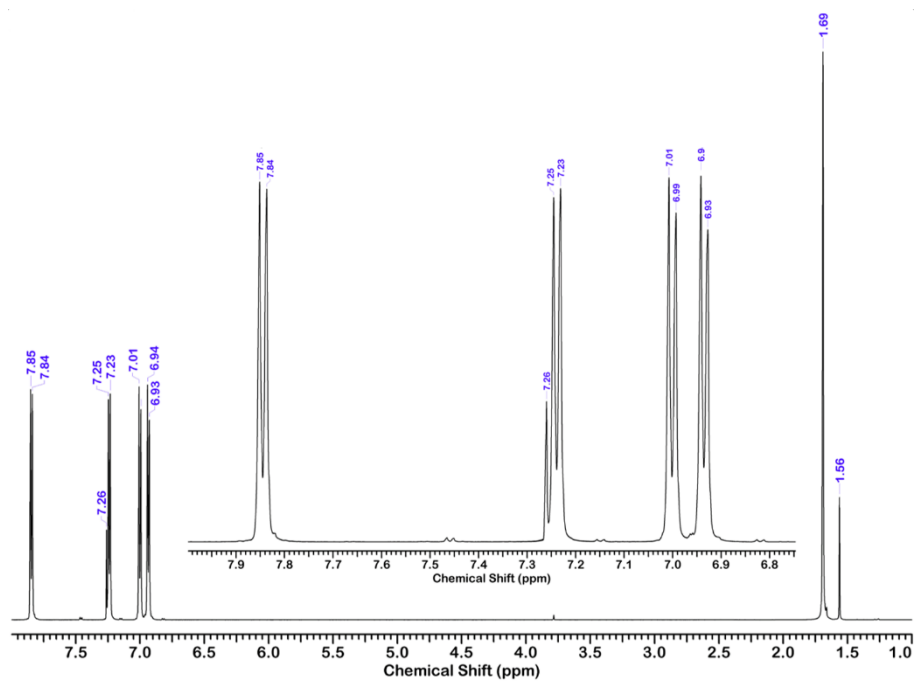


Figure B. 7. <sup>1</sup>H-NMR spectra of commercial PSF, using CDCl<sub>3</sub> as the NMR solvent.

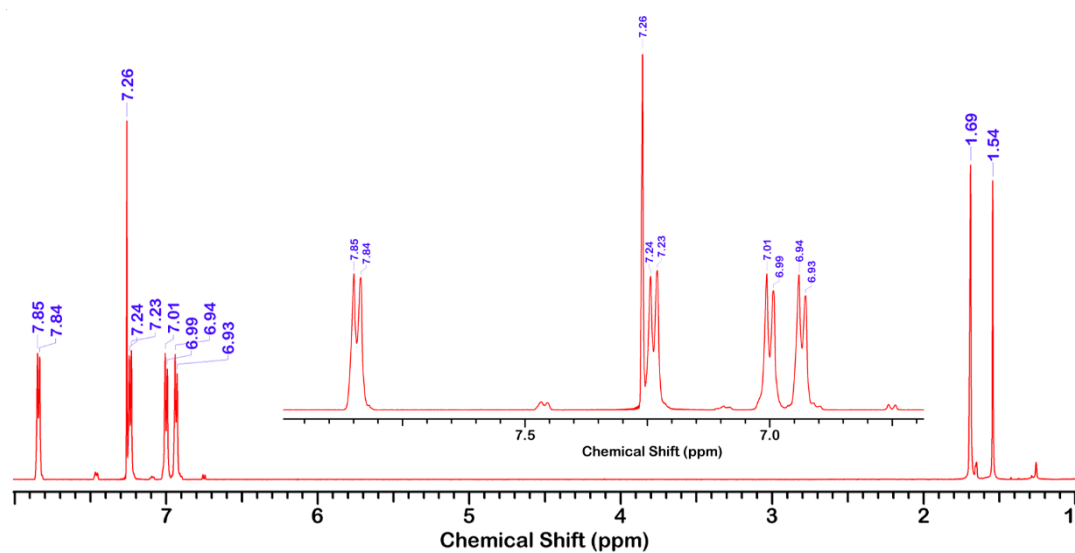


Figure B. 8.  $^{13}\text{C}$ -NMR spectra of conventional synthesised PSF, using  $\text{CDCl}_3$  as the NMR solvent.

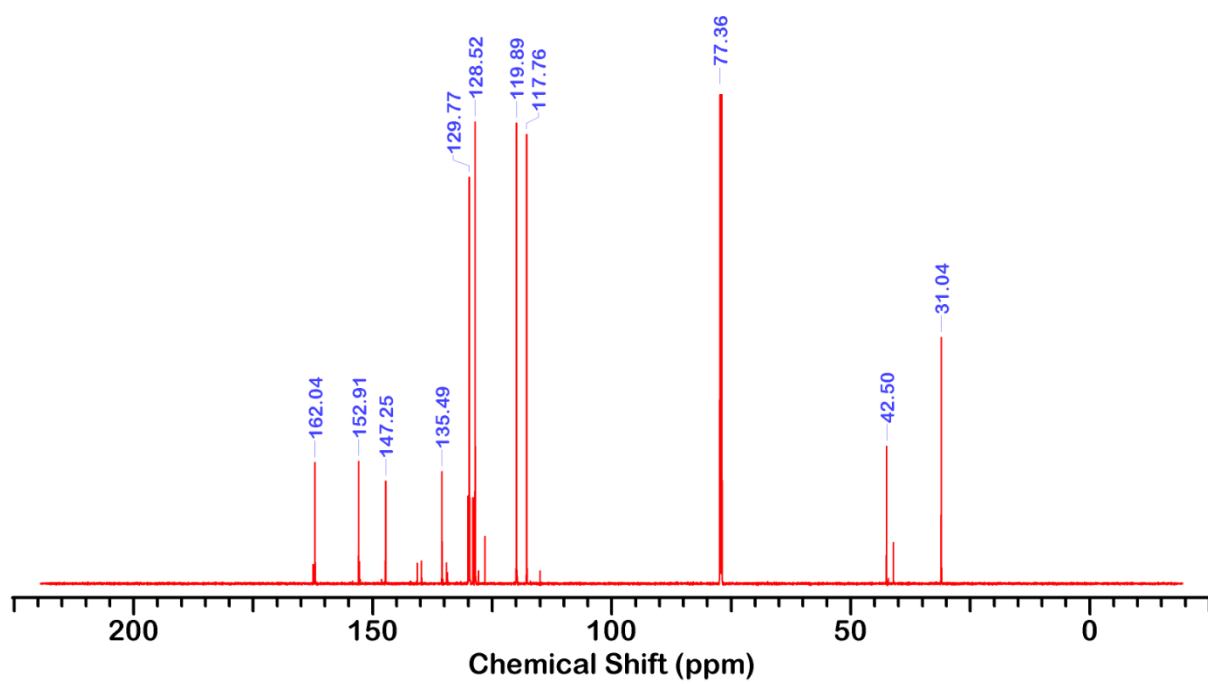


Figure B. 9.  $^{13}\text{C}$ -NMR spectra of conventional prepared PSF, using  $\text{CDCl}_3$  as the NMR solvent.

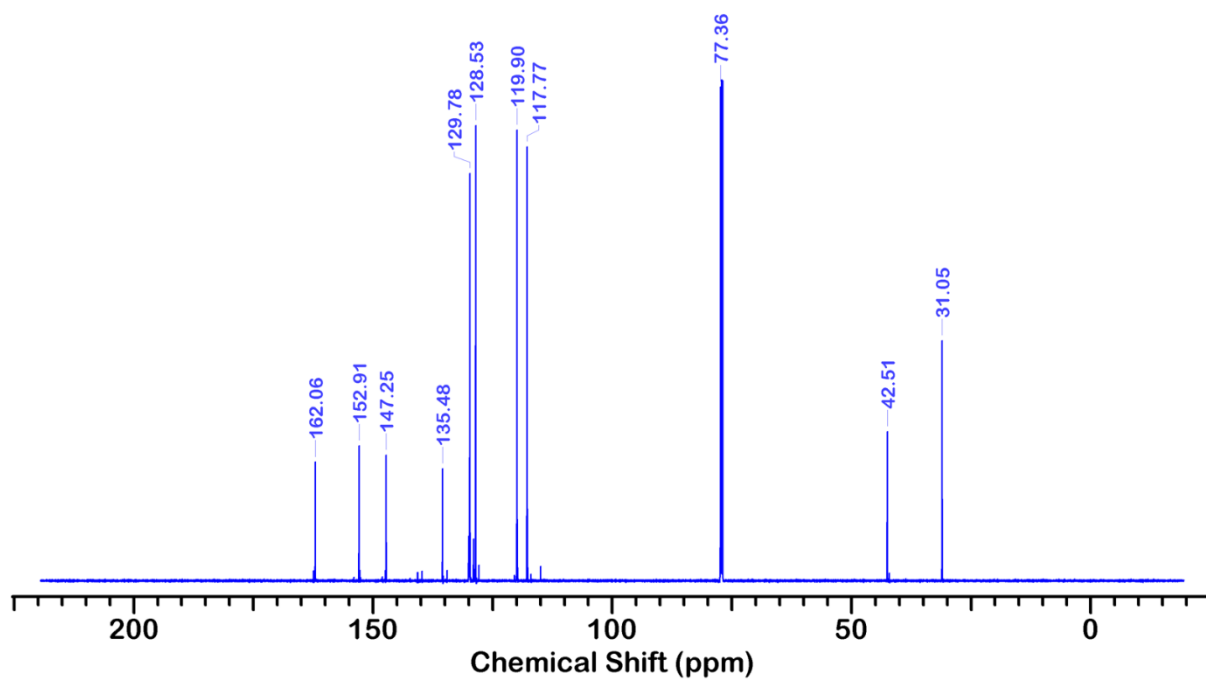


Figure B. 10.  $^{13}\text{C}$ -NMR spectra of VFD synthesised PSF at  $\omega$  6k rpm, T 160 °C,  $\theta$  45 tilt angle, and 60 min reaction time, using  $\text{CDCl}_3$  as the NMR solvent.

#### B.4. Chapter references

1. Igder, A., et al., *Vortex fluidic mediated synthesis of polysulfone*. RSC Adv, 2020. **10**(25): p. 14761-14767.

## Appendix C

### **Electronic Supplementary Information (ESI) of “Vortex fluidic mediated fabrication of polysulfone ultrafiltration membranes incorporating graphene oxide”**

Aghil Igder<sup>a,b</sup>, Wanling Cai<sup>b,c</sup>, Xuan Luo<sup>b</sup>, Ahmed Hussein Mohammed Al-Antaki<sup>b</sup>, Kasturi Vimalanathan<sup>b</sup>, Alireza Keshavarz<sup>a</sup>, Ataollah Nosrati<sup>a</sup>, and Colin L. Raston <sup>\*b</sup>

---

*a. School of Engineering, Edith Cowan University, Joondalup, Perth, WA 6027, Australia.*

*b. Flinders Institute for Nanoscale Science and Technology, College of Science and Engineering, Flinders University, Adelaide, SA 5042, Australia.*

*E-mail: [colin.raston@flinders.edu.au](mailto:colin.raston@flinders.edu.au).*

*c. School of Environmental Science and Engineering, Fujian Normal University, Fuzhou 350007, Fujian Province, China.*

## C.1. Experimental setup

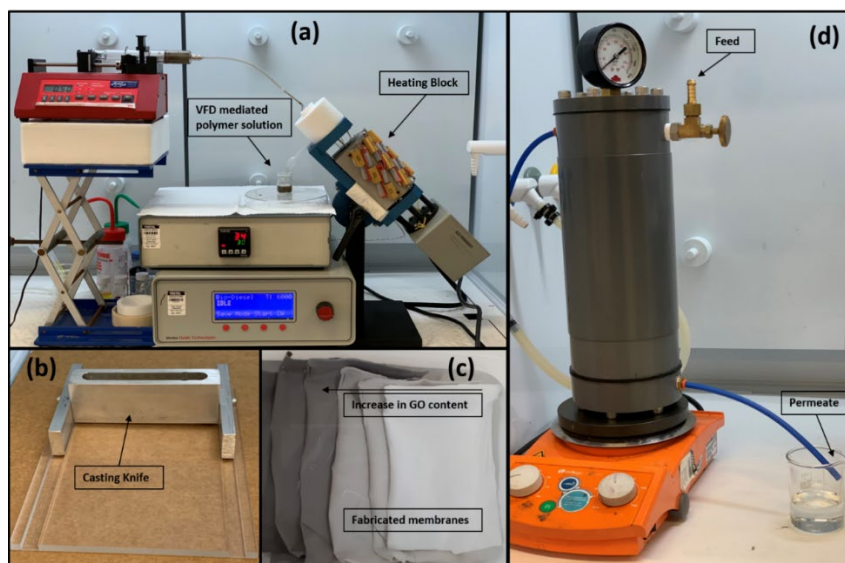


Figure C. 1. Experimental setup for the membrane fabrication steps including (a) continuous VFD setup, (b) adjusted casting knife on a glass surface, (c) fabricated membranes (pure PSF and GO/PSF composite membranes), (d) Dead-end filtration system adjusted on a magnet stirrer for stirring the solution inside the system and pressurising the solution using nitrogen gas up to 4 bar to generate the final permeate.

## C.2. Thermal stability

Thermal stability of the membranes was evaluated using thermogravimetric analysis on a Perkin Elmer STA 8000. Membranes were heated up to 850 °C from 30 °C at 10 °C/min under a nitrogen atmosphere and then held isothermal at 850 °C for 1 min followed by heating up again to 1050 °C with the same ramping rate now under an atmosphere of air.

Table C. 1. STA measurements settings

Sample name	PSF and GO/PSF membranes
Sample mass [mg]	≈ 5
Crucible	Ceramic
Temperature Program	50 ... 850 ... 1050 °C
Heating rate	10 °C / min
Atmosphere	Nitrogen, switch to air at 850 °C

### C.3. Contact angle measurements

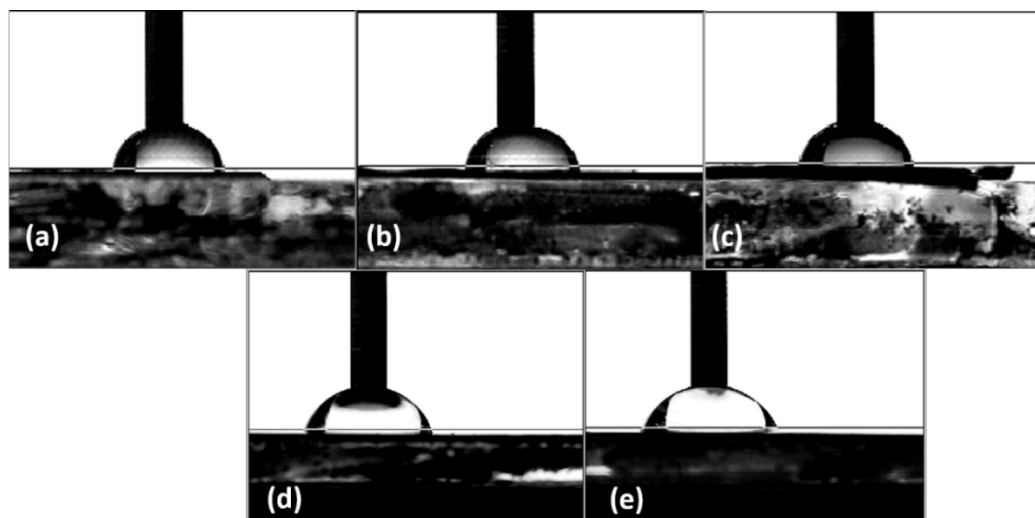


Figure C. 2. Images of captive needle drop on (a) pristine PSF and GO/PSF composite membranes with (b) 0.25, (c) 0.5, (d) 1, and (e) 2 wt.% GO content, while 5  $\mu$ L milli-Q water was dispensed on their surface for a period of 10 seconds, whereupon the droplet surface contact angle was recorded.

### C.3. SEM images

#### C.3.1. SEM of the top of the membranes

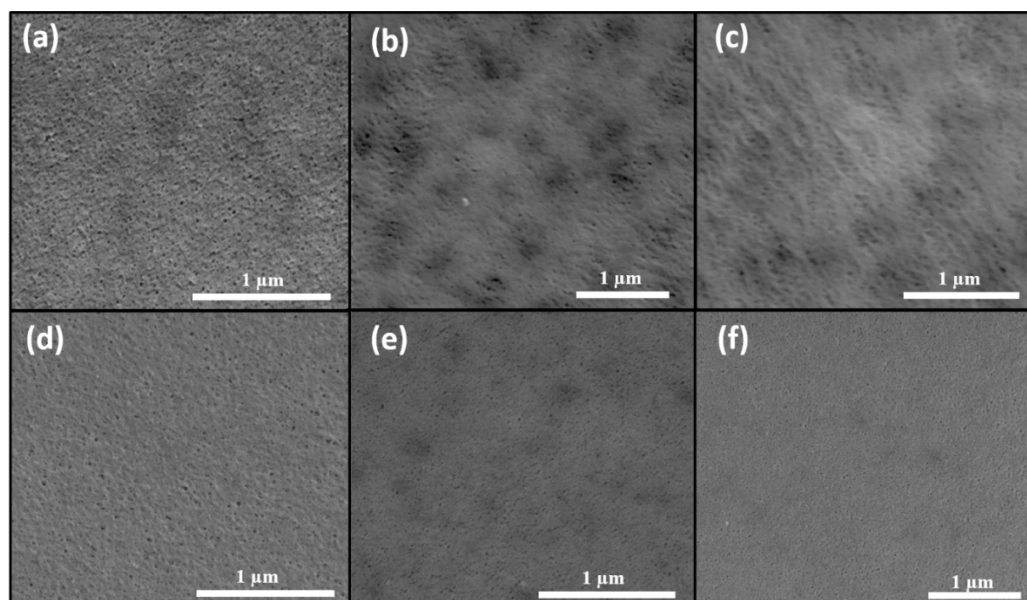


Figure C. 3. SEM images from the top surface of the bare PSF membranes obtained from a 15% PSF solution (a) conventional mixed, mediated in the VFD at 30  $^{\circ}$ C, 45 $^{\circ}$ , and 0.5 mL/min with different rotational speeds (b) 4k, (c) 5k, (d) 6k, (e) 7k, and (f) 8k rpm.

### C.3.2. SEM of the bottom of the membranes

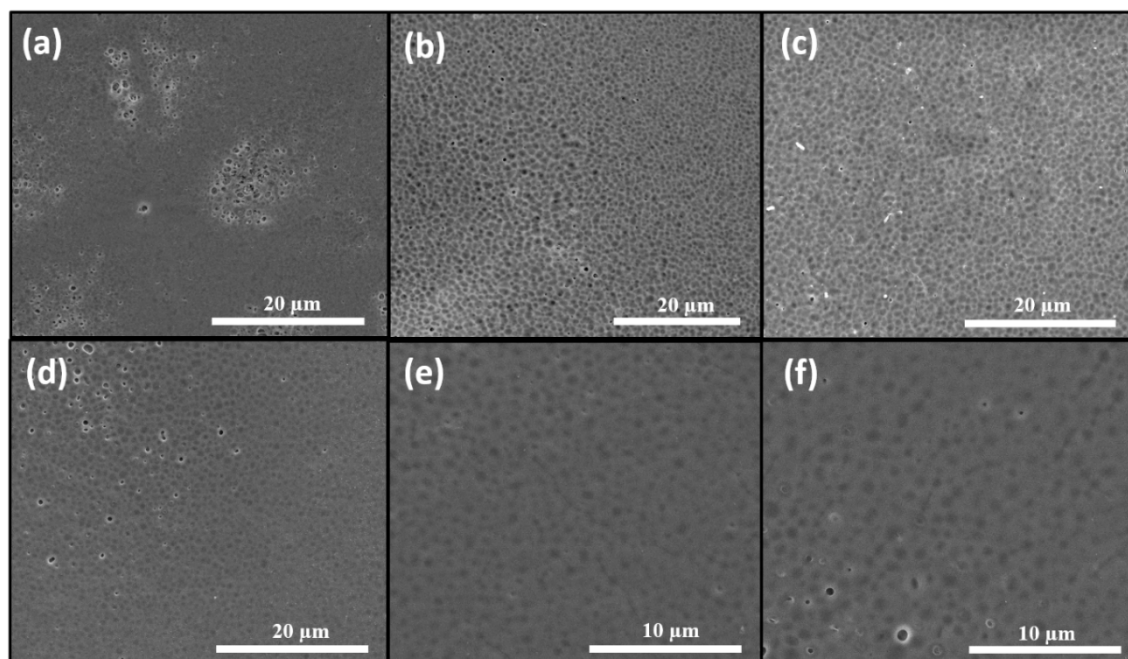


Figure C. 4. SEM images from the bottom surface of the bare PSF membranes obtained from a 15% PSF solution (a) conventional mixed, mediated in the VFD at 30°C, 45°, and 0.5 mL/min with different rotational speeds (b) 4k, (c) 5k, (d) 6k, (e) 7k, and (f) 8k rpm.

### C.4. BSA rejection using UV light absorbance

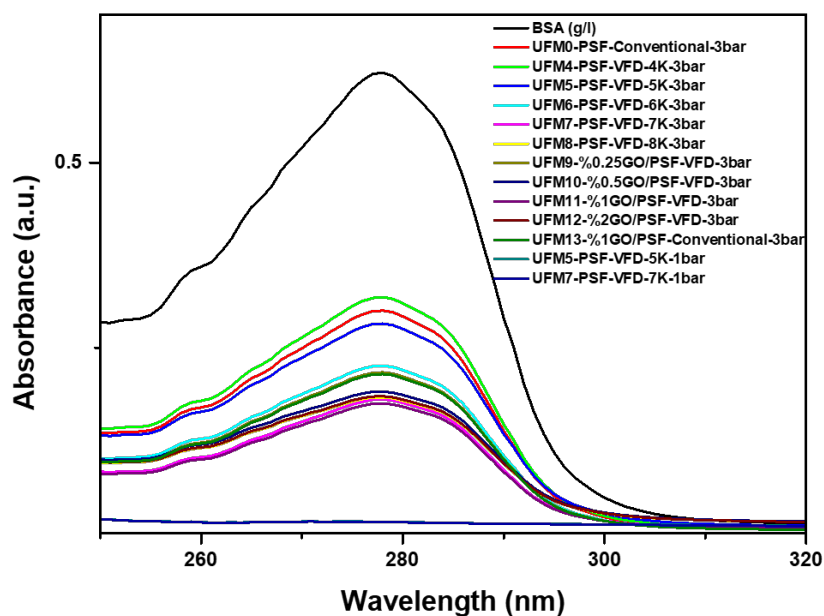


Figure C. 5. UV-vis spectra of BSA from the permeate of the BSA filtration process for a 1000 mg/L solution, using pure PSF or GO/PSF membranes in a dead-end filtration system under 3 bars and 1 bar pressures.



## C.5. Mechanical properties

### C.5.1. Effect of PSF concentration in the VFD on tensile strength and elongation to break.

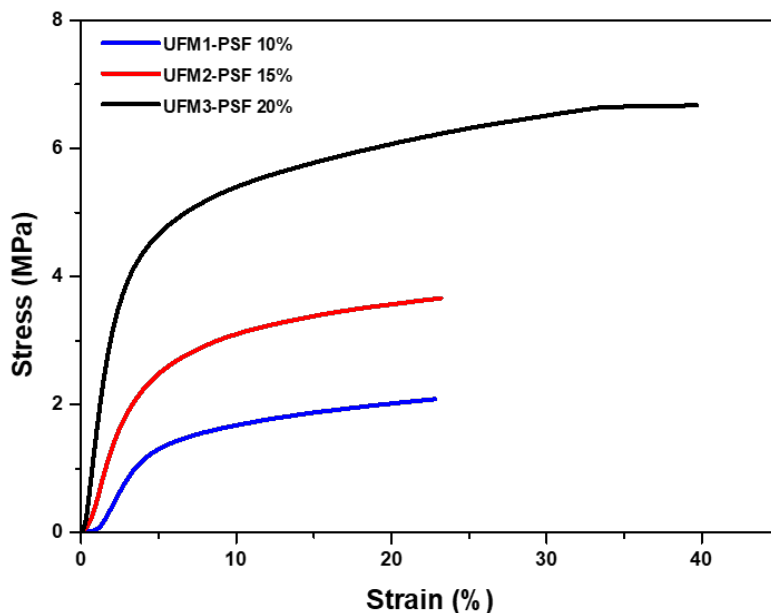


Figure C. 6. Typical stress–strain curves of PSF membranes fabricated in different PSF concentrations (10, 15, 20%) using VFD mixing.

### C.5.2. Effect of VFD rotational speed on tensile strength and elongation to break.

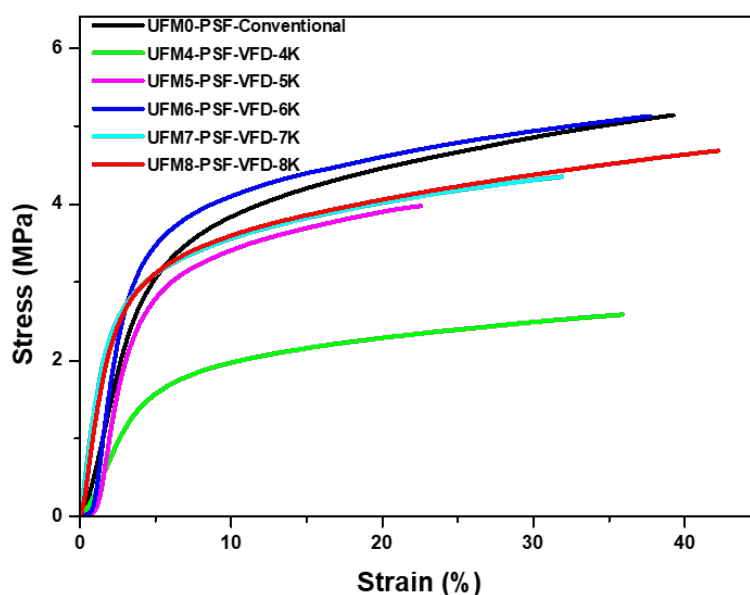


Figure C. 7. Typical stress–strain curves of PSF membranes fabricated from 15% PSF solutions from VFD mixing process in different rotational speeds using conventional mixing process.

### C.5.3. Effect of GO content on tensile strength and elongation to break of the VFD mediated membranes

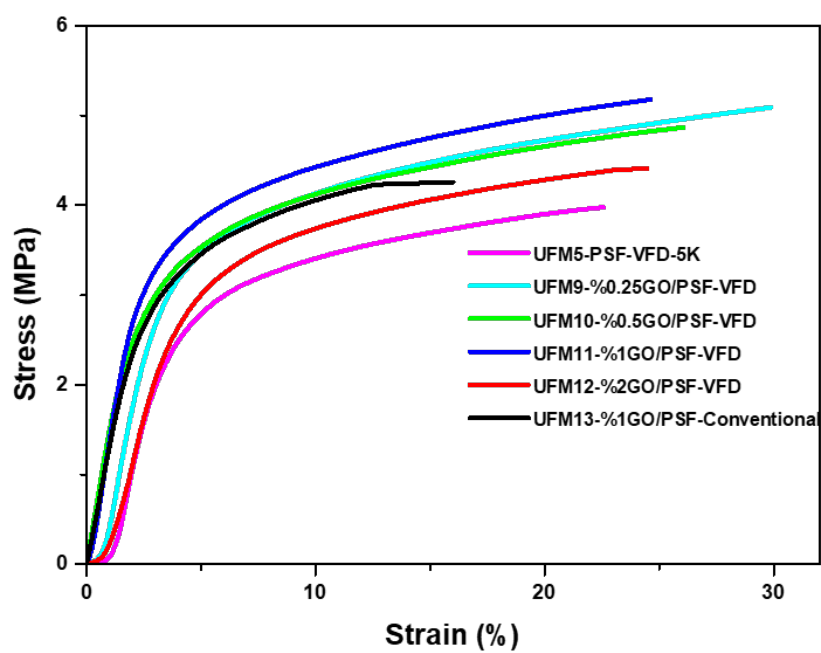


Figure C. 8. Typical stress–strain curves of bare PSF membrane and GO/PSF composite membranes fabricated from 15% PSF solutions with different GO content (0.25-2%) using VFD and conventional mixing processes.

## Appendix D

This section is a subdivision of a massive joint research work [1], with the below title and authorship list which has been submitted to ChemRxiv with the mentioned DOI. Author in this chapter intends to just bring the sections of the work which have been investigating the topological fluid flow in the VFD which resulted in introducing a new phenomenological shear stressed molecular drilling in the thin film of polysulfone in the VFD while fabricating ultrafiltration membranes. Noteworthy to mention that these results about molecular drilling and double helical flow in the VFD have been obtained on the way to fabricate the ultrafiltration membrane and supported the other research groups work in introducing:

### **Sub-micron moulding topological mass transport regimes in angled vortex fluidic flow**

*Thaar M. D. Alharbi,<sup>1,2,8</sup> Matt Jellicoe,<sup>1,8</sup> Xuan Luo,<sup>1,3,8</sup> Kasturi Vimalanathan,<sup>1</sup> Ibrahim K. Alsulami,<sup>1</sup> Bediea S. AL Harbi,<sup>1</sup> Aghil Igder,<sup>1,4</sup> Xianjue Chen,<sup>5</sup> Keith A. Stubbs,<sup>6</sup> Justin M. Chalker,<sup>1</sup> Wei Zhang,<sup>3</sup> Ramiz A. Boulos,<sup>1,7</sup> Darryl B. Jones,<sup>1</sup> Jamie S. Quinton,<sup>1</sup> and Colin L. Raston<sup>\*1</sup>*

1. Flinders Institute for Nanoscale Science and Technology, College of Science and Engineering, Flinders University, Bedford Park, SA 5042, Australia [colin.raston@flinders.edu.au](mailto:colin.raston@flinders.edu.au)
2. Physics Department, Faculty of Science, Taibah University, Almadinah Almunawarrah 42353, Saudi Arabia
3. Centre for Marine Bioproducts Development, College of Medicine and Public Health, Flinders University, Adelaide, SA 5042, Australia.
4. School of Engineering, Edith Cowan University, Joondalup, Perth, WA 6027, Australia.
5. School of Chemistry, University of New South Wales, Sydney, NSW 2052, Australia.
6. School of Molecular, The University of Western Australia, 35 Stirling Hwy, Crawley, WA 6009, Australia.
7. BrightChem Consulting, Suite 16, 45 Delawney Street, Balcatta, WA 6021, Australia.
8. Authors contributed equally to this work.
9. For the full paper refer to: <https://doi.org/10.26434/chemrxiv.13141352.v1>

## Contents of the full paper

1. General materials and methods
2. Temperature change in the VFD for different solvents at different rotational speeds ( $\omega$ ) and inclination angle ( $\theta$ )
3. Mixing times of water at different rotational speeds and inclination angle in a 10 mm OD tube.
4. Captured images from high speed photography of a thin film in a 10 mm OD VFD glass tube,  $\theta = 45^\circ$
5. Average film thickness as a function of  $\omega$ , at  $\theta = 45^\circ$
6. Manipulating graphene oxide in DMF in the VFD
7. Controlling the assembly of fullerene C<sub>60</sub>
8. Moulding of polysulfone (PSF) in the VFD, molecular drilling control experiments and real time VFD processing small angle neutron scattering (SANS) (**Focus of this Appendix**)
9. BSA polymerisation with glutaraldehyde
10. MOF-5 fabrication
11. Fluid dynamics within the VFD

## Abstract

Induced mechanical energy in a thin film of liquid in an inclined rapidly rotating tube in the vortex fluidic device (VFD) can be harnessed for generating non-equilibrium conditions, which are optimal at  $45^\circ$  tilt angle, but the nature of the fluid flow is not understood. Through understanding that the fluid exhibits resonance behaviours from the confining boundaries of the glass surface and the meniscus that determines the liquid film thickness, we have established specific topological mass transport regimes. These topologies have been established through materials processing, as circular flow normal to the surface of the tube, ***double-helical flow across the thin film***, and spicular flow, a transitional region where both effects contribute. This includes new phenomenological shear stressed crystallization and ***molecular drilling***. The manifestation of these patterns has been observed by monitoring mixing times, temperature profiles, and film thickness against rotational speed of liquids in

the tube. The grand sum of the different behavioural regimes is a general fluid flow model that accounts for all processing in the VFD at an optimal tilt angle of  $45^\circ$ , and provides a new concept in the fabrication of novel nanomaterials and controlling the organisation of matter.

## D.1. Introduction

Controlling organisation and forces in liquids under non-equilibrium conditions is fundamental for building complex systems and the function of living cells [2]. Shear stress in dynamic thin films, as in vortex fluidics, can be harnessed for generating non-equilibrium conditions. A rapidly rotating inclined tube in the vortex fluidic device (VFD) imparts shear stress (mechanical energy) into a thin film of liquid, depending on the physical characteristics of the liquid and rotational speed,  $\omega$ , tilt angle,  $\theta$ , and diameter of the tube [3-8]. However, the nature of the fluid flow in this thin film microfluidic platform is not understood. Understanding fluid flow in general is important in microfluidics where processing has primarily focused on manipulating liquids through channels [9]. A less developed area of microfluidics involves films of liquid  $\leq 500\ \mu\text{m}$  thick which are centrifugally generated by passing liquids over rotating surfaces, as in spinning disc processors (reactors) [10, 11], horizontally aligned rotating tube processors [11, 12] and in the vortex fluidic device (VFD) [3-8]. The latter is a variant of the rotating tube processor but where the orientation of the tube,  $\theta$ , can be varied [3-8] and is distinctly different to Couette flows where liquids are periodically forced between two surfaces [13]. These processors are also distinctly different to conventional microfluidics and do not suffer from clogging. They are effective in controlling chemical reactions, probing the structure of self-organised systems, and in the top down and bottom up synthesis of nanomaterials [3, 10, 11]. Control of the flow environment in the VFD itself has been shown effective in a variety of applications, including in accelerating enzymatic reactions [4], folding proteins [5], slicing carbon nanotubes [6], exfoliating graphene [7], and wrapping bacteria in graphene oxide [8]. For the standard 20 mm diameter (internal diameter 17.5 mm) quartz or glass tube in the VFD, changing the fluid flow behaviour with the rotational speed ( $\omega$ ) over the range of 3k to 9 k rpm has revealed benefits of the device most effectively at a  $\theta = 45^\circ$  tilt angle [3]; 9k rpm rotational speed is the upper limit of the VFD housing a 20 mm (or 10 mm) OD tube.

Establishing the nature of the complex fluid dynamics within the VFD for utility in chemical processing has proved challenging. A general model for determining the film thickness and the distance it extends up the tube, depending on  $\theta$  and  $\omega$ , has been established [14], but there is the realisation that other factors must be involved, beyond vibrations within the system [15, 16]. Experimental attempts to observe the fluid flow in the VFD have been hampered by unavoidable distortions, estimated to be  $<100\text{ }\mu\text{m}$ . Direct measurement of fluid flow at the dimensionality of processing materials ( $\sim 1$  to  $5\text{ }\mu\text{m}$ ), for example, in scrolling graphene oxide (GO) [17] and generating cones of assembled fullerene  $\text{C}_{60}$  [18], is a longstanding issue. Interestingly, it has been demonstrated that standing waves on the surface of a liquid provide templates for microscale materials to assemble into ordered structures, which take on the shape defined by the standing wave [19]. We hypothesised that this relationship could be inverted to provide insight into the spatial arrangement of mass transport patterns within the VFD at micron and sub-micron dimensions, depending on the experimental conditions, as moulding or templating materials processing outcomes. The range of structures can be explained by identifying which fluid flow phenomena dominate in the VFD at an inclination angle of  $\theta = 45^\circ$ , which is the optimal angle for applications of the VFD [3-8]. The fluid flow phenomena include rotational speed dependent Coriolis driven circular flow; double-helical topological flow associated with the onset of Faraday waves, previously reported as a mechanical response from vibrations [15], that couple with the Coriolis driven circular flow; and the combined interplay of these giving spicular flow [1]. From the abovementioned fluid behaviour, in this section, the effect of double helical flow which results in a new phenomenological shear stressed *molecular drilling* is investigated with the experiments leading to these findings as described below.

## D.2. General materials and characterisation methods for polymer moulding

High molecular weight polymer beads of polysulfone (PSF) were purchased from Sigma Aldrich. Dichloromethane (DCM) (99.8%), toluene (99.5%) and hexane fraction were purchased from Chem-Supply.

PSF thin film samples were characterized using scanning electron microscopy (SEM) performed using a FEI Quanta 450, coated with 5 nm platinum. Real-time SANS experiments

were done at the Australian Nuclear Science and Technology Organisation (ANSTO), using the Quokka instrument. Other materials and techniques for full characterisations also have been used in this research which were not the focus of polymer moulding and were elaborated in the full paper to support our results.

### D.3. Moulding of PSF in the VFD

Different concentrations of a PSF solutions were explored to generate a uniform thin-film adhering to the inner surface of the tube. Ultimately this led to using 1 mL of 50 mg/ml of PSF dissolved in dichloromethane (DCM) to generate such a film, Figure D. 1. This involved adding a solution of the polymer to a VFD tube (20 mm OD, 17.5 mm ID) tilted at 5° which was then spun at 6k rpm for ~15 min. Evaporation was facilitated by high mass and heat transfer in the tube which was left open to the atmosphere. The film was washed several times with hexane and then dried under a flow of dry nitrogen. Sections of the film was then peeled from the surface of the tube at three different locations, Figure D. 2. Figure D. 3 shows that the thin film created in the VFD is relatively uniform with occasional deformations on the upper surface (air contact) whereas the lower surface (glass contact) is smooth - devoid of any structure variation.

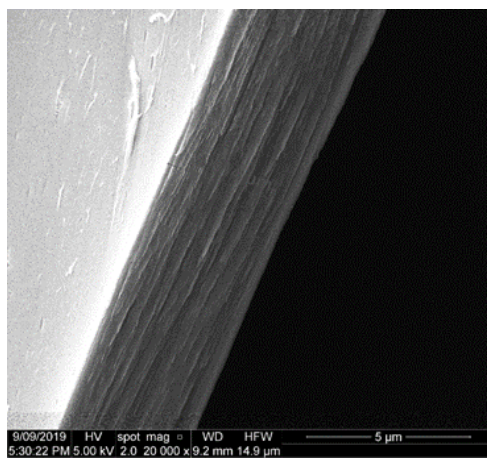


Figure D. 1. SEM image of the thin-film of PSF created in the VFD tube (20 mm OD, 17.5 mm ID) at 6k rpm rotational speed,  $\theta = 5^\circ$  and room temperature during 15 min, after adding 1 mL of 50 mg/ml of PSF dissolved in DCM.

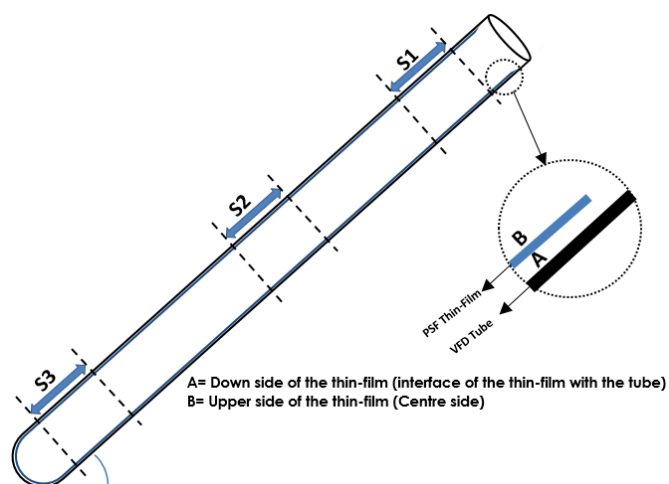


Figure D. 2. Locations of samples S1, S2 and S3 taken from the PSF thin-film formed in the VFD; sample S1A and S1B refer to the interface of film with the tube and air from the bottom of the tube respectively, and similarly S2A and S2B, and S3A and S3B, from the middle and top of the tube.

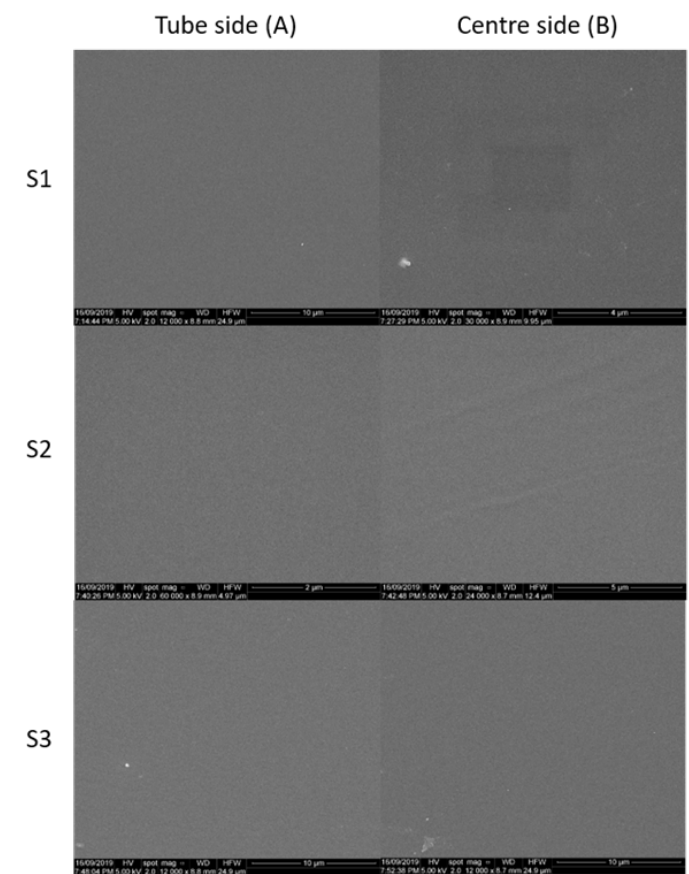


Figure D. 3. SEM images of S1, S2, and S3 from both sides (left: bottom of the thin film, right: upper side of the thin-film) of a thin-film created in the VFD (20 mm OD tube) at 6k rpm,  $\theta = 5^\circ$ , at room temperature during 15 min of processing.



Toluene and water (0.5 mL) were independently added to a VFD tube coated with a thin film of PSF, in which the polymer is only sparingly soluble, and the tube was rotated at 7k rpm at  $\theta = 45^\circ$ , at room temperature, for one hour. After processing, the liquid was drained, and the film washed with hexane several times and purged with nitrogen gas for drying purposes, for 2h. A section of the film was removed from the middle of each tube and studied using SEM, Figure D. 4 and Figure D. 5, for toluene and water respectively, with the red arrow essentially parallel to the rotation axis of the tube when  $\theta = 45^\circ$ , and in the direction of the upper lip. This revealed arrays of indentations and some holes on the side A of the polymer film processed in toluene, with a limited number of such structures for water. SEM imaging the other side of the PSF film (side B) post-VFD processing using the same conditions revealed smooth surface, for both toluene or water (Figure D. 6). Given the structures revealed on surface SA for toluene, all subsequent processing was done in toluene followed by washing with hexane, and as a control, processing in toluene and not washing with hexane afforded the same morphology, Figure D. 7. The change in morphology of the surface of the PSF film that was in contact with the glass during VFD in toluene provides information on the fluid behaviour, as shown diagrammatically in Figure D. 8 and Figure D. 9.

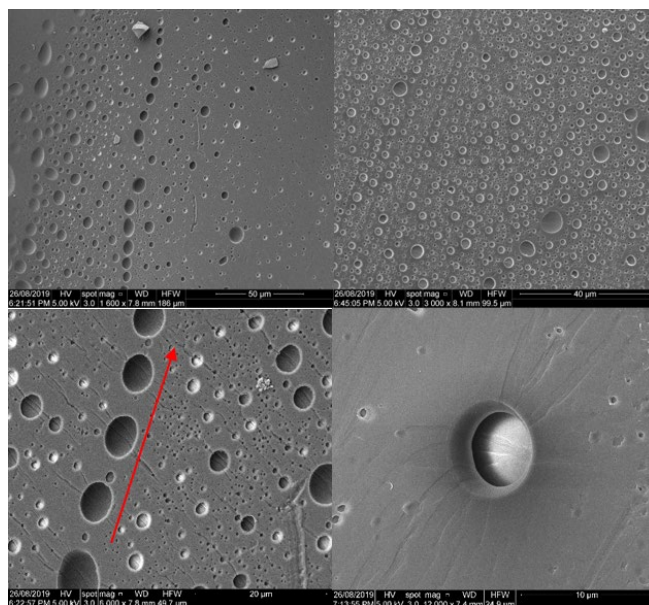


Figure D. 4. SEM images of the central inner surface of the film (S2A) after VFD processing (20 mm OD, 17.5 mm ID tube) in toluene, at room temperature  $\omega$  7k rpm,  $\theta$   $45^\circ$  for  $\sim$ 1h, after washing with hexane.

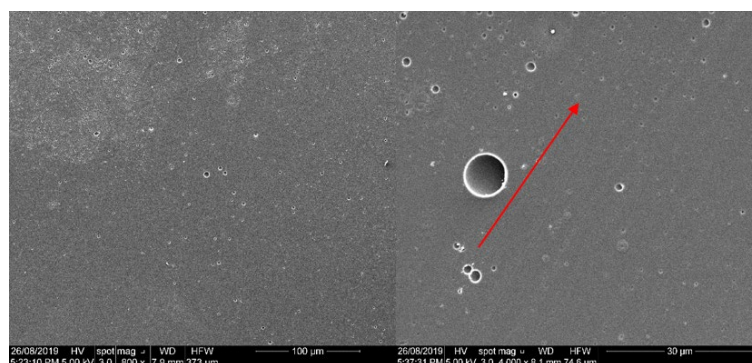


Figure D. 5. SEM images of the central inner surface of the film (S2A) after VFD processing (20 mm OD tube) in water, at room temperature,  $\omega$  7k rpm,  $\theta$  45°, for ~1h, after washing with hexane.

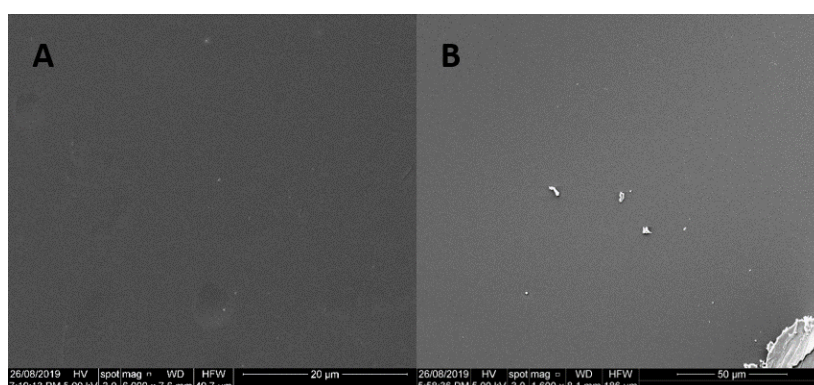


Figure D. 6. SEM images of the central upper surface (S2B) after VFD processing, at room temperature  $\omega$  7k rpm,  $\theta$  45° for ~1h, in (A) toluene and (B) water, after washing with hexane and drying with nitrogen gas for 2h.

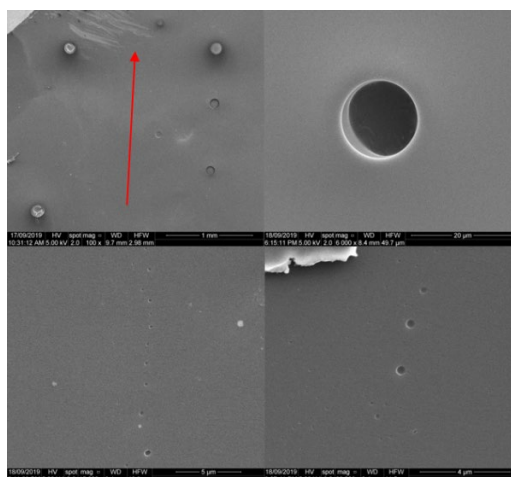


Figure D. 7. SEM images of the central inner surface of the film (S2A) after VFD processing (20 mm OD tube) in toluene, at room temperature  $\omega$  7k rpm,  $\theta$  45° for ~1h, and drying with nitrogen gas for 2h, without washing with hexane prior to SEM imaging.

## D.4. Discussion

These findings showed that double helical flow along with the other fluid dynamic behaviour in the VFD will impact on the movement of the liquid (mixing), and consequently, the resultant heat and mass transfer. They also reveal that there are domains of fluid flow in the VFD where any outcome of processing is not limited by conventional bulk diffusion control, but rather this is compounded by orientation effects associated with diffusion or mass transport that appears within the different topological flow regimes.

The presence of double helices in the film is illustrated below for the case of ‘drilling holes’ in thin film of polymers attached to the inside of the tube, where preferential etching occurs due to increased localised mass transport regimes), and amplified where the film thickness change is dramatic and readily measurable.

We explored the possibility of double-helical flow generating holes in a thin layer of polymer attached to the inner surface of the tube, with polysulfone as the polymer of choice. Surprisingly the arrangement of holes that potentially arise from double-helices was determined from the surface of the polymer attached to the glass tube rather than the surface in contact with the liquid.

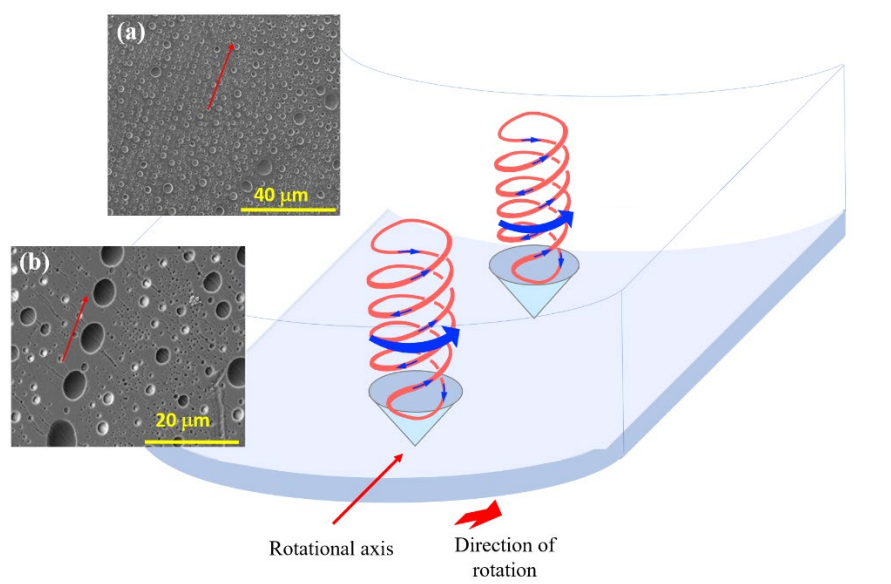


Figure D. 8. Signature of the pattern of the double-helical flows formed at the interface of the glass tube and a thin film of polysulfone (ca 5 μm) formed in toluene at 20 °C,  $\theta = 45^\circ$ , 7k rpm rotational speed, along the length of the tube, with the arrow representing the rotational direction of the axis of the tube [\[1\]](#).

Peeling the polymer from the glass surface revealed lines of regularly arranged holes several  $\mu\text{m}$  in diameter, Figure D. 8 when the solvent here was toluene with the tube rotating at 7k rpm, where double-helical flow prevails, (and more supplementary Information from the control experiments in Figure D. 11-19).

The holes are arranged in lines co-parallel to the rotational axis of the glass tube. This arrangement demonstrates points of localisation where the diffusion of material is highest, and can explain the ability of double-helical flow to exfoliate graphene from graphite<sup>6</sup> and the unscrolling of GO into flat sheets, (Figure 3(a) in the main manuscript, [1]), between rows of vertically arranged double-helices that are the liquid analogy of adjacent rollers used to produce flat sheet products. The original proposed mechanism involved exfoliation at the interface of the graphite flakes and the surface of the tube, and/or at the interface of the liquid and graphite held parallel to the surface of the tube [7]. The mechanism of formation of these holes, Figure D. 9, is potentially understood by the notion of double-helical ‘molecular drills’ piercing the polymer film, and when they move to other locations, the centrifugal force results in collapse of the holes, trapping liquid at the base, with smoothing of the upper surface. The ability for the fluid flow to pierce the polymer layer is consistent with the friction associated with the double-helical flow striking the surface of the tube thereby increasing the temperature of the liquid, and the melting the polymer which has an onset of glass  $> 120\text{ }^{\circ}\text{C}$  [20]. In addition, the pattern of holes is commensurate with the presence of arrays of Faraday waves on larger length scales.

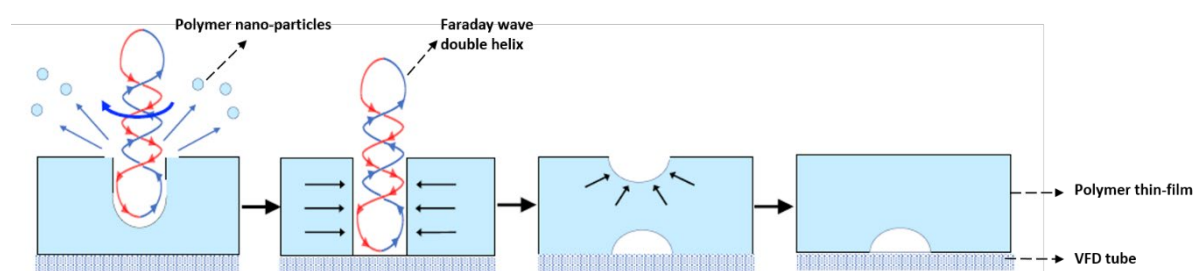


Figure D. 9. Schematic steps of shear stress ‘molecular drilling’ of holes on polysulfone with their signature retained at the glass-polymer interface post positional shift of the double-helical fluid flow [1].

This hypothesis was supported with the other results obtained from the other material processing research, mentioned by details in the main manuscript, as well as with the control experiments as elaborated below. Below mentioned control experiments were carried out to

monitor the effect of fluid flow on the polymeric thin film which finally resulted in the significant effect of the double-helical fluid flow at the optimal rotational speeds (>7k rpm) for this specific solvent and polymer of choice.

## D.5. Molecular drilling control experiments

Table D. 1. Control experiments for determining the ‘molecular drilling’ on a PSF thin film in the VFD tube, in high shear fluid flow at room temperature. \*

Sample	Rotational Speed (k rpm)	$\theta$ (°)	Volume of Toluene (mL)	Time (min)
Thin-film	6k	5	----	15
1	7k	45	0.85	30
2	5k	45	1.9	30
3	3.5	45	5	30
4	7	30	0.75	30
5	5	30	1.7	30
6	3.5	30	4.7	30
7	7	60	1	30
8	5	60	2.1	30
9	3.5	60	5.4	30

\* Notes:

- (i) The first entry is for creating the PSF thin-film in a VFD tube (20 mm OD, 17.5 mm ID) from a solution of the polymer in dichloromethane at 6k rpm, with  $\theta = 5^\circ$  to ensure the film is formed close to the full length of the tube during the evaporation of the solvent, ca 15 min.
- (ii) The volume of polymer solution for each sample corresponds to that required to create a film across the entire length of the tube at  $\theta = 5^\circ$ , with the then ‘molecular drilling’ experiments carried out at  $\theta = 30, 45$  and  $60^\circ$ .
- (iii) The films of PSF in the VFD were washed with hexane and purged with nitrogen gas prior to peeling off the glass tube.

- (iv) Three sections of the films (S1, S2 and S3, Figure D. 2) were taken from every sample, with both sides (A and B) studied using SEM, affording six images for each sample, designated S1A, S2A, S3A, S1B, S2B and S3B, as elaborated below.

### Thin-film

Rotational speed : 6k rpm

Tilt angle,  $\theta$  :  $5^\circ$

Solvent :  $\text{CH}_2\text{Cl}_2$

Time : 15 min

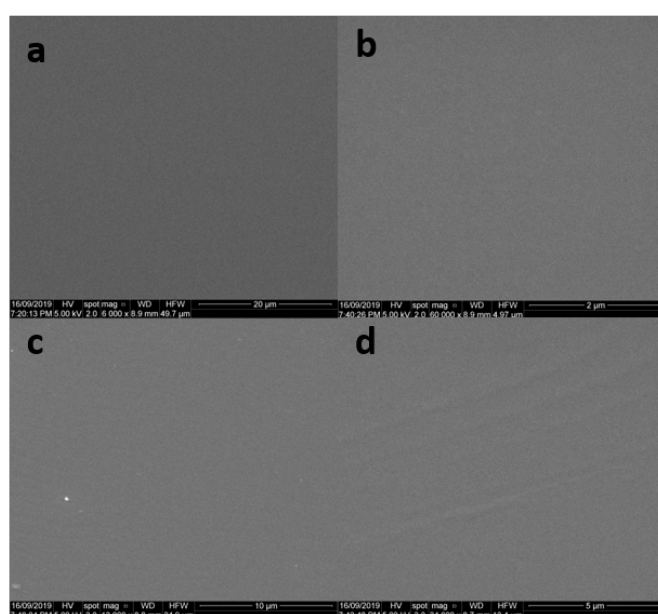


Figure D. 10. SEM images of PSF thin-film created in the VFD tube (20 mm OD) at 6k rpm,  $\theta = 5^\circ$  at room temperature during 15 min of evaporation of DCM: (a) S1A, (b) S2A, (c) S3A and (d) S2B, revealing smooth surfaces present, prior to processing in toluene.

### Notes:

- ✓ All the images shown in Figure D. 9-17:
  - were taken from the thin films processed in toluene, at specified  $\omega$  and  $\theta$  (mentioned in Table D. 1), room temperature and 30 min.
  - After processing in toluene, all of the samples were washed with hexane, and dried under nitrogen gas.
- ✓ The red arrows define the direction of rotation axis of the tube, directed out of the tube.



### Sample 1:

Rotational speed : 7k rpm

Tilt angle,  $\theta$  : 45°

Solvent : Toluene

Time : 30 min

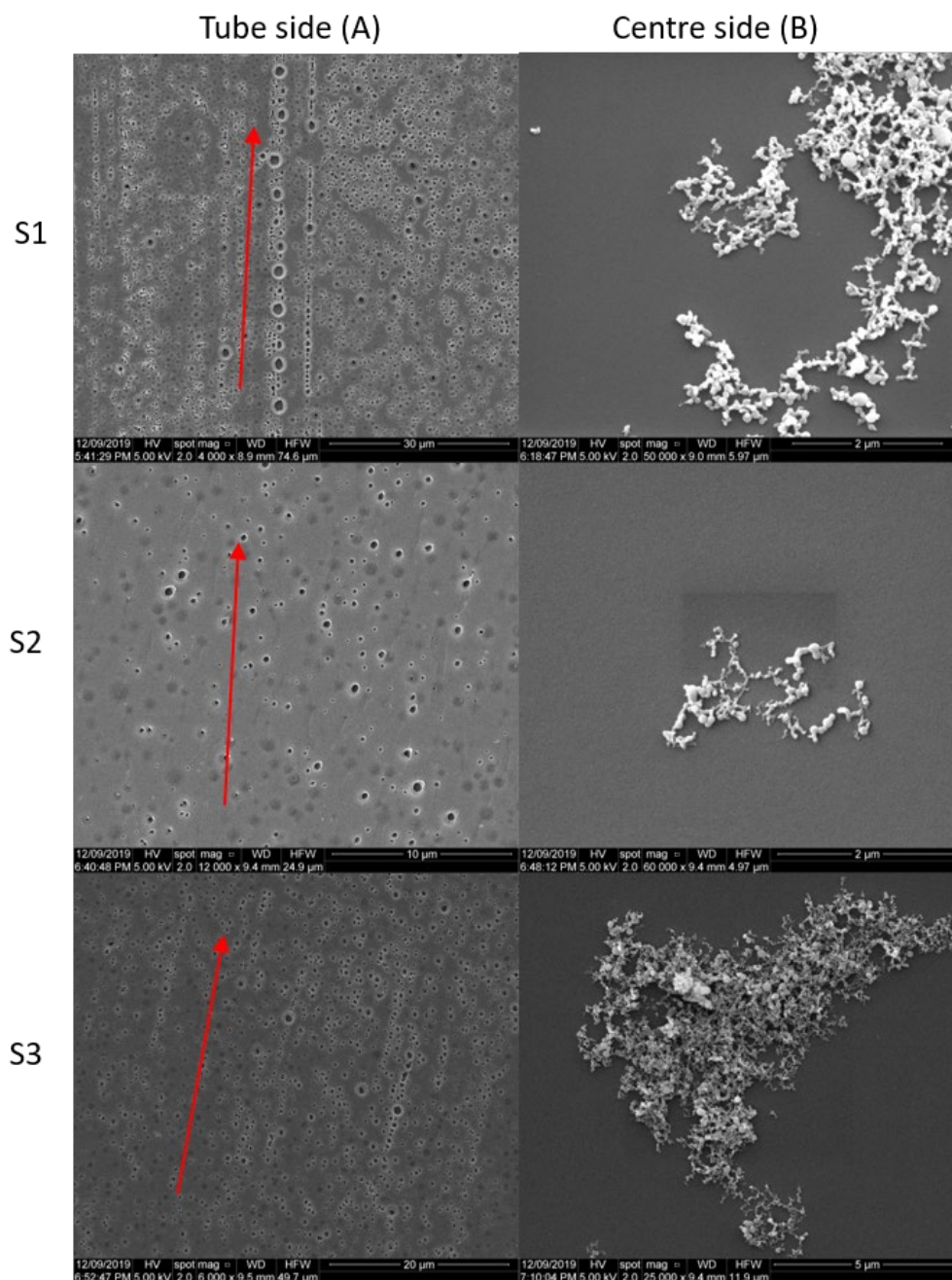


Figure D. 11. SEM images of S1, S2, and S3 from both sides (left: bottom of the thin film (A), right; upper side of the thin-film (B) of the thin-film processed in toluene at 7k rpm,  $\theta = 45^\circ$ , room temperature, and 30 min processing, then washed with hexane, and dried under nitrogen gas.

### Sample 2:

Rotational speed : 5k rpm

Tilt angle,  $\theta$  : 45°

Solvent : Toluene

Time : 30 min

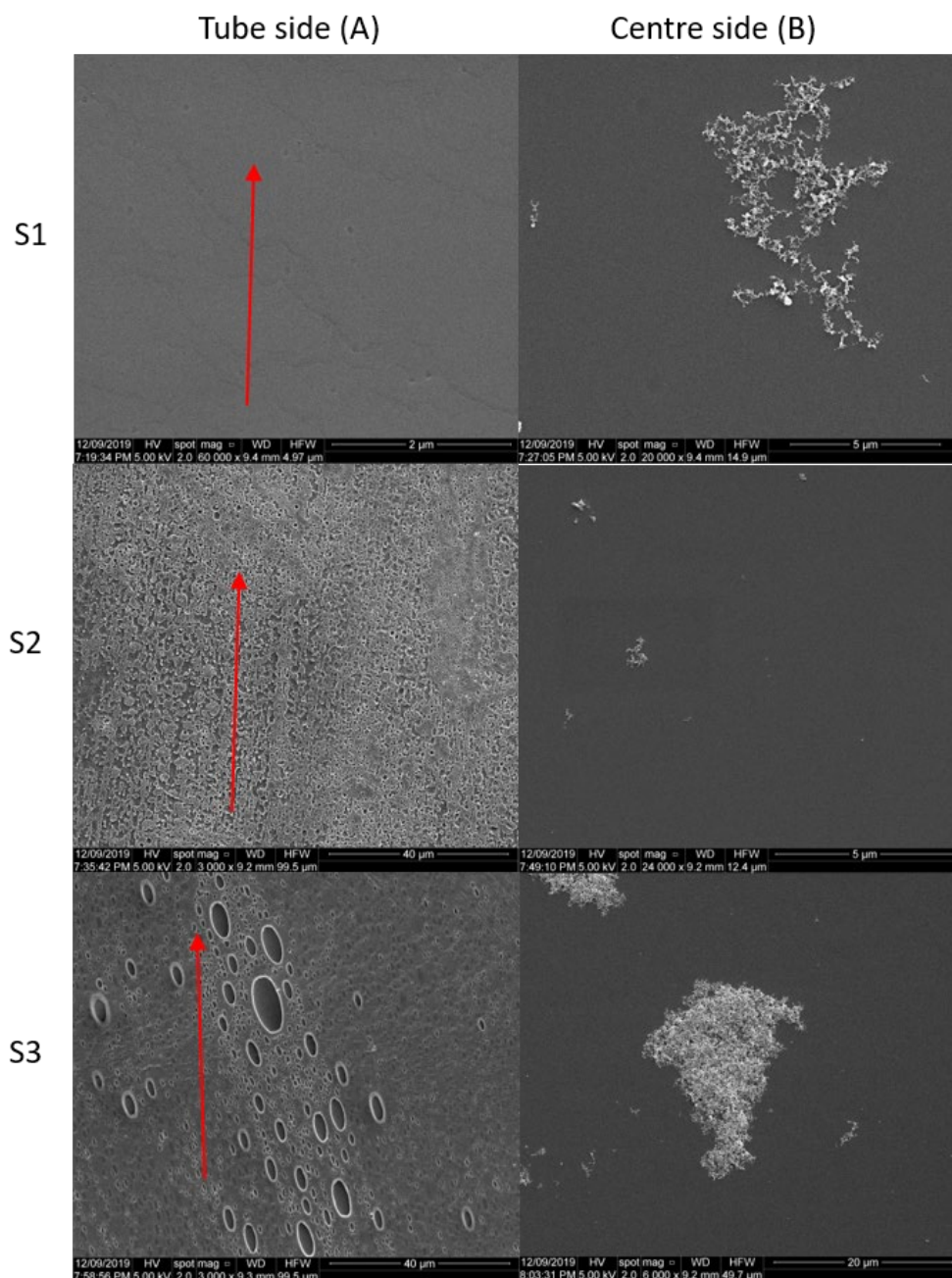


Figure D. 12. SEM images of S1, S2, and S3 from both sides (left: bottom of the thin-film (A), right; upper side of the thin-film (B) of the thin-film processed in toluene at 5k rpm,  $\theta = 45^\circ$ , room temperature, for 30 min processing.



### Sample 3:

Rotational speed : 3.5k rpm

Tilt angle,  $\theta$  : 45°

Solvent : Toluene

Time : 30 min

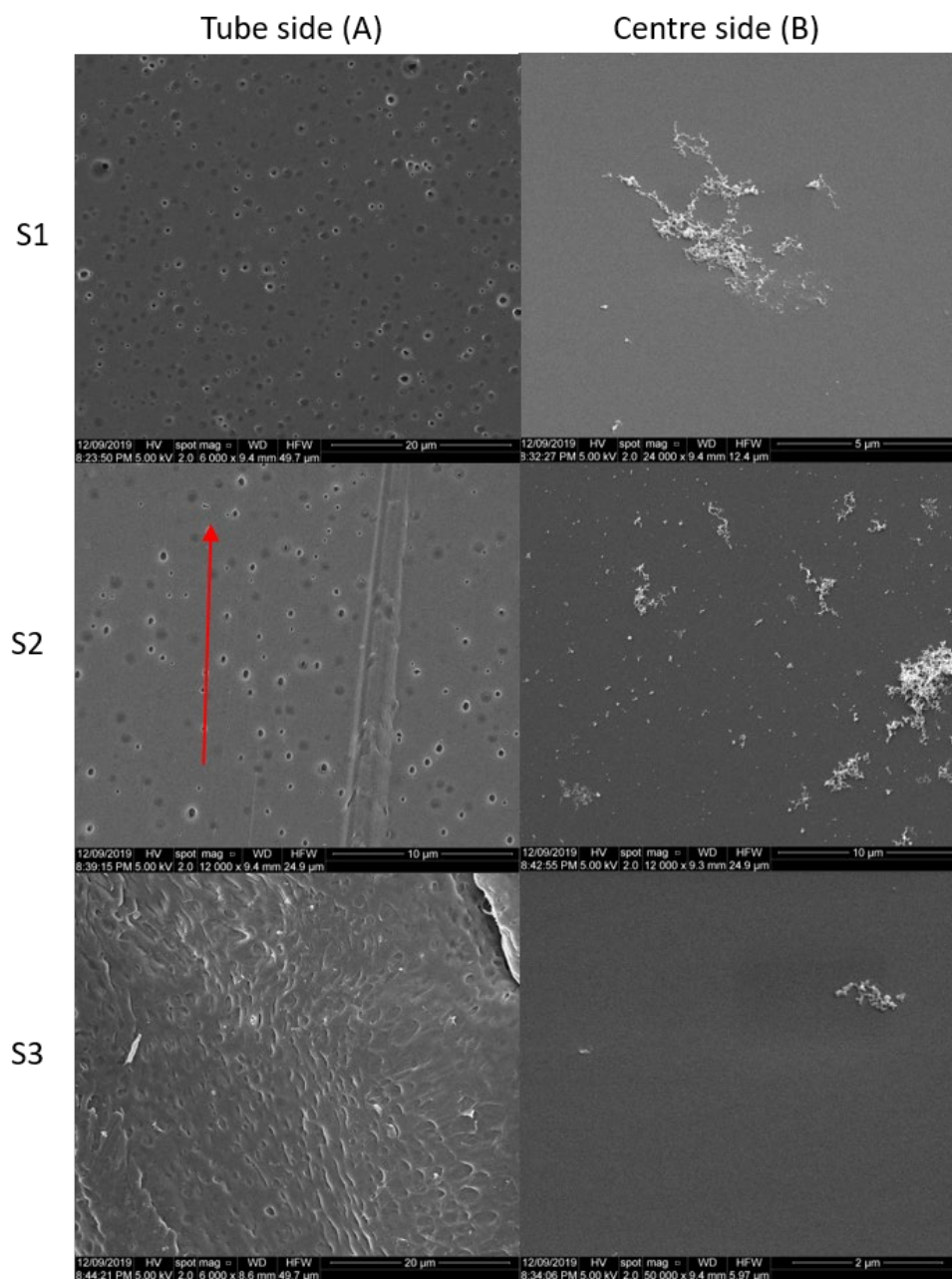


Figure D. 13. SEM images of S1, S2, and S3 from both sides (left: bottom of the thin film (A), right; upper side of the thin-film (B) of the thin-film processed in toluene at 3.5k rpm,  $\theta = 45^\circ$ , room temperature, for 30 min.

#### Sample 4:

Rotational speed : 7k rpm

Tilt angle,  $\theta$  : 30°

Solvent : Toluene

Time : 30 min

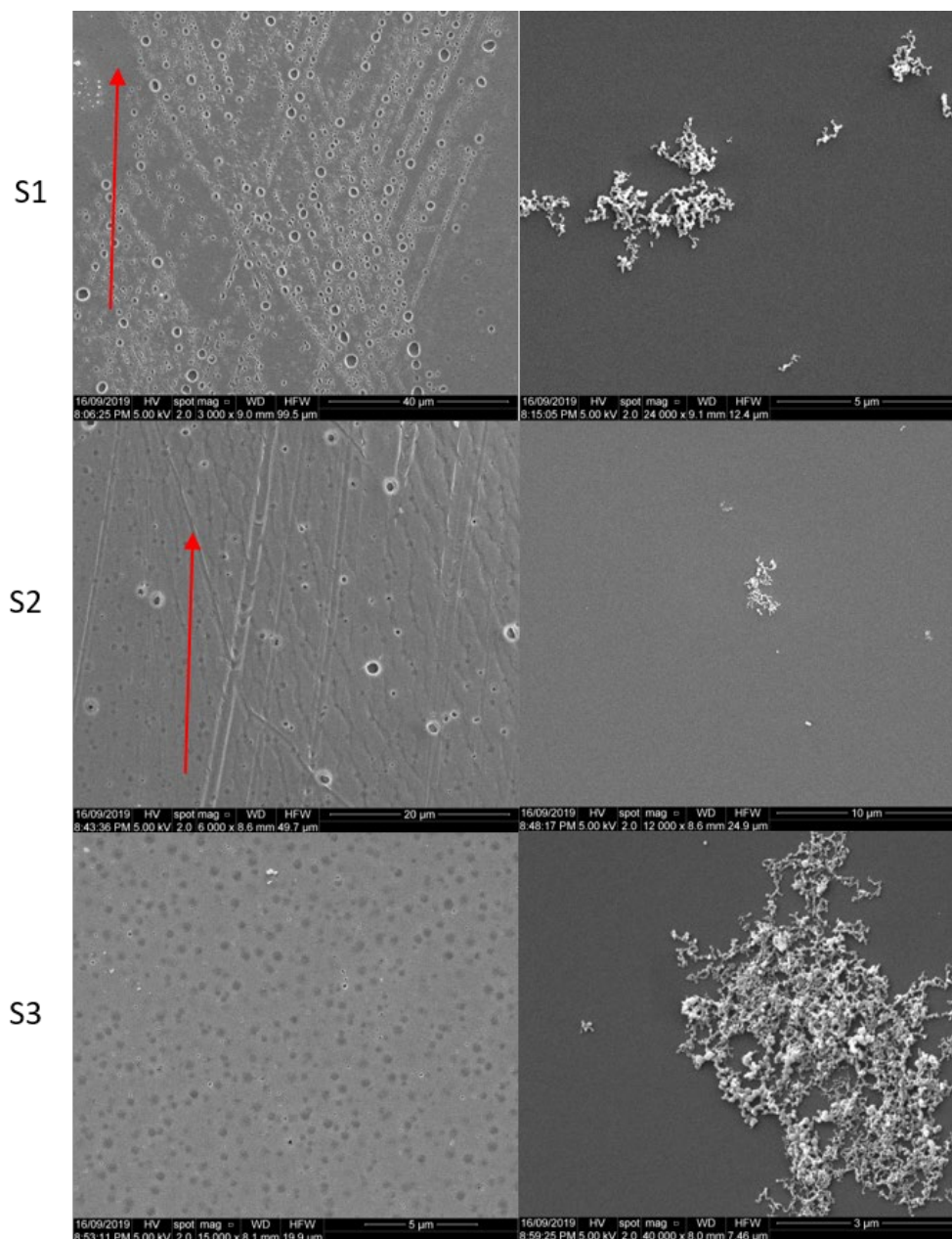


Figure D. 14. SEM images of S1, S2, and S3 from both sides (left: bottom of the thin film (A), right; upper side of the thin-film (B) of the thin-film processed in toluene at 7k rpm,  $\theta = 30^\circ$ , room temperature, for 30 min.

### Sample 5:

Rotational speed : 5k rpm

Tilt angle,  $\theta$  :  $30^\circ$

Solvent : Toluene

Time : 30 min

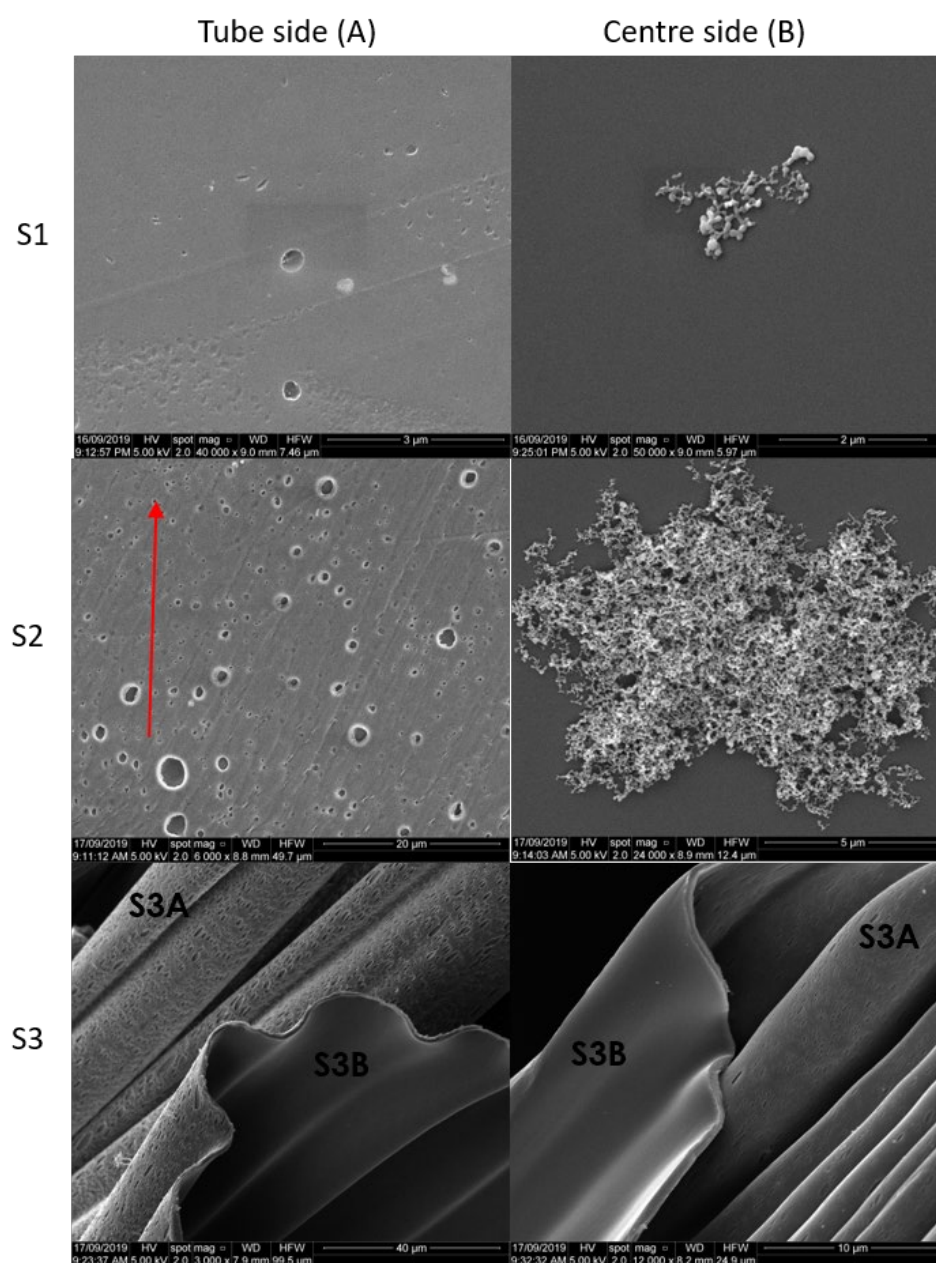


Figure D. 15. SEM images of S1, S2, and S3 from both sides (left: bottom of the thin film (A), right; upper side of the thin-film (B) of the thin-film processed in toluene at 5k rpm,  $\theta = 30^\circ$ , room temperature, for 30 min.

### Sample 6:

Rotational speed : 3.5k rpm

Tilt angle,  $\theta$  : 30°

Solvent : Toluene

Time : 30 min

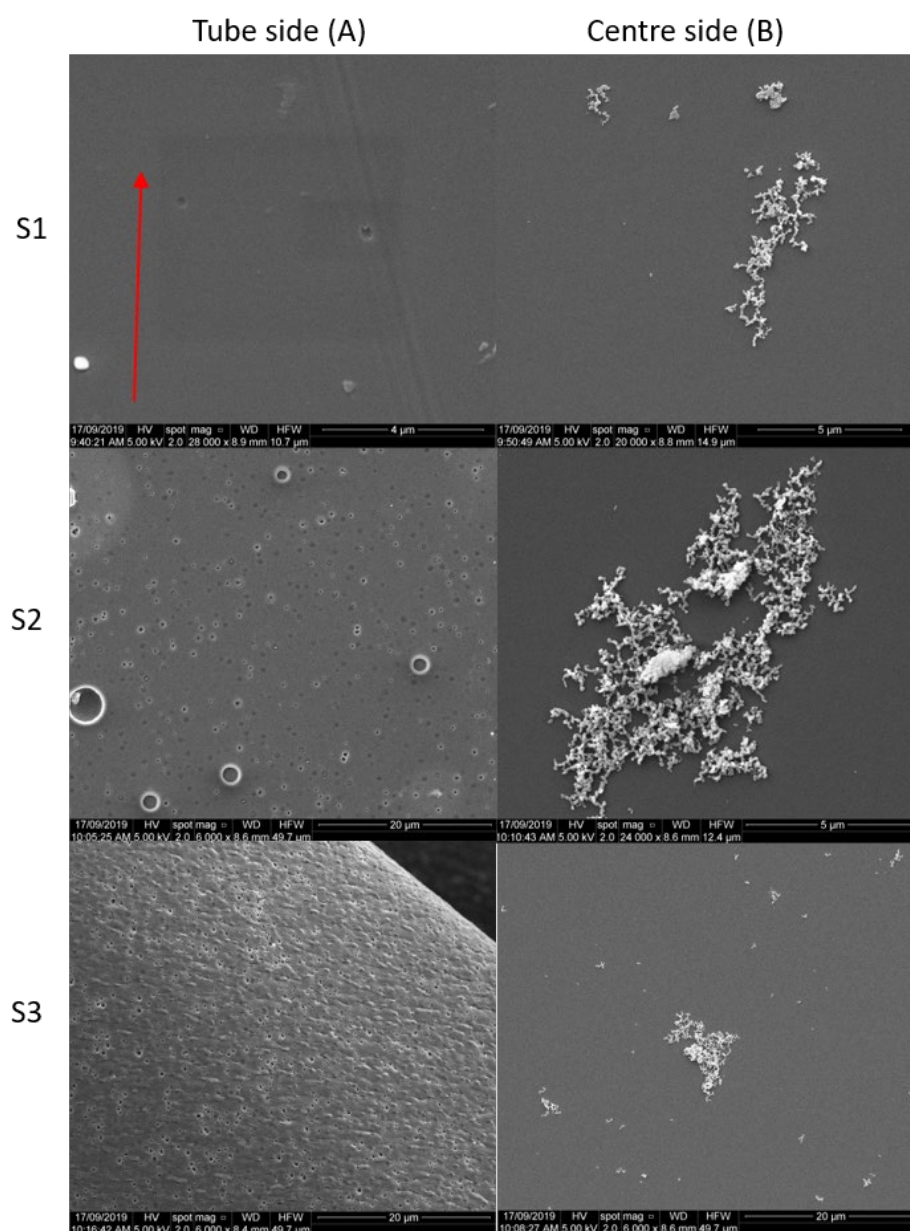


Figure D. 16. SEM images of S1, S2, and S3 from both sides (left: bottom of the thin film (A), right; upper side of the thin-film (B) of the thin-film processed in toluene at 3.5k rpm,  $\theta = 30^\circ$ , room temperature, for 30 min.



### Sample 7:

Rotational speed : 7k rpm

Tilt angle,  $\theta$  :  $60^\circ$

Solvent : Toluene

Time : 30 min

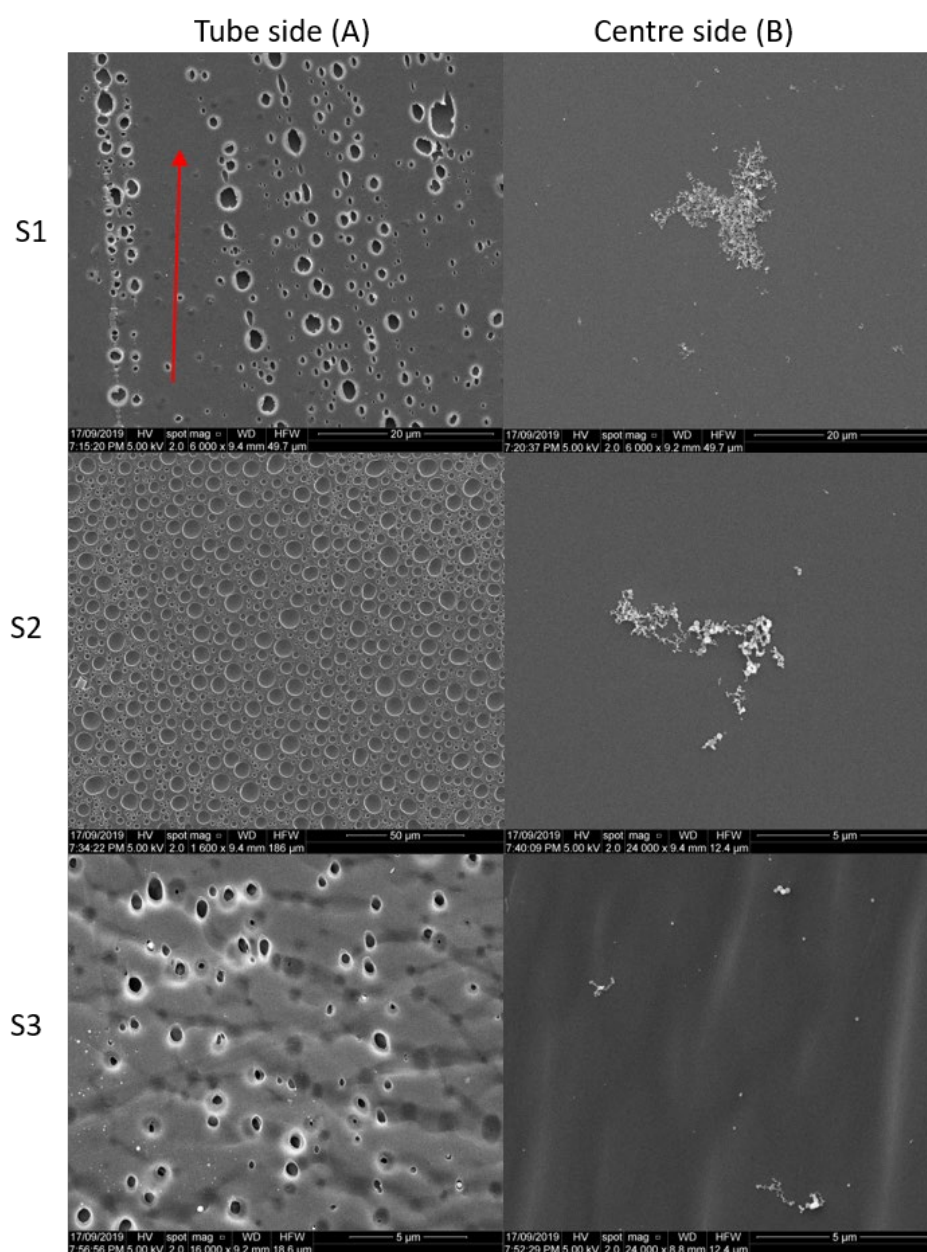


Figure D. 17. SEM images of S1, S2, and S3 from both sides (left: bottom of the thin film (A), right; upper side of the thin-film (B) of the thin-film processed in toluene at 7k rpm,  $\theta = 60^\circ$ , room temperature, for 30 min.

**Sample 8:**

Rotational speed : 5k rpm

Tilt angle,  $\theta$  : 60°

Solvent : Toluene

Time : 30 min

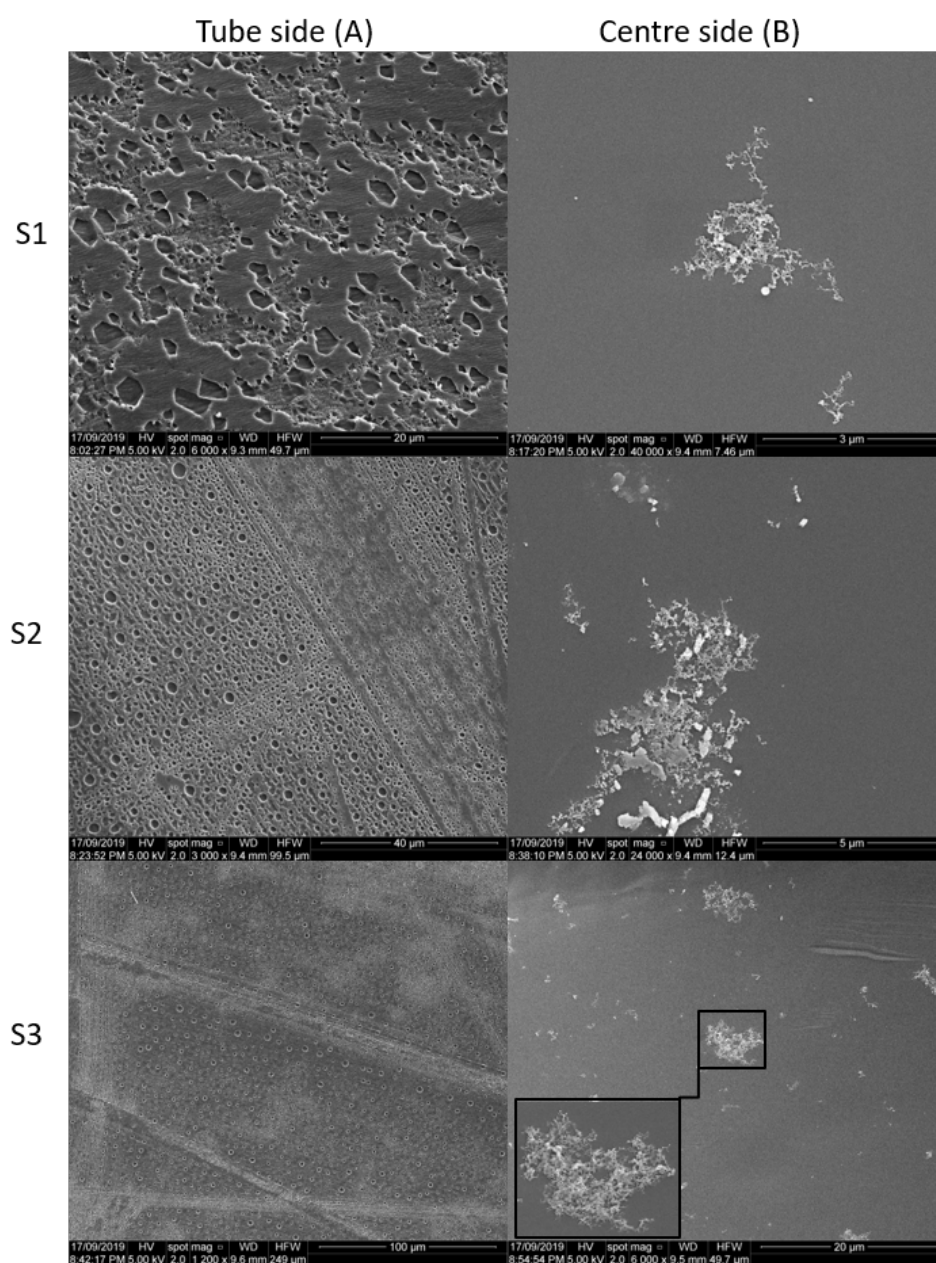


Figure D. 18. SEM images of S1, S2, and S3 from both sides (left: bottom of the thin film (A), right; upper side of the thin-film (B) of the thin-film processed in toluene at 5k rpm,  $\theta = 60^\circ$ , room temperature, for 30 min.

### Sample 9:

Rotational speed : 3.5k rpm

Tilt angle,  $\theta$  : 60°

Solvent : Toluene

Time : 30 min

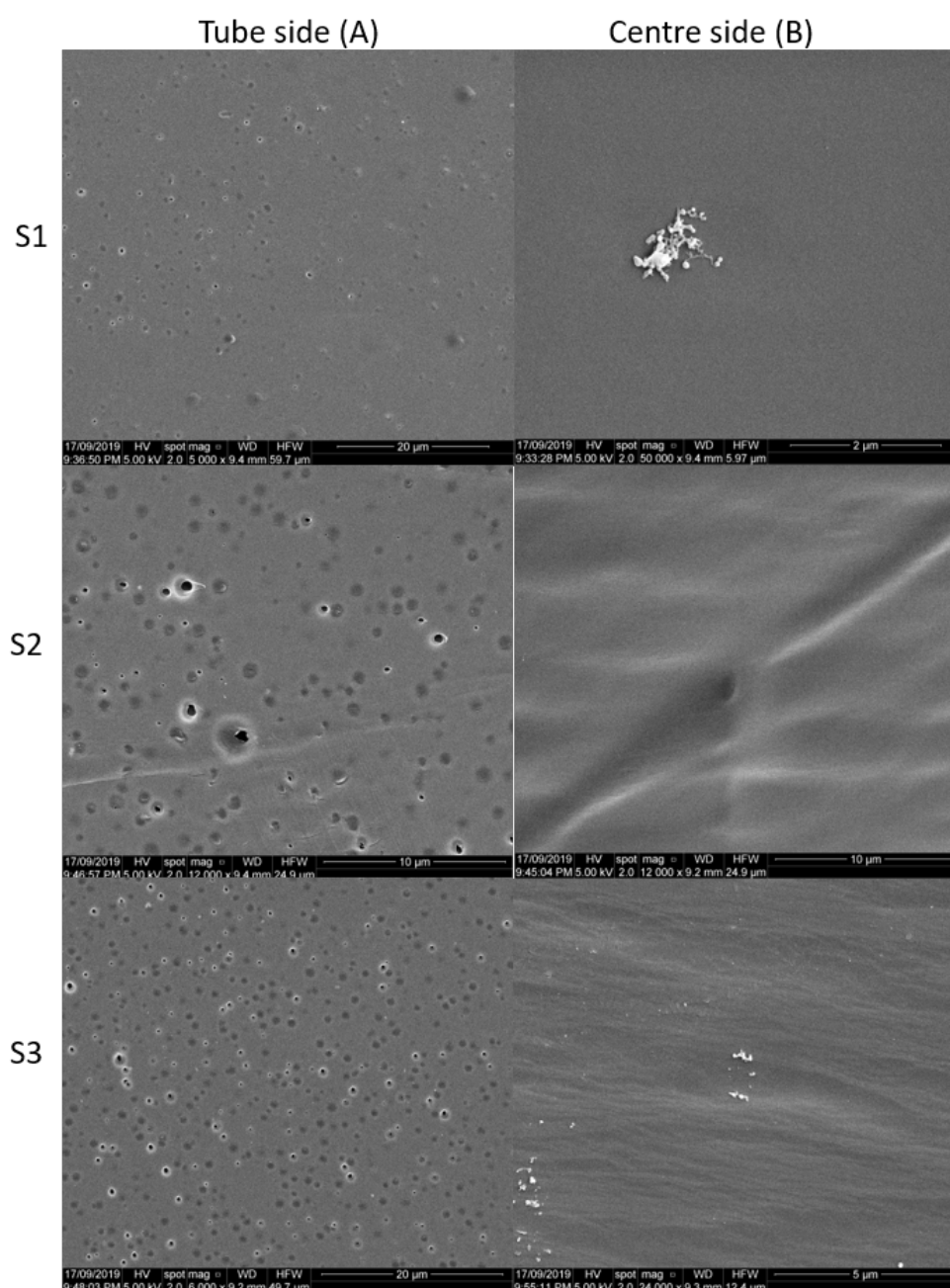


Figure D. 19. SEM images of S1, S2, and S3 from both sides (left: bottom of the thin film (A), right; upper side of the thin-film (B) of the thin-film processed in toluene at 3.5k rpm,  $\theta = 60^\circ$ , room temperature, for 30 min.

Figure D. 3 and Figure D. 10 show that thin-films of PSF formed in the VFD (20 mm OD, 17.5 mm ID tube) involving evaporation of a DCM solution of the polymer, have smooth surfaces, both on the surface in contact with the glass, and the surface exposed to air. Processing then with toluene in the tube reveals indentations/holes on the surface attached to the glass, with periodic regularity and alignment with the direction of rotation of the tube, for  $\theta = 45^\circ$ , for rotational speeds  $\geq 5$  k rpm, with the indentations/holes smaller and more uniform compared with those created at 5k rpm, and for  $\omega = 3.5$  k rpm the films have fewer holes, with no evidence of them being ordered. This finding for toluene is in accord with the signature for toluene, where double helical flow prevails  $> 6$  k rpm, (Figure 2 in the main manuscript). Processing of toluene solutions at  $\theta = 30$  and  $60^\circ$  also show ‘molecular drilling’, but these angles are not optimal for any applications of the VFD. While the upper surfaces (SB) of the films are almost devoid of holes, regions of agglomerated particles of the polymer are evident, ca 100 nm in diameter, for example in Figure D. 12. These particles are likely formed during the ‘molecular drilling’ process, when the double helical flow strikes the surface of the tube, Figure D. 9, but attempts to measure them using DLS were unsuccessful, and we then turned to using small angle neutron scattering (SANS) for further characterisation, with the findings reported below.

## **D.6. Real time VFD processing small angle neutron scattering (SANS)**

Understanding the effect of the fluid flow in the VFD (confined mode) was explored using real time SANS. This was to determine any change in morphology of the surface of the polymer film and identify any nanoparticles of the polymer extruded from the polymer film during ‘molecular drilling’ (double helical flow) into the dynamic thin film of toluene.

A 20 mm OD (17.5 mm ID) VFD quartz tube containing 2 mL of toluene-d8 was rotated at 5k rpm and the scattered neutrons were counted for 2 hours in both high and low Q-range, at 1.3 and 14-meter camera length respectively. Combining both Q-range data resulted in flat curves shown in Figure D. 20. The internal surface of quartz VFD tubes were then coated with a PSF thin-film at  $\theta = 5^\circ$ ,  $\omega = 6$  k rpm, at room temperature during 15 min (as discussed above). 5, 2 and 1 mL of toluene-d8 was then added to these tubes and individually studied using real-time SANS, for  $\omega = 3.5$  k, 5k and 7k rpm, respectively, using both 1.3 and 14-meter camera



lengths. Scattering for the whole Q-ranges of PSF films in the presence of toluene-d8 at these rotational speeds are plotted in Figure D. 21.

The recorded scattering curves for toluene-d8 (no PSF film in the tube) are similar to scattering curves for toluene-d8 and PSF film, taking into account thinner films of toluene for high rotational speeds. The thickness of the PSF thin-film was  $\sim 4 \mu\text{m}$  which is out of range of SANS capabilities, as is the case for pores of the size commensurate with the morphology of the films post VFD processing, established using SEM. Importantly there was no scattering associated with nanoparticles of polymer present in solution during the processing. The presence of such particles was expected given the presence of small amounts of aggregates of them post VFD processing, albeit only on the upper surface of the PSF film (SB), ca 100 nm in diameter. Thus, such particles present during processing are in low concentration, beyond the level of perturbing the scattering curve for the *in situ* SANS experiments. This finding is consistent with such generated particles being constantly taken up in the polymer film, driven by the associated centrifugal force in the VFD, with the only particles present representing a snapshot of nanoparticles in equilibrium with the polymer film. Moreover, this is also consistent with the smoothing out of holes generated by the ‘molecular drilling’, with their presence inferred from the pocket of liquid trapped on the surface of the PSF film in contact with the surface.

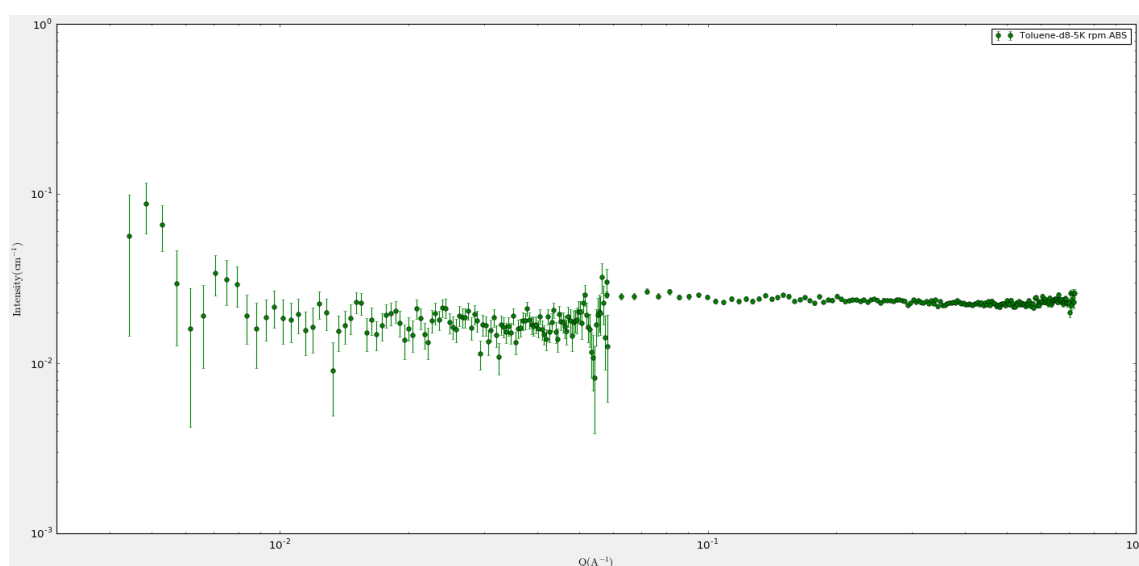


Figure D. 20. Real time SANS scattering in the VFD for 2 mL of toluene-d8 in a 20 mm OD quartz tube (no PSF coating) rotated at 5k rpm for 2 hours, at room temperature,  $\theta = 45^\circ$  [1].

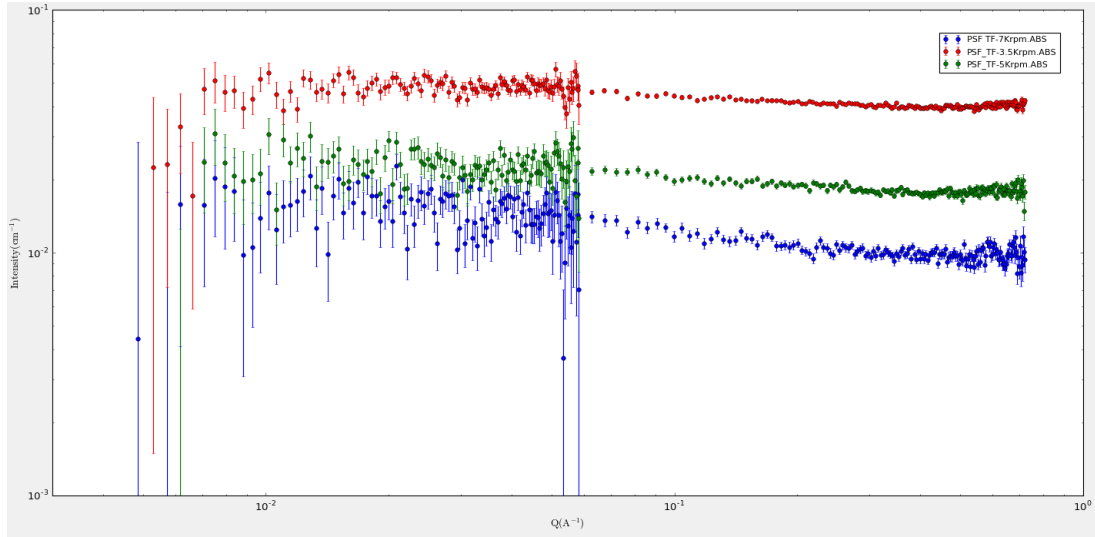


Figure D. 21. Real time SANS scattering in the VFD for toluene-d8 in a PSF coated 20 mm OD quartz rotated at 3.5k, 5k and 7k rpm (using 5, 2 and 1 mL of toluene-d8, respectively), for 2 hours room temperature,  $\theta = 45^\circ$  [1].

## D.7. Representation of the different fluid flows in the VFD

The above results provide a hypothesis of molecular drilling in polymeric thin film which corresponds to the double helical flow in the VFD under certain conditions. This results supported by the results of the other parts of this research (refer to the main manuscript) [1], provide a model of fluid flow within the VFD that can empirically describe the behaviour that is thought to occur to produce the very real nanostructures observed, Figure D. 22.

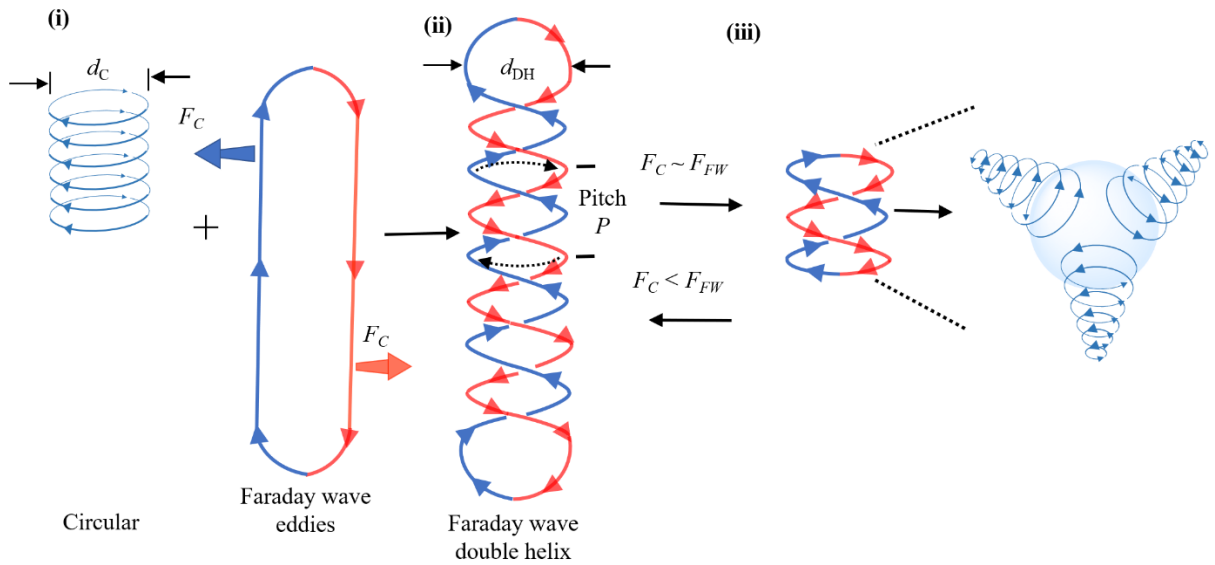


Figure D. 22. Representation of the different fluid flows, and the collapse of circular Coriolis force flow and double-helical flow from Faraday waves into spicular flow [1].

At the minimum mixing time, the high shear circular flow, at most a few  $\mu\text{m}$  in diameter, is thought to prevail. Beyond this rotational speed, the model considers Faraday waves combining with Coriolis circular flow, with the lines of high shear fluid flow on the surface of a spicule. At greater rotational speeds as the mixing times peak, Faraday waves dominate, where double-helical eddies associated with them are normal to the thin film. For other liquids, double-helical flow dominates across values of rotational speed. Eddies associated with Faraday waves are twisted into double-helices by the circular flow, with flow up one strand of each helix, and down the other. Superimposing the associated vectors of flow with those of the circular flow, the length scales of the flows are comparable ( $F_C \sim F_{FW}$ ), which necessarily creates a flow of liquid around a sphere [1]. Here a full turn of the double-helix being the diameter of the double-helical Faraday waves eddies corresponds to the diameter of the circular flow, Figure D. 22.

## D.8. Conclusion

From what have been elaborated in this chapter about molecular drilling and double helical flow along with the results obtained from the other parts of this research (refer to the full paper) [1], we have established the topological features of high shear fluid flow in the vortex fluidic device (VFD) at sub-micron dimensions, at a tilt angle of  $45^\circ$ , which corresponds to the optimal angle for a myriad of applications of the device [3-8]. The rotational speeds for high shear circular flow ( $F_C > F_{FW}$ ), spicular flow ( $F_C \sim F_{FW}$ ) and double-helical flow ( $F_C < F_{FW}$ ) can be determined by measuring changes in temperature and mixing times, and average film thickness as a unique signature for any liquid. Sudden increases in temperature of the liquid correspond to discontinuities in fluid flow, with a sudden reduction in film thickness for increasing rotational speed rather than continuously changing film thickness, as a new phenomenon in thin films. The present work also established that the VFD is effective in creating systems in non-equilibrium states, in establishing a new form of crystallization induced by shear stress, adding to the ubiquitous methods of sublimation, cooling and evaporating, and also stripping away surfactants [21]. Also of note is the ability to create novel spicule structures which map out the high mass topologies in a liquid, or the ‘negative’ of these structures where material formed in the spicular fluid flow under high shear assemble

at the closest points of low shears, in between the spicules. With the VFD and an understanding of its operating regimes, structures are moulded with predictable shapes by the mechanical force of fluid flow and diffusion of species within the liquid. Fundamentally, the vast differences in the morphology of the resultant structures between the three topological fluid flow regimes must result from unique diffusion behaviour within the liquid. Thus, the VFD demonstrates the ability to mediate or control both the forces exerted by the liquid on nanostructures and the diffusion of species supplied to their surface. The findings also have implications on using shear stress driven boundary mediated control of fluid flow for controlling self-assembly and chemical reactions under non-equilibrium conditions, and manipulating cells under tuneable stress regimes, which are areas we are currently investigating.

## D.8. Chapter references

1. Alharbi, T.M.D., et al., *Sub-micron moulding angled vortex fluid flow*. Chem.Rxiv, 2020: p. <https://doi.org/10.26434/chemrxiv.13141352.v1>.
2. Ross, T.D., et al., *Controlling organization and forces in active matter through optically defined boundaries*. Nature, 2019. **572**(7768): p. 224-229.
3. Britton, J., et al., *Vortex Fluidic Chemical Transformations*. Chem. Eur. J., 2017. **23**(1521-3765 ).
4. Britton, J., et al., *Accelerating Enzymatic Catalysis Using Vortex Fluidics*. Angewandte Chemie International Edition, 2016. **55**(38): p. 11387-11391.
5. Yuan, T.Z., et al., *Shear-stress-mediated refolding of proteins from aggregates and inclusion bodies*. Chembiochem : a European journal of chemical biology, 2015. **16**(3): p. 393-396.
6. Alharbi, T.M.D., et al., *Controlled slicing of single walled carbon nanotubes under continuous flow*. Carbon, 2018. **140**: p. 428-432.
7. Chen, X., J.F. Dobson, and C.L. Raston, *Vortex fluidic exfoliation of graphite and boron nitride*. Chem. Commun., 2012. **48**: p. 3703-3705.
8. Wahid, M.H., et al., *Microencapsulation of bacterial strains in graphene oxide nano-sheets using vortex fluidics*. RSC Advances, 2015. **5**(47): p. 37424-37430.
9. Whitesides, G.M., *The origins and the future of microfluidics*. Nature, 2006. **442**(7101): p. 368-373.
10. Brechtelsbauer, C., et al., *Evaluation of a Spinning Disc Reactor for Continuous Processing1*. Organic Process Research & Development, 2001. **5**(1): p. 65-68.
11. Chen, X., et al., *Controlling nanomaterial synthesis, chemical reactions and self assembly in dynamic thin films*. Chemical Society Reviews, 2014. **43**(5): p. 1387-1399.
12. Lodha, H., R. Jachuck, and S. Suppiah Singaram, *Intensified Biodiesel Production Using a Rotating Tube Reactor*. Energy & Fuels, 2012. **26**(11): p. 7037-7040.
13. Sitepu, E.K., et al., *Continuous flow biodiesel production from wet microalgae using a hybrid thin film microfluidic platform*. Chemical Communications, 2018. **54**(85): p. 12085-12088.
14. Solheim, T.E., et al., *Neutron imaging and modelling inclined vortex driven thin films*. Scientific Reports, 2019. **9**(1): p. 2817.
15. Britton, J., S.B. Dalziel, and C.L. Raston, *Continuous flow Fischer esterifications harnessing vibrational-coupled thin film fluidics*. RSC Advances, 2015. **5**(3): p. 1655-1660.
16. Britton, J., S.B. Dalziel, and C.L. Raston, *The synthesis of di-carboxylate esters using continuous flow vortex fluidics*. Green Chemistry, 2016. **18**(7): p. 2193-2200.
17. Alharbi, T.M.D., et al., *Shear stress mediated scrolling of graphene oxide*. Carbon, 2018. **137**: p. 419-424.

18. Vimalanathan, K., et al., *Surfactant-free Fabrication of Fullerene C60 Nanotubules Under Shear*. Angewandte Chemie International Edition, 2017. **56**(29): p. 8398-8401.
19. Chen, P., et al., *Microscale Assembly Directed by Liquid-Based Template*. Advanced Materials, 2014. **26**(34): p. 5936-5941.
20. Alsulami, I.K., et al., *Controlling the growth of fullerene C60 cones under continuous flow*. Chemical Communications, 2018. **54**(57): p. 7896-7899.
21. Rosi, N.L., et al., *Hydrogen Storage in Microporous Metal-Organic Frameworks*. Science, 2003. **300**(5622): p. 1127.